The development and application of structural priors for diffuse optical imaging in infants from newborn to two years of age

Liam Hywel Collins Jones

A thesis submitted for the degree of Doctor of Philosophy (Ph.D.) at University College London

Research Degree: Medical Imaging [RRDMEISING01]

Department of Medical Physics and Biomedical Engineering, UCL

2022

Declaration

I, Liam Hywel Collins Jones confirm that the work presented in this thesis is my own. Where information has been derived from other sources, I confirm that this has been indicated in the thesis.

Liam Hywel Collins Jones

Abstract

This thesis describes the development and application of age-appropriate structural priors to improve the localisation accuracy of diffuse optical tomography (DOT) approaches in infants aged from birth to two years of age. Knowledge of the target cranial anatomy, known as a structural prior, is required to produce three-dimensional images localising concentration changes to the cortex. A structural prior would ideally be subject-specific, i.e. derived from structural magnetic resonance imaging (MRI) data from each specific subject. Requiring a structural scan from every infant participant, however, is not feasible and undermines many of the benefits of DOT.

A review was conducted to catalogue available infant structural MRI data, and selected data was then used to produce structural priors for infants aged 1- to 24-months. Conventional analyses using functional near-infrared spectroscopy (fNIRS) implicitly assume that head size and array position are constant across infants. Using DOT, the validity of assuming these parameters constant in a longitudinal infant cohort was investigated. The results show that this assumption is reasonable at the group-level in infants aged 5- to 12-months but becomes less valid for smaller group sizes. A DOT approach was determined to illicit more subtle effects of activation, particularly for smaller group sizes and expected responses.

Using state-of-the-art MRI data from the Developing Human Connectome Project, a database of structural priors of the neonatal head was produced for infants aged pre-term to term-equivalent age. A leave-one-out approach was used to determine how best to find a match between a given infant and a model from the database, and how best to spatially register the model to minimise the anatomical and localisation errors relative to subject-specific anatomy. Model selection based on the 10/20 scalp positions was determined to be the best method (of those based on external features of the head) to minimise these errors.

Impact statement

The infant brain undergoes significant functional changes in early life. To study functional development, magnetic resonance imaging (MRI) can be applied; however, MRI does not permit the brain to be studied in infants when awake, nor does it enable the brain to be studied in naturalistic environments. Employing diffuse optical tomography (DOT), which is silent, portable and much more motion tolerant than MRI, will enable these constraints to be overcome. Despite this, DOT requires prior structural information to produce images, and requiring structural MRI data to be acquired from every infant participant undermines many of the benefits of DOT.

The work in this thesis has led to:-

- The development and release of a large-scale database of individual-level structural priors for infants, negating the requirement of subject-specific structural MRI data.
- The development of structural priors for infants aged 6-24 months of age.
- A demonstration of the importance of array positioning, head model selection and image reconstruction in longitudinal populations.
- A study of how head model selection methods affect optical localisation error.

There have been several established outputs from the work presented in this thesis. The work presented in Chapter 2 to produce a structural prior for 6-month-old infants was employed to support the first functional imaging study using wearable high-density DOT hardware in infants. Further, the database of structural priors in Chapter 4 has been implemented to support the first study of resting state functional connectivity using wearable high-density DOT in infants. Chapter 3 demonstrates the validity of group-level fNIRS analyses in a longitudinal population, which validates findings in numerous previous infant fNIRS studies. The analysis methods developed throughout this PhD

project were applied in a collaboration with a research group at the University of Oxford to study executive function in a large cohort of infants, improving confidence in where activation is being localised in the brain.

The work presented in this thesis also opens possibilities for future impact.

- The production and validation of infant structural priors permits more sophisticated neuroimaging methodologies to be applied to expand knowledge of infant brain development in low-resource settings in low- and middle-income countries.
- The brain of pre-term neonates is particularly vulnerable to brain injury, which can lead to the development of cerebral palsy (CP). The database of neonatal structural priors produced in this project will improve the precision of bedside brain imaging to improve understanding of the neural basis of CP, leading to earlier identification of brain injury when the brain is most susceptible to treatment.
- It is known that differences in brain activation can be measured in infants before they begin to show signs of autism spectrum disorder (ASD), affecting at least 1 in 100 people in the UK. Early intervention is key to support the development of infants with ASD as best as possible. The techniques described in this thesis can be extended in future to develop methodologies enabling widespread brain imaging to identify infants who are likely to receive a future ASD diagnosis, enabling earlier intervention to be implemented.

Acknowledgements

Firstly, I would like to thank every member of the DOT-HUB research group for being enthusiastic, motivating and supportive.

I would like to thank everyone working as part of the BRIGHT project, whose innovative work has enabled me to carry out really exciting research. I thank Dr Chiara Bulgarelli for her tremendous help when it came to the intricacies of fNIRS data analysis. I thank Dr Anna Blasi for being supportive throughout my PhD. I thank Dr Sarah Lloyd-Fox for her much appreciated help with developing research ideas, for indispensable help with manuscript writing, and for going beyond to support me during uncertain times. I also thank Dr Sophie Moore for stepping in to keep my project on track.

I thank Dr Tomoki Arichi for hosting me at the Centre for the Developing Brain and Dr Tanya Poppe for helping expand my knowledge of neuroimaging.

I am thoroughly grateful for the help and support of Dr Sabrina Brigadoi. I have learnt an awful lot from Sabrina and she's been a reliable port of call for advice throughout my PhD.

I would like to thank my supervisors. I thank Prof Clare Elwell for taking me on as a PhD student and seeing potential in me, and inspiring me to pursue research. I thank Prof Jem Hebden for his support and guidance, particularly when it came to thesis writing and embarking on a research career. I would like to thank Dr Rob Cooper for being a cracking supervisor. Rob's support and enthusiasm has been fantastic. I am particularly grateful for Rob's encouragement, helping me transition from considering myself a student to considering myself a scientist.

Finally, I would like to thank my family. Diolch to my parents, Jill and Pete, who have always gone above and beyond to support me. I thank my sister Mererid and brother-in-law Dan for being stunningly encouraging. Mabli, croeso i'r byd!

My partner Fran has been thoroughly supportive and has been exceptionally helpful to get me through several tricky situations throughout my PhD – diolch. I give a huge thank you to my grandmother Mary for being enthusiastic, encouraging and inspiring.

This work has been supported by the EPSRC, grant reference EP/N509577/1.

The results in Chapters 4 and 5 were obtained using data made available from the Developing Human Connectome Project funded by the European Research Council under the European Union's Seventh Framework Programme (FP/2007-2013)/ERC Grant Agreement no. (319456).

Publications relating to this thesis

Peer reviewed publications

Collins-Jones, L. H., Arichi, T., Poppe, T., Billing, A., Xiao, J., Fabrizi, L., Brigadoi, S., Hebden, J. C., Elwell, C. E., & Cooper, R. J. (2021). Construction and validation of a database of head models for functional imaging of the neonatal brain. *Human Brain Mapping*, *42*(3), 567-586. https://doi.org/10.1002/hbm.25242

Collins-Jones, L. H., Cooper, R. J., Bulgarelli, C., Blasi, A., Katus, L., McCann, S., Mason, L., Mbye, E., Touray, E., Ceesay, M., Moore, S. E., Lloyd-Fox, S., & Elwell, C. E. (2021). Longitudinal infant fNIRS channel-space analyses are robust to variability parameters at the group-level: an image reconstruction investigation. *NeuroImage*, *237*, 118068. https://doi.org/10.1016/j.neuroimage.2021.118068

Blanco, B., Molnar, M., Carreiras, M., **Collins-Jones, L. H.**, Rosas, E. E. V., Cooper, R. J., & Caballero-Gaudes, C. (2021). Group-level cortical functional connectivity patterns using fNIRS: assessing the effect of bilingualism in young infants. *Neurophotonics*, *8*(2), 1–19. https://doi.org/10.1117/1.NPh.8.2.025011

Frijia, E. M., Billing, A., Lloyd-Fox, S., Vidal Rosas, E., **Collins-Jones, L.**, Crespo-Llado, M. M., Amadó, M. P., Austin, T., Edwards, A., Dunne, L., Smith, G., Nixon-Hill, R., Powell, S., Everdell, N. L., & Cooper, R. J. (2021). Functional imaging of the developing brain with wearable high-density diffuse optical tomography: A new benchmark for infant neuroimaging outside the scanner environment. *NeuroImage*, *225*, 117490. https://doi.org/10.1016/j.neuroimage.2020.117490

Zhao, H., Frijia, E. M., Rosas, E. V., **Collins-Jones, L.**, Smith, G., Nixon-Hill, R., Powell, S., Everdell, N. L., & Cooper, R. J. (2021). Design and validation of a mechanically flexible and ultra-lightweight high-density diffuse optical tomography system for functional neuroimaging of newborns. *Neurophotonics*, *8*(1), 1–18. https://doi.org/10.1117/1.NPh.8.1.015011

Siddiqui, M.F., Pinti, P., Lloyd-Fox, S., Jones, E. J., Brigadoi, S., **Collins-Jones, L.**, Tachtsidis, I., Johnson, M.H., & Elwell, C. E. (2022). Regional Haemodynamic and Metabolic Coupling in Infants. *Frontiers in Human Neuroscience*, 15, 780076. https://doi.org/10.3389/fnhum.2021.780076

Conference talks

Collins-Jones, L. H., Elwell, C.E., & Cooper, R. J., Neonatal Head Model Selection to Improve Spatial Localisation in Diffuse Optical Tomography When Subject-Specific Structural Data is Unavailable. *European Conference on Biomedical Optics*, **invited speaker**, online, June 2021. Abstract: http://opg.optica.org/abstract.cfm?URI=ECBO-2021-EM2C.1

Collins-Jones, L. H., Elwell, C.E., & Cooper, R. J., Neonatal Head Model Selection to Improve Spatial Localisation in Diffuse Optical Tomography When Subject-Specific Structural Data is Unavailable. *BioMedEng21*, Sheffield, UK, September 2021.

Collins-Jones, L. H., Arichi, T., Poppe, T., Hebden, J.C., Elwell, C.E., & Cooper, R. J., Construction and Validation of a Database of Neonatal Structural Priors for Use in Diffuse Optical Tomography. *BioMedEng19*, London, UK, September 2019.

Conference posters

Collins-Jones, L. H., Arichi, T., Poppe, T., Billing, A.N., Xiao, J., Brigadoi, S., Hebden, J.C., Elwell, C.E., & Cooper, R. J., Validating the use of individual-level structural prior matching for neonatal functional neuroimaging. *Organisation of Human Brain Mapping Annual Meeting*, online, June 2020.

Collins-Jones, L. H., Cooper, R. J., Blasi, A., Lloyd-Fox, S., McCann, S., Kischkel, L., Mason, L., Arichi, T., Hebden, J. C., The BRIGHT project team, & Elwell, C. E., Advancing optical methods to reconstruct the first images of infant functional activation in Africa. *Organisation of Human Brain Mapping Annual Meeting*, Rome, Italy, June 2019.

Collins-Jones, L. H., Cooper, R. J., Hebden, J.C., & Elwell, C. E., A 4D infant head atlas for use in optical image reconstruction of brain function over the first two years of life. *fNIRS 2018*, Tokyo, Japan, October 2018.

Collins-Jones, L. H., Arichi, T., Poppe, T., Billing, A.N., Xiao, J., Hebden, J.C., Elwell, C.E., & Cooper, R. J., A Database of Individual Neonatal Structural Priors for Use in Diffuse Optical Tomography. *fNIRS UK*, Birmingham, UK, September 2019.

Collins-Jones, L. H., Cooper, R. J., Hebden, J.C., & Elwell, C. E., A 4D infant head atlas for use in optical image reconstruction of brain function over the first two years of life as part of the Brain Imaging in Global Health (BRIGHT) project. *UCL Neuroscience Symposium*, London, UK, June 2018.

Pre-prints

Fiske, A., de Klerk, C., Lui, K. Y. K., **Collins-Jones, L. H.**, Hendry, A., Greenhalgh, I., Hall, A., Scerif, G., Dvergsdal, H., & Holmboe, K. (2021). The Neural Correlates of Inhibitory Control in 10-month-old Infants: A Functional Near-infrared Spectroscopy Study. *PsyArXiv*. https://doi.org/https://doi.org/10.31234/osf.io/r8m9b

Blanco, B., Molnar, M., Carreiras, M., **Collins-Jones, L. H.**, Vidal, E., Cooper, R. J., & Caballero-Gaudes, C. (2020). Monolingual and bilingual infants rely on the same brain networks: Evidence from resting-state functional connectivity. *BioRxiv*, 2020.04.10.035469. https://doi.org/10.1101/2020.04.10.035469

Table of contents

List of figures

List of tables

Map of the 10/5 positions

The 10/5 system is a convention for describing positions on the scalp, originally intended for high-density electrode positioning in EEG (Oostenveld & Praamstra, 2001). The 10/5 positions will be referred to throughout this thesis. A map of the 10/5 positions is provided below.

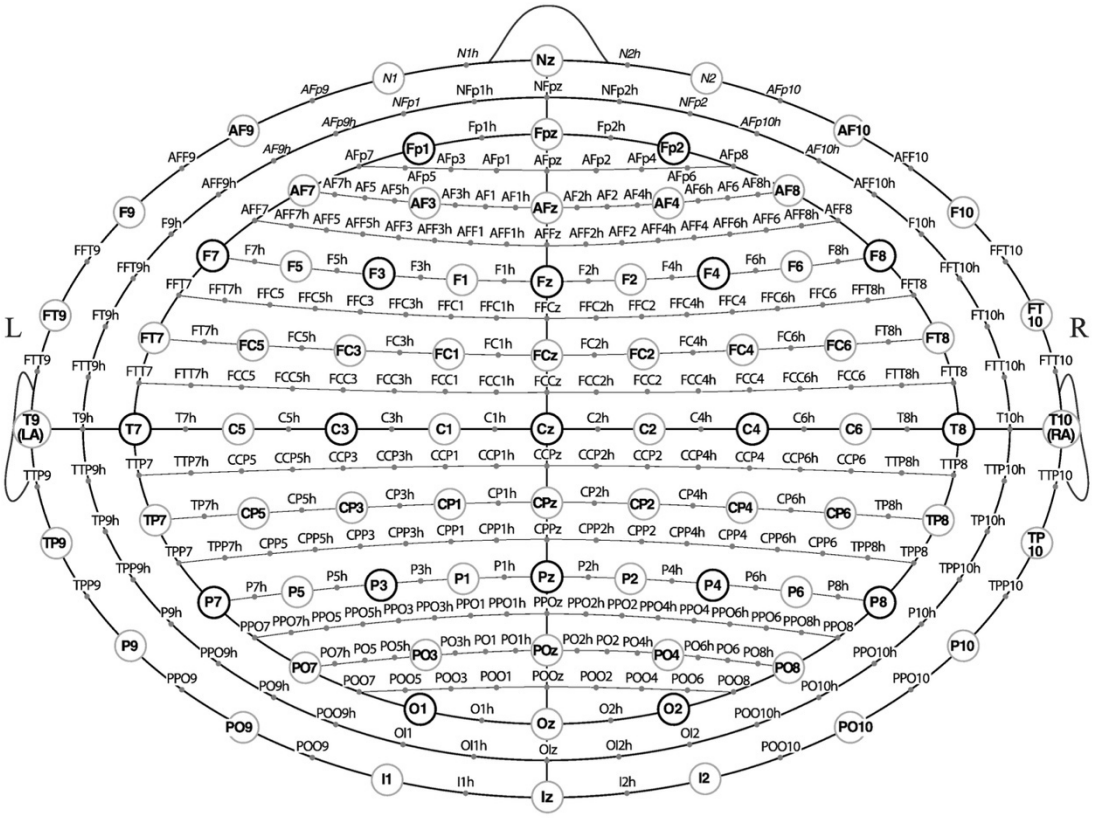

Figure 0.1: A map of the 10/5 positions. Figure adapted from Tsuzuki & Dan (2014), licensed under CC BY 3.0.

Chapter 1

Introduction

1.1 An introduction to biomedical optics

Biomedical optics is the study of how light interacts with tissue. Two main phenomena determine light transport in tissue, which are both wavelength dependent (Bigio, 2016):-

1. Absorption, a process where energy from a photon is taken by the medium through which the light is travelling, resulting from the interaction of light with various compounds found in tissue.
2. Scattering, which describes a range of light-tissue interactions resulting in the direction of a photon being altered.

1.1.1 Absorption

1.1.1.1 Lambert-Bouguer law

The Lambert-Bouguer law describes the absorption of light within an absorbing medium. In the eighteenth century, Pierre Bouguer (1698-1758) observed that within a purely absorbing material composed of successive layers, each with identical thickness, the absorbed fraction of a radiation beam with intensity I is exclusively dependent on the layer thickness ∂d. Johann Lambert (1728-1777) expressed this mathematically, which can take the form

$$\frac{\partial I}{I} = -\mu_a \partial d \tag{1.1}$$

where $\frac{\partial I}{I}$ is the fractional change in the intensity of the beam of radiation, and μ_a is the absorption coefficient, which is related to the probability of absorption per unit length. In a purely absorbing medium, the inverse of the absorption coefficient is the expected value (i.e. average) of the distance travelled by a photon before absorption.

Integrating Equation (1.1) yields the expressions

$$\int \frac{\partial I}{I} = \int -\mu_a \partial d \tag{1.2}$$

which, following integration, gives us

$$\ln(I) = -\mu_a d + constant. \tag{1.3}$$

When thickness d is zero, the constant of integration is equal to the natural logarithm of I at the point of incidence, denoted as I_0 such that

$$\ln(I) = -\mu_a d + \ln\,(I_0) \tag{1.4}$$

and therefore

$$I = \; I_0 \exp\,(-\mu_a d). \tag{1.5}$$

Equation (1.5) describes the intensity I of a pencil beam of light in a purely absorbing medium given the initial intensity of the beam, the distance travelled within the medium and the absorption coefficient of the medium.

1.1.1.2 Beer-Lambert law

The Beer-Lambert law develops on the Lambert-Bouguer law. August Beer (1825-1863) showed that, for an absorbing substance (termed a *chromophore*) dissolved in a non-absorbing solvent, the logarithm of light transmission (I/I_0) is proportional to the concentration of the solution multiplied by its *molar extinction coefficient* (Perrin, 1948; Swinehart, 1962).

From this, the absorption coefficient, μ_a, for a given chromophore can be defined as

$$\mu_a = \alpha c \tag{1.6}$$

where c is defined as chromophore concentration, and α is the molar extinction coefficient whose value which indicates the level of absorption in a substance per mole of chromophore per unit volume of solution per unit length of optical path (commonly given units $mol^{-1}L^{-1}cm^{-1}$).

As such, the Beer-Lambert law may be expressed as

$$I = I_0 \exp(-\alpha c d). \tag{1.7}$$

Attenuation, A, is defined as the intensity of light at incidence (that is, when $d = 0$) divided by the intensity of light after travelling a distance d within a medium, which is expressed as

$$A = \frac{I_0}{I} = \exp(\alpha c d). \tag{1.8}$$

Taking the natural logarithm of both sides gives us:-

$$\ln(A) = \alpha c d \tag{1.9}$$

Equation (1.9) has great implications for measuring changes in chromophore concentration, which will be explored in Section 1.1.3.2.

1.1.1.3 The near-infrared window

Equation (1.9) shows that variation in chromophore concentration will lead to variation in optical absorption in tissue. The main chromophores and absorbing compounds in tissue are (Bigio, 2016):-

- **Water**
- **Haemoglobin**: responsible for carrying oxygen in the blood circulation. This chromophore primarily exists in two forms, oxy- and deoxy-haemoglobin.
- **Lipids**: the primary constituent of fat.
- **Myoglobin**: responsible for storing oxygen in muscle tissue.
- **Beta-carotene**: An orange-coloured chromophore, which can be found in the liver and human fatty tissue.
- **Melanin**: a chromophore in the basal layer of the skin, responsible for absorbing ultraviolet light.
- **Cytochrome c**: a protein found in mitochondria, which is involved in electron transport to synthesise adenosine triphosphate. This chromophore's absorption property changes with its redox state, and so its concentration can be used as a marker of the metabolic rate in tissue.

The absorption spectrum for water, oxy-haemoglobin and deoxy-haemoglobin is shown in Figure 1.1. Above approximately 600 nm the absorption coefficients of both forms of haemoglobin begin to decrease substantially (Weissleder, 2001). A window can be seen in Figure 1.1 from 650 nm to 900 nm where a decrease in the absorption coefficient of oxy- and deoxy-haemoglobin coincides with the relatively low absorption of water. This is referred to as the *near-infrared window*, enabling light to penetrate deeper into tissue.

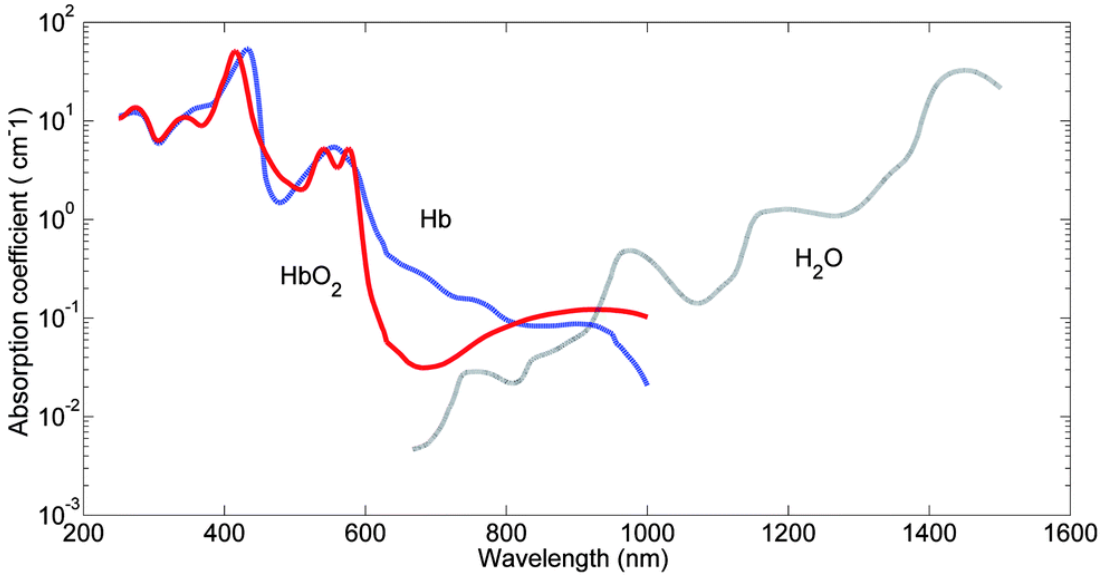

Figure 1.1: The absorption spectra of oxy-haemoglobin (red line), deoxy-haemoglobin (green line) and water (dark blue line). The near-infrared window exists between approximately 650 nm and 900 nm, where the relatively low absorption coefficients of the haemoglobins and water coincide. Figure adapted from Li et al. (2014), reprinted with permission of Royal Society of Chemistry[1].

1.1.2 Scatter

1.1.2.1 The scattering coefficient

An expression analogous to the Beer-Lambert law that describes the intensity of a beam of light within a purely scattering non-absorbing medium *along the direction of the beam* is

$$I = I_0 \exp(-\mu_s d). \tag{1.10}$$

Here, μ_s is the scattering coefficient, defined as the probability per path length that a photon will be scattered from its current direction of travel. Equation (1.10) assumes that there is negligible probability that any photon will undergo multiple scattering events in the medium. The scattering coefficient, therefore,

[1] Republished with permission of Royal Society of Chemistry, from Wavelength selection method based on test analysis of variance: Application to oximetry, Li W., Lin L., & Li G., *Analytical Methods*, *6*(4), Copyright (2014); permission conveyed through Copyright Clearance Center, Inc.

is not appropriate to describe light transport through tissue where many scattering events occur.

1.1.2.2 Anisotropy and the reduced scattering coefficient

Scattering is the dominant light-tissue interaction at near-infrared wavelengths. The anisotropy factor, g, is the average cosine of the scattering angle (Bigio, 2016): a value of 0 denotes scattering is completely isotropic within the medium, values approaching 1 denote the medium is highly forward scattering while values approaching -1 indicate the medium is highly backscattering. In tissue, g has values ranging from approximately 0.7 to 0.99 (Cheong et al., 1990) signifying that tissue is highly forward scattering.

Despite the forward scattering tendency, scattering is the dominant light-tissue interaction in the near-infrared range and so photons will lose their original directionality after travelling only a few millimetres through tissue. Near-infrared light within tissue can therefore be assumed to be isotropically distributed.

The reduced scattering coefficient, μ'_s, is defined as the number of isotropic scattering events per unit length, and can expressed as

$$\mu'_s = \mu_s(1 - g). \tag{1.11}$$

1.1.3 Measuring changes in concentration

1.1.3.1 The haemodynamic response

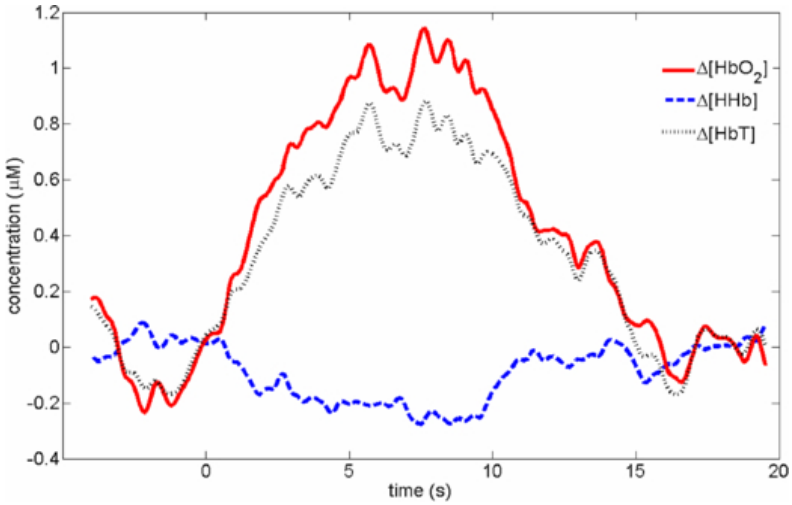

Figure 1.2: A typical infant haemodynamic response function. The increase in oxy-haemoglobin concentration (red line) reaches its peak between 5 and 10 s after the beginning of stimulus presentation (with block length 10 s). Total haemoglobin concentration (dotted black line) also increases though to a lesser extent than for oxy-haemoglobin due to a decrease in deoxy-haemoglobin concentration (dashed blue line). Figure taken from Correia et al. (2012). Reprinted with permission from IOP Publishing, Ltd[2].

Due to their high concentration in biological tissue, both oxy- and deoxy-haemoglobin are the dominant chromophores within the near-infrared window (Dehghani et al., 2009; Ferrari & Quaresima, 2012). When a brain region is activated, there is an instantaneous increase in electrical activity due to neuronal cell depolarisation which requires an increased metabolic demand, leading to an increase in blood flow to the activated region of the brain in the seconds that follow (León-Carrión & León-Domínguez, 2012). This increase in blood flow comes as a result of local capillary dilation, and this relationship

[2] Republished with permission of IOP Publishing, Ltd, from Three-dimensional optical topography of brain activity in infants watching videos of human movement, Correia, T., Lloyd-Fox, S., Everdell, N., Blasi, A., Elwell, C., Hebden, J. C., & Gibson, A., *Physics in Medicine & Biology*, *57*(5), Copyright (2012); permission conveyed through Copyright Clearance Center, Inc.

between neuronal activation and increased blood flow is known as neurovascular coupling.

This increase in blood flow to an activated region of the brain is known as the haemodynamic response. One may naïvely expect that, as a result of the increased metabolic demand, the concentration of deoxy-haemoglobin will increase following neuronal activation. However, due to an overcompensation in blood flow to the activated region through neurovascular coupling, an increase in oxy-haemoglobin concentration is observed alongside a decrease at a lesser magnitude in deoxy-haemoglobin concentration, leading to an overall increase in total haemoglobin concentration (Villringer & Chance, 1997). Figure 1.2 displays a typical haemodynamic response in an activated region of the brain in an infant (Correia et al., 2012). Due to its relationship to neuronal activation via neurovascular coupling, the haemodynamic response is used as a marker of brain activation.

1.1.3.2 Calculating changes in concentration

One could aim to use the Beer-Lambert law and near-infrared light to measure absolute haemoglobin concentration in the brain. However, there are several modifications to the Beer-Lambert law that need to be made which enable *changes* in haemoglobin concentration to be calculated.

During the timescale of an experiment investigating brain activation (approximately 1 hour), the concentration of most chromophores other than the haemoglobins and cytochrome c can be assumed to be constant. Though melanin is a strong absorber at near-infrared wavelengths, its concentration in tissue is much lower than haemoglobin. In addition, the absorption spectrum of cytochrome c is similar to that of haemoglobin; however, given the limited concentration of cytochrome c, perturbations in the redox state of this

chromophore due to changes in the cerebral metabolic rate will have little impact on the absorption spectrum of tissue.

Oxy- and deoxy-haemoglobin are the principal absorbing compounds in tissue in the near-infrared window. To measure changes in both oxy- and deoxy-haemoglobin, the Beer-Lambert law can be re-written as a sum of the concentration of these two chromophores ($c_{HbO}$and c_{HbR}) multiplied by their respective molar extinction coefficients (α_{HbO} and α_{HbO}) (Lloyd-Fox et al., 2010). However, in order to calculate the unknown concentrations of these two chromophores, two known wavelengths of near-infrared light are needed to illuminate the brain. Equation (1.9) can be rewritten as simultaneous equations for the case of two wavelengths, where the two measured attenuations are represented by A_{λ_1} and A_{λ_2} in the expressions

$$\ln(A_{\lambda_1}) = (\alpha_{HbO}(\lambda_1)c_{HbO} + \alpha_{HbR}(\lambda_1)c_{HbR})d \tag{1.12}$$

and

$$\ln(A_{\lambda_2}) = (\alpha_{HbO}(\lambda_2)c_{HbO} + \alpha_{HbR}(\lambda_2)c_{HbR})d. \tag{1.13}$$

Note that the molar extinction coefficients are wavelength dependent. The above expression can be solved for c_{HbO} and c_{HbR} when expressed in matrix form; this holds true for a purely absorbing medium in which the molar extinction coefficients of oxy- and deoxy-haemoglobin at each wavelength are known.

Tissue, in particular grey matter and white matter in the brain, is highly scattering (Fukui et al., 2003). The loss in intensity of near-infrared light probing the brain therefore cannot be solely attributed to absorption. Equation (1.12) and Equation (1.13) both assume that the attenuation of light in the medium can be solely attributed to absorption, which is not true for tissue.

Two new terms need to be considered. The first is G, which accounts for losses due to scattering. The next term is the differential pathlength factor, DPF (Kocsis et al., 2006; Sassaroli & Fantini, 2004), a correction factor which depends on the reduced scattering coefficient. Light will typically migrate along a tortuous path through tissue, and so DPF can be multiplied by the source-detector separation, d, to estimate the average distance travelled by a photon through the medium (Delpy et al., 1988; Wray et al., 1988):-

$$\ln(A) = \alpha c d \cdot DPF + G. \tag{1.14}$$

Age-dependent estimates for the DPF have been determined empirically (Duncan et al., 1995; Scholkmann & Wolf, 2013). Estimating G is near impossible because it is dependent on intensity losses due to scattering (Kocsis et al., 2006) which cannot be distinguished from losses due to absorption. However, an assumption is made that these scattering losses remain constant, even after an increase in chromophore concentration (Obrig & Villringer, 2003). As a result, if *changes* in attenuation are measured then *changes* in haemoglobin concentration can be calculated – for instance, the change in oxy- and deoxy-haemoglobin concentration after stimulus presentation compared to baseline can be measured (Delpy & Cope, 1997).

Subtracting the attenuation measured for a given wavelength (λ_1) measured during a baseline state where no activation is expected ($A_{1,\lambda 1}$) from the attenuation measured for the same wavelength taken at a time-point during an activated state ($A_{2,\lambda 1}$) leads to the effect of G being eliminated (assuming that G remains constant). The same can be said for measurements taken at another wavelength (λ_2).

Applying this to equations (1.12) and (1.13) we obtain

$$\ln(\Delta A_{\lambda_1}) = (\alpha_{HbO}(\lambda_1)\Delta c_{HbO} + \alpha_{HbR}(\lambda_1)\Delta c_{HbR})d \cdot DPF \tag{1.15}$$

$$\ln(\Delta A_{\lambda_2}) = (\alpha_{HbO}(\lambda_2)\Delta c_{HbO} + \alpha_{HbR}(\lambda_2)\Delta c_{HbR})d \cdot DPF \tag{1.16}$$

where

$$\Delta A_{\lambda_1} = A_{2,\lambda_1} - A_{1,\lambda_1} \tag{1.17}$$

$$\Delta A_{\lambda_2} = A_{2,\lambda_2} - A_{1,\lambda_2}. \tag{1.18}$$

Equation (1.15) and Equation (1.16) can be expressed in matrix form as

$$\begin{bmatrix} \ln(\Delta A_{\lambda_1}) \\ \ln(\Delta A_{\lambda_2}) \end{bmatrix} = \begin{bmatrix} \alpha_{HbO}(\lambda_1) & \alpha_{HbR}(\lambda_1) \\ \alpha_{HbO}(\lambda_2) & \alpha_{HbR}(\lambda_2) \end{bmatrix} \begin{bmatrix} \Delta c_{HbR} \\ \Delta c_{HbO} \end{bmatrix} \cdot d \cdot DPF \tag{1.19}$$

which can be rearranged to solve for Δc_{HbO} and Δc_{HbR}, the change in concentration of oxy- and deoxy-haemoglobin:-

$$\begin{bmatrix} \Delta c_{HbR} \\ \Delta c_{HbO} \end{bmatrix} = \begin{bmatrix} \alpha_{HbO}(\lambda_1) & \alpha_{HbR}(\lambda_1) \\ \alpha_{HbO}(\lambda_2) & \alpha_{HbR}(\lambda_2) \end{bmatrix}^{-1} \begin{bmatrix} \ln(\Delta A_{\lambda_1}) \\ \ln(\Delta A_{\lambda_2}) \end{bmatrix} \cdot \frac{1}{d \cdot DPF}. \tag{1.20}$$

To reduce sensitivity to noise in the measured concentration changes during an fNIRS measurement, the head is illuminated with two wavelengths of near-infrared light, either side of the isosbestic point at approximately 800 nm (Wray et al., 1988). At wavelengths below the isosbestic point, the absorption of deoxy-haemoglobin is dominant, while at wavelengths above the isosbestic point, the absorption of oxy-haemoglobin is dominant. To ensure a well-conditioned matrix, the attenuation measurements for a given chromophore should be anti-correlated at both wavelengths. Using wavelengths either side

of the isosbestic point therefore increases the likelihood that the matrix in Equation (1.20) will be well-conditioned.

1.1.3.3 Functional near-infrared spectroscopy

Figure 1.3: An fNIRS array placed on an infant's head. The head is illuminated with near-infrared light from sources (red) and reflected light is measured using detectors (green).

Functional near-infrared spectroscopy (fNIRS) is an optical imaging technique which uses the principles discussed in this chapter to measure changes in the concentration of the haemoglobins in the brain which, due to the haemodynamic response function, are markers of functional activation (Ferrari & Quaresima, 2012; Tak & Ye, 2014). An array consisting of sources and detectors of near-infrared light (embedded within a cap or headband – see Figure 1.3) is placed in contact with the scalp surface. Near-infrared light illuminates the brain after initially propagating through the scalp and skull tissue. An fNIRS channel is defined as a source-detector pair at two wavelengths; each channel measures the near-infrared light that has propagated from the channel's source and has exited the head at the point of the channel's detector. Generally, in the fNIRS field, it is assumed that concentration changes measured for a given channel occur approximately halfway between the source and detector at a depth equal to half the source-detector separation (Lloyd-Fox, Richards, et al., 2014).

1.2 Diffuse optical tomography

Diffuse optical tomography (DOT) is an extension of fNIRS where image reconstruction methods are applied to produce a three-dimensional image, usually mapping changes in haemoglobin concentration in superficial brain tissues. DOT enables images to be produced which spatially localise activation in the brain rather than relying on the position of sources and detectors on the scalp to interpret results, as is done in conventional fNIRS data analysis approaches.

1.2.1 Optical image reconstruction

Let us define a vector, y, whose values are the optical intensity measurements for each channel in an optical array. Let us also define x as the spatial distribution of the absorption properties within the head. The variables y and x can be related to each other as

$$y = F(x) \tag{1.21}$$

where F is the forward operator. After determining F, inverting the forward operator would yield an expression to calculate the distribution of the absorption properties within the head given the optical intensity for each channel. Mathematically and computationally, this may be very difficult as the forward operator is likely to be nonlinear. Absolute values for optical absorption within the head are therefore difficult to obtain. Absolute values would also include unknown losses due to coupling i.e. due to variable contact of sources and detectors with the scalp. However, absolute values for optical absorption may not be necessary for functional imaging.

It is a *change* in haemoglobin concentration (which will result in a change in optical absorption) which is a marker of functional activation. Equation (1.21) can be expanded using a Taylor series as

$$y = y_0 + F'(x_0)(x - x_0) + F''(x_0)\frac{(x - x_0)^2}{2!} + F'''(x_0)\frac{(x - x_0)^3}{3!} \ldots \quad (1.22)$$

where y_0 is the initial value of a channel-wise vector of optical intensity for each channel preceding a change, and x_0 is the initial spatial distribution of the absorption properties preceding a change. Neglecting higher order terms, we get:-

$$y - y_0 = F'(x_0)(x - x_0). \quad (1.23)$$

Using Δ to denote changes in y and x, Equation (1.23) can be expressed as:-

$$\Delta y = J(\Delta x) \quad (1.24)$$

where $J \equiv F'(x_0)$ is known as the Jacobian, the first derivative of the forward operator in Equation (1.21) which predicts the change in optical intensity that would be measured by each channel given a small change in the optical properties of the tissues within the head.

There are three main steps to producing images using DOT:-

1. Compute a *forward model* of light transport that approximates the Jacobian (J) in Equation (1.24).
2. Mathematically invert the forward model to reconstruct an image.
3. Multiply the inverse of the Jacobian with optical data.

1.2.2 Modelling light transport

Once source and detector positions on the scalp surface have been determined, photon propagation from source to detector can be simulated for each channel. Photon migration is only simulated for channels which are needed for image reconstruction; the source-detector separation of channels used in image reconstruction are typically around 30 mm or less (Boas & Dale, 2005; Cooper et al., 2012; Custo et al., 2010), though modern DOT imaging system can use data from channel separations of upwards of 40 mm (Frijia et al., 2021).

The reversibility of photon propagation is used to simplify the computational burden of computing a sensitivity matrix (Arridge & Cooper, 2015). The propagation of light from source to detector can be computed as the product of the field propagating from the source and the field propagating from the point at which the detector is located *as though* there were a source located at the same position (see Figure 1.4). Our focus will now turn to methods to simulate light transport in media with arbitrarily varying optical properties.

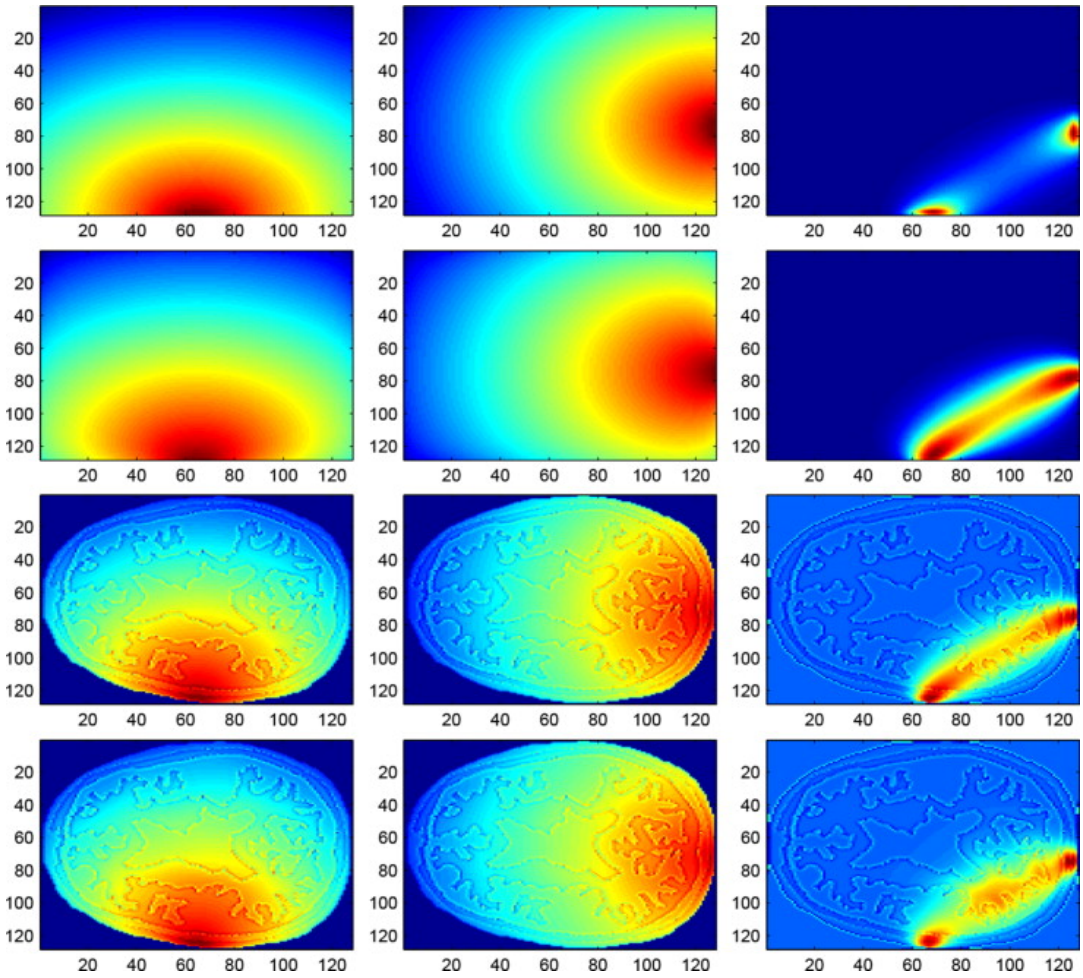

Figure 1.4: Example sensitivity profiles of photon propagation. Left column: The light field resulting from a source. Middle column: The light field resulting from a source at the position of a detector. Right column: The two fields are multiplied to calculate the resultant sensitivity function for the channel. From top row to bottom: photon propagation modelled in an infinite space; a space with square boundary conditions; a head model with homogenous optical properties; and a head model with realistic optical properties. Image taken from (Arridge & Cooper, 2015). Reprinted with permission from Elsevier[3].

1.2.2.1 Radiative transfer equation

The r*adiative transfer equation* (RTE) describes the transport of particles through various media. Fundamentally, the RTE states that the rate of change in the number of photons is equal to the rate of gain of photons, minus the rate

[3] Reprinted from Elsevier Science, Arridge, S., & Cooper, R. J. (Ed.: A. W. Toga), Optical Image Reconstruction, *Brain Mapping: An Encyclopedic Reference*, Vol. 1, pp. 217–222, Copyright (2015), with permission from Elsevier

of loss of photons (Arridge, 1999). The number of photons travelling in a given direction s, at a given time t, per unit volume at point r is represented by $\phi(r, \hat{s}, t)$. The rate of gain of photons is defined as an integral involving the scattering phase function $\theta(\hat{s}, \hat{s}')$, defined as the probability of a photon scattering from direction $\hat{s}$ to direction $\hat{s}'$, plus a source term, $q(r, \hat{s}, t)$. The rate of loss of photons is a result of absorption and scattering; the absorption (μ_a) and scattering coefficients (μ_s) are added to one another to obtain the total attenuation coefficient, μ_t. These terms are related to each other by the following expression, the radiative transfer equation (Arridge, 1999):-

$$\left(\frac{1}{c}\frac{\partial}{\partial t} + \hat{s}.\nabla + \mu_t(r)\right)\phi(r, \hat{s}, t) = \mu_s(r)\int \theta(\hat{s}, \hat{s}')\phi(r, \hat{s}, t)d\hat{s}' + q(r, \hat{s}, t) \quad (1.25)$$

where c denotes the speed of light in a vacuum.

1.2.2.2 Diffusion approximation

In practice, the RTE is particularly computationally expensive to solve for media with arbitrarily varying optical properties and is rarely ever used to model light transport in tissue (Arridge & Cooper, 2015; Hielscher et al., 1998). In practice, the *diffusion approximation* to the RTE is used. The underpinning principle of the diffusion approximation is that light travels diffusively within tissue. This holds if the absorption coefficient μ_a is much smaller than the reduced scattering coefficient μ'_s (Arridge, 1995, 1999); in this case, the mean free path between effectively isotropic scattering events is small and so photon propagation is assumed to be isotropic.

The diffusion approximation takes the form

$$-\nabla . k(r)\nabla\varphi(r,t) + \mu_a\varphi(r,t) + \frac{1}{c}\frac{\partial\varphi(r,t)}{\partial t} = q_0(r,t) \quad (1.26)$$

where $\varphi(r,t)$ is the photon density at point r at time t, k is the diffusion coefficient defined by $k = (3(\mu_s' + \mu_a))^{-1}$, and $q_0(r,t)$ represents the source term (Arridge, 1999).

For the assertion of a diffusive field to hold, it is assumed in tissue that $\mu_s' \gg \mu_a$ (Bigio, 2016). Scatter is the predominant light-tissue interaction at near-infrared wavelengths, and so this assumption is appropriate. However, in areas of low scatter, at tissue boundaries, and in areas proximate to source positions, the diffusion approximation is likely to be inaccurate as photon propagation may become anisotropic.

1.2.2.3 Finite element method

The diffusion approximation can be solved analytically for simple geometries (Boas et al., 1994); however, a complex distribution of optical properties is found in tissue, and so the diffusion approximation requires the finite element method (FEM) to be solved numerically (Arridge et al., 1993). In FEM, the volume (the head in the case of DOT) can be separated into smaller volumes known as elements, which are each assigned optical properties. Using FEM to solve the diffusion approximation enables photon density to be estimated in each element (or at each node) within the volume, resulting in a forward model which is a discrete approximation of the Jacobian in Equation (1.24). To produce a forward model with an increased level of accuracy, a realistic model

of structural anatomy can be used; this is known as a *structural prior* and will be discussed in depth in Section 1.3.

1.2.2.4 Monte Carlo modelling

Another photon propagation simulation method is Monte Carlo modelling (Boas et al., 2002; Fang, 2010; Hiraoka et al., 1993; Wang et al., 1995). This is based on statistical modelling of the paths of individual photons. The elements of the structural prior, based on their tissue types, are assigned specific values of the absorption coefficient and the reduced scattering coefficient. Photons with an initial weight, representing a certain amount of energy, are released from a source and travel within the structural prior along a random path of varying step lengths in varying directions. At first release, each photon is assigned a random path length (known as a scattering length) and a random angle (the scattering angle) based on the probability distribution provided by the scattering phase function and using the local values of the reduced scattering coefficient. If, after a scattering length, the photon remains within the bounds of the volume then the process is repeated until the photon leaves the volume. The initial weight of the photon is attenuated using the Beer-Lambert law based on the distance travelled and the local values of the absorption coefficient; the weight that is lost by the photon in a given element is assigned to that element.

This process is repeated for many photons and for each source and detector position to produce a model of the steady-state photon density within the structural prior for each channel that is needed for image reconstruction.

1.2.3 Solving the inverse problem

The sensitivity matrix must be inverted to reconstruct an image. The forward model has dimensions [number of measurements] x [number of elements in the structural prior]. The number of elements in the structural prior tends to be vastly greater than the number of measurements (i.e. number of channels), and so there are far more unknowns than there are measurements. The

sensitivity matrix is therefore not square, making it a highly underdetermined problem, so it has no exact inverse.

Despite this, matrix inversion techniques exist to produce a so-called *pseudo-inverse* of the sensitivity matrix. The generalised Moore-Penrose inverse may be used (Eggermont et al., 1981). Here, this can take the form

$$\Delta x = J^T(JJ^T + \lambda I)^{-1}\Delta y \tag{1.27}$$

where Δx, Δy, and J are defined as in Equation (1.24), I is the identity matrix, and λ is known as the Tikhonov regularisation parameter. The regularisation parameter will have a substantial effect on the scale of the reconstructed images (Arridge & Cooper, 2015). Several methods exist to determine a value for λ; one such method is the L-curve approach (Correia et al., 2009; Hansen & O'Leary, 1993).

The *image norm* is a measure of noise in the image, while the *data norm* is a measure of the difference between the measured data and the data that would be obtained if the image was used to simulate the data. If λ is increased, the contribution of the image norm is increased, leading to the image Δx becoming less sensitive to perturbations in the measured data (i.e. Δy) and therefore more blurred. A smaller value for λ puts more emphasis on the contribution of the data norm, leading the image to become more sensitive to perturbations in the measured data and therefore more susceptible to noise (Correia et al., 2009).

In the L-curve approach, several images are reconstructed using several different values of λ. The image norm is then plotted against the data norm, as shown in Figure 1.5. The value of λ is taken to be the value corresponding to the point of maximum curvature on the plot; this is typically the nearest point of the curve to the origin and so minimises the image norm and the data norm.

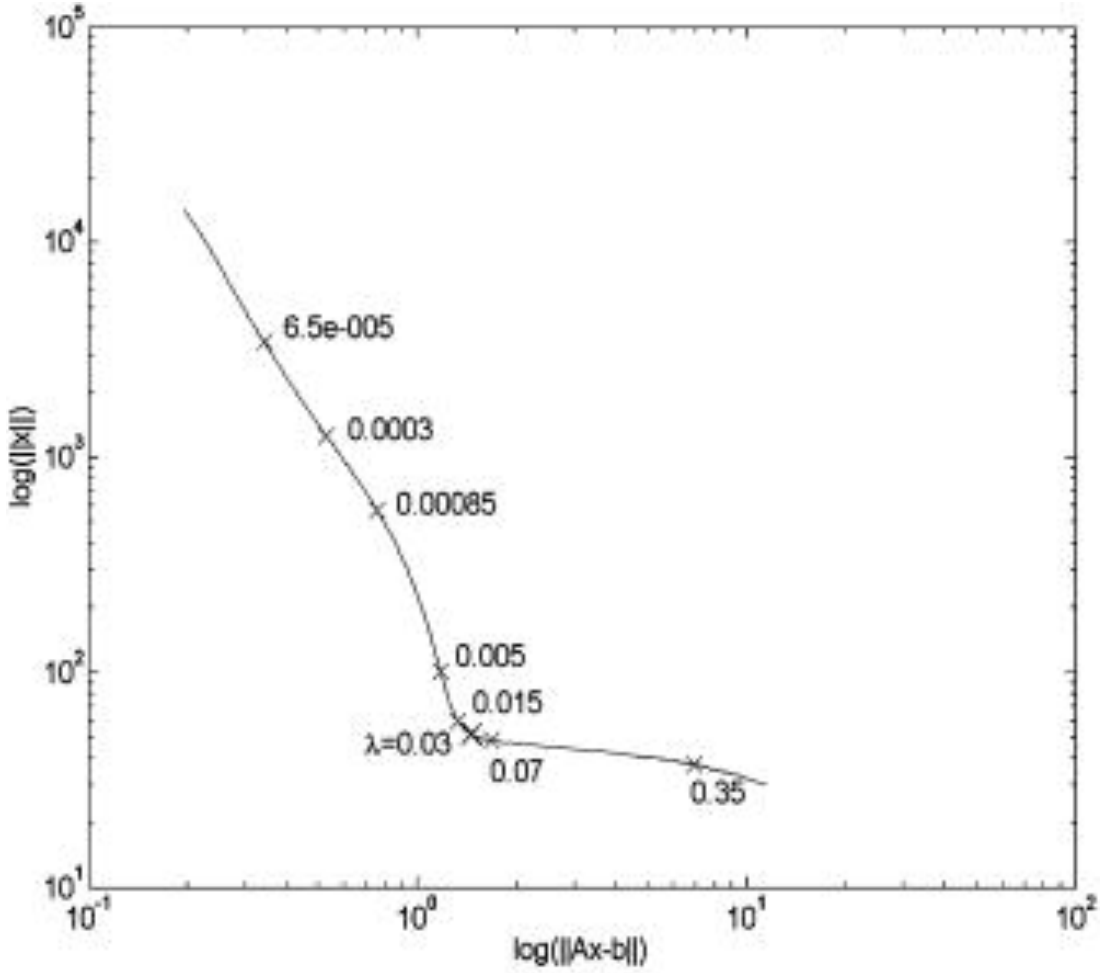

Figure 1.5: The L-curve method to determine the regularisation parameter, λ. The data norm on the x-axis is plotted against the image norm on the y-axis for several values of λ. The value of λ is taken at the point of maximum curvature, denoted in the figure by "$\lambda = 0.03$". Figure taken from Correia et al. (2009). Reprinted with permission from SPIE[4].

[4] Reprinted from *Journal of Biomedical Optics*, *14*(3), Correia, T. M., Gibson, A. P., Schweiger, M., & Hebden, J. C., Selection of regularization parameter for optical topography, 1-11, Copyright (2009), with permission from SPIE and one of the authors (J.C. Hebden).

1.3 Atlas-guided DOT

1.3.1 Structural priors

In DOT, a structural prior is a model of structural anatomy that delineates the different tissues within the head and should be closely representative of the anatomy of the individual under investigation. As DOT measurements provide no structural information about the target object, an appropriate structural prior is critical. The more realistic the structural prior, the higher the accuracy of the photon propagation model that underpins image reconstruction, and therefore the more accurate the reconstructed images (Ferradal et al., 2014). Structural priors are derived from structural MRI data, given its high soft tissue contrast and high spatial resolution (Makropoulos, Counsell, et al., 2018; Makropoulos, Robinson, et al., 2018). To achieve the highest accuracy, an individual's own structural MRI data should be used to produce a *subject-specific* structural prior (Cooper et al., 2012).

The key advantages of DOT are that it is silent, portable, and is much more motion tolerant than MRI. This enables the brain to be investigated in subjects performing tasks outside a restrictive scanner environment. Necessitating an MRI scan for every subject, therefore, undermines the benefits of DOT.

An atlas is a structural prior derived from MRI data that is not specific to a given subject. Atlases can consist of spatially-averaged MRI data from a group of individuals from a population of interest, which are intended to be representative of that population (Brett et al., 2002; Tsuzuki & Dan, 2014). Such atlases will be referred to as *population-level* atlases. In contrast, an *individual atlas* is a structural prior that is derived from the MRI data of a single individual.

1.3.2 Data to build structural priors

Within the head there are 5 tissues with distinct and optical properties known to a reasonable degree of accuracy (Cheong et al., 1990): scalp, skull,

cerebrospinal fluid (CSF), grey matter and white matter. However, the scalp and the skull present a challenge in that it is difficult to distinguish these two tissues on an MRI scan, particularly among infants. Since scalp and skull have relatively similar optical properties (Choi et al., 2004), these two tissues can be combined into a single tissue label which is referred to as the *extra-cerebral tissue*.

For an individual-atlas or a subject-specific structural prior, segmentations for these tissues can be obtained from an individual's MRI scan using one of many segmentation methods. To produce a population-atlas, there are several different forms of averaged data that can be used to produce tissue segmentations. Figure 1.6 shows each data form that will be described under this heading, using the MNI152 model (a population-level atlas for adults produced from MRI data from 152 individuals) as an example (Fonov et al., 2009). There is no consensus on the nomenclature of various forms of averaged MRI data, and so definitions will be provided in the following sub-headings for these data forms that will be used in this PhD thesis.

1.3.2.1 Intensity templates

An *intensity template* in this thesis is defined as a group of intensity MRI images for a specific contrast that have been registered to a common space where an average intensity value is assigned to each voxel. The data is typically from a group of subjects from a population of interest. Such a template can include only data on the brain, a *brain intensity template*, or include data from the entire head, a *head intensity template*.

1.3.2.2 Tissue probability maps & tissue segmentations

Individual MRI images can be segmented to produce tissue segmentations for grey matter, white matter, CSF and extra-cerebral tissue. For a group of subjects, the tissue segmentations from each individual for a given tissue can then be registered to a common space.

In this thesis, a *tissue probability map* is defined as an image mapping the spatial distribution of the probability that each tissue would exist in a given voxel at the population-level. For a given sample of individuals, the tissue segmentations for each individual are registered to a common space and averaged across images. Tissue probability maps are most often available for grey matter, white matter and CSF.

A tissue segmentation maps the spatial distribution of a single tissue. To produce tissue segmentations from tissue probability maps, a majority vote algorithm can be used, where the tissue assigned to each voxel in the common space is the tissue with the highest probability in that voxel. Tissue segmentations can be combined to produce a structural prior.

1.3.2.3 Atlas

In this thesis, an *atlas* is defined as a structural prior which is not specific to a given subject. When in voxel form, this structural prior is referred to as a *tissue mask*.

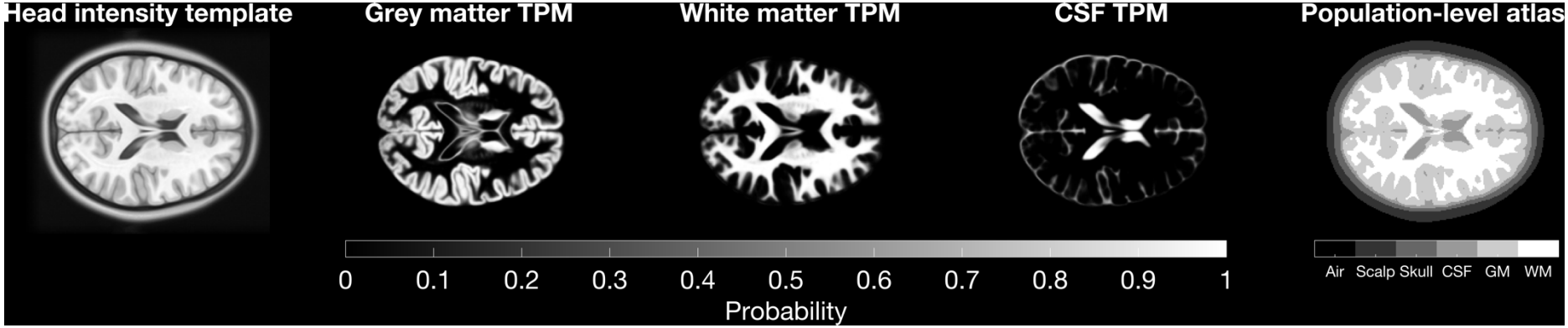

Figure 1.6: Example adult structural MRI data to produce the MNI152 population-level atlas, produced using T_1-weighted MRI data. Far left: T_1-weighted head intensity template. Centre right: grey matter tissue probability map (TPM). Middle: white matter tissue probability map. Centre right: CSF tissue probability map. Far right: population-level atlas mapping the spatial distribution of grey matter, white matter, CSF, skull and scalp (see colourbar). Data for figure taken from Fonov et al. (2009) and https://www.ucl.ac.uk/medphys/research/borl/resources/. Copyright (C) 1993–2004 Louis Collins, McConnell Brain Imaging Centre, Montreal Neurological Institute, McGill University.

1.3.2.4 Tissue optical properties

In Chapter 3, optical data are analysed which were acquired using an imaging system emitting light at wavelengths 780 nm and 850 nm. As either little or no data is available on the optical properties of tissues at the wavelengths required, a model is needed to estimate the absorption and scattering coefficients at the required wavelengths.

Some researchers have attempted to build models of tissue optical properties from estimating tissue chromophore content; for example, see the approach taken by Correia et al. (2010) to derive absorption and scattering spectra for skin and brain. However, assumptions on absolute concentrations of various chromophores in tissue are a source of potential error with such an approach.

Another approach has been adopted by my group – the Diffuse Optical Tomography in the Human Brain (DOT-HUB) group – which uses a simple linear fit over the near-infrared range. This is a reasonable approach given what little data exists on the optical properties of different tissues. To determine the optical properties for each tissue at each wavelength, a regression was fit linearly to the values for the absorption and reduced scattering coefficients from three studies: Strangman et al. (2003), Bevilacqua et al. (1999) and Ferradal et al. (2014). The resulting models of these coefficients as a function of wavelength are shown in Figure 1.7. The values in Table 1.1 were taken as the values of the regression lines for each tissue at 780 nm and 850 nm. Values for the extra-cerebral tissue are calculated as the mean of the skull and skin regression lines.

Table 1.1: Table of optical properties used in this work for each tissue. μ_a: absorption coefficient. μ'_s: reduced scattering coefficient. N: refractive index.

Tissue type	Optical properties					
	780 nm			850 nm		
	μ_a (mm^{-1})	μ'_s (mm^{-1})	N	μ_a (mm^{-1})	μ'_s (mm^{-1})	N
ECT	0.0168	0.8267	1.3	0.0196	0.7505	1.3
CSF	0.0024	0.1094	1.3	0.0035	0.1660	1.3
GM	0.0184	0.7869	1.3	0.0192	0.6726	1.3
WM	0.0180	1.1368	1.3	0.0208	1.0107	1.3

The values used by Strangman et al. and Bevilacqua et al. have been employed in several DOT studies in the past decade (for example, see Eggebrecht et al. (2012), Ferradal et al. (2016) and Zhan et al. (2012)), and therefore justify their use in this thesis. Nonetheless, it must be acknowledged that other more sophisticated and accurate methods may be developed to determine optical properties as a function of wavelength rather than relying on linear regression. This therefore represents a limitation of this work.

It must also be acknowledged that there are no widely agreed upon values for the absorption and scattering coefficients as a function of wavelength. Furthermore, the choice of which values to use is made more difficult given that many DOT studies do not disclose the optical properties they use. For future studies employing the methods in this thesis using the diffusion approximation, a reduced scattering coefficient of 0.3 mm^{-1} is recommended for CSF rather than the values used in this work (see Section 2.4.5 for a discussion on the optical properties of CSF).

Appropriate values for refractive index are similarly difficult to determine. In the work presented in this thesis, a refractive index of 1.3 was assigned to each tissue, which was taken from a study by Heiskala et al. (2009) on neonatal head modelling. However, values for the refractive index vary by publication. Binding et al. (2011) find that the refractive index of the rat brain is

approximately 1.35 in the 1000-1200 nm range. Berke et al. (2016) note that the refractive index in biological tissue ranges from 1.36 in skin to 1.55 in bone. Dehghani et al. (2005) suggest that refractive index values from 1.3 to 1.4 are appropriate in image reconstruction of breast tissue using the diffusion approximation.

The refractive index used in this thesis is lower than the values quoted for most biological tissues (Khan et al., 2021), and future researchers implementing the methods developed in this thesis should consider using a refractive index of 1.4 as is commonly used in DOT studies.

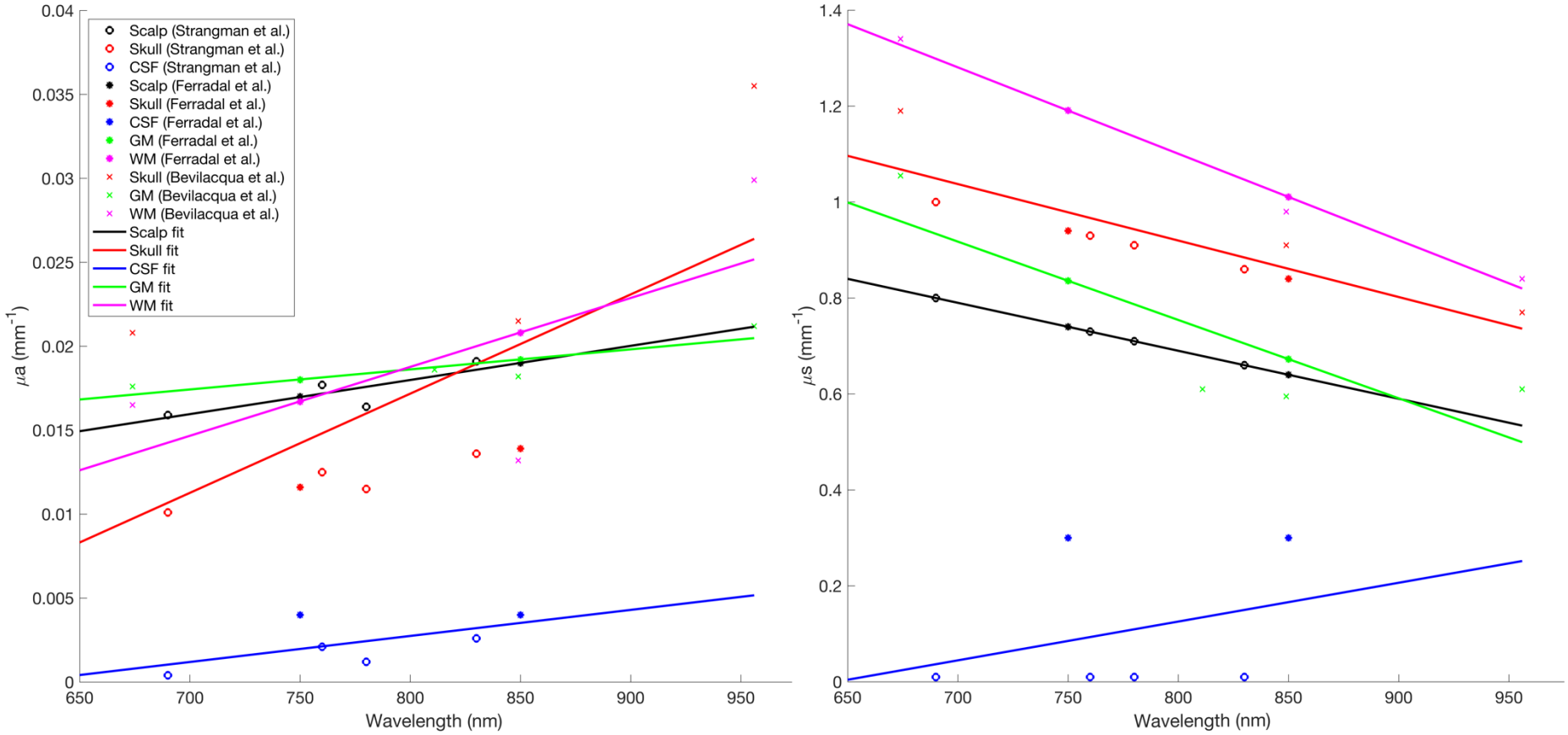

Figure 1.7: Model of absorption coefficients (μ_a) and reduced scattering coefficients (μ'_s) used in this thesis for the different tissues of the head.

1.3.3 Sources of error

A DOT approach that employs an atlas will incur error. Custo et al. (2010) investigated the error that using a population-level atlas in lieu of a subject-specific head model would incur. Optical data collected from three healthy subjects during median-nerve stimulation was used as the input data for image reconstruction. Two different structural priors were used for each subject's data: a subject-specific head model derived from their MRI scan, and another using the MNI152 atlas. The authors conclude that it is possible to reconstruct the location of brain activation to the expected gyrus using atlas-guided DOT, though the area of activation in the reconstructed image was larger when using the population-level atlas.

Cooper et al. (2012) carried out a more extensive validation of the error incurred in atlas-guided DOT. The authors employed the Colin27 individual atlas. Absorption changes were simulated across the cortical surfaces of 32 subject-specific head models, and the resulting changes in optical intensity resulting from each absorption change was computed. Using each set of synthetic changes in optical intensity, absorption change images using subject-specific and atlas head models were reconstructed and compared. The authors noted three factors accounting for the error in the reconstructed locations of absorption changes using the atlas model:-

1. The inherent localisation error associated with diffuse optical imaging methods.
2. Differences in anatomy between the atlas and the individual's anatomy.
3. Imperfect registration of the atlas to the dimensions of the individual.

The authors conclude that the cost of using an atlas is a doubling of the localisation error, from the inherent error of 1 cm to 2 cm. However, it was concluded that reasonable localisation can be achieved with atlas-guided DOT.

A study conducted by Ferradal et al. (2014) compared functional data acquired from the same subjects in response to the same task, validating atlas-guided

DOT against functional MRI (fMRI) data. Relative to fMRI, the authors found a mean localisation error of 6.8 mm for the oxy-haemoglobin response and 7.2 mm for the deoxy-haemoglobin response at the individual-level for atlas-guided DOT. The authors conclude that atlas-guided DOT is a viable approach when subject-specific data is not available, stating that the localisation error values are below the average value for gyral width in the adult.

1.4 Longitudinal studies with fNIRS & DOT

The period of the first thousand days post-conception – through gestation until two years of age – is a critical stage in the development of the brain and nervous system (Bornstein, 2014; Cusick & Georgieff, 2012; Mendez & Adair, 1999; Powell et al., 1995). Previous research highlights the detrimental impact of exposure to various factors during development, though far less is known about the neural basis of these consequences. The past twenty years have seen the adoption and optimisation of neuroimaging methods to further our understanding of development during this integral period of human life. However, while longitudinal studies of brain function play an important role in understanding development, less than a third of developmental neuroimaging studies published between 2008 and 2019 employed a longitudinal design (Azhari et al., 2020).

While there has been an overall decreasing trend in published neuroimaging infant studies over the past decade (Azhari et al., 2020), recently and conversely there has been an increase in the number of studies employing functional near-infrared spectroscopy. Longitudinal study designs are of particular importance when it comes to understanding the impact of early adversity on brain and cognitive development. I would now like to highlight the adoption of the longitudinal framework to two categories of infant studies: in global health project, and in neonatal brain development.

1.4.1 Global health projects

Globally, 1 in every 4 children are undernourished before the age of 5 (UNICEF, 2013), whilst half of all children are believed to live in poverty (Currie & Almond, 2011). Crucially, one in three preschool-aged children living in low- and middle-income countries fail to meet their developmental milestones (McCoy et al., 2016)

Recently, fNIRS has found particular application in global health projects where the portability, low-cost relative to fMRI, and accessibility of the technology have enabled studies to be undertaken in low-resource settings (Blasi et al., 2019). Recent examples include studies of visual working memory in rural India (Wijeakumar et al., 2019); social selectivity in urban Bangladesh (Perdue et al., 2019); and monitoring treatment of malnutrition in infants and children in Guinea-Bissau (Roberts et al., 2017, 2020).

A leading project collecting fNIRS data in a low-resource setting is the Brain Imaging for Global Health (BRIGHT) project. This is a longitudinal study investigating early neurocognitive development during the first 2 years of life, aiming to gain an insight into the effects that malnutrition, an increased risk of disease as well as social or environmental difficulties may have on infant brain development, in addition to other issues linked to living a low-resource environment. The project aims to establish brain function-for-age curves for infants both in the UK and the Gambia

The fNIRS array used as part of BRIGHT is designed to investigate the posterior superior temporal sulcus and temporoparietal junction. In adults, this area is known to be involved in the visual interpretation of socially complex scenes in addition to being known to change with new experiences of actions (Lloyd-Fox et al., 2013). As such, fNIRS data collected as part of BRIGHT aims to investigate this association during infant brain development. Lloyd-Fox et al. (Lloyd-Fox, Papademetriou, et al., 2014) detail the first study of infants in the Gambia, acknowledged to be the first study of functional brain imaging in infants in Africa. Data from the BRIGHT project has also been analysed to investigate age-related changes in the neural responses to tasks such as assessing working memory (Begus et al., 2016), social cognition (Lloyd-Fox et al., 2017; Lloyd-Fox, Papademetriou, et al., 2014), and habituation and novelty detection (Lloyd-Fox et al., 2019).

Channel-space fNIRS analyses assume a constant head size and a constant array position across participants. Variation in either of these parameters will influence the distribution of near-infrared light transmitted from source to detector, and will influence measures of brain activation. Variation in head size and array position is fundamentally related to the three-dimensional anatomy of the subject; therefore, to isolate the effects of variation in these parameters, an analysis approach is required which employs a light transport modelling and image reconstruction approach. To enable an image reconstruction approach with BRIGHT data, population-level atlases will be constructed in Chapter 2 for the age-range 1- to 24-months. These models will be employed in Chapter 3 to conduct an analysis to assess how variation in head size and array position would influence inferences drawn from analysing the data using a conventional channel-space approach.

1.4.2 Neonatal brain development

In recent years, DOT has been emerging as an important tool for clinicians and neuroscientists to study the neonatal brain (Lee et al., 2017), and wearable technology advances in recent years will enable the neonatal brain to investigated in a much wider array of settings inside and outside the clinic.

Neonatal infants are particularly vulnerable to brain injury. Those suffering such an injury may subsequently develop cerebral palsy, a group of life-long movement disorders which can have a serious negative impact on quality of life. Early diagnosis is crucial to enable clinical interventions to be implemented as early as possible when the brain is highly adaptable, and treatment is far more likely to have a positive impact. A study by Gibson et al. (Gibson et al., 2006) is an early example of applying DOT to study neonates, investigating evoked motor responses.

The ANIMATE project aims to develop a new generation of wearable DOT technology to study the development of the motor cortex in neonatal infants to

provide objective measures to enable infants with cerebral palsy to be identified and monitored.

Despite recent advances in wearable hardware, there have not been advances in recent years in structural priors to be used in DOT image reconstruction. Structural MRI data from the Developing Human Connectome Project, a study imaging the brains of hundreds of neonatal infants aiming to map brain connectivity in early life, has been emerging during the course of this PhD (Makropoulos, Robinson, et al., 2018).

Such high-quality data from a huge cohort of infants scanned from pre-term to term-equivalent age therefore presented an exciting opportunity to produce head models to enable recent DOT hardware advances to be implemented to their highest accuracy in terms of spatial resolution and to enable new methods such as connectivity analyses to be implemented. Chapter 4 of this thesis will detail the construction of a database of individual atlases for neonatal infants using data from the Developing Human Connectome Project. Chapter 5 will then investigate how to select and spatially register these individual atlases to minimise error in reconstructed images, mimicking a situation where no infant-specific MRI data is available.

Chapter 2

Producing atlases for infants aged 1- to 24-months

2.1 Introduction

This chapter will describe how structural priors were constructed for infants aged 1- to 24-months, which corresponds to the age range under investigation as part of the BRIGHT project. The chapter will also include an investigation of the effect that longitudinal anatomical changes have on light transport. A brief background will be provided in this introduction section on previous works in infant optical image reconstruction and previous attempts at localising activation in infant fNIRS from the past decade.

The first study to highlight was conducted by Correia et al. (2012). Here, the authors used fNIRS data from a previous study by Lloyd-Fox et al. (2011), which were acquired from infants observing adults performing natural movements. To produce a forward model, the head was assumed to be a slab with homogenous optical properties. A tomographic approach was used to reconstruct three dimensional images of changes in oxy-haemoglobin concentration using optical data averaged on a channel-wise basis across infants. Concentration change images were then displayed topographically in the xy plane parallel to the surface at the depth of greatest change (see Figure 2.1), and displayed in the perpendicular xz plane which displays the depth-dependence of the activation (see Figure 2.2).

Despite these images demonstrating spatial localisation of activation and depth discrimination, two crucial components are missing from this study:-

1) An accurate and realistic multi-layered structural prior being used to produce a forward model.
2) Localising activation to an anatomical region of the cortex.

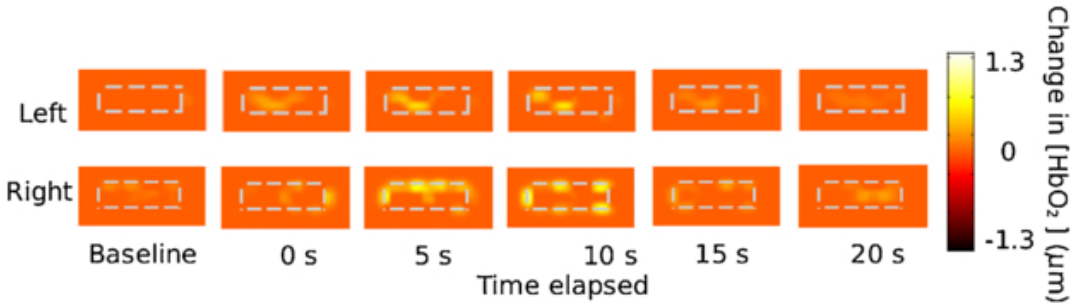

Figure 2.1: Group-level reconstructed images of the oxy-haemoglobin response in 5-month-old infants to observing adults performing natural movements with their hands, assumed to be at a depth of approximately 7 mm underneath the scalp in the temporal cortex. Figure taken from Correia et al. (2012). Reprinted with permission from IOP Publishing, Ltd[5].

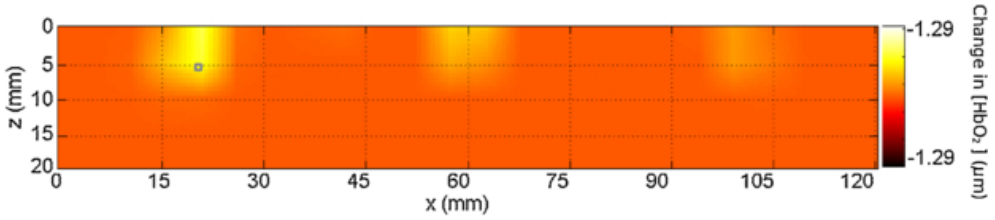

Figure 2.2: Group-level reconstructed image of the oxy-haemoglobin response in the temporal cortex of 5-month-old infants to observing adults performing natural movements. This image displays the depth-dependence of the response shown by the z-axis. Figure taken from Correia et al. (2012). Reprinted with permission from IOP Publishing, Ltd[5].

Another study to highlight is that conducted by Papademetriou et al. (2013), who also employed a tomographic approach. Optical data acquired from a 6-month-old infant in response to auditory stimuli were used in an image reconstruction pipeline, assuming the head to be a slab of homogenous optical properties. The reconstructed image in the xy plane parallel to the surface at depth 1.5 cm was registered to a two-dimensional representation of the individual's T_2-weighted MRI scan, shown in Figure 2.3.

[5] Republished with permission of IOP Publishing, Ltd, from Three-dimensional optical topography of brain activity in infants watching videos of human movement, Correia, T., Lloyd-Fox, S., Everdell, N., Blasi, A., Elwell, C., Hebden, J. C., & Gibson, A., *Physics in Medicine & Biology*, *57*(5), Copyright (2012); permission conveyed through Copyright Clearance Center, Inc.

This study succeeded in demonstrating a method to localise concentration changes to the cortex by using anatomical data, localising activation to the temporal lobe as shown in Figure 2.3. Despite this, the head is assumed to be a homogenous medium. The anatomical data was not used as a structural prior to produce a forward model. Due to the inherent inhomogeneous nature of optical properties in the head, this may lead to significant inaccuracies in the forward model used in the reconstruction.

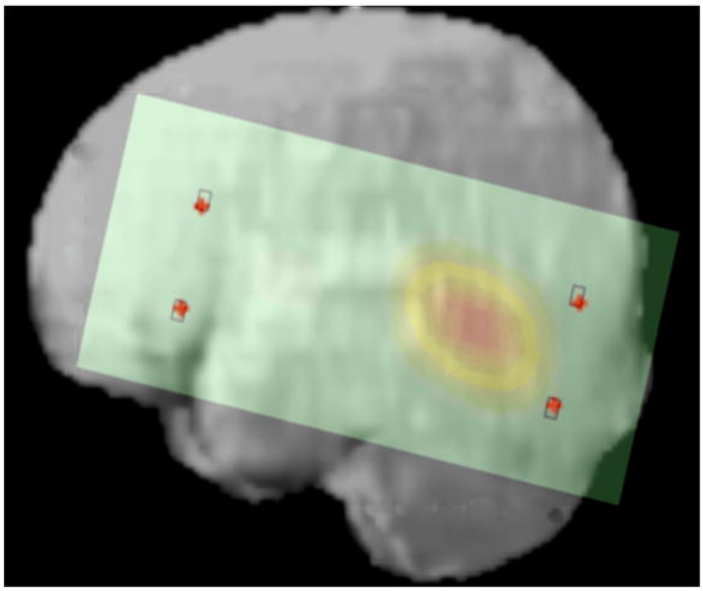

Figure 2.3: Reconstructed image of changes in oxy-haemoglobin concentration in response to auditory stimuli in a 6-month-old infant. The two-dimensional reconstructed image is co-registered to the space of a two-dimensional representation of the infant's T_2-weighed brain image. Figure taken from Papademetriou et al. (2013). Reprinted with permission from Springer[6].

An image reconstruction approach using a realistic structural prior has three main benefits:-

➔ It yields a **more accurate model of light transport** and thus a more accurate forward and more accurate images (Arridge & Cooper, 2015).

[6] Republished with permission of Springer, from Cortical mapping of 3D optical topography in infants, Papademetriou, M. D., Richards, J., Correia, T., Blasi, A., Murphy, D. G., Lloyd-Fox, S., Johnson, M. H., & Elwell, C. E., *Oxygen Transport to Tissue XXXV*, *789*, Copyright (2013); permission conveyed through Copyright Clearance Center, Inc.

- ➔ It aids the **anatomical interpretation** of reconstructed images. The resulting images are inherently registered to a head model, allowing concentration changes to be visualised on a model of cortical anatomy (Yücel et al., 2017). Parcellation atlases can be incorporated into the analysis of reconstructed images, permitting cortical labels to be attributed to elements in the structural prior which enables the response in equivalent cortical areas to be compared across populations.
- ➔ It provides anatomical information enabling the registration of reconstructed images to a common space; this permits DOT data to be **compared with data acquired from several complementary functional imaging modalities** such as electroencephalography (EEG), magnetoencephalography (MEG), and fMRI.

The overarching aim of the work presented in Chapter 2 and Chapter 3 of this thesis is to develop a novel image reconstruction pipeline using atlases produced from age-appropriate structural data. To implement an image reconstruction pipeline with infants, structural priors of infant head anatomy needed to be produced. This chapter addresses the following aims:-

1. To catalogue what MRI data are available for infants aged 1-24 months which might be used to produce structural priors appropriate for implementing a DOT approach with BRIGHT project data. Structural data from adults do not accurately represent the patterns of maturation seen in the developing brain, and so the infant brain cannot simply be treated as a smaller version of the adult (Fonov et al., 2011; Richards et al., 2016; Richards & Xie, 2015). This is addressed in Section 2.2.
2. To use the most appropriate structural data to build population-level atlases for the ages corresponding to those under investigation as part of the BRIGHT project. This is addressed in Section 2.3.
3. To conduct a preliminary sensitivity analysis with these head models to determine the how longitudinal anatomical changes in infants affect light transport within the head. This is addressed in Section 2.4.

2.2 Cataloguing infant structural MRI data

2.2.1 Methodology

This section describes the search for available infant structural MRI data. Criteria were determined for the desired properties:-

- **Cohort characteristics**: The age-range of infants must be 1-24 months of age with no known neurological conditions or anatomical anomalies.
- **Brain tissues**: There must be data present on the spatial distribution of brain tissues (grey matter, white matter and CSF), taking the form of tissue segmentations, tissue probability maps, or an intensity template.
- **Extra-cerebral tissue**: Data on extra-cerebral tissue must be present, taking the form of a tissue segmentation or a head intensity template.
- **Data quality**: Any MRI data must be of high enough quality, where voxel size is less than 3 mm in any dimension, ideally 1mm^3 isotropic.
- **Average data**: MRI data packages must contain averaged MRI data from a population at a given age or age-range.

  Contrast: Data must be either T_1- or T_2-weighted structural data.

2.2.2 Available MRI data on infant head structure

Four MRI data packages appropriate for infants in the age-range were found. Details about these data packages are shown in Table 2.1. All data packages contained data on the spatial distribution of extra-cerebral tissue in the form of a head intensity template. Each data package will be discussed in turn below.

Table 2.1: Published average MRI data packages for infants aged 1-24 months.

Publication	T_1 or T_2 data?	Head intensity template	Brain tissue segmentation	Age range	Field strength	N	TPMs	ECT data
Shi et al., 2011	T_1	T_1	CSF, GM, WM	12- and 24-months	3 T	95	CSF, GM, WM	Yes
Altaye et al., 2013	T_1	T_1	No	9-15 months	1.5 T	76	CSF, GM, WM	Yes
Akiyama et al., 2013	T_1 & T_2	T_1	No	6-months	1.5 T	60	No	Yes
Sanchez et al., 2011	T_1 & T_2	T_1 & T_2	CSF, GM, WM	2 weeks-4.5 years	1.5 T & 3 T	See Table 2.2	CSF, GM, WM	Yes

2.2.2.1 Shi et al. (2011)

Data published by Shi et al. (2011), available at https://www.nitrc.org/projects/pediatricatlas, were longitudinally acquired from a cohort of infants (N = 95) at ages newborn (T_2-weighted data), 12-months (T_1-weighted data) and 24-months (T_1-weighted data) at field strength 3 T. For each age, the data package included tissue probability maps and a brain intensity template (see Figure 2.4), as well as a head intensity template and population-level tissue segmentations. Each infant's scan at 24-months was segmented using an automated method to create tissue segmentations for grey matter, white matter and CSF. Each individual's tissue segmentations at 24-months were registered to their intensity images at newborn and 12-months for use as a structural prior for the segmentation procedure.

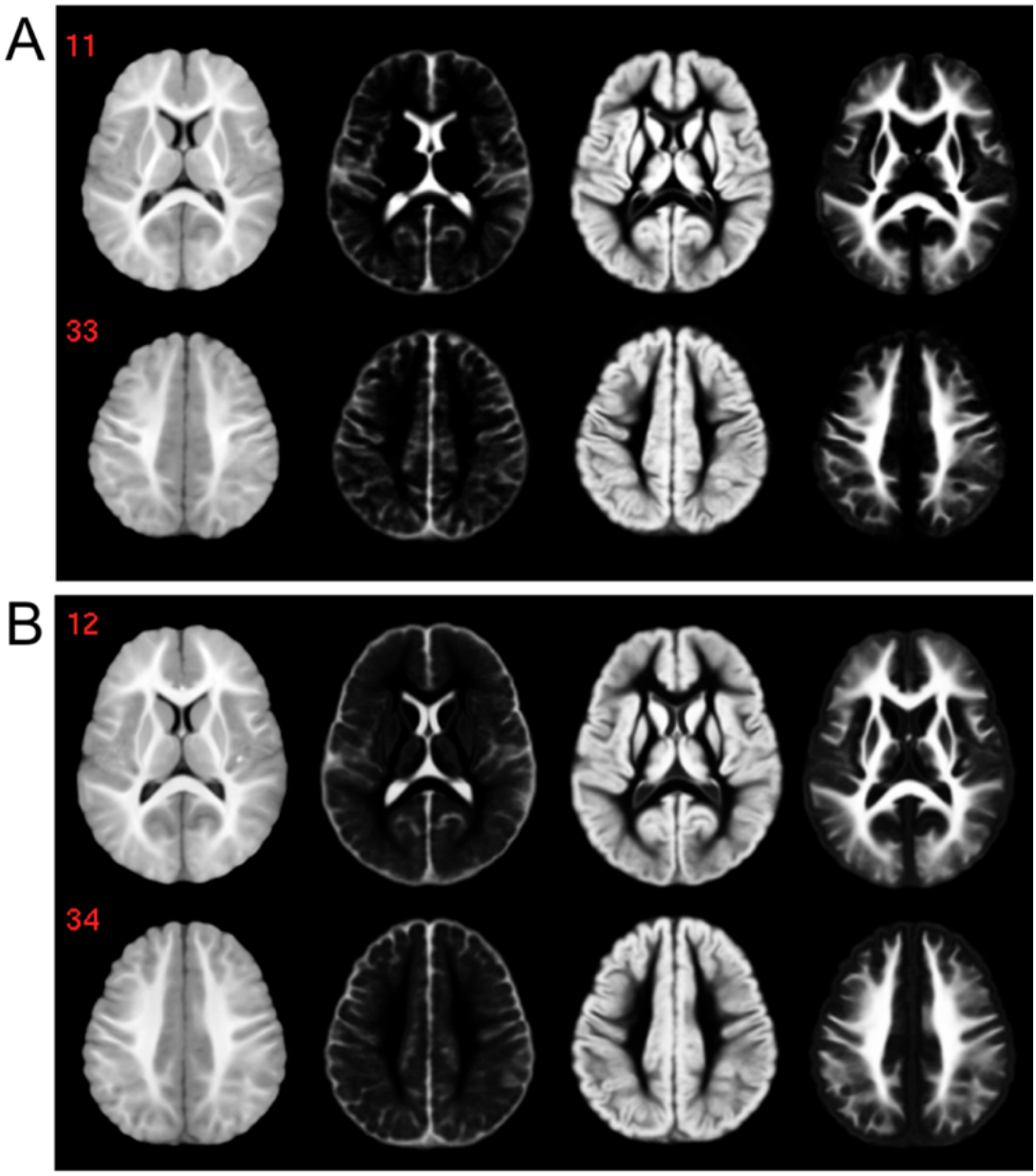

Figure 2.4: T_1-weighted averaged MRI data for 12-month-old infants (A) and 24-month-old infants (B). Far left column: T_1-weighted brain intensity template. Centre left column: CSF tissue probability map. Centre right column: grey matter tissue probability map. Far right column: white matter tissue probability map. Figure adapted from Shi et al. (2011).

2.2.2.2 Altaye et al. (2008)

Altaye et al. (2008) produced tissue probability maps and a T_1-weighted head intensity template using data acquired at field strength 1.5 T from infants aged from 9- to 15-months (N = 76). These are shown in Figure 2.5.

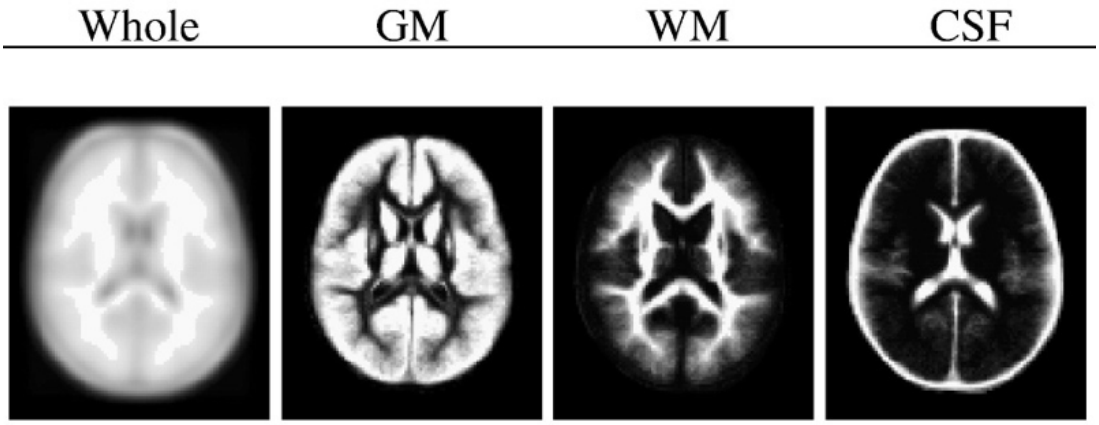

Figure 2.5: T_1-weighted averaged MRI data for infants aged 9-15 months produced by Altaye et al. Far left: T_1-weighted head intensity template. Centre left: grey matter tissue probability map. Centre right: white matter tissue probability map. Far right: CSF tissue probability map. Figure taken from Altaye et al. (2008). Reprinted with permission from Elsevier[7].

[7] Reprinted from *NeuroImage*, *43*(4), Altaye, M., Holland, S. K., Wilke, M., & Gaser, C., Infant brain probability templates for MRI segmentation and normalization, 721–730, Copyright (2008), with permission from Elsevier.

2.2.2.3 Akiyama et al. (2013)

Akiyama et al. (2013) produced T_1-weighted head intensity templates using data from infants aged 6-months. The authors produced one template using data acquired at field strength 1.5 T (N = 27), another template using data acquired at 3 T (N = 33), and a template combining data at both field strengths (N = 60). These templates are shown in Figure 2.6.

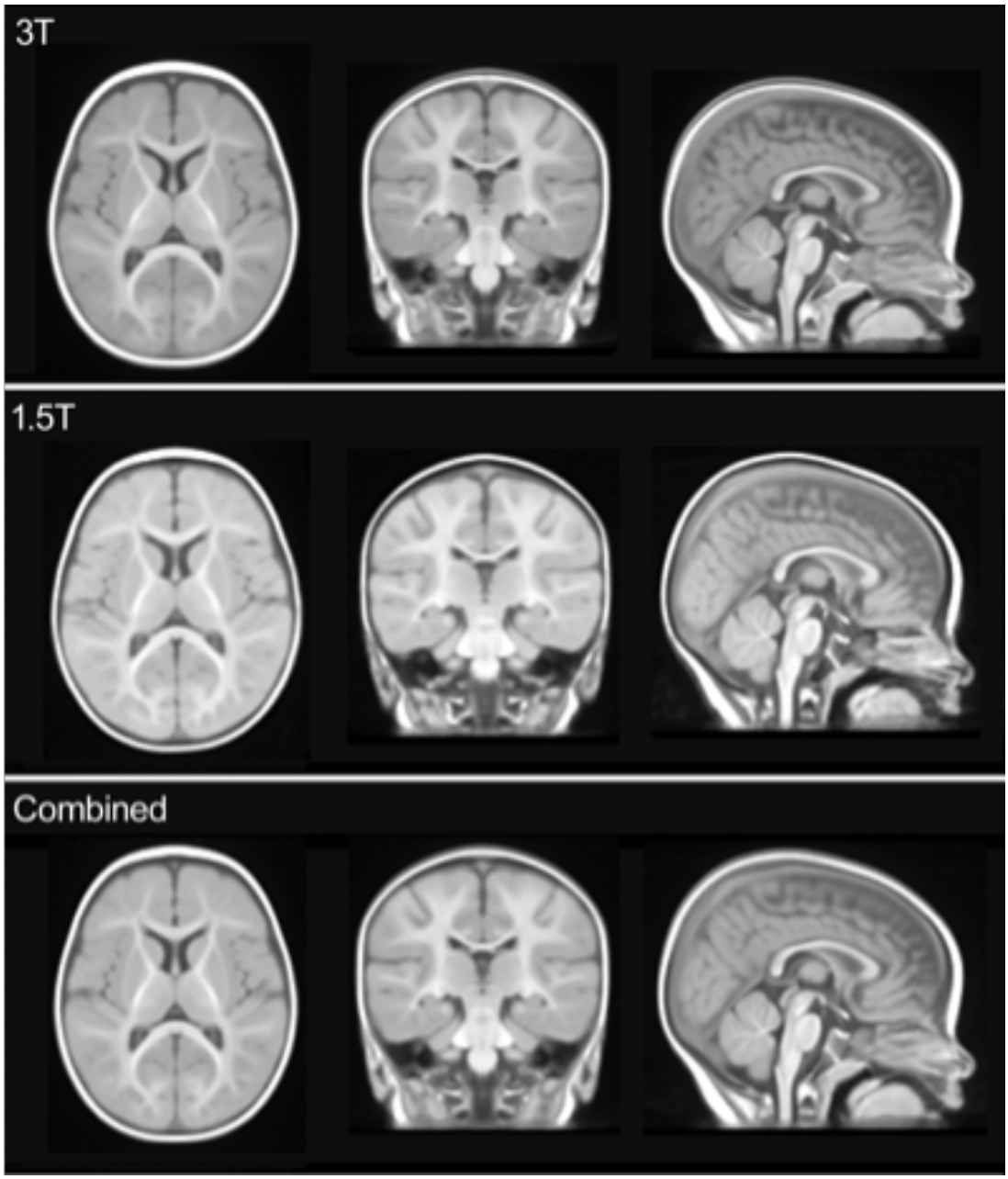

Figure 2.6: T_1-weighted head intensity templates for 6-month-old infants produced by Akiyama et al. Top row: head intensity template using 3 T data (N = 33). Middle row: head intensity template produced using 1.5 T data (N = 27). Bottom row: head intensity template produced using combined 1.5T and 3T data (N = 60). Figure taken from Akiyama et al. (2013), licensed under CC0 1.0.

2.2.2.4 Sanchez et al. (2012)

A data package was published by Sanchez et al. (2012) for ages 2 weeks to 4.5 years. These data include tissue probability maps and a head intensity template for infants at ages 1-, 4.5-, 6-, 7.5-, 9-, 12-, 18- and 24-months. Table 2.2 has details on the numbers of infant MRI datasets that were included at each age. These ages are either exactly those under investigation as part of BRIGHT or, in the case of the 6- and 9-month data, very close to ages 5- and 8-months. The infant MRI data used to produce these age-appropriate data packages were sourced from two MRI data repositories:-

1. National Institutes of Health MRI Study of Normal Brain Development Objective 2, a study of typical brain development, acquiring MRI data from infants aged from birth to 4 years 5 months at field strength 1.5 T (Almli et al., 2007; Evans, 2006)
2. University of South Carolina McCausland Center for Brain Imaging, acquired at 3 T.

Table 2.2: Number of subjects per age in the NIHPD objective 2 and the MCBI-USC databases, respectively.

Age	NIHPD objective 2 (1.5T)	MCBI-USC (3T)	Total N
2 weeks	23	-	23
3 months	22	10	32
4.5 months	-	10	10
6 months	32	10	42
7.5 months	-	10	10
9 months	29	4	33
12 months	25	6	31
15 months	32	-	32
18 months	32	-	32
24 months	27	-	27

It was ascertained that that the Sanchez et al. data exist as part of a larger database, the Neurodevelopmental MRI Database (Richards et al., 2016) (see https://jerlab.sc.edu/projects/neurodevelopmental-mri-database/). After making contact, data were shared by the database owner, Professor John

Richards. The averaged structural data for these ages – including intensity templates and tissue probability maps – are shown in Figure 2.7. Though data are available on tissue segmentations for grey matter, white matter and CSF, there are clearly inaccuracies in these segmentations as grey and white matter voxels appear within the CSF (see Figure 2.7).

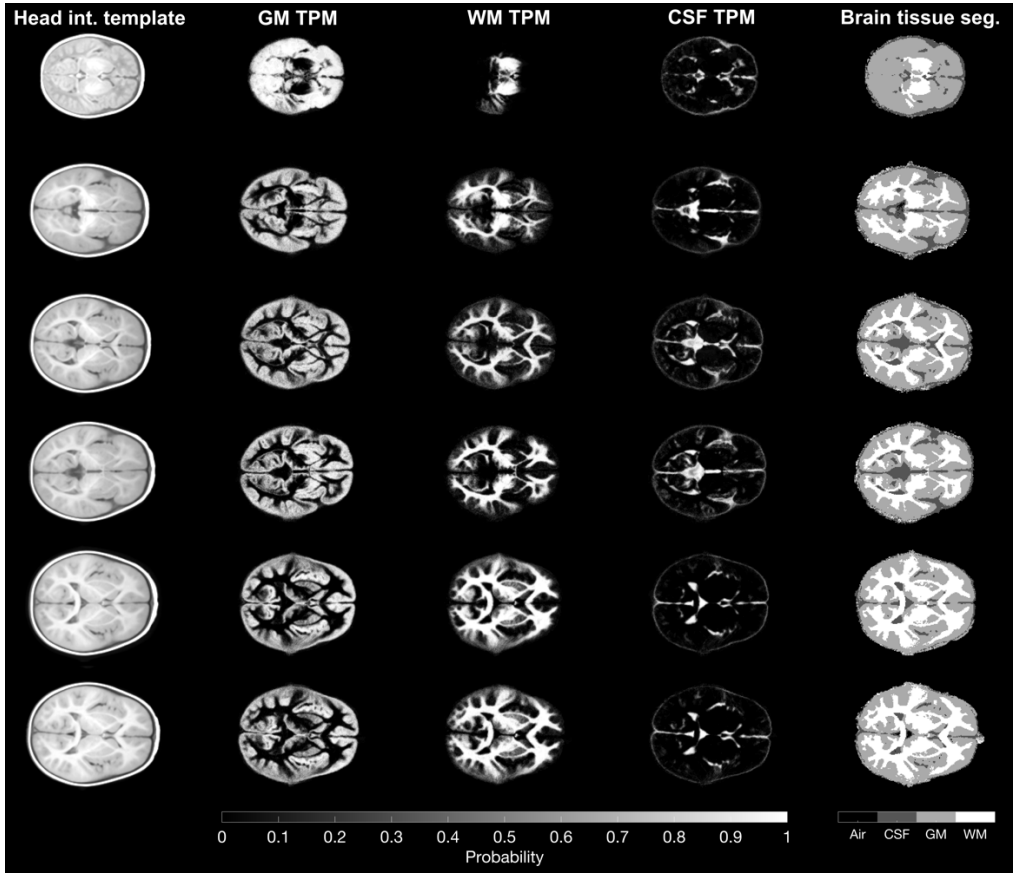

Figure 2.7: T_1-weighted averaged MRI data from data published by Sanchez et al. (2012). Left column to right: head intensity (int.) template, grey matter tissue probability map (GM TPM), white matter tissue probability map (WM TPM), CSF tissue probability map (CSF TPM), and brain tissue segmentations (seg.). Top row to bottom: data at 1-, 6-, 9-, 12-, 18-, and 24-months. Data for the figure are detailed in Sanchez et al. (2012) and Richards et al. (2016) and are available from the Neurodevelopmental MRI database, licensed under CC BY-NC-ND 3.0.

2.2.3 Most appropriate datasets

The Akiyama et al. data package contained no segmentations or tissue probability maps that could be used to produce a brain tissue mask. An approach could have been taken to automatically segment the average template, though blurring in the template as a result of the averaging process could cause issues with the segmentation procedure. These data were therefore not the most appropriate for producing a structural prior with a realistic spatial distribution of tissues.

The Altaye et al. data package could have been used to produce a population-level atlas as tissue probability maps for brain tissues were provided and the extra-cerebral tissue could have been segmented from the head intensity template. However, the data correspond to a wide age-range, and so it was deemed not the most appropriate in terms of age-specificity.

Because of its wide span of age-specific data closely corresponding to the ages of interest and its inclusion of data for both brain and extra-cerebral tissues, the Sanchez et al. data was deemed appropriate for producing structural priors for infants aged 1- to 24-months. The data package from Shi et al. could also be used to produce a head model and included ages that were investigated as part of the BRIGHT project. Section 2.3 will detail how the data published by Sanchez et al. and Shi et al. were used to produce structural priors appropriate for DOT.

2.3 Producing head models

2.3.1 Outline

The aim of the work described in this section was to produce structural priors using each age-appropriate data package from Shi et al. and Sanchez et al. Tissue segmentations in voxelised-form will be referred to as *masks*. In outline, three components need to be delineated:-

- ➔ A **brain tissue mask**: this is produced by summing together tissue segmentations for grey matter, white matter and CSF (combined data for outer CSF and ventricles). For the Sanchez et al. data, the tissue probability maps needed to be used to first produce the tissue segmentations.
- ➔ A **head mask**: this is a mask whose outer boundary is determined by the outer scalp boundary.
- ➔ An **inner skull boundary**: this demarcates the boundary between the skull (which appears as a high-contrast feature in T_1-weighted intensity data) and the CSF. The inner skull boundary and the head mask can then be used to produce a mask for extra-cerebral tissue. The brain tissue mask and extra-cerebral tissue mask are then summed together to produce a four-layer tissue mask.

2.3.2 Head model production using Sanchez et al. data

Data packages produced by Sanchez et al. were shared by the database owner, Professor John Richards, for ages 1-, 4.5-, 6-, 7.5-, 9-, 12-, 18- and 24-months. The data packages at each age included:-

- Tissue probability maps for grey matter, white matter and CSF.
- A T_1-weighted head intensity template.
- A T_1-weighted brain intensity template, extracted from the head template.

In this section, the method will be described to produce a four-layer tissue mask for the data packages at each age. The data packages at 4.5- and 7.5-months were not used as the number of individual infant datasets used to produce the averaged MRI data were much lower at these ages than at 6- and 9-months (see Table 2.2).

2.3.2.1 Majority vote to produce brain tissue mask

To produce masks for grey matter, white matter and CSF, a *majority vote* approach was taken to produce segmentations using the tissue probability maps. For the corresponding voxel in each tissue probability map, the tissue which has the highest probability is the tissue to which that voxel is assigned. The three probabilities in each voxel should sum to 1. However, this was not the case for all voxels, likely arising due to errors in the method used to register each individual's segmentations to a common space. The tissue probability maps were summed together, and all voxels with summed values below 1/3 were excluded from tissue segmentations.

2.3.2.2 Producing a head mask

The head intensity template was used to produce a head mask. In an initial method to produce a head mask, the lowest threshold at which a closed outer scalp boundary could be obtained was manually determined, and the head mask was defined as all voxels within this boundary in the axial plane. Due to the methodological inconsistency of having to determine a manual threshold for each age, the automated Betsurf method (Jenkinson et al., 2005) was used to determine an outer scalp boundary. Betsurf is a well-established tool that uses the intensity distribution of an MR image, constrained to a robust range, to find the scalp surface. The head mask was defined as all voxels that were within the outer scalp boundary in the axial plane. This is shown in Figure 2.8

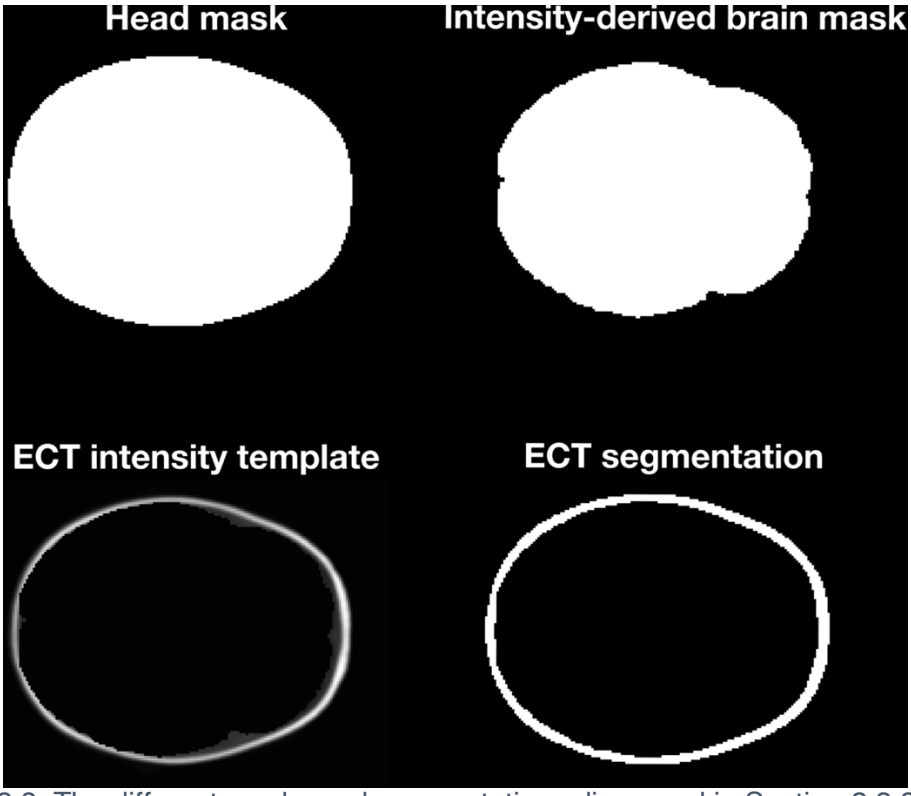

Figure 2.8: The different masks and segmentations discussed in Section 2.3.2.2 and Section 2.3.2.3. Extra-cerebral tissue is abbreviated to ECT.

2.3.2.3 Determining the inner skull boundary

In theory, the brain intensity template could be extracted from the head intensity template to recover an intensity template for extra-cerebral tissue. This was part of an initial head model creation pipeline. The highest threshold intensity at which a closed boundary could be obtained was manually determined from the extra-cerebral intensity template to obtain the inner skull boundary.

There were, however, some issues with the extra-cerebral tissue and brain intensity templates:-

Issue 1: Some skull voxels were present in the brain intensity template, and so the extra-cerebral intensity template did not contain all skull voxels.

Issue 2: Not all CSF voxels were present in the brain intensity template. A substantial population of outer CSF (i.e. not ventricular CSF) voxels

existed in both the brain intensity template and the extra-cerebral tissue intensity template.

Let us first discuss issue 1. The brain intensity template contains high intensity voxels in what appears to be the outer CSF. These voxels are assumed to be skull voxels that were erroneously included following the skull-stripping procedure to produce the brain intensity template.

Here, the first objective was to recover the skull voxels from the brain intensity template. The white matter segmentation (produced earlier through majority vote) was used to exclude all high-intensity white matter voxels from the brain intensity template. The brain intensity template was then thresholded at the value of the 95th percentile of its non-zero values. All voxels within the outer boundary of this thresholded template in the axial plane were included to create what is termed the *intensity-derived brain mask* (see Figure 2.8). The *extra-cerebral tissue intensity template* was defined as all the voxels in the head intensity template that were not present in the intensity-derived brain mask (see Figure 2.8).

This extra-cerebral tissue intensity template contains all skull voxels that were erroneously assigned to the brain intensity template following brain extraction. However, the extra-cerebral tissue intensity template also contains a population of outer CSF voxels, which brings us to issue 2. The extra-cerebral tissue intensity template was thresholded at the 85th percentile of its non-zero values. This value of the 85th percentile was chosen based on manual trial-and-error.

All voxels within the head mask that lay between in the inner border of the thresholded extra-cerebral tissue intensity template – which demarcates the inner skull boundary – and the outer scalp boundary were defined as extra-cerebral tissue to produce an *extra-cerebral tissue segmentation* (see Figure 2.8).

2.3.2.4 Assembling the four-layer tissue mask

Any voxels of the brain tissue mask that were not contained in the intensity-derived brain mask were assigned a non-tissue value. The brain tissue mask was added to the extra-cerebral segmentation mask to produce a four-layer tissue mask; extra-cerebral tissue is assigned an index of 1, CSF (including both outer and ventricular CSF) is assigned an index of 2, grey matter 3 and white matter 4. All voxels assigned a non-tissue value that lay within the bounds of the head mask were assigned to be CSF; these are the CSF voxels that were contained in the extra-cerebral tissue intensity template but excluded from the thresholded extra-cerebral tissue intensity template.

2.3.2.5 Modifications of the four-layer tissue mask

Two issues exist with this initial four-layer tissue masks, as follows:-

- **CSF appeared to be in contact with background voxels**. The solution to this is simple: if a voxel assigned to CSF is in contact with a voxel without a tissue assignment (in other words, a voxel assigned to the background), the CSF-assigned voxel is reassigned to be extra-cerebral tissue.
- **Small islands of white matter exist which appear in grey matter** (and vice versa) which don't appear anatomically plausible. Within the tissue several small islands appear. In three dimensions, a voxel shares a face with 6 other voxels. This method assumes that if a small volume of tissue is surrounded by a tissue of a different type, then it is likely that the small volume of tissue has been misclassified, and so the small volume of tissue is reassigned to the tissue that surrounds it. Imagine a central voxel; if 5 (or more) of the 6 surrounding voxels have the same tissue classification as one another but a different classification to the central voxel then the central voxel is reassigned to belong to the tissue of the 5 (or more) surrounding voxels. This procedure is iterated until two masks produced from consecutive iterations are identical. Figure 2.9 shows the tissue mask before and after de-islanding.

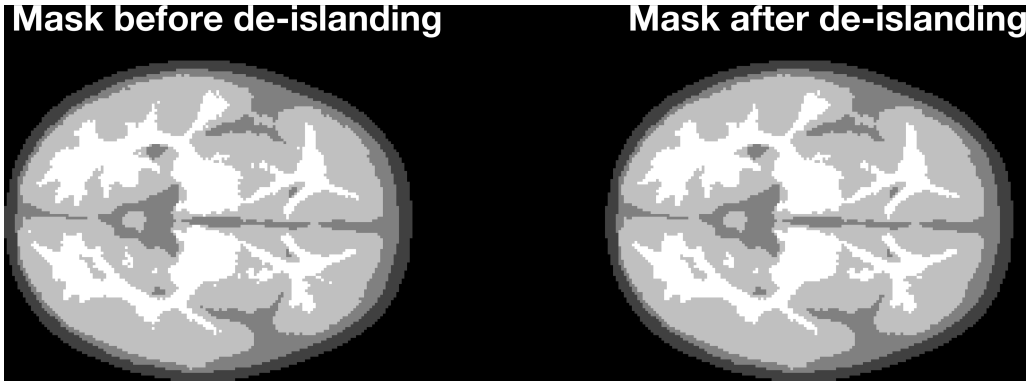

Figure 2.9: Four-layer tissue mask before undergoing the de-islanding procedure (left) and after undergoing the de-islanding procedure (right).

2.3.2.6 Converting from voxel space to mesh space

The iso2mesh toolbox (Fang & Boas, 2009) was used to convert the four-layer tissue masks for each age from voxel space to mesh space to produce a four-layer tetrahedral volume mesh as well as surface meshes for grey matter and scalp surfaces. Using the CGAL mesher option, the maximum element size was set to 1.25 mm^3, while the maximum radius of the Delaunay sphere was set to 1 mm.

The elements in volume meshes are tetrahedral, which has the advantage that element sizes can vary. As a result, volumes which require many voxels to be represented in voxel space may be represented by fewer elements in mesh space, reducing the computational burden when simulating photon migration. Furthermore, triangles can better approximate curves. In voxel space, a curve may only be represented by step changes in voxels, whereas triangles can be tilted by a given angle along the curve direction.

2.3.2.7 Calculating 10/5 positions

A convention for describing positions on the scalp surface of each model is helpful in determining equivalent scalp surface positions across different subjects, for spatially registering structural priors and for determining appropriate positions of optodes or any other equipment placed on the scalp surface.

The 10/5 system is a convention for describing positions on the scalp, originally intended for high-density electrode positioning in EEG (Oostenveld & Praamstra, 2001). The 10/5 system is computed using the coordinates of the cranial landmarks, corresponding to the nasion (Nz), the inion (Iz), the left pre-auricular point (Al), the right pre-auricular point (Ar) and the approximate location of the vertex of the head (Cz). These five landmarks were determined manually on the head model. The ITK-SNAP software (Yushkevich & Gerig, 2017) was used to provide a visualisation of the external scalp surface (using the head mask) and a single voxel was selected to represent the location of each landmark. The coordinates of the nodes in the head volume mesh closest to the centres of each voxel were then taken as the updated coordinates of each landmark in the volume mesh space. The positions of the cranial landmarks on the scalp surface are shown in Figure 2.10. Each node in the mesh was rigidly transformed to a coordinate system in which the origin is defined as Iz, the y-axis is defined as a vector joining Iz to Nz, and mesh nodes are rotated around the y-axis such that the z-coordinates of Ar and Al are approximately equal.

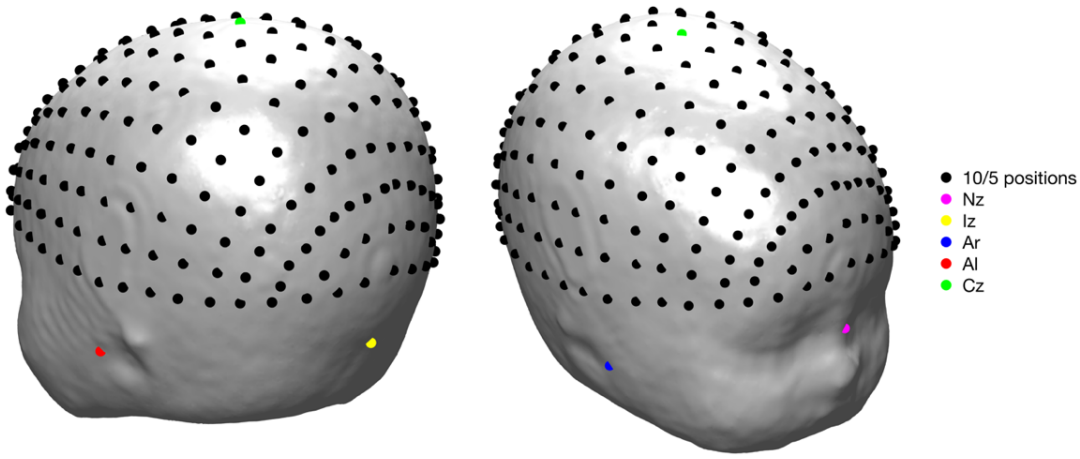

Figure 2.10: The positions of the cranial landmarks and 10/5 positions (see legend) on the scalp surface mesh of the 6-month head model. Cranial landmarks (and their abbreviations): nasion (Nz), inion (Iz), right pre-auricular point (Ar), left pre-auricular point (Al), vertex of the head (Cz).

For every individual, the coordinates of the 10/5 locations were then calculated using a curve-walk procedure ((Aasted et al., 2015), see Homer2:

www.nitrc.org/projects/homer2)[8]. Given three points on the mesh surface, a plane can be computed. The coordinates for Nz, Iz and Cz are used to define a plane, and all nodes on the scalp surface that lie within 0.6 mm of the intersection of the plane were identified to define a curve. A 3D spline interpolation of these surface nodes was then used to smooth the curve. The positions along the smoothed curve from Nz to Iz via Cz were then calculated by dividing the total length of the curve into 5% intervals. This curve is referred to as the sagittal reference curve. The same process was used to compute the coronal reference curve using points Ar, Al and Cz to define the intersection with the scalp surface, and the positions along the curve were computed at 5% intervals. An axial reference curve was then defined for the entire circumference of the head by calculating two curves: using FPz, T7 and Oz on the left and FPz, T8 and Oz on the right, and dividing both curves into 5% intervals. The length of the axial reference curve is taken to be the head circumference. The remainder of the 10/5 positions are calculated along curves defined by equivalent positions on the right and left sides of the axial reference curve via equivalent positions in the sagittal reference curve. The 10/5 positions are shown on the scalp surface in Figure 2.10.

2.3.2.8 Results

The process above was completed for ages 1-, 6-, 9-, 12-, 18- and 24-months. Figure 2.11 displays example axial slices from these models at each age. The head model at 1-month has an implausibly thick cortex and limited white matter coverage; the model at this particular age is therefore inappropriate to be used as a structural prior. It was noted by an MRI specialist that, for ages 6-months and onwards, the white matter mask appears to encompass certain deep grey matter structures. Despite this inaccuracy, due to the limited penetration of depth of reflected near-infrared light, the inaccuracy in the labelling of deep brain structures is unlikely to be a significant source of error when modelling photon transport.

[8] The method described here to calculate 10/5 positions is an adaption of a method first developed by Dr Sabrina Brigadoi of the University of Padova.

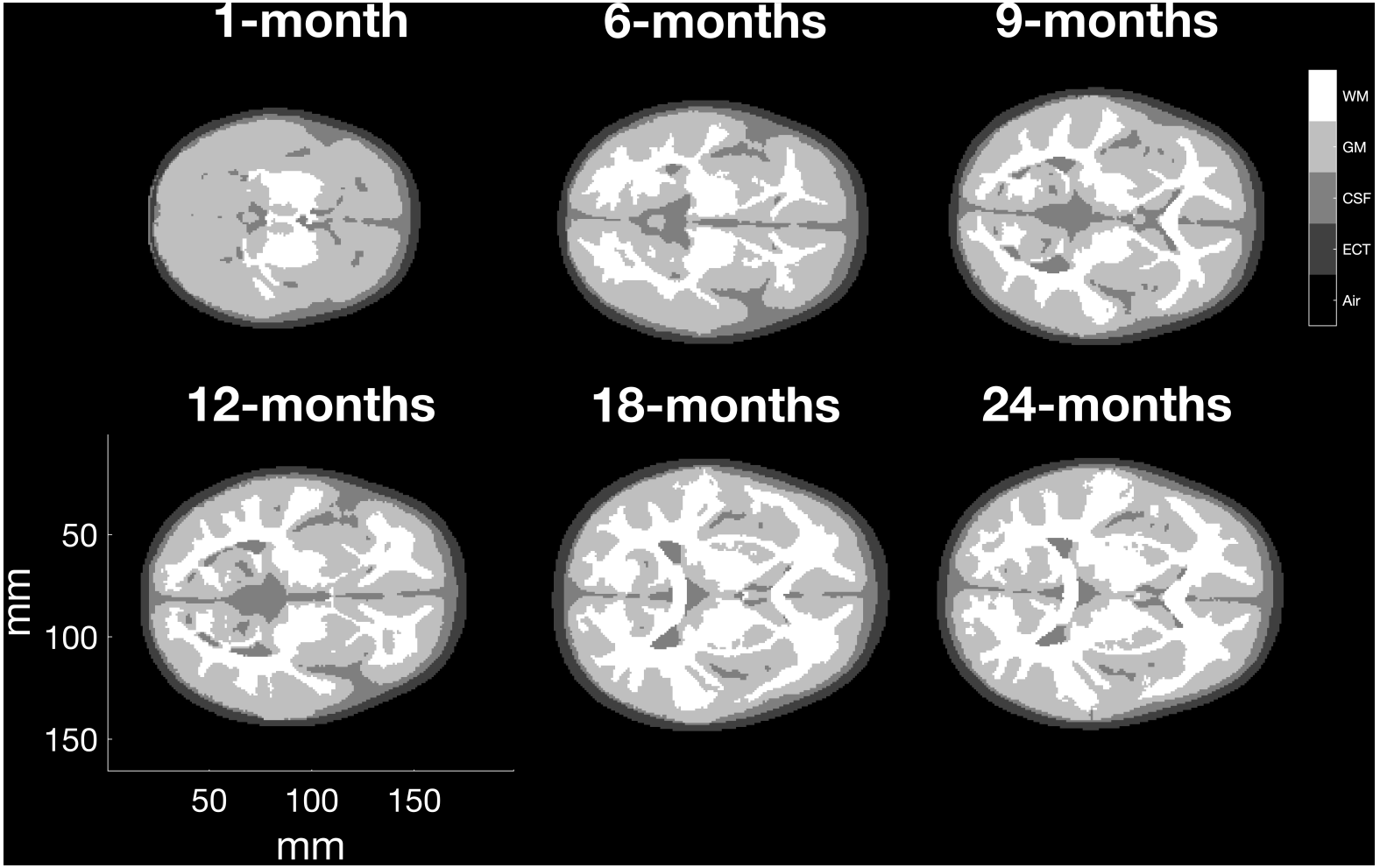

Figure 2.11: Structural priors in voxelised form produced from the Sanchez et al. data for infants at ages 1-, 6-, 9, 12-, 18- and 24-months. The tissues represented here are extra-cerebral tissue (ECT), CSF, grey matter (GM) and white matter (WM).

2.3.3 Head model production using Shi et al. data

Averaged MRI data from Shi et al. including the following components were available for infants at ages 12-months, 24-months and newborn:-

- Tissue segmentations for grey matter, white matter and CSF.
- A T_1-weighted head intensity template.

As brain tissue segmentations were available, producing a brain mask just required adding together the tissue segmentations for grey matter, white matter and CSF. The Betsurf procedure was used to produce a head mask from the head intensity template. It appeared on visual inspection of the head intensity template that the entirety of the CSF was included in the CSF segmentation. As such, the outer boundary of the brain tissue mask (i.e. the outer boundary of the CSF) was used to demarcate the inner skull border. Therefore, an extra-cerebral tissue segmentation was defined by excluding voxels from the head mask that were present in the brain mask. No cerebellum tissue is represented in the head model, though as only the temporal lobe, parietal lobe and inferior frontal gyrus are sampled in the BRIGHT project, the lack of a cerebellum is not a major limitation.

As before, a tissue mask was assembled by summing together the brain tissue mask and the extra-cerebral tissue mask. The model was converted from voxel space to produce a tetrahedral volume mesh using the iso2mesh software as was described in Section 2.3.2.6; the maximum element size was set to 1.25 mm^3, while the maximum radius of the Delaunay sphere was set to 1 mm. The 10/5 positions were calculated in the same method as for the Sanchez et al. data in Section 2.3.2.7. The head model can be seen in Figure 2.12.

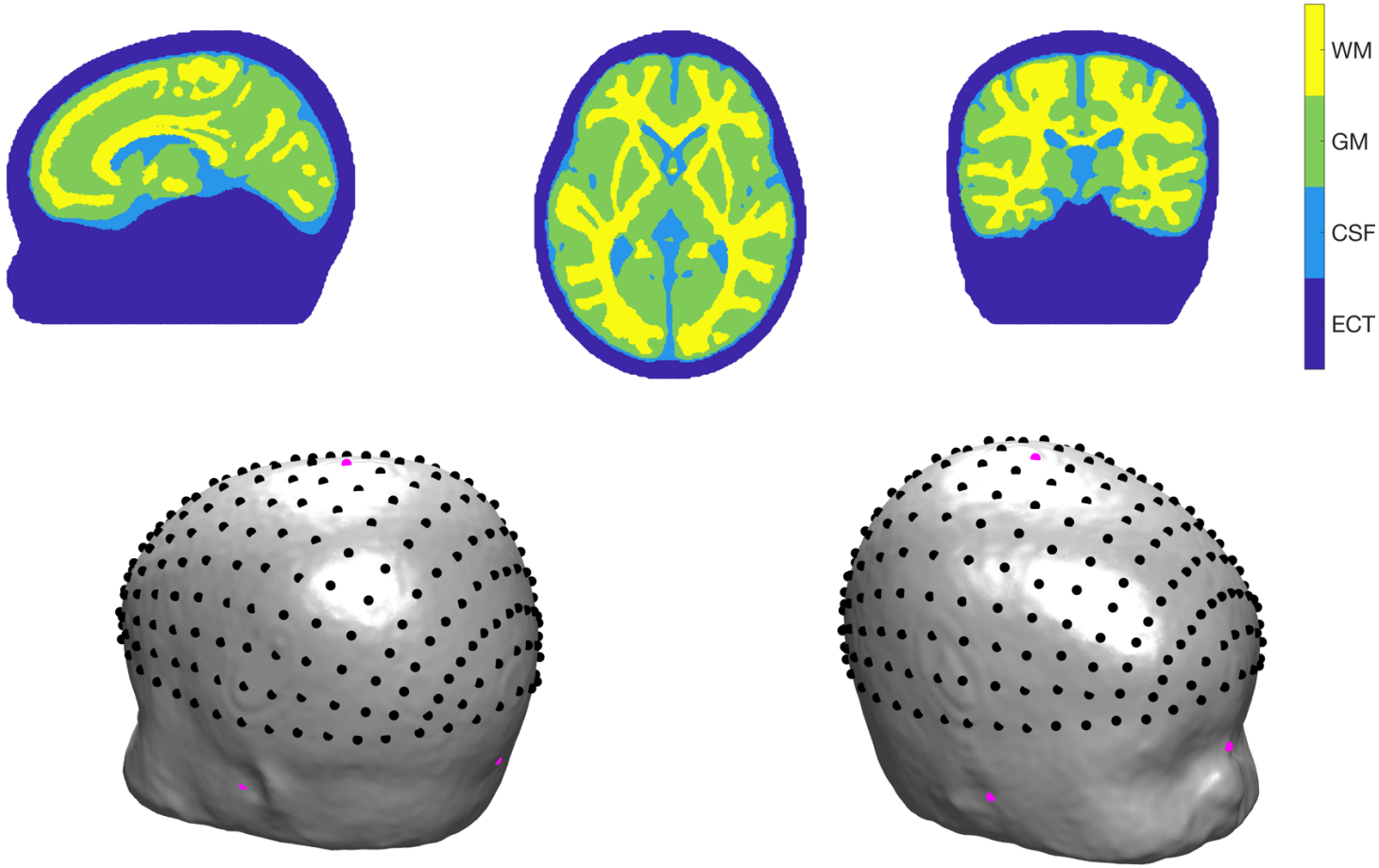

Figure 2.12: The head model produced from Shi et al. data at 12-months. Top row: example sagittal, axial and coronal sections of the four-layer tetrahedral volume mesh showing the distribution of white matter (WM), grey matter (GM), cerebrospinal fluid (CSF) and extra-cerebral tissue (ECT). Bottom row: the position of the cranial landmarks and 10/5 positions (in black) and cranial landmarks (in magenta) on the scalp surface.

2.3.4 Discussion

In this work, a pipeline has been developed to produce population-level atlases from averaged MRI data produced by Sanchez et al. and Shi et al. which can be used in place of subject-specific structural priors in DOT.

On reflection there are aspects of the head model production pipeline which could be improved to strengthen the consistency and quantitative nature of the pipeline. Though the head mask appears on visual inspection to be a good approximation of the scalp surface, the error associated scalp surface segmentation was not quantified. In addition, more work could have been completed to optimise the Betsurf parameters for scalp segmentation. These methods could have been validated using manual segmentation.

A more quantitative method could have been developed to demarcate the inner skull border. For the Sanchez et al. data, a previously extracted brain intensity template was relied upon to extract extra-cerebral tissue from the head intensity template before applying various empirically-determined thresholds. For future head model production pipelines, skull-stripping techniques such as Betsurf could be implemented and optimised to automatically segment the inner skull boundary in infant data. This would also need to be validated using manual segmentation.

One issue with using a head intensity template to segment the outer scalp and inner skull boundaries is that there is a level of blurring in the boundary due to the averaging procedure. This would affect the performance of automated segmentation methods.

The structural models produced in this section account for age-appropriate structural changes in this age-range. In Section 2.4, an analysis is described which aimed to determine what effect these longitudinal changes in structure have on photon propagation.

2.4 Sensitivity analysis of age-related changes in head structure

2.4.1 Aim

At the time the head models were produced, fNIRS data from the BRIGHT project were pre-processed and available for infants aged 5-, 8- and 12-months. The aim of the research described in this section is to conduct a preliminary sensitivity analysis to assess the effect of longitudinal anatomical changes on light transport through the head, using the age-appropriate head models at 6-, 9- and 12-months using the Sanchez et al. data.

2.4.2 Methods

2.4.2.1 BRIGHT headgear & array registration

The BRIGHT source-detector array configuration consists of one array placed over the right hemisphere and an equivalent array placed over the left hemisphere, composed of 6 sources and 7 detectors (source-detector separations 2 cm), each forming 17 channels per hemisphere (see Figure 2.13). The design of the fNIRS array enabled responses in lateral frontal to posterior temporal brain regions to be investigated, which included the inferior frontal gyrus; middle and superior temporal regions; and the temporo-parietal junction.

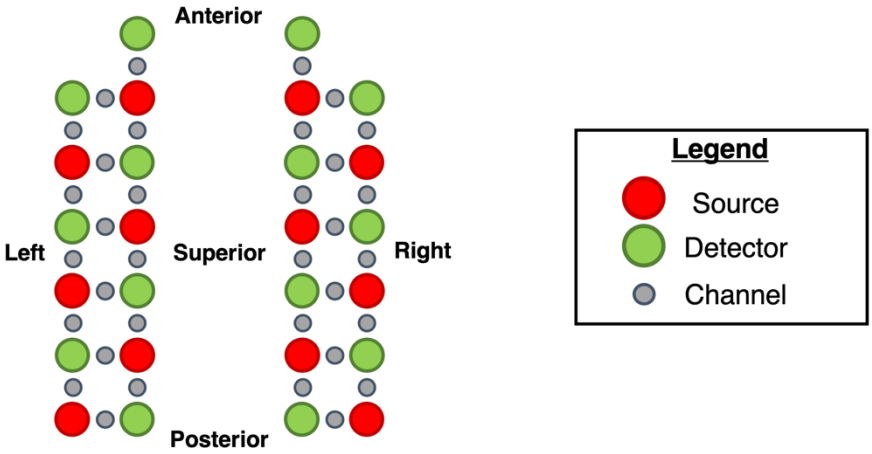

Figure 2.13: Representation of the BRIGHT array, outlining the positions of sources and detectors (see legend).

The placement of the headgear was assessed laterally by overlaying a set of axes on images of the participants' heads to quantify the displacement of a reference optode. This was previously conducted by another member of the BRIGHT project, and this method was first demonstrated by Blasi et al. (2014). The intended placement of the headgear was such that the third lower optode from the posterior, used as a reference optode (see Figure 2.14), was above the tragus.

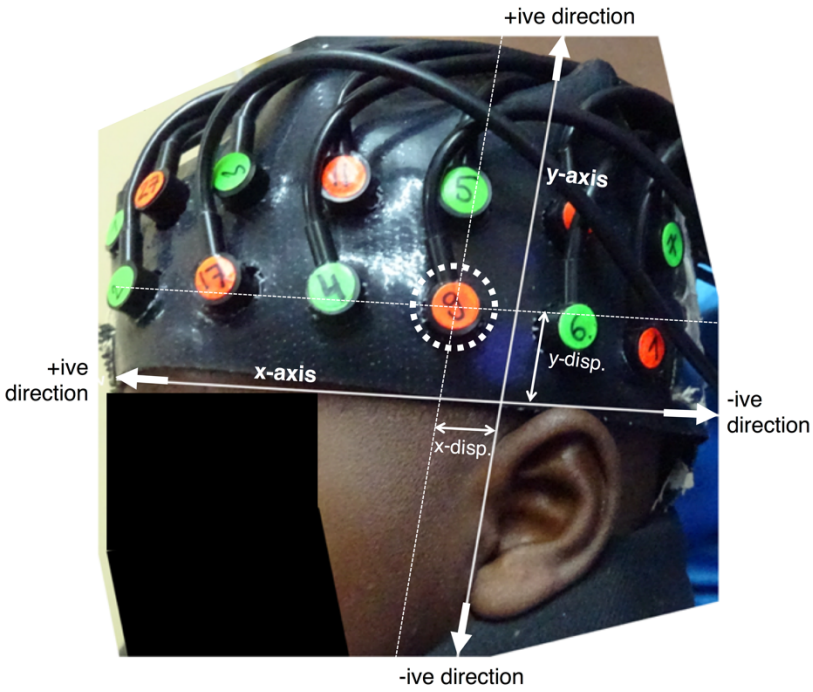

Figure 2.14: Lateral assessment of headgear placement. The displacement of a reference optode, highlighted by a dotted circled, in directions parallel to the x- and y-axes is measured (denoted by "x-disp." And "y-disp."). Displacement in the anterior or superior directions were taken to be positive, while displacement in the posterior or inferior directions were taken to be negative.

The overlaid x-axis was defined on the head model as a line from the top of the eyebrows running along the superior-most point of the ear, while the y-axis was defined as a line passing through the tragus and the anterior of the helix (see Figure 2.14). Displacement in the directions of both x- and y-axes were measured; displacement towards the anterior or superior direction was defined as positive, while displacement towards the posterior or inferior direction was defined as negative. The x-displacement of the reference optode was measured, while the vertical displacement of the bottom headband at that x-

displacement value was measured and then added to the value of the lower band thickness to obtain the y-displacement.

For each hemisphere the approximated x-axis on the warped head model was defined as a curve along the scalp surface from Iz to FPz along the lateral side of the head, and the y-axis was approximated by defining a curve from the preauricular point to CCPz on the midline of the head (see Figure 2.15).

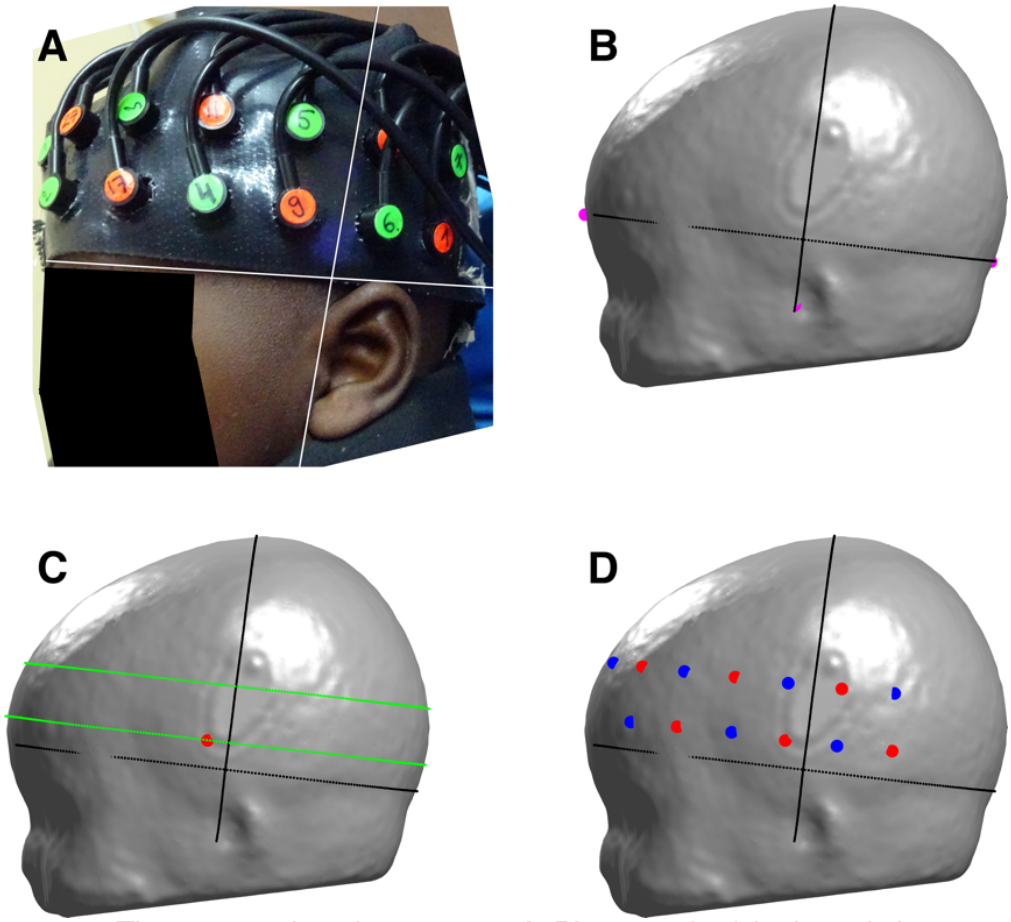

Figure 2.15: The array registration process. A: Photograph of the lateral placement of the array on an example infant, with the x- and y-axes overlaid. B: The x- and y-axes approximated on the head model. C: Curves (in green) parallel to the Iz-FPz curve which were used to register optodes in relation to the reference optode, shown as a red circle. D: All optodes registered to the head model, where detectors are represented by blue circles and sources are represented by red circles.

The x- and y-displacement values of the reference optode extracted from photographs were used in a curve-walk procedure to register the reference optode to the head model. The x-displacement value was used to walk

horizontally along the x-axis curve from the x-y axis intersection, and a curve was defined parallel to the x-axis. Similarly, the y-displacement value was used to walk vertically along the y-axis curve to define another curve parallel to the y-axis. These new curves parallel to the x- and y-axes intersect at the position of the reference optode. Using a source-detector separation of 2 cm between nearest neighbours, the other optodes in the lower row of optodes in the array were registered to the head model in relation to the reference optode along the curve parallel to the x-axis. The same process was repeated using the y-displacement value increased by 1 cm to position the optodes on the upper row. An example of a registered array on the head model compared to the corresponding participant photograph is provided in Figure 2.15.

2.4.2.2 Initial analysis

Array positioning data from 5 arbitrarily chosen participants at 5-months were used to register the array to the head models at 6-, 9- and 12-months. There were, in total, 15 combinations of head models and array positions (see Table 2.3). The size of each head model was not scaled to the size of each infant.

Table 2.3: All possible combinations of head models and array positions. There are 15 combinations in total.

		Head model		
		6-months	**9-months**	**12-months**
Array position	***Array pos. 1***	6-month model, *array pos. 1*	9-month model, *array pos. 1*	12-month model, *array pos. 1*
	Array pos. 2	6-month model, *array pos. 2*	9-month model, *array pos. 2*	12-month model, *array pos. 2*
	Array pos. 3	6-month model, *array pos. 3*	9-month model, *array pos. 3*	12-month model, *array pos. 3*
	Array pos. 4	6-month model, *array pos. 4*	9-month model, *array pos. 4*	12-month model, *array pos. 4*
	Array pos. 5	6-month model, *array pos. 5*	9-month model, *array pos. 5*	12-month model, *array pos. 5*

For each array position and head model combination, the TOAST++ software was used to model near-infrared light transport to produce a forward model at 780 nm and 850 nm using the diffusion approximation ((Schweiger & Arridge, 2014), see http://toastplusplus.org). The optical properties used at both of these wavelengths are shown in Table 1.1. The mean sensitivity values at

each node at both wavelengths were computed from the forward models. The centre of mass of the sensitivity distribution for each channel was computed, using a weighted sum of node coordinates where each node's sensitivity value was used as a weight.

Therefore, there were three centre of mass positions for each channel across all age models. For a given array position, all centre of mass positions were non-linearly transformed to the space of the 6-month model using ANTS registration (http://stnava.github.io/ANTs/), which was used as a common space. The brain masks at 6-, 9- and 12-months were used to compute the registration. For each array position, the Euclidean separation between equivalent channel positions at each age in the common space was computed. This is termed to be the *between-age variability* in channel position. This variation will be largely affected by choice of head model, in other words by age-appropriate anatomy, and should not be affected by variation in array position.

There were five centre of mass positions per channel in each age model. For each age, the Euclidean separation between equivalent channel positions was computed. This is termed the *within-age variability* in channel position. This variation will be largely affected by variation in array position, and will not be affected by age-related changes in anatomy.

2.4.2.3 Longitudinal anatomical changes

To isolate the effect of longitudinal changes in anatomy on light propagation, the above process was repeated with two key differences:-

1. Each head model was scaled to be the same head circumference as the 6-month head model. A scale factor was calculated by dividing the model's head circumference by the 6-month head model's head circumference. Each node's x-, y- and z-coordinates were multiplied by the scale factor.

2. There is variation in each head model due to cranial landmarks positions being determined independently for each model. To remove this source of variation, cranial landmarks positions form the 6-month model were registered (using ANTS registration, based on head mask registration) to the 9-month and 12-month models to recalculate scalp positions for registering the head model and then used to register the array.

For each array position, the array was registered to each head model, light transport was modelled for each channel using TOAST++, and the centre of mass of each channel was computed.

2.4.2.4 Variation in head size

To isolate the effect of head size, the head model created using data from Shi et al. was scaled to be the same head circumference as the age-appropriate head models created using the Sanchez et al. data. This removes variation due to age-related anatomical changes.

For each array position and for each scaled head model, the array was registered, light transport was modelled for each channel using TOAST++, and the centre of mass of each channel was computed.

2.4.2.5 Variation in cranial landmarks positions

The positions of cranial landmarks were determined on the surface of each model created using the Sanchez et al. data. These positions were therefore determined independently, which could lead to variation in cranial landmarks positions between the head models at different ages. Using ANTS registration, the registration between the head mask from Sanchez et al. data and Shi et al. data was computed, and was used to transform the positions of the cranial landmarks from each age-appropriate model to the space of the Shi et al. model which had not undergone head scaling.

2.4.3 Results

Figure 2.16 shows the between-age variability and the within-age variability in channel centre of mass for each of the four analyses described. The most important plot to highlight is for longitudinal anatomical changes (the second row of the figure). The median between-age variability is 2.4 mm, which is a measure of the effect of longitudinal changes in anatomy on light transport (given the available age-appropriate averaged structural data). However, the within-age variability, where centre of mass positions were computed using different array positions, is substantially greater. The distribution of within-age variability and the distribution of between-age variability (both combined across all channels) were compared using a two-sample T-test ($p < 0.0001$, median 7.3 mm, median absolute deviation 3.7 mm).

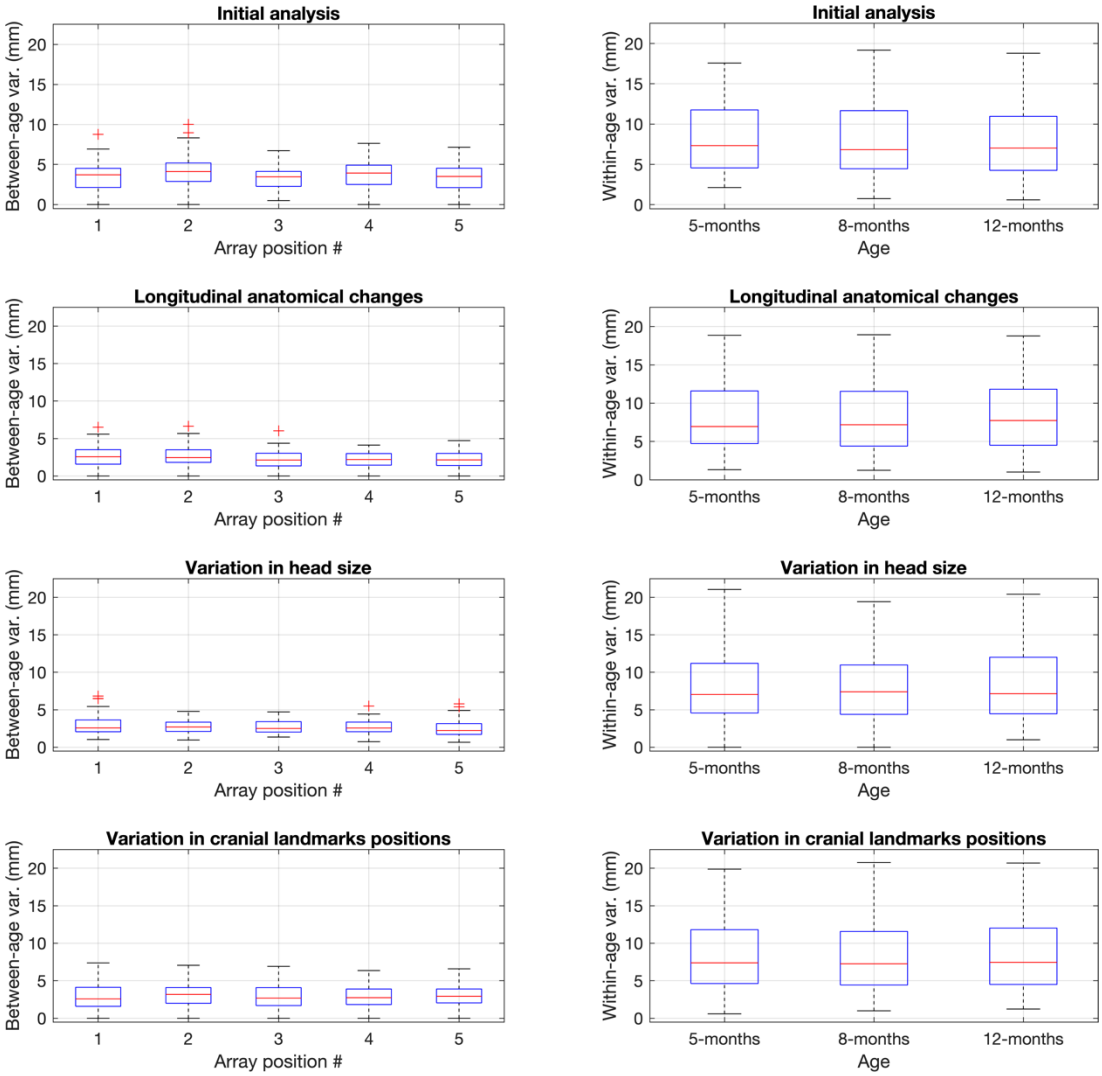

Figure 2.16: Between-age variability and within-age variability quantifying the effects on light transport of the different parameters investigated in the sensitivity analysis.

2.4.4 Discussion & conclusion

The results from this preliminary analysis demonstrate that variation in array position is the dominant factor which drives differences in channel centre of mass positions, which is substantially greater than variation due to head size, cranial landmarks positions and age-related anatomy. In the age range 5- to 12-months, the effect of longitudinal changes in anatomy on light transport is much lower than the influence of array position and justifies the use of a single model across ages.

In this work, specific channels were localised to cerebral anatomy based on a *forward modelling* approach to infer a cortical label using a weighted sum of sensitivity values for each channel. Similar approaches to channel localisation have been conducted: one such example is Perdue et al. (Perdue et al., 2019) where the point of maximum sensitivity for each channel in a forward model is used to assign an anatomical label.

Another approach to channel localisation is *channel projection*. Typically, the position midway between source and detector for each channel is determined on the scalp surface of a head model. Each midway position is then projected to the nearest point on the cortical surface. An example of this approach was demonstrated by Lloyd-Fox, Richards, et al. (2014) who used a brain parcellation atlas to determine an anatomical label for each projected channel location. This method does not involve forward modelling, and so was not appropriate to study the effect of longitudinal changes in anatomy on light transport.

In future, it would be interesting to conduct this analysis using an adult head model such as the MNI152 model. The results from this preliminary analysis suggest that age-appropriate anatomy in this age range has a much smaller effect on light transport than array position, but repeating this analysis using an adult model would enable us to ascertain whether infant-specific anatomy offers an improvement.

Longitudinal anatomical changes have a significantly and substantially smaller effect on light transport than variability in array position, which justifies the use of a single head model to be used for infants in this age-range. In addition, a more well-defined cortical surface could be extracted using the Shi et al. averaged data (see Figure 2.17) and the data package included a parcellation atlas registered to the space of the model. The head model produced using the Shi et al. data will therefore be used in Chapter 3 as a structural prior for performing image reconstruction with the BRIGHT project data.

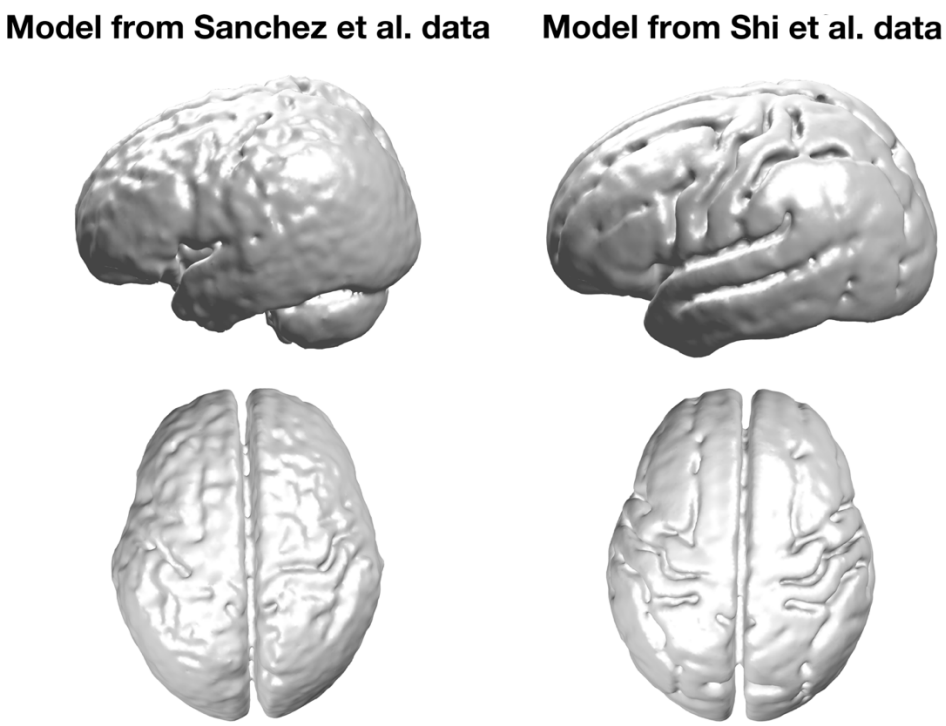

Figure 2.17: Comparing the cortical surfaces of models produced using Sanchez et al. and Shi et al. data. The cortical surface produced from the Shi et al. data exhibits much higher levels of gyrification and cortical detail, which will aid anatomical interpretation of images reconstructed using this model as a structural prior.

2.4.5 The role of CSF

The CSF is a medium with a relatively low scattering coefficient. In deriving the diffusion approximation to the RTE, it is assumed that the scattering pathlength is sufficiently short that scattering events can be considered nearly isotropic. The effective scattering pathlength is given by the inverse of the reduced scattering coefficient. For most human tissues, this pathlength is on

the order of 1 mm. However, for CSF with the optical properties assigned here (μ'_s(780 nm) = 0.1094 mm^{-1} and μ'_s(850 nm) = 0.1660 mm^{-1}), the effective scattering pathlengths are 9.14 mm and 6.02 mm at 780 nm and 850 nm respectively. These values are much larger than the values for CSF thickness in infants (Beauchamp et al., 2011), and so photons will more likely than not traverse the CSF without experiencing a scattering event. The assumptions underpinning the diffusion approximation are therefore invalid in the CSF, which is likely an additional source of error in the forward modelling procedure used in this Chapter.

There exist several studies employing Monte Carlo modelling to assess the accuracy of using the diffusion approximation in a head model containing CSF. Custo et al. (2006) found that increasing the reduced scattering coefficient from 0.1 to 0.3 mm^{-1} in the CSF did not lead to significant variation in forward modelling. The authors found that the sensitivity to the cortex is not reduced by using the diffusion approximation to model light transport but that the sensitivity is concentrated to the superficial cortex.

In adults, Okada & Delpy (2003) found the plausible range of the reduced scattering coefficient in CSF to be from 0.16 mm^{-1} to 0.32 mm^{-1}. The values used in the forward modelling procedure in this Chapter are at the lower end of or below this range. Koyama et al. (2005) conclude that using 0.3 mm^{-1} as the value for the reduced scattering coefficient of CSF is best to minimise errors when employing the diffusion approximation, and state that error in forward models increases steeply when a value below 0.1 mm^{-1} is used for the reduced scattering coefficient in CSF.

There exist other approaches to address the issue of representing CSF. Forward modelling approaches employing the diffusion approximation are historically much faster at modelling light transport than Monte Carlo approaches. A hybrid approach is described by Hayashi et al. (2003) where the diffusion approximation is used to compute light transport in high-scattering

tissues (white matter, grey matter and extra-cerebral tissue) while Monte Carlo modelling is used to model light transport in the CSF. The authors found good agreement between light transport models produced using the hybrid method and Monte Carlo, noting that computation time for the hybrid method was greatly reduced compared to pure Monte Carlo modelling.

An approach employed by Dehghani et al. (2000) applies the radiosity-diffusion model to calculate light transport in the CSF. The diffusion approximation is used to calculate light transport in the high-scattering tissue, while light is modelled to travel rectilinearly (i.e. travelling in a straight line) through the CSF (Arridge et al., 2000; Firbank et al., 1996). The CSF, however, is not purely non-scattering. There exist fine arachnoid trabeculae which cause faint scattering in the outer CSF, and this low-level of scattering cannot be accounted for by either the diffusion approximation or the radiosity-diffusion model.

2.4.6 Why focus on anatomical changes?

A question fundamental to the motivations of this work is this: why focus on optimising head models using age-appropriate anatomy rather than focussing on other sources of error?

Other sources of error exist in this sensitivity analysis which were not investigated. For example, mesh quality metrics were not compared between the different head models. Degenerate (i.e. highly irregular) tetrahedra in the mesh can lead to numerical errors in the forward model of light transport. Small volumes of tissue existing (implausibly) within other tissues would have made the mesh more liable to including degenerate tetrahedral elements. The de-islanding procedure used in head model production will have rid the models of most of these small islands of tissue. It is unlikely that meshing errors would have substantially altered the results of the sensitivity analysis.

There exists significant uncertainty in the measured optical properties of tissues, as shown by the variance in the several sources of values used to determine the optical properties in this work (see Figure 1.7). These values represent the best estimates of optical properties in tissue given the available data. It is therefore difficult to comment on what impact the uncertainty in these values may have had in this sensitivity analysis.

When it comes to image reconstruction, the choice of regularisation parameter has a huge impact on the resultant images. Further, it is assumed that changes in absorption are linearly related to changes in intensity and that changes are small relative to background optical properties: another potential source of error.

So, why has this work focussed on age-appropriate anatomy and – more widely – why does this thesis focus on developing structural priors? In this Chapter, studies have been highlighted that detail the age-related changes in anatomy that the infant brain (and head) undergoes, but how do these changes impact light transport? This question has not been sufficiently answered in the infant population. Structural data exist which enable these questions to be addressed; the notable age-related changes that occur in infant cranial anatomy therefore justify investigations of what effect anatomical changes have in the context of fNIRS and DOT.

Chapter 3

Using image reconstruction to investigate the robustness of longitudinal infant fNIRS channel-space analyses to variation in head size and array position

3.1 Introduction

As stated in Chapter 1, the period from conception to two years post-birth is a critical stage in the development of the brain and nervous system. Given the recent increase in the number of longitudinal developmental studies using fNIRS (as highlighted in Section 1.4), particularly within the new frontier of global health neuroimaging research, it is of paramount importance that analytical approaches are utilised that are appropriate across a range of contexts such as age and changes in head size.

Typically, the analysis of fNIRS data occurs in the channel-space, where data from each channel is pre-processed and statistically examined on a channel-by-channel basis. Group-level channel-space analyses are then predicated on the notion that data acquired from the same channel of the same array can be compared between (and combined across) individuals. This approach makes two assumptions. The first assumption is that **differences in scalp positions of sources and detectors relative to cranial landmarks are negligible across individuals.** The second assumption is that **a given scalp location has the same spatial relation to underlying cortical anatomy across all individuals**, implying that an anatomically equivalent cortical volume is being probed in different individuals. The validity of this assumption is particularly pertinent in longitudinal studies over the first year of life, where head circumference increases by almost a quarter from 1- to 12-months of age (World Health Organization, 2007). This issue concerns not only scalp-cortex correspondences, but also differences in cortical depth linked to variation in head size.

The assumptions stated above inherently imply that channel-space analyses assume a constant head size and a constant array position across participants. Variation in either of these parameters will influence the distribution of near-infrared light transmitted from source to detector, and will therefore influence measures of brain activation. The work presented in this Chapter aimed to provide an analysis to isolate the effects of the variation in

head size and array position on the analysis of longitudinally-acquired infant fNIRS data. Because these effects are fundamentally related to the three-dimensional anatomy of the subject, such an analysis requires a light transport modelling and image reconstruction approach. Using such an approach, the effects of head size and array position can be compared in a consistent anatomical space. An image reconstruction approach was therefore implemented to isolate the effects of variation in these parameters, which can then be used to infer the effects of variation in these parameters on conclusions about fNIRS data analysis drawn from channel-space analyses. In this work, image reconstruction is therefore used as a tool to investigate the validity of assuming constant array position and constant head size in channel-space analysis of longitudinal infant fNIRS data. Specifically, the work in this chapter will:-

1. investigate whether the application of a best-practice image reconstruction approach can result in different statistical inferences compared to a standard channel-space analysis.
2. use image reconstruction approaches to investigate the effect of variation in array position and head size on the interpretation of fNIRS data.
3. use image reconstruction approaches to investigate whether group size has an impact on differing statistical and anatomical inferences between a best-practice image reconstruction approach and an image-space equivalent to channel-space analysis.

To address these objectives, data from the Brain Imaging for Global Health (BRIGHT) project is used. Due to its large sample size and its inclusion of data acquired at three age points up to 12-months of age, the dataset from The Gambian cohort of the BRIGHT project is highly suited to address the objectives outlined above.

3.2 Methods

3.2.1 Participants

Recruitment of participant families was conducted by field researchers and occurred at the Medical Research Council (MRC) Unit The Gambia at the London School of Hygiene and Tropical Medicine (MRCG@LSHTM) field station in Keneba, The Gambia, during antenatal clinic visits. In order to avoid confounds relating to language translation, only families of the Mandinka group, the ethnic majority in the region (Hennig et al., 2017), were recruited. All infants included in the current study were required to have been born at term (37-42 weeks gestation). Datasets from 104 infants aged 5-months, 97 infants aged 8-months, and 97 infants aged 12-months in the Gambian cohort of the BRIGHT study were available at the time of conducting this analysis. Only datasets from the Gambian cohort were included in this analysis. This was because the Gambian cohort had a particularly large sample size, particularly in the context of longitudinal infant studies. Furthermore, this avoided the potential confounds related to cohort demographics that would come by mixing data from the two cohorts.

In the West Kiang District, where Keneba is situated, moderate to severe growth faltering is prevalent in infants from roughly 3 months of age, due to several factors which include prenatal growth retardation, poor-quality (often contaminated) foods and a high incidence of infection (Lunn et al., 1991; Lunn, 2000; van der Merwe et al., 2013). As part of the BRIGHT project, growth measurers were acquired at each age point, though infants with an indication of severe growth faltering (i.e. weight-for-height z-score or head circumference z-score greater than 3 below the median values stated in the World Health Organisation standards (World Health Organization, 2007)) were not excluded.

Ethics approval for the BRIGHT study was obtained from the joint Gambia Government/MRC Unit The Gambia Ethics Committee (‘Developing brain

function for age curves from birth using novel biomarkers of neurocognitive function', SCC number 1451v2). Full, informed consent was obtained from all participating families prior to recruitment.

3.2.2 Procedure

The acquisition of fNIRS data was also conducted by field researchers in The Gambia. Infants wore custom-built fNIRS headgear consisting of two arrays, one over each of the left and right hemispheres, embedded within a custom-made soft silicone-based head band. As stated in Section 2.4.2.1, the arrays contained a total of 6 sources and 7 detectors per hemisphere (source-detector separations 2 cm), constituting 17 channels per hemisphere (Figure 3.1). Data were acquired with the NTS fNIRS system (Gowerlabs Ltd. London, UK) which uses two continuous wavelengths of light at 780 nm and 850 nm and has a sampling rate of 10 Hz (Everdell et al., 2005). The design of the fNIRS array enabled responses in lateral frontal to posterior temporal brain regions to be investigated, which included the inferior frontal gyrus, middle and superior temporal regions, and the temporo-parietal junction.

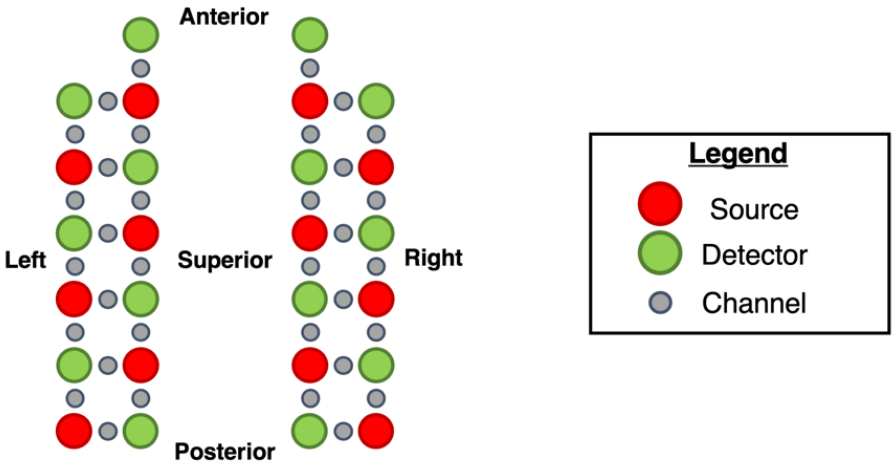

Figure 3.1: Representation of the BRIGHT array, outlining the positions of sources and detectors (see legend), which was first shown in Figure 2.13.

Any cases where displacement of the headband occurred that could compromise the stability of its fit were excluded from further analyses, as this could lead to coupling issues between optodes and the scalp surface. This was assessed by researchers from the BRIGHT project. To assess headgear

placement, photographs of the array were taken on each participant's head pre- and post-experiment. Over the anterior of the head, the intended placement of the headgear should align a vertical line denoting the centre of the band to the midline (in line with the participant's nasion landmark) and such that the silicone band lay just above and in line with the eyebrows. Infants where the headband was displaced both horizontally (with reference to the midline) and vertically (with reference to the eyebrows) were excluded from further analyses on the grounds of poor placement of headgear. Examples of three included infants with horizontal but no vertical displacement (A), vertical but no horizontal displacement (B), and no horizontal or vertical displacement (C) over the anterior of the head are shown in Figure 3.2

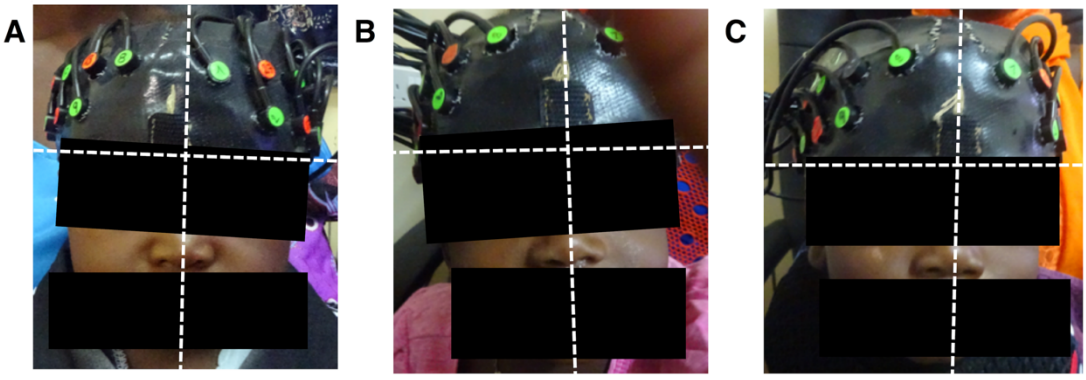

Figure 3.2: Anterior headgear placement of three infants included in the study. The horizontal dotted line denotes the level of the top of the eyebrows, and the vertical dotted line denotes the midline. A: vertical line denoting middle of the headband is uncentered relative to the midline, but the bottom of the headband is not displaced relative to the top of the eyebrows. B: bottom of headband is displaced superiorly with respect to the top of the eyebrows, but is centred relative to the midline. C: headgear is centred relative to the midline and is in line with the top of the eyebrows.

The placement of the headgear was assessed laterally by overlaying a set of axes on the images of the head to quantify the displacement of a reference optode, as detailed in the preliminary sensitivity analysis in Section 2.4.2.1. If the x-displacement value was greater than or equal to 1.6 cm, channels were re-indexed such that the array was shifted either forward or backward one full channel space. If the y-displacement was greater than 1.6 cm, the infant was

excluded from further analyses on the grounds of poor headgear placement. This analysis was completed by researchers from the BRIGHT project.

In addition, head circumference, tragus-to-tragus distance and nasion-to-inion distance were measured for each participating infant. All infants without a head circumference measurement were excluded.

3.2.3 Experimental paradigm

Participants were assessed using an auditory-visual social perception paradigm first described by Lloyd-Fox, Papademetriou, et al. (2014) and subsequently used in a number of other studies of infant brain function (Frijia et al., 2021; Lloyd-Fox et al., 2012, 2013, 2017, 2018; Perdue et al., 2019). This was completed by field researchers in The Gambia.

The paradigm included three experimental conditions and a baseline condition. During each condition, visual-social videos were presented, showing Gambian adults moving their eyes left or right, or performing hand games. The duration of these videos ranged from 9 to 12 s. In the *visual-social silent* (VS) condition, these visual-social videos were presented in silence with no accompanying audio. At the onset of two in every three trials, auditory stimuli were presented, lasting a total duration of 8 s (consisting of four different sounds). The *auditory vocal* (V) condition was where infants were presented with non-speech vocalisations of two adult speakers (who were either coughing, crying, laughing or yawning) alongside the visual-social videos. The *auditory non-vocal* (NV) condition was where common environmental sounds familiar to the infants that were not human- or animal-generated were presented alongside the visual-social videos.

Experimental conditions were altered one after the other, and the same order of conditions (VS, NV, V, VS, V, NV) was presented until the infant showed signs of fussiness or boredom or up to the point that 5 presentations of each condition has been reached. During fNIRS data acquisition, videos of the

infants were recorded to perform eye-tracking to monitor the time the infant was looking at the screen for each trial, which was used as an indication of the infant's attention. A baseline condition was presented between experimental conditions, where images of types of transport (such as helicopters, cars, and trains) were displayed. A graphical representation of the paradigm is shown in Figure 3.3.

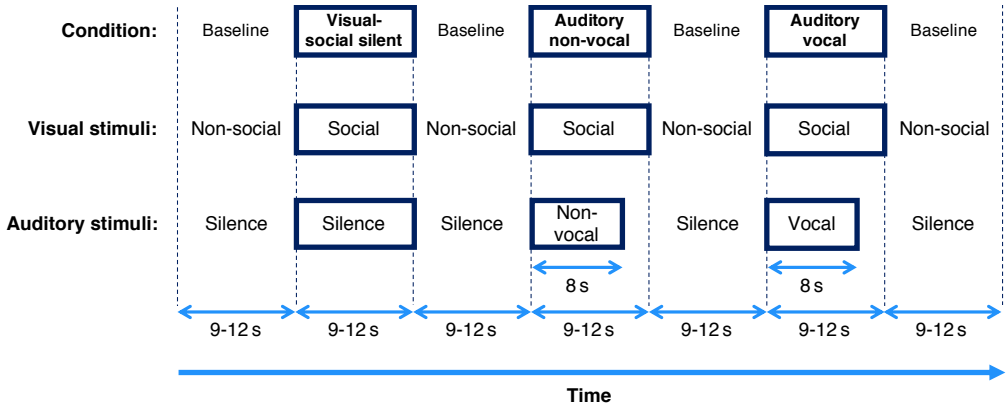

Figure 3.3: Representation of stimulus presentation in the experimental paradigm.

In this work, only the response to the auditory vocal condition was investigated. Usually, the response to this condition is studied in the context of its contrast with the response to the auditory non-vocal condition. However, here the aim was to investigate whether different data analysis approaches (in both image- and channel-space) can lead to different inferences drawn from the data rather than the contrast between the two conditions. In response to the auditory vocal condition, activation is expected in the temporal lobe (particularly in the posterior part) and the inferior frontal gyrus (Lloyd-Fox et al., 2009).

3.2.4 fNIRS data pre-processing

In this work, fNIRS data was used that had already undergone pre-processing. The fNIRS data were pre-processed using NirsPlot (Hernandez & Pollonini, 2020) and Homer2 (MGH–Martinos Center for Biomedical Imaging, Boston, MA, USA) (Huppert et al., 2009), which were both implemented in MATLAB. The specific pipeline and analysis have previously been reported by Bulgarelli

et al. (Bulgarelli et al., 2020) and Hernandez & Pollonini (Hernandez & Pollonini, 2020).

The first step in the processing stream was channel pruning. Based on previous experience with the NTS fNIRS system, channels with intensity readings lower than a certain threshold were immediately excluded. The data were then subjected to a cardiac-signal and spectral analysis assessment based on a method first proposed by Pollonini et al. (2016). This inspection was done within each channel in the array. Channels that did not pass these quality assessments were excluded from further analysis. If more than 40% of channels from a given dataset were deemed invalid, then the whole dataset was excluded from further analysis.

For each of the four experimental conditions, raw intensity data from surviving channels were processed in a pipeline in Homer2. The first step converted raw intensity data to optical density. Motion artifacts were corrected using a combination of spline interpolation and wavelet-based filtering in the method proposed by Di Lorenzo et al. (Di Lorenzo et al., 2019). Following motion artifact correction, sections of the data still affected by noise were flagged manually: if such an artifact was detected, a time window wider than the extent of the flagged section was defined on either side of the artifact. Trials within this time window were excluded from the analysis, where trial exclusion was applied within each channel. The data were band-pass filtered with high- and low-pass frequencies of 0.02 and 0.6 Hz respectively in order to correct for slow baseline drifts in the data as well as to eliminate high-frequency noise. The modified Beer-Lambert law was employed to convert optical density data into concentration changes in oxy- and deoxy-haemoglobin (Delpy & Cope, 1997). The differential pathlength factors were calculated for each wavelength and age using the formula proposed by Scholkman & Wolf (Scholkmann & Wolf, 2013)[9].

[9] The output of the pre-processing pipeline developed by Bulgarelli et al. (2020) and Hernandez & Pollonini (2020) is a block-averaged time course of

Based on the looking time measures, trials where the infant was looking at the screen for less than 60% of the trial's duration were excluded, and infants with less than a minimum of three valid trials for the auditory vocal condition were excluded. In Homer2, all the remaining trials (after exclusion for looking time and excessive noise due to motion) for each participant were block-averaged for each condition: the block duration was defined starting at t = -2 seconds from stimulus onset and ending at t = 20 seconds from stimulus onset. The total duration of the block was therefore 22 seconds.

3.2.5 Processing streams

In this work, five data processing streams were devised: a channel-space analysis and four image reconstruction pipelines (see Figure 3.4).

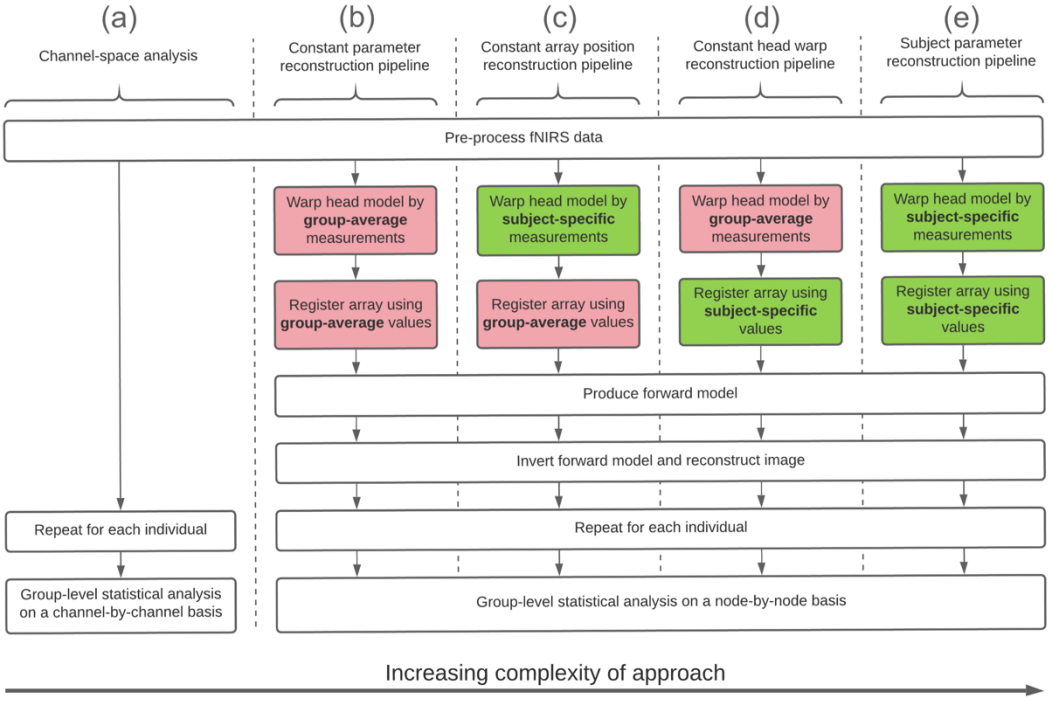

Figure 3.4: Outline of the different processing streams compared in this study.

changes in concentration. For image reconstruction in this work, the concentration change data are converted back to changes in optical density using the same differential pathlength factors as used for the conversion to concentration change data. There is no theoretical need to employ differential pathlength factors here, and future versions of this image reconstruction method will seek to remove this redundancy.

In the channel-space analysis, the block-averaged values of concentration changes across infants during a response window were compared to baseline for the auditory vocal condition. For each image reconstruction processing stream, each individual's block-averaged concentration changes were converted back to changes in optical density values using the modified Beer-Lambert law. The changes in optical density were then used as an input in the image reconstruction step. Changes in optical density were used instead of changes in raw intensity because the log of the intensity ratio is required to linearise the inverse problem when using the Rytov approximation method for image reconstruction (Boas et al., 2001).

The basic outline for each of the imaging processing streams was as follows:-

1. Warp a head model on the basis of certain head measurements.
2. Register optode positions to that warped head model.
3. Produce a forward model, which defines the fNIRS measurement sensitivity distribution associated with each channel.
4. Invert the forward model, and use it as an input alongside a given infant's block-averaged changes in optical density data into a reconstruction function to produce a series of images of the distribution of haemoglobin concentration changes on the cortical surface.
5. Repeat steps 1-4 for all participants.
6. Perform group-level statistical analysis on a node-by-node basis, comparing the concentration change values across participants in a response window to baseline.

For step 1, the head model could be warped on the basis of either (a) subject-specific head measurements, or (b) group-average head measurements. For Step 2, there were two options for registering the array to the head model: (a) register by subject-specific array positioning data, or (b) register by group-average array positioning data. Given these two steps in the processing pipeline, each with two options, there were a total of four possible image

reconstruction processing streams. All four of these processing streams are outlined in Figure 3.4(b-e).

The ***constant parameter reconstruction*** pipeline, outlined in Figure 3.4(b), used group-average head measurement data to warp the head model and group-average array position data to register the array. This processing stream employed the same assumptions as the channel-space analysis, and so can be considered as an image-space equivalent to channel-space analysis. While some fNIRS analyses may not attempt to account for head size, a reasonable minimum step for research groups to take is to obtain a population average measure of head size and use that measurement to warp a head model for each age group.

The ***constant array position reconstruction*** pipeline, outlined in Figure 3.4(c), used group-average head measurement data to warp the head model but subject-specific array position data to register the array. This pipeline aimed to isolate the effects of variation in array position.

The ***constant head warp reconstruction*** pipeline, outlined in Figure 3.4(d), used subject-specific head measurement data to warp the head model but group-average array position data to register the array. This pipeline aimed to isolate the effects of variation in head size.

The ***subject parameter reconstruction*** pipeline, outlined in Figure 3.4(e), used subject-specific head measurement data to warp the head model and subject-specific array position data to register the array. Given that this processing stream attempted to account for array position and head size on a subject-specific basis, this was effectively the best-practice image reconstruction pipeline that could feasibly be applied to this dataset.

Some common fNIRS pipelines do not account for head size at all, and so further analysis pipelines were devised to mimic the case where a single-sized

head model is used for all infants. The constant parameter pipeline was re-run twice for the fNIRS data at each age, using the head measurements of the other ages.

3.2.6 Head modelling

A four-layer mesh model of the infant head was used as part of the image reconstruction process, which was constructed using structural MRI data from a cohort of 12-month-old infants presented by Shi et al. (Shi et al., 2011), whose construction is detailed in Section 2.3.3. A single head model was used across ages and spatially warped appropriately. A preliminary sensitivity analysis, whose results are presented and discussed in Section 2.4, demonstrated very little differences in sensitivity as a result of anatomical difference (i.e. spatial distribution of tissues but not model size) across the age-appropriate models produced using data from Sanchez et al. Using a single model across ages also negated the need to register different head models to a common space for comparison across ages, which would undoubtedly have incurred some level of error itself.

A parcellation atlas, the Automated Anatomical Labelling (AAL) atlas, consisting of 90 volumes of interest, accompanied the Shi et al. data and was used to parcellate the brain in the head model. The coordinates of the centre of each voxel in the AAL atlas were computed and were transformed to the space of the 12-month head model based on the affine transformation information in its file header. Each node in the grey matter surface mesh was assigned the parcellation label of the nearest voxel centre in the AAL atlas.

The coordinates of five cranial landmarks (the nasion (Nz), the inion (Iz), the left pre-auricular point (Al), the right pre-auricular point (Ar) and vertex (Cz)) were determined manually using ITK-SNAP (Yushkevich & Gerig, 2017). Based on a curve-walk procedure (Aasted et al., 2015), the 10/5 positions on the scalp surface of the head model were computed using the cranial

landmarks coordinates as described in Section 2.3.2.7. The mesh nodes were then transformed to a coordinate system where:

- the position of Iz defines the origin
- a line joining Iz to Nz defines the y-axis
- the z-coordinates of Ar and Al are approximately equal following rotation of mesh nodes around the y-axis.

3.2.7 Head model warping

To account for variation in head size and shape, the head model needed to be warped. The head model could be warped to the shape of a particular individual based on their head measurements taken at experiment; this enables variation in head size and shape at the individual-level to be accounted for. Alternatively, the head model could be warped by the age-cohort average head measurements; this enables the validity of assuming a constant head size across individuals in a given age-cohort to be assessed.

As part of this work, a method was devised to iteratively warp the head model using data on head circumference, tragus-to-tragus via Cz (approximated to be the Ar-Cz-Al) distance, and nasion-to-inion via Cz (Nz-Cz-Iz) distance. For the pipelines that required the use of subject-specific head measurements (subject parameter and constant array position pipelines), these measures were used to warp the infant head model to each participant's head dimensions. For the pipelines that did not require subject-specific head measurements (constant head warp and constant parameter pipelines), the mean values of these measures were calculated at each age and used to iteratively warp the infant head volume mesh. At the 5-month assessment timepoint, measurement of the Nz-Cz-Iz distance was not taken, and so the head model was warped according to head circumference and Ar-Cz-Al distance. The grey matter surface mesh was also iteratively warped by the same values as the head model.

At each step in this iterative warping procedure, the nodal coordinates are multiplied by a certain warp factor; each step therefore can be likened to an affine transformation. For a given participant, the head model was initially scaled according to head circumference; a warp factor was calculated by dividing the subject-measured (or group mean) head circumference by the head model's initial head circumference. Each node's x-, y- and z-coordinates were multiplied by the warp factor. The warped model's head circumference, Ar-Cz-Al distance and Nz-Cz-Iz distance were then computed, and the measurement with the greatest difference between its corresponding subject-measured (or group mean) value was then used to re-warp. For whichever distance had the greatest difference, the warped model-measured value was divided by the subject-measured (or group mean) value to yield another warp factor which was then multiplied by the relevant node coordinates (x- and z-coordinates if Ar-Cz-Al; y- and z-coordinates if Nz-Cz-Iz; x-, y- and z-coordinates if head circumference). The process was repeated until the error for the Ar-Cz-Al distance was below 6 mm, the error for the Nz-Cz-Iz distance was below 6 mm, and the error for head circumference was below 3 mm. Allowing a degree of tolerance with regards to head measurements (which themselves are prone to a degree of error) removes the potential for over-fitting the head warping procedure to head measurements, which can lead to anomalous and anatomically implausible head shapes. The parameters chosen were a balance between over-fitting, accuracy and computation time.

3.2.8 Array registration

The array was registered to the head model as detailed in Section 2.4.2.1. For the subject parameter and constant head warp pipelines, subject-specific values were used to register optodes to the head model. For constant parameter and constant array position pipelines, age-cohort mean x- and y-displacement values were used. An example of a registered array on the head model compared to the corresponding participant photograph is provided in Figure 3.5, which is a repeat of Figure 2.15 in Section 2.4.2.1.

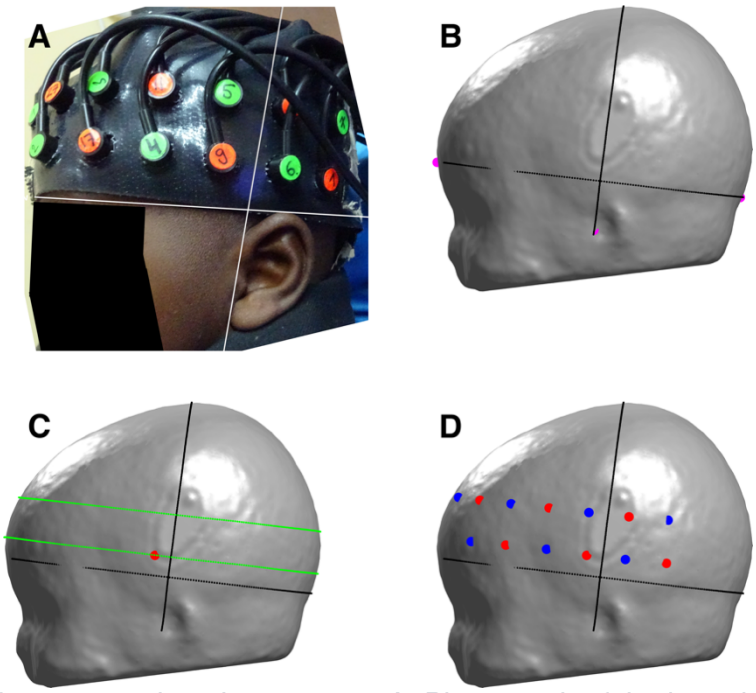

Figure 3.5: The array registration process. A: Photograph of the lateral placement of the array on an example infant, with the x- and y-axes overlaid. B: The x- and y-axes approximated on the head model warped on the basis of the infant's head measurements. C: Curves (in green) parallel to the Iz-FPz curve which were used to register optodes in relation to the reference optode, shown as a red circle. D: All optodes registered to the head model, where detectors are represented by blue circles and sources are represented by red circles.

3.2.9 Light transport modelling and image reconstruction

For each infant dataset in each processing stream, TOAST++ (Schweiger & Arridge, 2014) was used to model near-infrared light transport to produce a forward model for each wavelength. Using a regularization hyperparameter of 0.1, a zeroth-order Tikhonov regularised reconstruction was performed. No data from overlapping channels, a requirement for depth discrimination, were used in this analysis, and so image reconstruction was constrained to the grey matter nodes of the volume mesh. This has been shown in previous topographic approaches to increase the accuracy of reconstructed images when data on cortical activation is being collected (Boas et al., 2004; Boas &

Dale, 2005). In addition, one would not expect to be sampling a substantial amount of white matter due to the source-detector separation in the array.

For each individual, the forward model was thresholded at 1% of the maximum value to produce a binary image, which was mapped to the grey matter surface mesh to create an individual-level grey matter mask. A group-level grey matter mask for each age-cohort was also produced, which consisted of nodes present in the individual-level grey matter masks of at least three quarters of participants, similar to the approach taken by Wijeakumar et al. (Wijeakumar et al., 2019). Data preparation, meshing, forward modelling and reconstruction were facilitated by the DOT-HUB Toolbox (www.github.com/DOT-HUB).

3.2.10 Statistical mapping of reconstructed images

Statistical mapping was performed for oxy-haemoglobin group-level images at each age and for each image reconstruction processing stream. This was also performed for the deoxy-haemoglobin group-level images for the subject parameter pipeline.

T-statistic maps were produced to compare the group-level response to the auditory vocal condition to baseline across participants for a given age. Statistical mapping was conducted in the space of the grey matter surface mesh. A time window of 12-16 s post-stimulus onset was used to signify the peak of the haemodynamic response in the image time-course. This choice of window was informed by previous data analysis approaches using the same paradigm in previous cohorts (Lloyd-Fox et al., 2017, 2013, 2012). A baseline window was defined as the 2 s period preceding stimulus onset.

For each participant, the response window consisted of a time-course of 40 concentration change values for each node. For each node in the group-level grey matter mask, these concentration change values from all participants were concatenated to produce a single vector of concentration change values for each node.

For each participant, the baseline window consisted of a time-course of 20 concentration change values for each node. The same approach as above was taken to produce node-wise vectors of concentration changes in the baseline period.

Equivalent node-wise response and baseline vectors were compared using a two-tailed two-sample T-test; this was completed for both oxy- and deoxy-haemoglobin data separately. To correct for multiple comparisons, the Bonferroni method was employed on the basis of the number of nodes in the grey matter surface mesh, as was performed by Frijia et al. (2021), which is an extremely conservative approach.

3.2.11 Statistical mapping of channel-space analysis

Channel-wise statistical analyses were conducted which compared the group-level response for the auditory vocal condition to baseline across all infants, in a method analogous to the statistical mapping approach for the imaging processing streams. Statistical analyses were performed separately for oxy- and deoxy-haemoglobin time-courses. To be included in the analysis for a given age-cohort, the channel had to be present (i.e. not pruned) in at least three quarters of individuals. Using a 12-16 s time window to represent the peak of response and a 2 s pre-stimulus baseline, a concatenated vector of concentration change values in these periods in each channel across all infants were compared using a two-tailed two-sample T-test. To correct for multiple comparisons, the Bonferroni method was employed on the basis of the number of channels (34 in total).

To enable the group-level channel-space analysis to be compared to reconstructed images, channel location positions on the scalp were projected onto the cortical surface. It is commonly assumed in fNIRS work that the region

of the brain to which a channel is maximally sensitive is halfway between the source and the detector, and at a depth from the scalp surface equal to approximately half the source-detector separation (Fukui et al., 2003; Lloyd-Fox, Richards, et al., 2014). Using this knowledge, previous work relating to fNIRS in infants has demonstrated cortical projection to determine the cortical label and position of channels (Lloyd-Fox, Richards, et al., 2014; Tsuzuki et al., 2017).

For each age, the head model was warped by the group-average head measurements and the group-average array positioning data was used to register optode positions. The midpoint on the scalp surface between source and detector for each channel was projected onto the cortex which employs the Möller-Trumbore algorithm (Mena-Chalco, 2009; Möller & Trumbore, 1997). The surface nodes of the volume mesh (i.e. the scalp surface) that were situated within a 5 mm radius of each source-detector midpoint were determined, and were used to fit a plane. Orthogonal to this plane, a vector was defined whose length was increased until it intersected with a face on the grey matter surface mesh. The position of this intersection was taken to be the cortical projection of the channel.

3.2.12 Window-averaged images

For each individual, the duration of the block-averaged pre-processed data for the auditory vocal condition for each channel is 22 s (consisting of a 2 s pre-stimulus onset baseline period plus a 20 s post-stimulus onset period), and so each infant's reconstructed image is a time-course of 221 frames. To obtain a single image for a given individual at a given age point, the mean value of each grey matter surface mesh node in a 12-16 s window post-stimulus onset was computed, to yield what will be termed a *window-averaged image*.

3.2.13 Metric extraction

To compare images between processing streams, two metrics were devised: *peak node offset* and *cortical label of peak node*, which were computed separately for both left and right hemispheres.

At the group-level in the oxy-haemoglobin analyses, the peak node was defined as the node in the group-level image with the greatest positive T-statistic value for oxy-haemoglobin concentration change. For the deoxy-haemoglobin analyses, the peak node was defined as the node in the group-level image with the greatest negative T-statistic value for deoxy-haemoglobin concentration change. In addition, the cortical label of the peak node was determined using the AAL parcellation atlas registered to the head model. This was completed for both hemispheres at each age and for both chromophores.

At the group-level in the oxy-haemoglobin analyses, the *peak channel* was defined as the channel with the greatest positive T-statistic value for oxy-haemoglobin concentration change. For the deoxy-haemoglobin analyses, the peak channel was defined as the channel with the greatest negative T-statistic value for deoxy-haemoglobin concentration change at the group-level. To enable comparison between channel-space analysis and subject parameter reconstruction, the cortical label of the peak channel projection was determined and used as an analogous metric to the cortical label of peak node. This was completed for both hemispheres at each age and for both chromophores.

At the individual-level, the peak node was defined as the node in the window-averaged image with the greatest positive change in oxy-haemoglobin concentration. This was completed for both hemispheres for each infant at each age. This analysis focusses only on changes in oxy-haemoglobin concentration due its larger response than deoxy-haemoglobin, which was an important consideration given the lower signal-to-noise ratio in the individual-level images.

At both the group- and the individual-level, the peak node offset was defined as the Euclidean separation between the peak node from a given processing stream and the peak node from the subject parameter reconstruction. This was calculated in the space of the relevant age-cohort constant head warp model.

3.2.14 Effect of longitudinal growth measures

As part of the investigation on the effect of head size, it was investigated whether there was any association between peak node offset and two other parameters: head circumference (as measured from the infants, not corrected for age and sex) and head growth trajectory (the change in head circumference z-score between two age points). The purpose of this comparison was to assess whether the use of subject-specific parameters was more impactful in infants whose head size deviated from the group mean at a given age or whose head growth trajectories diverged from the expected trajectories outlined by the World Health Organisation (WHO) growth charts (World Health Organization, 2007).

Differences in head size could potentially lead to notable differences in light transport through the head at different age points which may lead to artefactual statistical or anatomical inferences. In typical infant growth, it would be expected that he infant would remain in (or not deviate substantially from) their decile of head circumference as they age. A negative change in z-score between ages could be due to malnutrition, especially given the high prevalence of malnutrition in the infant population in the region where data collection took place. An association between peak node offset and change in z-score was investigated to see whether there could be a malnutrition-related mechanism at work which could alter light transport through the infant head, such as an atypical brain structure.

For each individual, the difference in head circumference from the group mean was calculated. For each age and each hemisphere, Pearson correlation was used to test for associations between individual-level peak node offset and:-

1. Difference in head circumference from group mean.
2. The *absolute value* of difference in head circumference from group mean (which disregards whether the difference is positive or negative).

Head circumference values were converted to z-scores on the basis of WHO references curves (World Health Organization, 2007). For infants who had data at two or more age points, a change in z-score was computed. Pearson correlation was used to test for an association between individual-level peak node offset and:-

1. Change in z-score.
2. The *absolute value* of change in z-score (which disregards whether the change is positive or negative).

3.2.15 Combinatorial analysis

Subject parameter reconstruction represents the best-practice analysis given the available data on head size and array position for this dataset, while the constant parameter reconstruction represents an imaging equivalent to channel-space analysis. A combinatorial analysis was conducted to investigate the effect of group size on how the interpretations of subject parameter and constant parameter reconstructions may differ. As group size tends to infinity, the effect of variation in head size and array position on the fNIRS data will tend to zero (assuming a normalised distribution of the value of each of these parameters). The combinatorial analysis therefore aimed to determine whether the influence of variation in these parameters were weakened as group size was increased to the numbers included in each cohort.

For each age and each hemisphere, a combinatorial analysis was conducted. To begin with, 100 sub-cohorts of 10 randomly chosen infants were selected.

The same statistical analysis as was performed on the full cohort was performed on each sub-cohort of 10 randomly-selected infants. The position and cortical label of the peak node was determined for both the subject parameter and constant parameter reconstructions for each of the 100 sub-cohorts of group size 10, and used to calculate:-

1. Mean peak node offset relative to subject parameter reconstructions for the group size.
2. The proportion of mismatching cortical labels for the group size.

This process was repeated for sub-cohort group sizes from 11 to the full cohort size.

3.3 Results

Of the datasets initially included in this study ($N_{5\text{-months}}$ = 104, $N_{8\text{-months}}$ = 97, $N_{12\text{-months}}$ = 97), infants were excluded due to the following criteria:

1. The infant was not tested because:-
    a. The infant was withdrawn ($N_{5\text{-months}}$ = 3, $N_{8\text{-months}}$ = 8, $N_{12\text{-months}}$ = 9)
    b. The infant missed the visit ($N_{5\text{-months}}$ = 1, $N_{8\text{-months}}$ = 2, $N_{12\text{-months}}$ = 2)
    c. NIRS data acquisition was not undertaken at visit ($N_{5\text{-months}}$ = 7, $N_{8\text{-months}}$ = 9, $N_{12\text{-months}}$ = 11)
2. The infant became fussy ($N_{5\text{-months}}$ = 6, $N_{8\text{-months}}$ = 5, $N_{12\text{-months}}$ = 9)
3. Experimental errors:-
    a. Photographs of headgear placement missing ($N_{5\text{-months}}$ = 5, $N_{8\text{-months}}$ = 4, $N_{12\text{-months}}$ = 1)
    b. Video of infant during fNIRS data acquisition was missing ($N_{5\text{-months}}$ = 8, $N_{8\text{-months}}$ = 5, $N_{12\text{-months}}$ = 3)
    c. Missing event markers in the task ($N_{5\text{-months}}$ = 1, $N_{8\text{-months}}$ = 0, $N_{12\text{-months}}$ = 0)
    d. Data not saved due to a technical glitch or due to human error ($N_{5\text{-months}}$ = 1, $N_{8\text{-months}}$ = 1, $N_{12\text{-months}}$ = 2).
4. Poor placement of headgear ($N_{5\text{-months}}$ = 5, $N_{8\text{-months}}$ = 12, $N_{12\text{-months}}$ = 6)
5. Number of channels surviving channel pruning below minimum threshold ($N_{5\text{-months}}$ = 5, $N_{8\text{-months}}$ = 1, $N_{12\text{-months}}$ = 1)
6. Not enough valid trials for the auditory vocal condition ($N_{5\text{-months}}$ = 3, $N_{8\text{-months}}$ = 3, $N_{12\text{-months}}$ = 4)
7. Missing head circumference measurement ($N_{5\text{-months}}$ = 6, $N_{8\text{-months}}$ = 7, $N_{12\text{-months}}$ = 4)

See Figure 3.6 for a flowchart visualisation of the breakdown. In total, the final sample size consisted of 53 infants aged 5-months (27 female, mean age ± SD = 163.2 ± 12.2 days), 40 infants aged 8-months (19 female, 245.5 ± 8.4 days), and 45 infants aged 12-months (24 female, 376.2 ± 16.3 days).

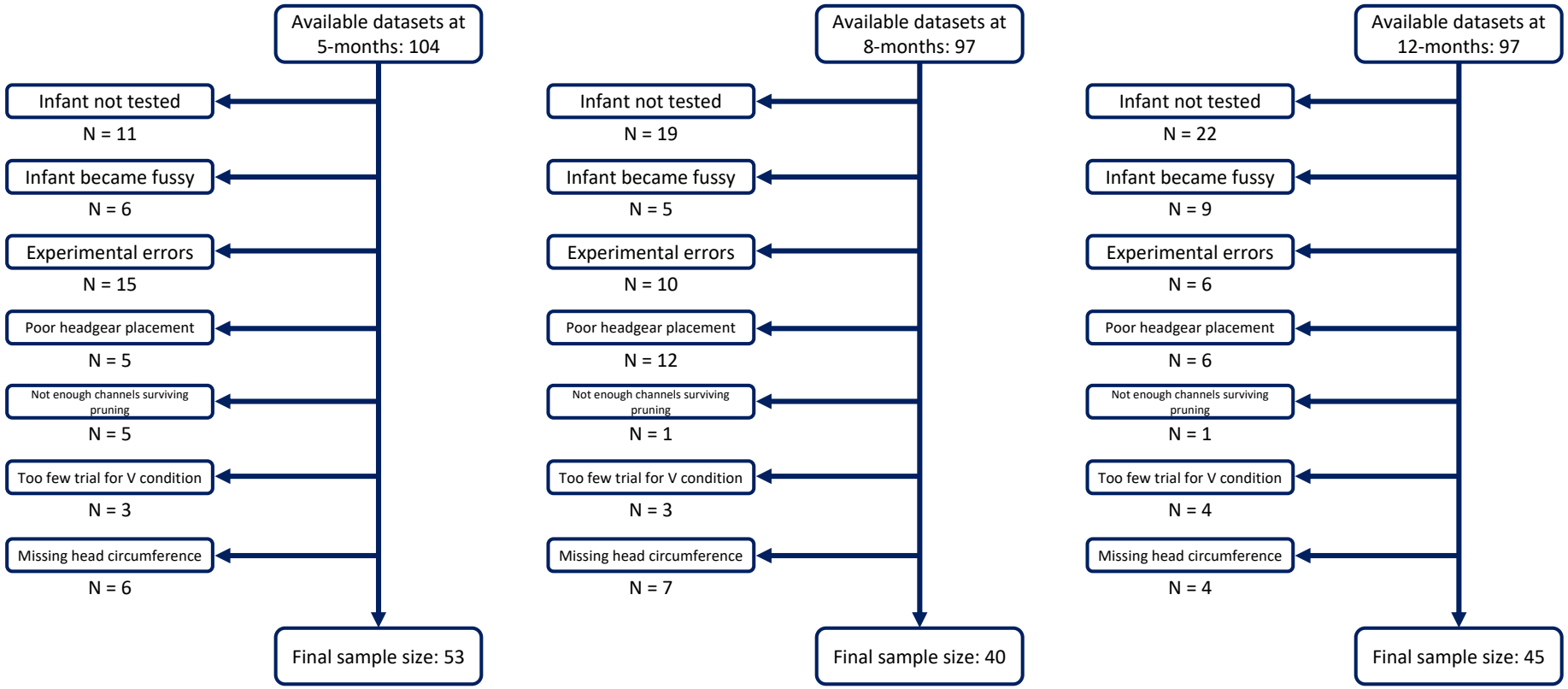

Figure 3.6: Flowchart of reasons for exclusion for each age cohort.

Figure 3.7 provides data on the accuracy of the iterative warping procedure in preserving participant-measured head measurements in the warped head models for each infant undergoing the subject parameter pipeline. This error rarely exceeded 2% for Nz-Cz-Iz and Ar-Cz-Al, and rarely exceeded 0.2% for head circumference.

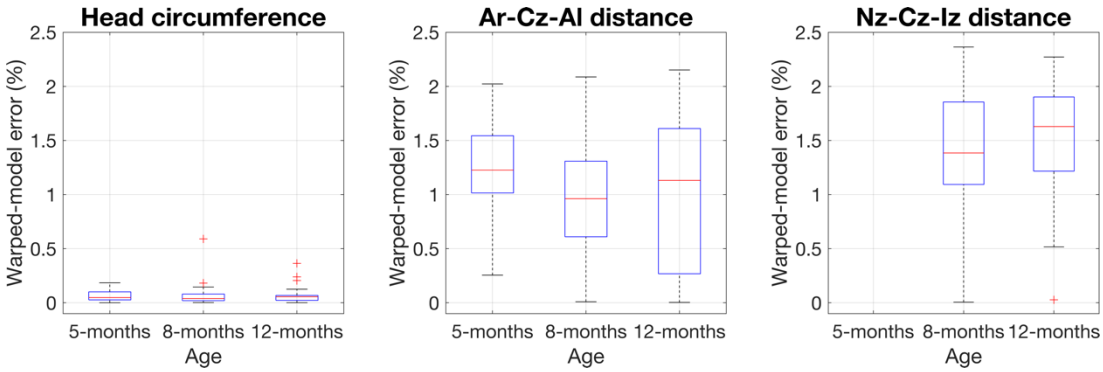

Figure 3.7: The error of head measurements from the warped head model in the subject parameter pipeline relative to the infant-measured values which were used as parameters to optimise the head warping process. Note: no Nz-Cz-Iz measurements were available for infants aged 5-months.

3.3.1 Directly comparing image reconstruction to channel-space

First, the subject parameter reconstruction pipeline and the channel-space analysis pipeline will be compared.

3.3.1.1 Oxy-haemoglobin

Figure 3.8 shows group-level cortical T-statistic maps for changes in oxy-haemoglobin concentration in a 12-16 s post-stimulus window with respect to baseline for subject parameter reconstructions. Also shown in Figure 3.8 are the cortical projections of group-level channel-wise T-statistic values comparing the same time windows.

The results appear very consistent between the two processing pipelines across all hemispheres at all ages in terms of spatial distribution, particularly in the temporal lobe. In addition, at all ages and across both hemispheres, the peak node and peak channel projection was observed in the middle temporal gyrus, demonstrating consistency in the results across the two processing streams at the group-level.

However, there are some areas where inferences subtly differ, particularly in the inferior frontal regions, as can be seen in Figure 3.8. In the left hemisphere at 5-months and the right hemisphere at 8-months, the group-level reconstructed images suggest larger changes in inferior frontal regions than can be inferred from channel-space, while in the right hemisphere at 12-months the group-level reconstructed image suggests more widespread concentration changes.

3.3.1.2 Deoxy-haemoglobin

Figure 3.9 shows the same analysis repeated using the deoxy-haemoglobin signal, replicating the analysis seen in Figure 3.8. As can be seen in Figure 3.9, in general these results also appear broadly consistent with one another.

The spatial distribution of activation shown by the channel-space deoxy-haemoglobin T-statistic values appears to emulate what is seen in image-space. However, the T-statistic values themselves appear to be much lower in the channel-space analysis, which is particularly evident in the left hemisphere at all ages and the right hemisphere at 12-months. In the deoxy-haemoglobin analysis, at all ages and across both hemispheres, the peak node and peak channel projection was observed in the middle temporal gyrus, as was the case in the oxy-haemoglobin analysis.

3.3.1.3 Quantitative comparison

The cortical projections of channel-space positions showed that there were four cortical areas where significant changes in oxy-haemoglobin concentration occurred at the group-level: inferior frontal gyrus, superior temporal gyrus, middle temporal gyrus and inferior temporal gyrus. The maximum absolute T-statistic value of a channel projected to each of these four areas in each hemisphere was noted for both the oxy- and the deoxy-haemoglobin analysis. The maximum absolute T-statistic value was also taken for each of these four cortical areas in the subject parameter reconstruction. In Figure 3.10, the differences between the channel-space maximum values and the subject parameter maximum values are shown. Consistently, one sees that the channel-space analysis underestimates the effect size relative to subject parameter reconstruction, and this is most evident at 12-months in the oxy-haemoglobin analysis and across ages in the deoxy-haemoglobin analysis.

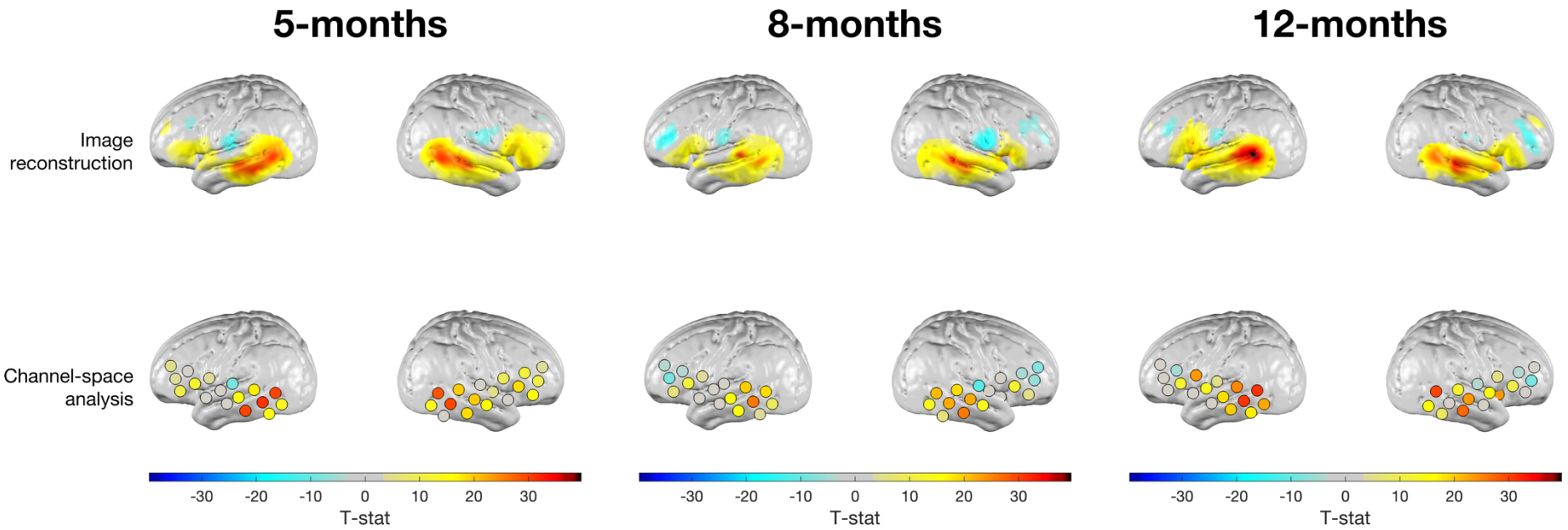

Figure 3.8: Group-level T-statistic images of changes in oxy-haemoglobin concentration in response to the auditory vocal condition relative to baseline for two approaches to analysing fNIRS data. Top row: subject parameter reconstruction pipeline. Bottom row: channel-space analysis. The displayed T-statistic values are thresholded at a value equivalent to $p < 0.05$, Bonferroni corrected on the basis of number of nodes in the grey matter surface mesh.

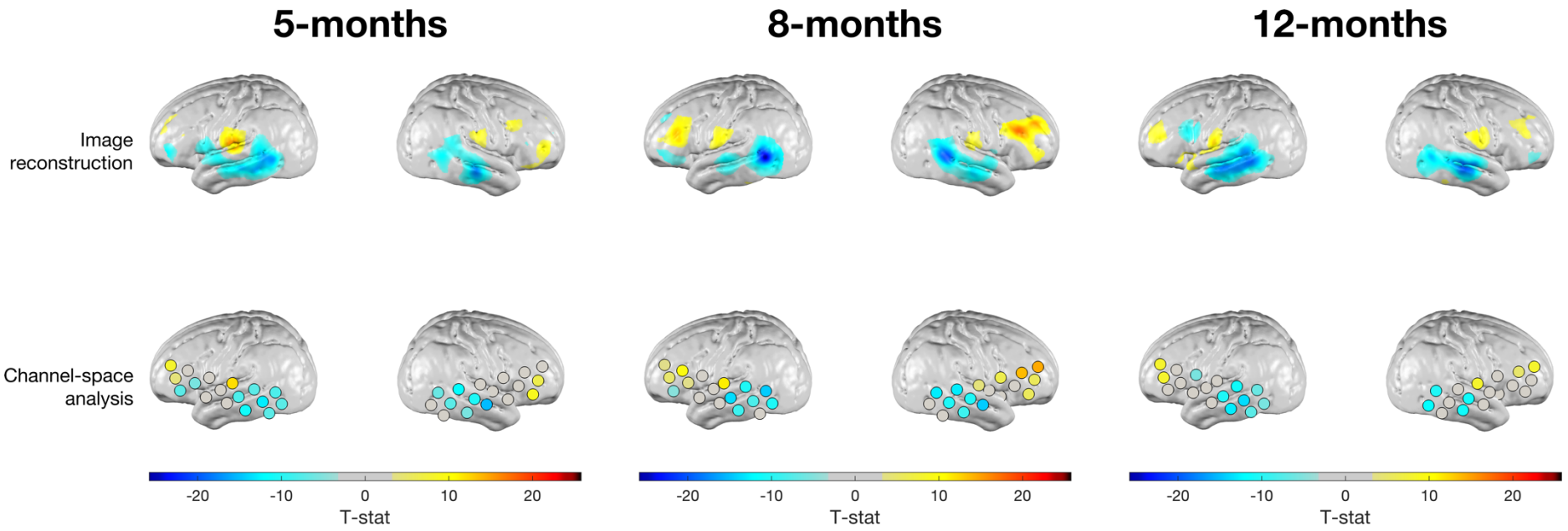

Figure 3.9: Group-level T-statistic images of changes in deoxy-haemoglobin concentration in response to the auditory vocal condition relative to baseline for two approaches to analysing fNIRS data. Top row: subject parameter reconstruction pipeline. Bottom row: channel-space analysis. The displayed T-statistic values are thresholded at a value equivalent to $p < 0.05$, Bonferroni corrected on the basis of number of nodes in the grey matter surface mesh.

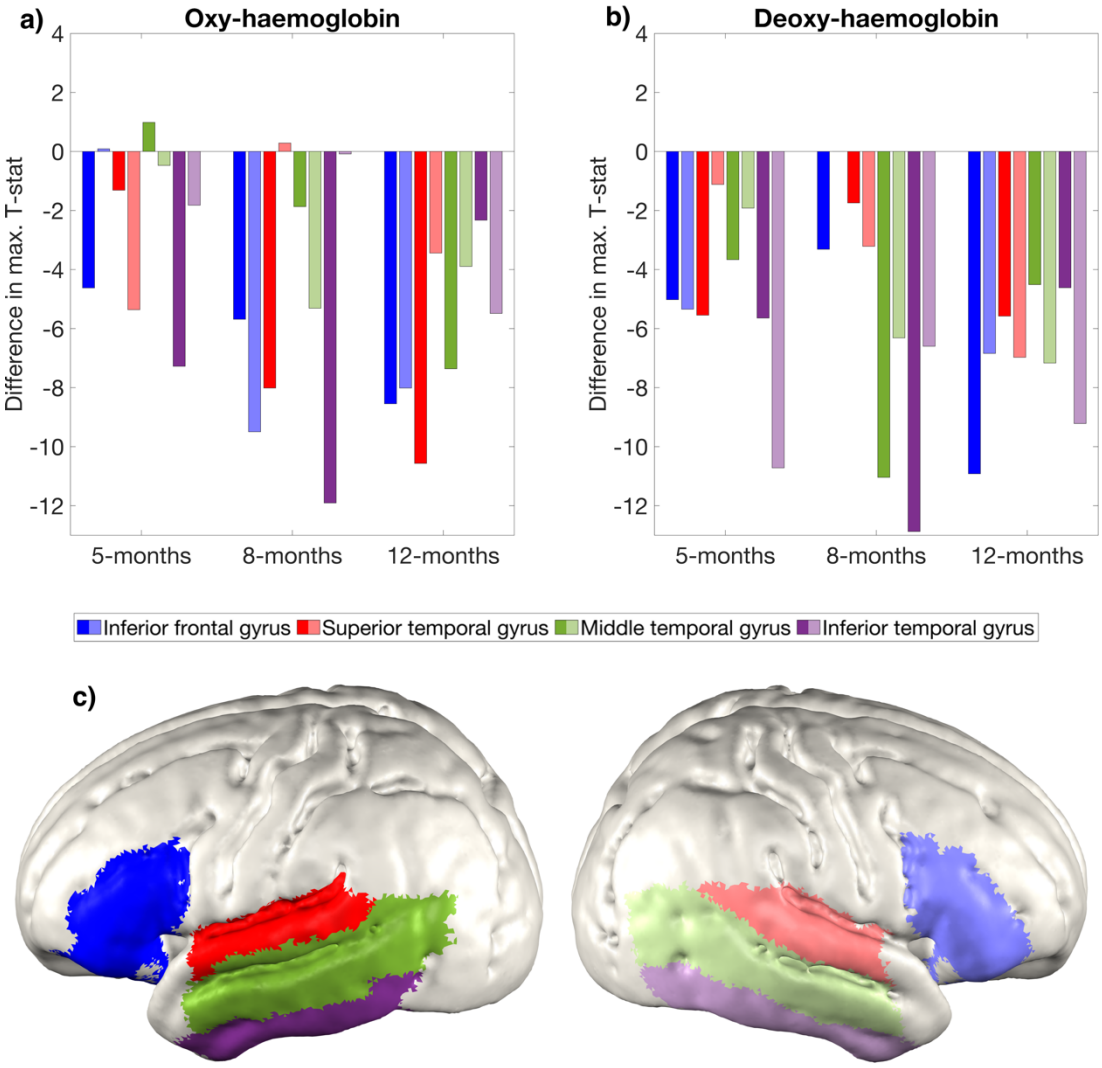

Figure 3.10: Differences in absolute maximum T-statistic values of the channel-space analysis relative to the subject parameter reconstruction for (a) oxy-haemoglobin and (b) deoxy-haemoglobin concentration changes across four cortical areas where activation is consistently seen in the oxy-haemoglobin channel-space analysis. For each pair of bars grouped by colour, the left bar represents the difference in that region in the left hemisphere and the right bar (with a more faded colour) represents the difference in that region in the right hemisphere. Note: at 8-months in the right hemisphere, no deoxy-haemoglobin concentration decrease was seen in the inferior frontal gyrus in either the channel-space analysis or subject parameter group-level image. The cortical areas are shown in (c).

3.3.2 Effects of variation in head size and array position

Another aim was to explore the effect that variation in head size and array position has on the analysis of fNIRS data. Comparisons were made at the group- and the individual-level between all four image reconstruction processing streams.

3.3.2.1 Group-level

Figure 3.11 shows group-level oxy-haemoglobin T-statistic maps for the four different image reconstruction processing streams: subject parameter, constant head warp, constant array position and constant parameter. Qualitatively, the subject parameter and constant head warp reconstructions appear similar, suggesting that within-cohort variation in head size does not have a large impact on the resulting group-level images. It can also be observed that the group-level constant parameter reconstruction images are similar to the group-level constant array position reconstruction images.

This qualitative observation is supported by the overlap between the images from the different processing streams where each group-level image is thresholded at 50% of its maximum value. Here, in both hemispheres at every age, we see greater levels of overlap between the thresholded constant head warp and subject parameter images than the other two processing streams (see Table 3.1). In each case, the 50% thresholded overlap is greatest between subject parameter images and constant head size images, though this is lowest (but still true) for the left hemisphere at 8-months. In this case, we see a less focal response across reconstruction pipelines, which is potentially due to this cohort having the smallest group size.

Despite the constant head warp pipeline appearing to most closely emulate the subject parameter pipeline, the group-level images across reconstruction pipelines are broadly consistent with one another. This suggests that group-level analyses are robust to variation in head size and array position.

To compare focality and the spatial characteristics of activation between the subject parameter and constant parameter pipelines (i.e. those which represent best practice and an image-space equivalent to channel-space analysis, respectively), each group-level T-statistic image from both pipelines for each age was normalised to its maximum value, and thresholded at values between 50% and 90% of that maximum value. There was a large spatial extent of the cortex covered when T-statistic values thresholded at low values which is not insightful about the neural response. It was therefore chosen to threshold the images at a minimum of 50% of their maximum value in this analysis, which is more likely to be related to the neural response. The upper value of 90% was chosen so as to be a high value but to ensure that there was still a decent spatial extent of the cortex covered by the thresholded values.

These results are shown in Figure 3.12. On visual inspection, the subject parameter images appear more focal, while the spatial distribution of T-statistic values in the constant parameter group-level images appears more dispersed.

To quantify this measure, the cumulative area of activation as a function of T-statistic value is also plotted in Figure 3.12. Toward the maximum T-statistic values, the area covered in subject parameter group-level images is consistently lower than is the case in the constant parameter group-level images. This demonstrates greater focality in the subject parameter images.

3.3.2.2 Individual-level

Figure 3.13 shows the peak node offset at the individual-level for the three processing streams relative to subject parameter reconstructions. This analysis was conducted using images of oxy-haemoglobin concentration changes. It can be observed that the constant head warp peak node offset is substantially lower at each age in each hemisphere than the other two processing streams. The difference between individual-level peak node offset in the constant head warp and constant parameter pipelines is statistically significant in all cases, and this is also true for the difference seen between

constant head warp and constant array position pipelines in all cases except the right hemisphere at 12-months.

At the individual-level peak node offset was computed between the subject parameter pipeline and the constant parameter pipeline, modified such that the size of the head model at each age was determined by the average head measurements at the other two age points. This was performed to assess the effect of using a single-sized head model across all age cohorts. No statistically significant difference was found between peak node offset obtained using group-level age-matched head measurements and using non-age-matched measurements. That is to say, using non-age-matched warped head models does not perform noticeably worse than the constant parameter pipeline. This result is shown in Figure 3.14.

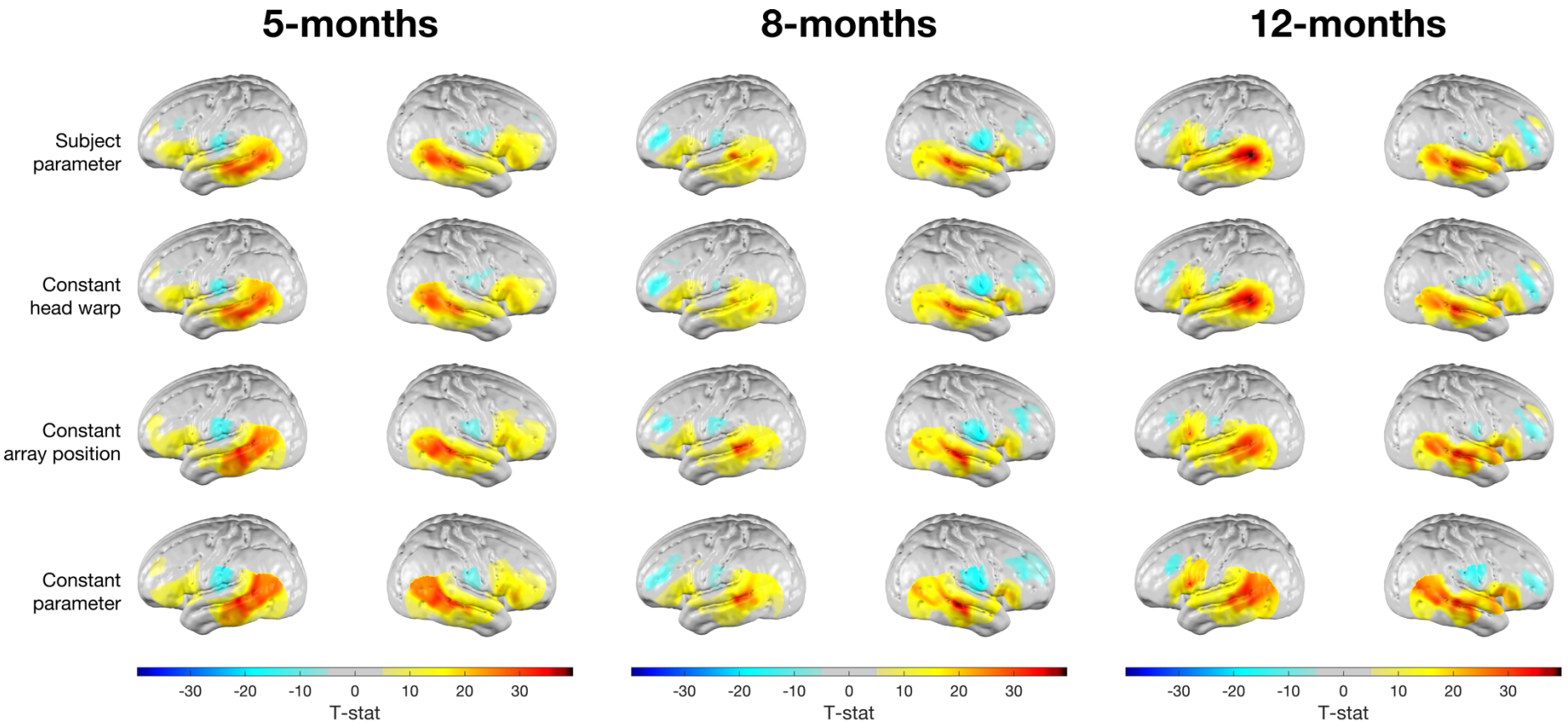

Figure 3.11: Group-level T-statistic images of changes in oxy-haemoglobin concentration in response to the auditory vocal condition relative to baseline for the four image reconstruction processing streams. From top row to bottom row: subject parameter reconstruction, constant head warp reconstruction, constant array position reconstruction, constant parameter reconstruction. The displayed T-statistic values are thresholded at a value equivalent to $p < 0.05$, Bonferroni corrected on the basis of number of nodes in the grey matter surface mesh.

Table 3.1: Jaccard index quantifying overlap of the thresholded group-level image for each processing stream with the thresholded group-level subject parameter image. Group-level images from each processing stream were thresholded at 50% of their maximum value. Here, the Jaccard index is defined as the number of nodes in the intersection of the thresholded images divided by the number of nodes of the union. A Jaccard index of 100% would indicate perfect overlap, while 0% would indicate no overlap at all.

Age	Number of infants	Group-level thresholded nodal overlap with subject parameter images (Jaccard index)					
		Left hemisphere			Right hemisphere		
		Constant head warp	Constant array position	Constant parameter	Constant head warp	Constant array position	Constant parameter
5-months	53	90.30%	71.90%	69.90%	83.00%	62.00%	58.20%
8-months	40	57.70%	48.10%	46.90%	74.20%	48.40%	50.60%
12-months	45	80.00%	61.90%	39.30%	78.80%	47.50%	39.70%

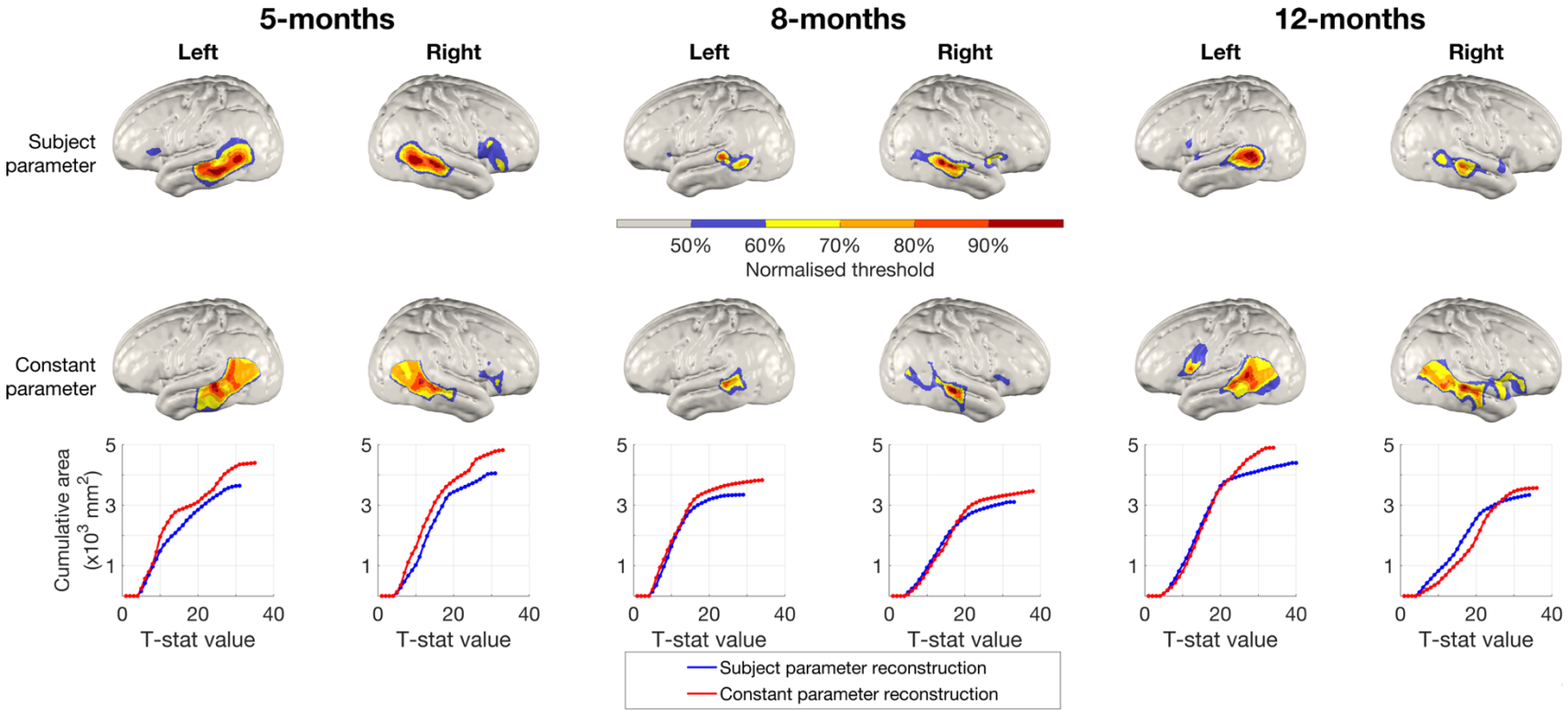

Figure 3.12: Top: normalised and thresholded group-level t-statistic images of changes in oxy-haemoglobin concentration in response to the auditory vocal condition relative to baseline for subject parameter (top row) and constant parameter (middle row) pipelines. Each image is thresholded at values between 50% and 90% of its maximum T-statistic value. Bottom row: cumulative area of activation as a function of T-statistic value. At larger T-statistic values, the cumulative area covered (i.e. the area in which any activation can be found) in subject parameter group-level images is consistently lower than is the case in the constant parameter group-level images, suggesting greater focality in images resulting from the subject parameter pipeline.

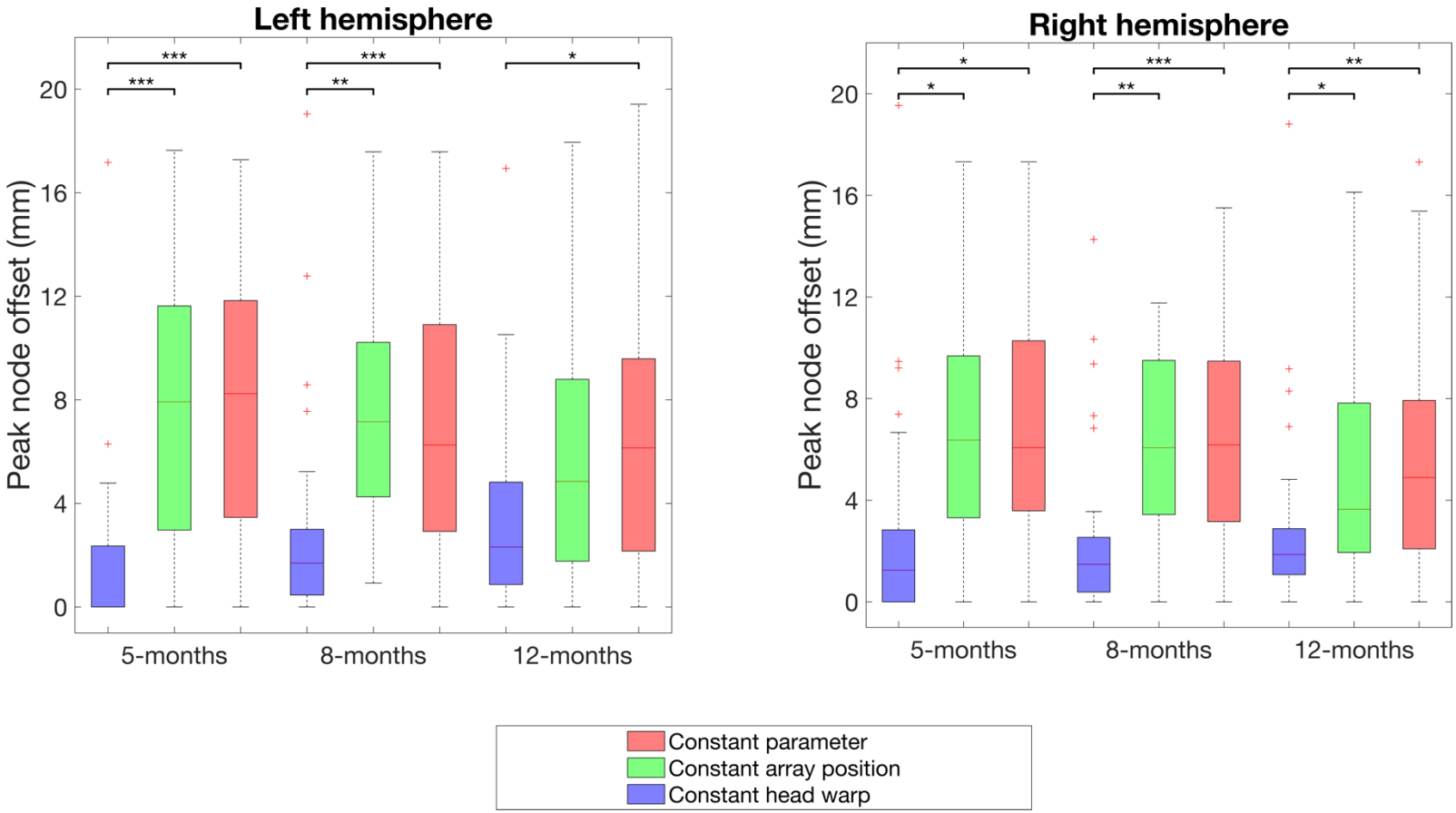

Figure 3.13: Peak node offset at the individual-level for each processing stream relative to subject parameter reconstructions. Peak node offset values were calculated in the space of the constant head warp model for each age. Significance levels were computed using paired T-tests. *represents $p < 0.05$ (corrected), ** represents $p < 0.01$ (corrected), *** represents $p < 0.001$ (corrected).

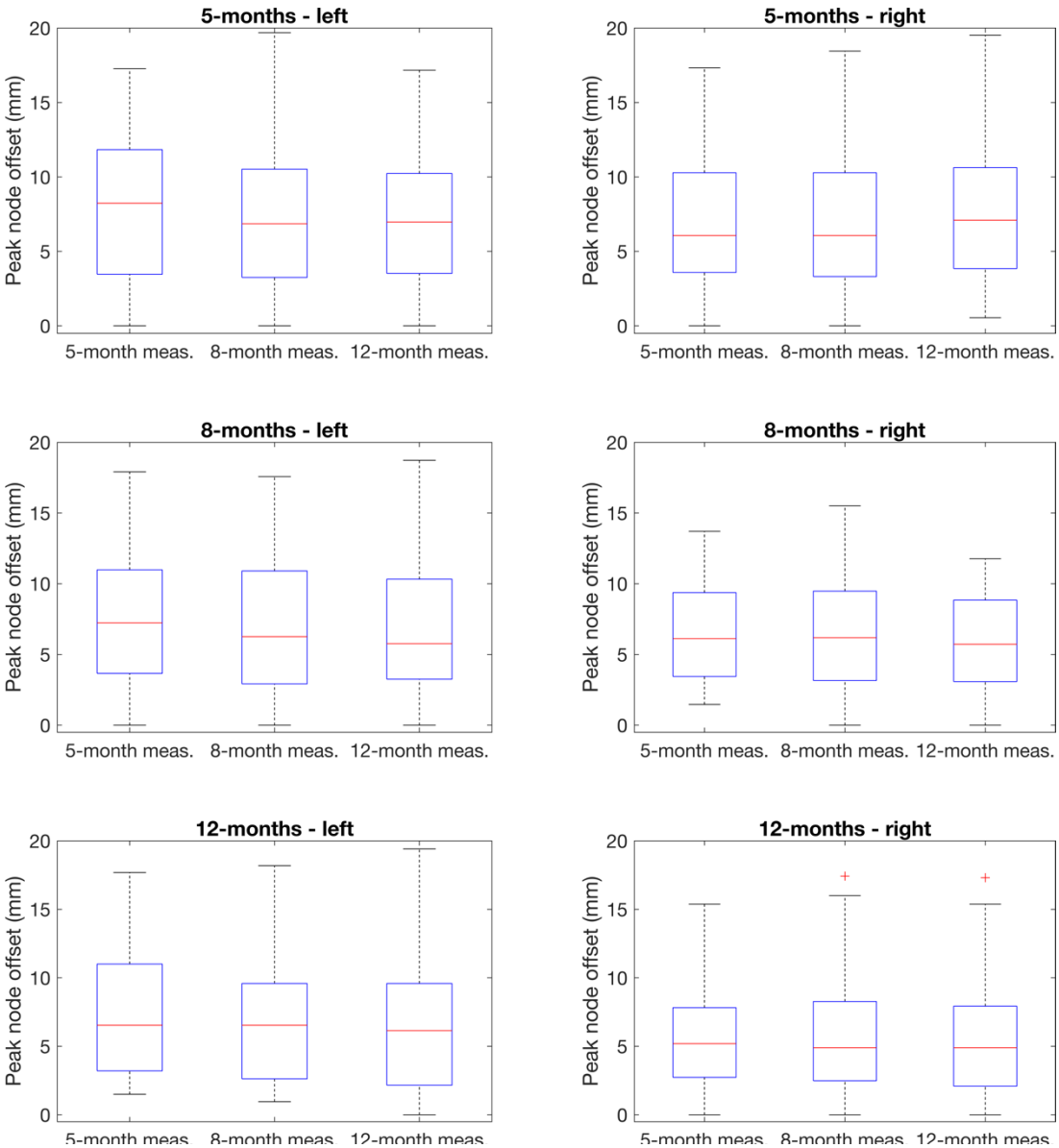

Figure 3.14: Individual-level peak node offset between the subject parameter pipeline and the constant parameter pipeline modified such that the head model size is determined by average head measurements at each of the three age points. There is no statistically significant difference between peak node offset between any of these distributions for a given hemisphere at a given age.

3.3.3 Peak node offset association with head size and growth trajectory

The data in Figure 3.11, Figure 3.13 and Figure 3.14 strongly suggest that array position is the dominant driver of differences between the subject parameter and constant parameter images at both the group- and the individual-level. However, an additional investigation was conducted to determine whether there was any association between individual-level peak node offset and the magnitude of difference in head size from the group mean.

There were 24 individuals with data at both 5- and 8-months, 20 with data at both 8- and 12-months, and 25 with data at both 5- and 12-months, enabling an analysis by trajectory of head size. The relationship between head circumference, head growth trajectory and peak node offset was investigated. In total, 36 Pearson Correlation tests were conducted to test for an association between:-

- Peak node offset and difference in head circumference from group mean (1 test per age, per hemisphere = 6 in total). See results in Table 3.2.
- Peak node offset and *absolute* difference in head circumference from group mean (1 test per age, per hemisphere = 6 in total). See results in Table 3.3.
- Change in head circumference z-score and peak node offset (1 test per age, per age range, per hemisphere = 12 in total). See results in Table 3.4.
- *Absolute* value of change in head circumference z-score and peak node offset (1 test per age, per age range, per hemisphere = 12 in total). See results in Table 3.5.

No statistically significant correlations were found between individual-level peak node offset and change in z-score or difference in head circumference from group mean at any age or for any of these age ranges. As such, there is

no evidence to suggest inferences made from constant parameter reconstructions are systematically biased by either head size deviation from group mean or head growth trajectory.

To further support this assertion, Figure 3.15 plots peak node offset as a function of difference in head circumference from group mean, and Figure 3.16 plots peak node offset as a function of change in head circumference z-score. No correlation is visibly apparent between head circumference or change in head circumference z-score and peak node offset.

Table 3.2: Peak node offset & difference in head circumference from group mean.

Age	Hemisphere			
	L		R	
5-months	r = 0.15	p = 0.30	r = 0.18	p = 0.19
8-months	r = -0.12	p = 0.48	r = -0.01	p = 0.97
12-months	r = 0.20	p = 0.19	r = -0.15	p = 0.33

Table 3.3: Peak node offset & absolute difference in head circumference from group mean.

Age	Hemisphere			
	L		R	
5-months	r = 0.13	p = 0.35	r = -0.02	p = 0.87
8-months	r = -0.13	p = 0.43	r = -0.29	p = 0.07
12-months	r = 0.05	p = 0.72	r = 0.09	p = 0.55

Table 3.4: Peak node offset & change in head circumference z-score.

Age range	Age	Hemisphere			
		L		R	
5- to 8-months	5-months	r = 0.05	p = 0.83	r = 0.13	p = 0.54
	8-months	r = 0.38	p = 0.07	r = 0.11	p = 0.62
8- to 12-months	8-months	r = 0.02	p = 0.95	r = 0.01	p = 0.95
	12-months	r = 0.38	p = 0.10	r = 0.26	p = 0.27
5- to 12-months	5-months	r = 0.10	p = 0.65	r = -0.05	p = 0.81
	12-months	r = 0.00	p = 1.00	r = 0.22	p = 0.28

Table 3.5: Peak node offset & absolute change in head circumference z-score.

Age range	Age	Hemisphere			
		L		R	
5- to 8-months	5-months	r = -0.21	p = 0.32	r = -0.18	p = 0.40
	8-months	r = 0.08	p = 0.70	r = -0.09	p = 0.66
8- to 12-months	8-months	r = -0.12	p = 0.63	r = -0.11	p = 0.65
	12-months	r = -0.16	p = 0.49	r = -0.34	p = 0.15
5- to 12-months	5-months	r = -0.17	p = 0.42	r = 0.01	p = 0.97
	12-months	r = -0.04	p = 0.84	r = -0.07	p = 0.74

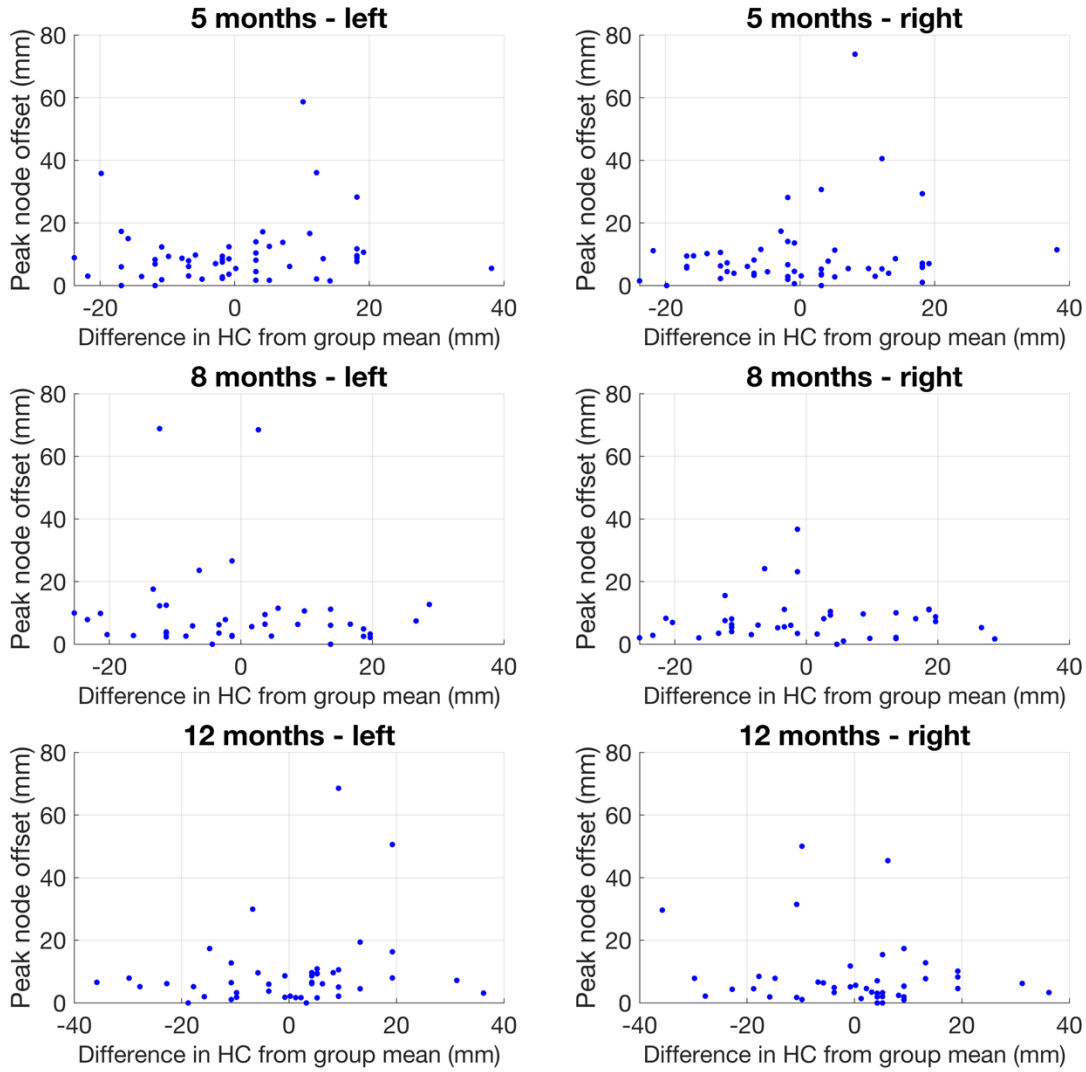

Figure 3.15: Peak node offset plotted against difference in head circumference from group mean for each age and hemisphere.

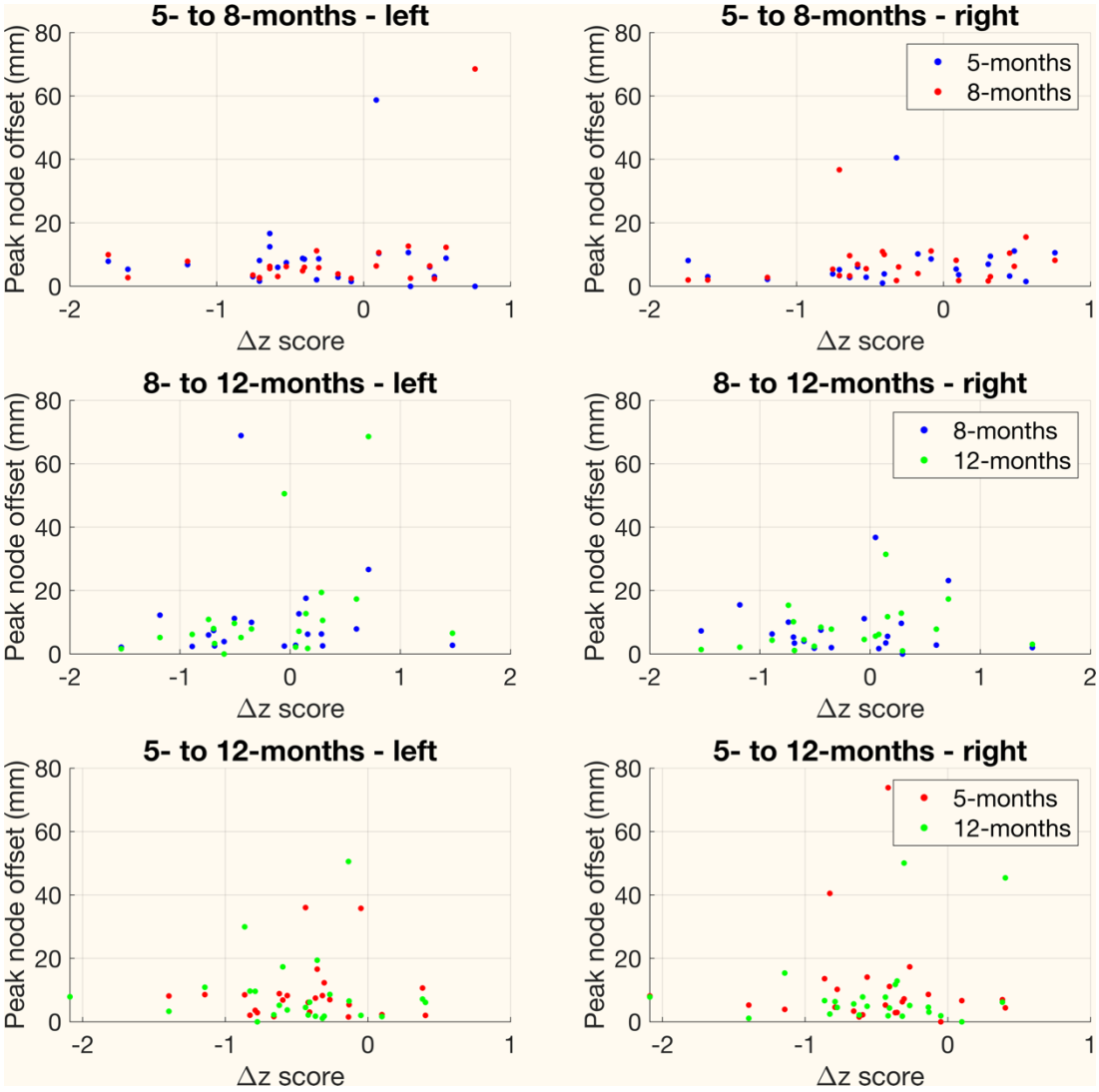

Figure 3.16: Peak node offset plotted against change in head circumference z-score between selected age points.

3.3.4 Effect of group size

In Figure 3.17, group-level oxy-haemoglobin T-statistic response maps are displayed for a sub-cohort of 10 randomly selected infants at ages 5-, 8- and 12-months. On visual inspection, differences between the two processing streams at equivalent ages and for equivalent hemispheres are more apparent than was the case for the full-sized cohort in Figure 3.11.

In Figure 3.18, mean peak node offset from groups of randomly assorted participants is plotted as a function of group size. In this context, peak node offset is defined as the Euclidean offset between the position of the peak node in the group-level T-statistic images from those of the subject parameter and constant parameter pipelines for each randomly assembled group. As group size increases, in general there is a decrease in the mean peak node offset.

There is also a decrease in the proportion of mismatched peak node cortical labels between the two processing streams as group size increases (see Figure 3.19), except for the left hemisphere at 12-months

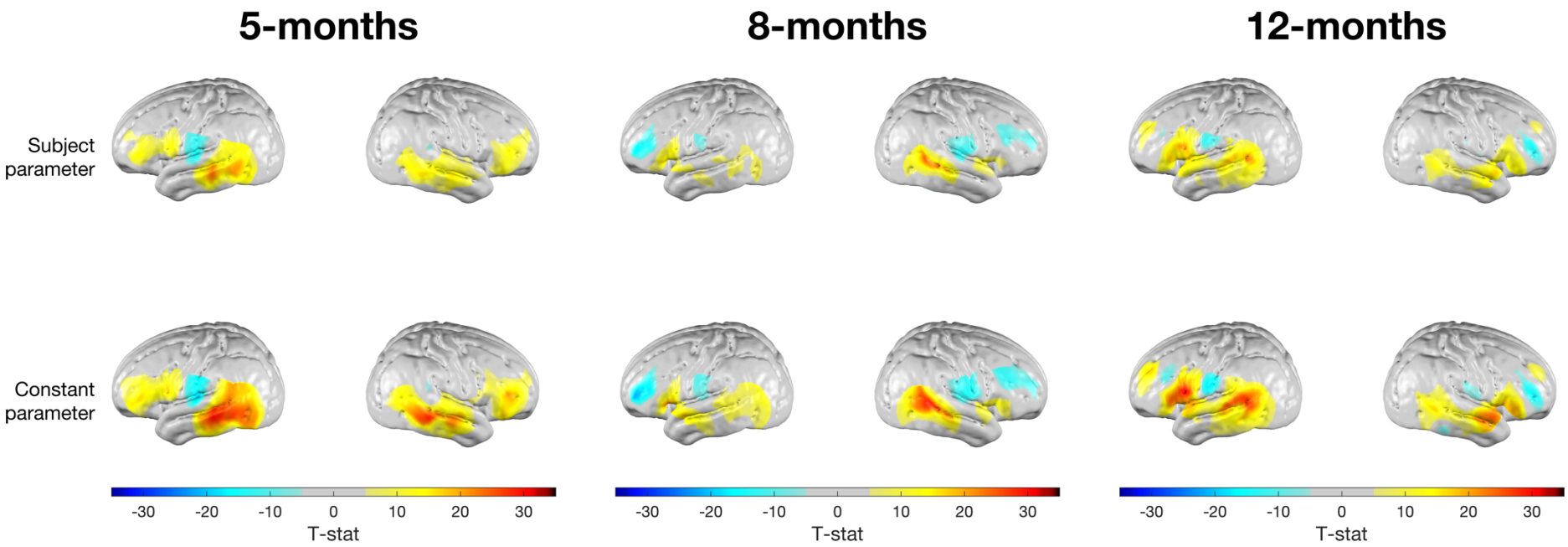

Figure 3.17: Group-level T-statistic images of changes in oxy-haemoglobin concentration in response to the auditory vocal condition relative to baseline for a sub-cohort of 10 randomly chosen infants at each age. Top row: subject parameter reconstruction pipeline. Bottom row: constant parameter reconstruction pipeline. The displayed T-statistic values are thresholded at a value equivalent to $p < 0.05$, Bonferroni corrected on the basis of number of nodes in the grey matter surface mesh.

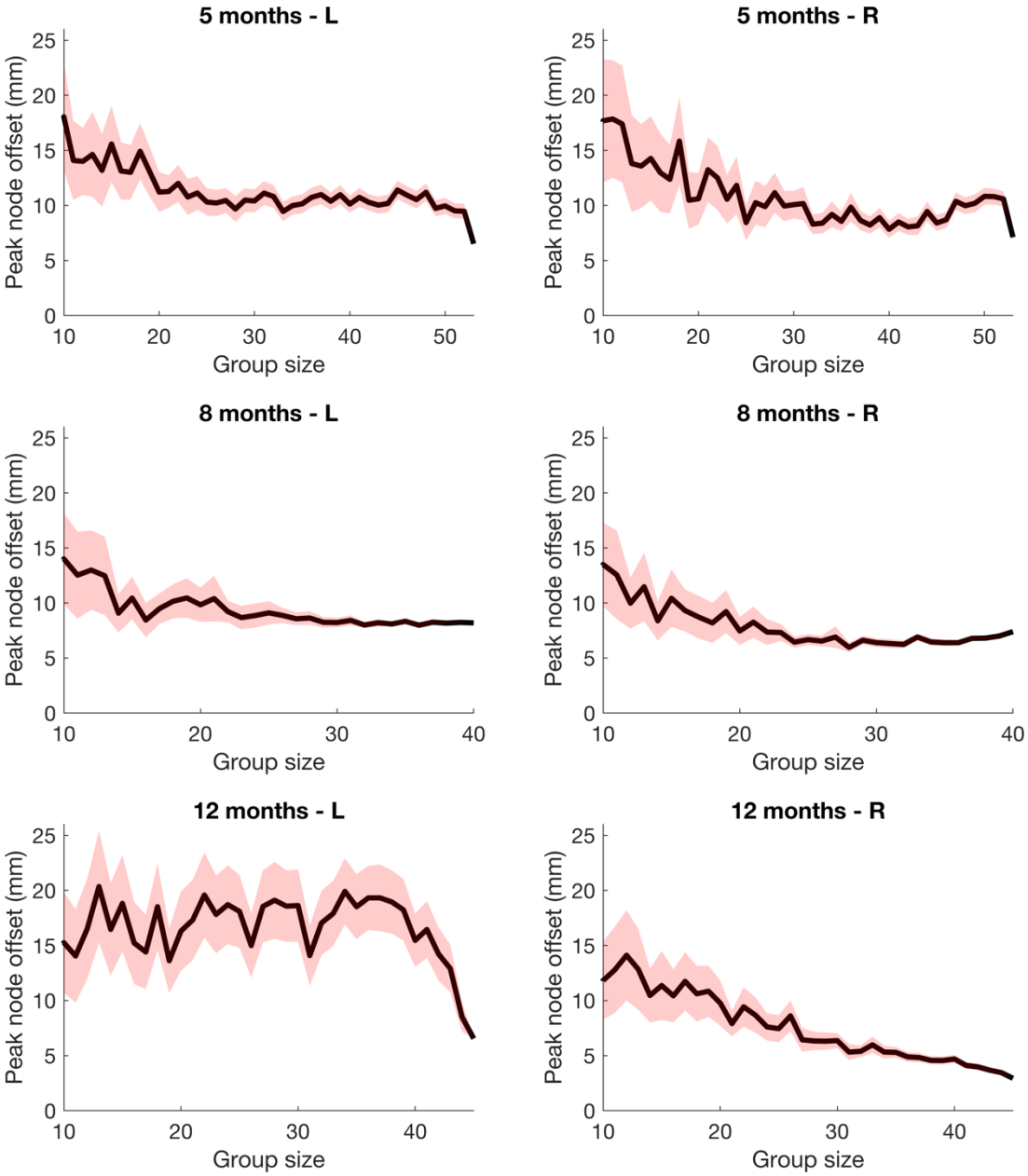

Figure 3.18: Peak node offset as a function of group size. Mean ± standard error is shown by the red shaded area. An increase in group size leads to a decrease in peak node offset and, by extension, a decrease in the likelihood of different inferences being drawn from the results at the group-level. Note: this effect is less evident at 12-months in the left hemisphere, but this likely relates to the fact that the constant parameter approach appears to yield two disparate peaks (one in the temporal lobe and one in the inferior frontal gyrus, see Figure 3.11).

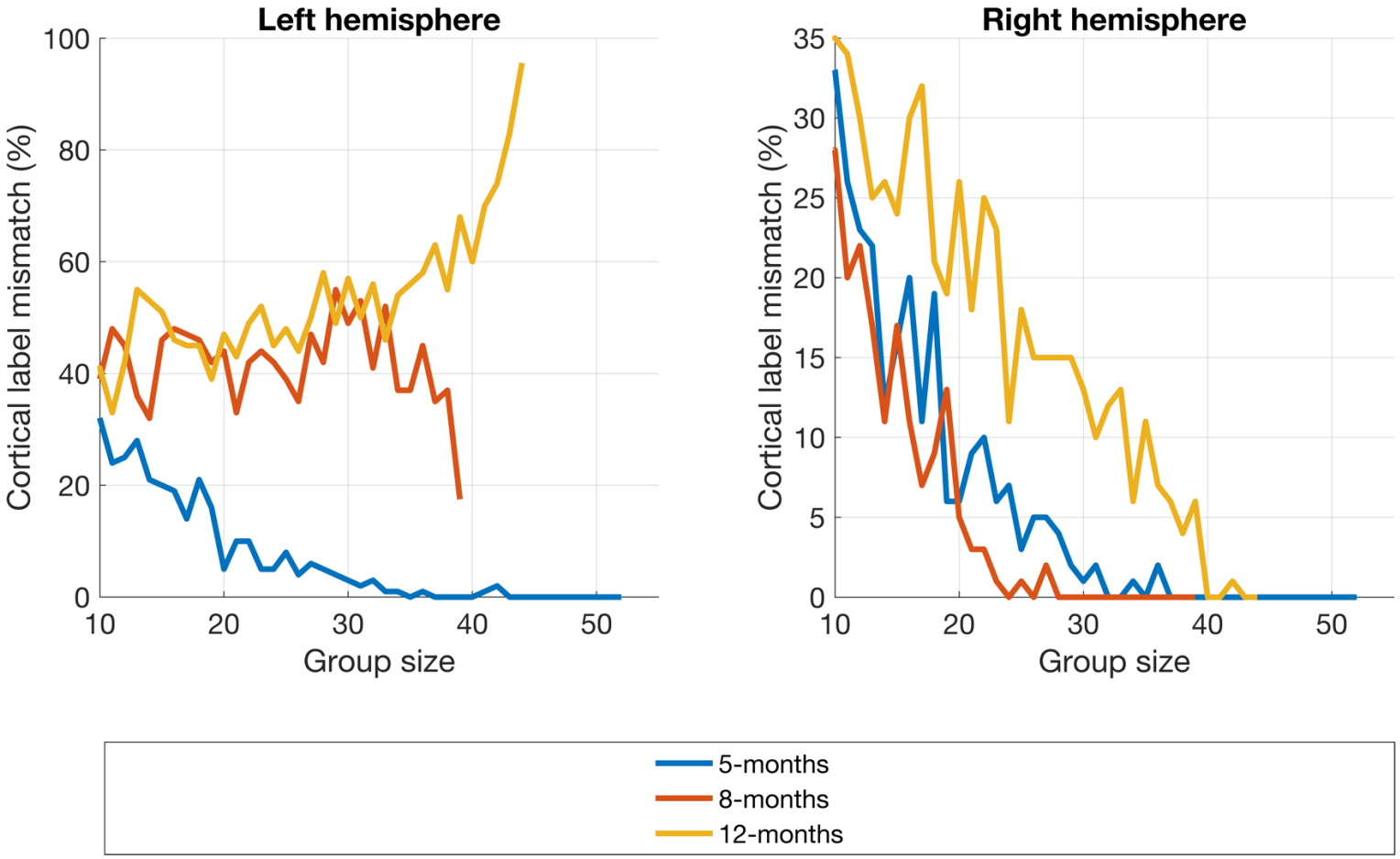

Figure 3.19: Cortical label mismatch between subject parameter and constant parameter reconstruction pipelines as a function of group size. Note: in the left hemisphere at 12-months, there appears to be a broad focus straddling the superior and middle temporal gyri in Figure 3.11, which helps to explain how a mismatch in peak node cortical label could have occurred at the full cohort size.

3.4 Discussion

The work in this chapter demonstrated an image reconstruction approach using fNIRS data acquired from a cohort of Gambian infants. Using image reconstruction to quantify and isolate the effects of variation in head size and array position, the results in this Chapter show that inferences drawn from group-level channel-space fNIRS analyses are unlikely to be significantly affected by these assumptions given the variation of these parameters in the dataset used, though their effect is much more influential at the individual-level. Variation in array position is the dominant factor that drives differences between channel-space analysis and best-practice image reconstruction at the individual- and group-level. The combinatorial analysis shows that the influence of variation in array position and head size on statistical and anatomical inferences is weakened as group size increases

3.4.1 Comparing channel-space and image reconstruction processing streams

This analysis sought to directly compare group-level analyses of fNIRS data in channel-space to subject parameter reconstruction, which represents a best-practice image reconstruction pipeline given the available data on head size and array position. As was shown in Figure 3.8 and Figure 3.9, group-level subject parameter reconstructions and channel space projections are notably consistent across the two processing streams. For both the oxy- and deoxy-haemoglobin analyses at the group-level, areas where activation is seen in the channel-space projections are also where activation is seen in subject parameter reconstructions, especially in the temporal lobe, demonstrating consistency between both processing streams at the group-level. In addition, the cortical labels of the peak node and peak channel were consistent between the two processing streams for each age, hemisphere and chromophore, which further demonstrates their consistency. This direct qualitative comparison of channel-space and best-practice image reconstruction provides evidence that the influence of variation in head size

and array position on statistical and anatomical inferences can be negligible when using a sufficiently large dataset.

For large effect sizes and large group sizes, it is therefore unlikely that analysing data in channel-space will lead to substantially different inferences about activation. However, for smaller effect sizes, an analysis using subject parameter image reconstruction will likely better resolve the effect. The channel-space analysis consistently underestimates the effect size seen in image space (see Figure 3.10). This likely pertains to the fact that image reconstruction uses models of light transport to account for differences in channel sensitivity across subjects, and thus when an average is taken, it is more likely that the signals contributing to that average are derived from the same cortical regions across subjects. While in this case the effect size is expected to be large, the fact that image reconstruction still results in greater significance suggests that investigations of smaller differences may benefit from an image-based analysis. Such investigations could explore age-related differences within a longitudinal cohort, investigations of the deoxy-haemoglobin response and studies with smaller group sizes.

3.4.2 Effect of head size and array position

The analyses presented in Section 3.3.2 aimed to isolate the effects of variation in head size and array position seen in the BRIGHT dataset on the analysis of fNIRS data. The constant parameter reconstruction pipeline represents an imaging approach that is conceptually equivalent to a channel-space analysis, insofar as it assumes a fixed array that is consistent across participants, as well as assuming a fixed model of the cerebral anatomy. In addition, the effect of variation in head size and array position can be isolated using subject-specific values for one parameter and group-average values for the other.

At the individual-level, the results show that differences between subject parameter and constant parameter reconstructions are driven by variation in

array position. It can be seen in Figure 3.13 that constant head warp reconstruction leads to the lowest level of peak node offset, while not accounting for array position (whether or not accounting for head size) leads to a much greater degree of peak node offset. No statistically significant differences were found between individual-level peak node offset obtained using group-level age-matched head measurements and using non-age-matched measurements (see Figure 3.14). The results show that using any single head model for all infants (warped to a size within the 5-12 month range) does not result in significantly worse performance than the constant parameter pipeline that uses group-level age-matched warping. This conclusion is anticipated given the dominance of variation in array position in driving different inferences.

The images obtained via constant head warp and subject parameter approaches at the individual- and the group-level are notably more similar than the other two pipelines are in comparison to subject parameter (see Figure 3.11 and Figure 3.13). The difference between the subject parameter and constant parameter pipelines is primarily driven by variation in array position and not in head size. It can therefore be concluded that collecting data on array positioning from each infant and employing an image reconstruction approach is essential to increase the reliability of fNIRS data analysis at the individual-level. Subject parameter reconstruction produces images with greater focality (see Figure 3.12); as such, accounting for subject-specific parameters can increase confidence in the spatial localisation of activation, and is likely able to better resolve features of activation particularly for smaller group sizes than is the case in channel-space analysis or constant parameter reconstruction.

One of the biggest differences between subject parameter and constant parameter images at the group-level is in the inferior frontal gyrus; this is particularly evident at 12-months in the left hemisphere where a larger peak T-statistic value is seen in the inferior frontal gyrus in the constant parameter image. The differences seen in frontal regions may well be due to their slightly

greater depth underneath the scalp, and so size and shape of the head model will have a greater impact on modelling photon transport in frontal areas than is the case for shallower cortical regions. Brain activation at a greater depth will influence fewer measured photons than activation at a shallower depth, and so activation occurring deeper will have a relatively reduced signal-to-noise ratio.

An investigation was conducted to illicit whether within-cohort head size variation and growth trajectory were associated with peak node offset in constant parameter reconstructions, a surrogate of whether there is a systematic bias in channel-space analysis linked to these factors. No evidence was found that such a link exists; the correlation between head circumference deviation from group mean or change in z-score and peak node offset was not significant for any correlation tested. In addition, there is also no clear pattern of peak node offset being larger at the extremes of either of these metrics (see Figure 3.15 and Figure 3.16). This signifies that there is no systematic error linked to these factors in channel-space analysis.

Fundamentally, combining data from equivalent channels across individuals implicitly assumes that equivalent channels probe equivalent anatomical volumes of the cortex. One possible explanation for why variation in array position has a substantially larger influence than variation in head size is due to correspondences between scalp positions and underlying anatomy. Tsuzuki et al. (Tsuzuki et al., 2017) demonstrated using a cortical projection method that the 10/10 system is sufficient to predict underlying macroanatomical cortical structures in infants from birth to 2 years. This suggests that an array positioned on two different sized heads (within a plausible anatomical range for a given age) is likely to be overlying the same cortical area. In contrast, if an array position deviates from the group-average position, it is very likely to be overlying (and, by implication, sampling) different regions of the cortex to what the average array position would suggest.

The effect of variation in array position appears to have a substantial influence on peak node offset at the individual-level but its influence is diminished at the group-level. This supports the idea that assuming constant head size and array position (a fundamental assumption implied in channel-space analysis) is valid at the group-level in fNIRS analyses. This finding is consistent with findings reported by Blasi et al. (2014), who found high test-retest reliability of group-level oxy-haemoglobin response in infants aged 4- to 12-months, but much lower reliability at the individual-level.

3.4.3 Combinatorial analysis and the effect of group size

In the combinatorial analysis, for each age and hemisphere, peak node offset decreases as group size increases; in other words, the constant parameter results converge towards (but never meet) the subject-parameter results as group size increases. This decrease shows that the effect of the variation in head size and array position becomes less evident as more individuals are included in each group. This has significant implications for channel-space analyses, where head size and array position are also generally assumed constant. Subject parameter reconstruction approaches are likely the superior analysis approach, but their benefit is particularly evident for smaller group sizes.

In all cases except for the left hemisphere at 12-months, the proportion of mismatched cortical labels between the two processing streams decreases as group size increases. At 12-months in the left hemisphere, there appears to be a broad focus that straddles the superior and middle temporal gyri, which helps to explain how a mismatch in the cortical label of the peak node could have occurred at the full cohort size.

The results demonstrate that there is a weakening of the effect of variation in head size and array position as group size increases. Though the results

suggest that using group-average values for these parameters is questionable at the individual-level, the influence of variation in these parameters (to the extent seen in the BRIGHT dataset) is weakened as group size increases. This further supports the claim that channel-space fNIRS analyses are robust to variation in these parameters in longitudinal infant studies at the group-level. This analysis, however, does not address the broader question as to what number of participants is an appropriate cohort size for field-based fNIRS studies; this question is highly dependent on the expected size of activation and other parameters of the experiment in question.

As infant-specific data has been used, this work cannot indicate whether similar results would be observed across different cohorts (e.g. adults with varying head sizes). However, given that the fundamental characteristics of the problem (optodes manually coupled to a head) are consistent across all ages, it does seem likely that an increasing group size will increase the robustness of the channel-space analysis, and that this robustness would be further increased (particularly when the cohort size is small) when a subject parameter image reconstruction approach is employed. In addition, this conclusion should be independent of the statistical analysis used; for example, a generalised linear model analysis should also benefit from employing subject parameter reconstruction.

3.4.4 The benefit of an image reconstruction approach

Image reconstruction in DOT is better suited to high-density arrays that contain overlapping channels, which are channels that exhibit sensitivity profiles that partially sample the same volume (Boas et al., 2004; White, 2010); this permits depth discrimination in the reconstructed images. A recent example of high-density DOT being applied in a field-based context is a study by Fishell et al. (2020) of Colombian children. A notable example of a high-density DOT study

in infants was conducted by Frijia et al. (2021) using the same paradigm as was used in this present study.

An image reconstruction approach produces images inherently registered to the head model, allowing concentration changes to be visualised on a model of cortical anatomy (Yücel et al., 2017). Using anatomical information present in the head model, reconstructed images can be registered to a common space to be compared with data acquired from several complimentary functional imaging modalities. This can enable longitudinally-acquired fNIRS data to be compared directly to fMRI data collected from child and adult populations, helping to bridge gaps in our understanding of functional development. The work in this chapter represents a significant step towards enabling such comparisons for longitudinal infant populations, particularly those in field-based studies. Such comparisons between fMRI and fNIRS data collected with high-density arrays have been conducted in adults (for example, Eggebrecht et al. (2014)).

Parcellation atlases can be incorporated into the analysis of reconstructed images in a similar fashion to how the AAL atlas was used in in this work, permitting cortical labels to be attributed to nodes or voxels in the head model which enables the response in equivalent cortical areas to be compared across populations. This can be completed without the need to rely on the position of sources and detectors on the scalp to interpret results, as is done in conventional fNIRS.

There is evidence, however, that using cortical projections of channel positions on the scalp can be reliably related to cortical anatomy using a channel-space approach without the need for image reconstruction. Lloyd-Fox, Richards, et al. (2014) used a parcellation atlas as well as head models derived from individual-level MRI data from over 50 infants aged 4.5- and 6-months to investigate the stability of channel positions projected to the scalp surface,

finding that there was a high level of stability in the cortical areas underlying fNIRS channels.

Despite this, constraining statistical and anatomical analysis to a discretised channel-space does not enable the intricacies of the spatial characteristics of activation on the cortex itself to be investigated. The reconstruction of spatially-continuous images of concentration changes on the cortex removes the need to assume a given channel and scalp location is associated with a single cortical position. Image reconstruction approaches can enable the development of longitudinal changes in the spatial distribution and focality of functional responses to be studied, as was demonstrated in this work.

To date, Wijeakumar et al. (2019) have conducted the only previous longitudinal image reconstruction study in a field-based setting with infants in this age range that has been published. However, this study does not explicitly investigate longitudinal imaging of infants aged 12-months and under, and has far fewer participants than the cohorts in the analyses presented in this chapter. The work presented in this chapter therefore forms the foundation of field-based longitudinal image reconstruction in infants up to 12-months of age. Improvements in infant image reconstruction approaches, building on the demonstration in this work, will help improve the localisation error and resolution of infant image reconstruction, but must also focus on doing so in the context of a low-resource setting where acquiring subject-specific MRI data, digitised optode positioning data and using high-density arrays may not be feasible.

3.4.5 Head modelling and image reconstruction

A model of head anatomy is required for image reconstruction. A head model would ideally be obtained from an individual's own MRI scan so as to be subject-specific; however, this approach was not feasible for the BRIGHT project. In the age-range studied here, there are several sources of age-appropriate MRI data. In this work, the head model employed was built from

structural data acquired and pre-processed by Shi et al. (2011) which I aim to include in the DOT-HUB group's toolbox on Github (www.github.com/DOT-HUB).

A single head model was used across ages and spatially warped appropriately, an approach justified by the results of the a preliminary sensitivity analysis in Chapter 2. The level of influence of longitudinal anatomical changes on light transport must also be placed in the context of the array registration method. Qualitatively, it can be seen in Figure 3.5 that this method is a reasonable approximation of array position, and the data used to register the array was extracted specifically from participants. However, given that data was not collected using a digitised positioning system and that sophisticated photogrammetry methods were not employed, it has not been possible to conduct a quantitative assessment of the array registration method. The error in the sensitivity distribution resulting from the array registration process is likely to be larger than the effect of longitudinal anatomical changes.

A benefit of using the same model across ages is that there is an explicit one-to-one nodal correspondence regardless of how the model has been warped. This removes the need to register different head models to a common space, which itself would be liable to a degree of error. This one-to-one nodal correspondence was used to display group-level images in a common space across ages.

In addition, given that a cortically-constrained reconstruction method was implemented, a cortical surface was desired which clearly displayed the principal gyri and sulci, which was another factor affecting the choice of head model. A more well-defined cortical surface could be extracted using the Shi et al. averaged data than was the case with the Sanchez et al. averaged data (see Section 2.4.4).

No MRI data was available from a cohort of West African infants to build a head model. It is unclear how the head model in this work, derived from infants living in a high-income country, may bias the results when used to represent head structure of Gambian infants. This is impossible to ascertain given the current lack of structural MRI data from this population, which may be difficult to obtain given the lack of MRI units in West Africa, in particular high-field imaging systems (Ogbole et al., 2018). In addition, no open-source individual-level data from infants at the ages under investigation were available to build reliable head models. This underlines the need for more publicly-available high-quality MRI data from infants in this age range.

In this work, a cortically-constrained image reconstruction approach is taken, which assumes the haemodynamic signal contributions come solely from the cortex. Though a valid assumption, the method in this work does not take advantage of a tomographic approach to produce images. This therefore presents a limitation of this work.

Typically, a value of 0.01 is used for the regularisation parameter in DOT image reconstruction. In this work, a value of 0.1 was used, which allows for a greater discrepancy between measured optical data and the resulting images. This larger regularisation parameter value was chosen as the array used was not optimised for image reconstruction and so a larger discrepancy would likely be needed to reflect this. This does, however, present another limitation of this work.

3.4.6 Limitations of the warping procedure

In this work, a mesh is warped in a linear and iterative manner to the dimensions of each individual as part of registration. This process, however, will have implications for the quality of the mesh. The quality of the mesh, as defined by the Joe-Liu index (see Section 4.2.4), will have been optimised in the meshing procedure that produced the original unwarped mesh. Following registration, the shape of the tetrahedra in the mesh are likely to change,

increasing the level of deformation in the tetrahedral elements, which will lead to a decrease in mesh quality.

Quality metrics of the meshes after being iteratively warped to each individual are shown in Figure 3.20. For most individuals, there is a decrease in mesh quality relative to the quality of the original mesh. At 5-months, the lowest value of mean mesh quality for any individual is 0.75; at 8-months and 12-months these values are 0.76 and 0.69 respectively. These values should be compared with pre-warped mesh quality value of 0.8298. In Figure 3.21, mean mesh quality of each warped mesh is plotted as a proportion of the mean mesh quality of the original mesh. The lowest of these relative values is 0.83, while the vast majority of these relative values are above 0.95.

A decrease in mesh quality can potentially lead to numerical errors in the computation of the forward model. While there is a clear decrease in mesh quality, it does not seem particularly excessive; the vast majority of elements exhibit a quality that falls within the range seen in the unwarped mesh. While the procedure employed is acknowledged as suboptimal, it seems unlikely this issue will have had a significant impact on the results in this work. Furthermore, warping the voxelised structural prior and then re-meshing the model for each individual would substantially increase computation time, and so the issues discussed here represent a conflict between accuracy and speed.

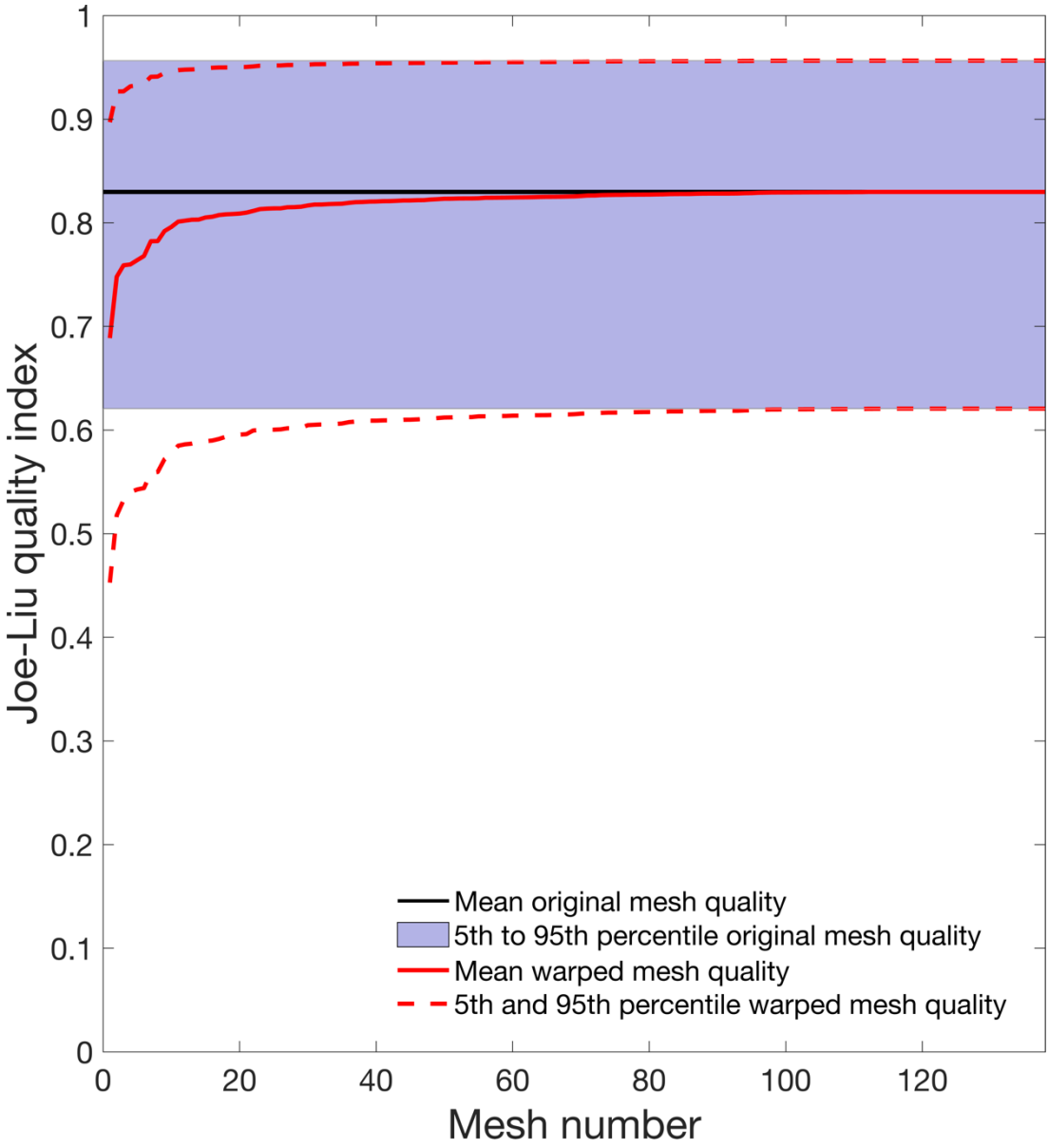

Figure 3.20: Mesh quality measures following the warping procedure to head measurements for each individual. The metrics are ordered from worst mean quality (mesh number 1) to highest mean quality (mesh number 138). The mesh quality of the original unwarped mesh is also shown as a black line.

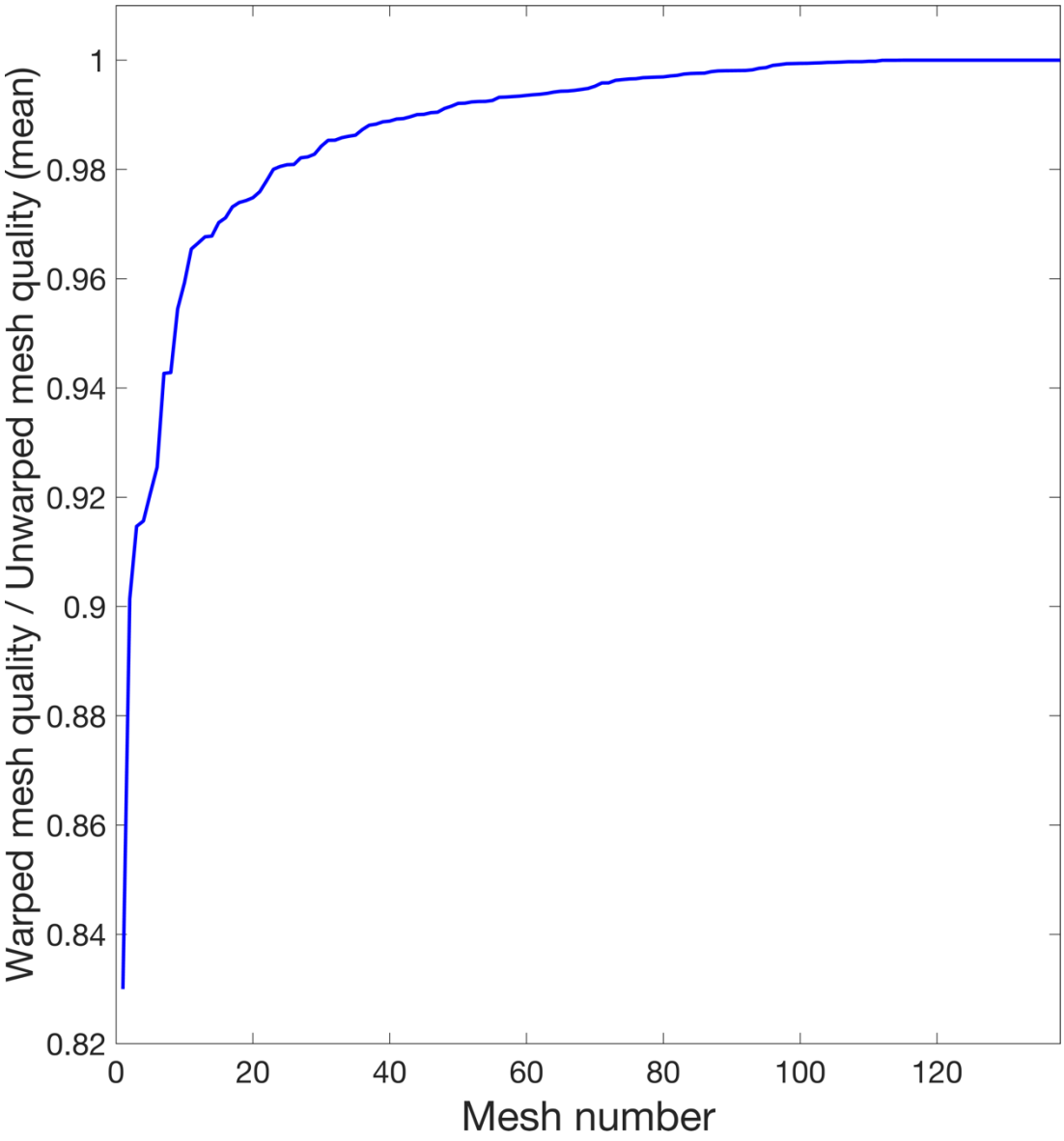

Figure 3.21: Mean mesh quality of warped mesh as a proportion of the mean mesh quality of the original mesh. The metrics are ordered from worst quality (mesh number 1) to highest quality (mesh number 138).

3.4.7 Discussion take-home messages

At the group-level, channel-space analysis provides results that are comparable to best-practice image reconstruction. Nonetheless, an image reconstruction approach does confer a benefit over channel-space analysis, particularly for smaller group sizes as shown by the combinatorial analysis, and this approach has highlighted some of the more subtle effects of the response. The subject parameter pipeline presented in this work is the best pipeline given the available data on head size and array positioning, but the conclusions of this work would have been strengthened if a more accurate method of determining optode positions had been employed.

3.4.8 Future work

The work presented in this chapter supports the idea that channel-space analyses are robust to variation in head size and array position at the group-level. These findings therefore bolster confidence in conclusions drawn from previous fNIRS studies in longitudinal (and other) cohorts. However, as has been outlined, an image reconstruction approach to analysing fNIRS data in its own right can be beneficial. While image reconstruction analyses are still relatively rare in fNIRS, they are not excessively complex and are likely to become ubiquitous in the coming years. Several packages are now available that can undertake image reconstruction-based processing (e.g. Homer3 (https://openfnirs.org/software/homer/), NeuroDOT (Eggebrecht & Culver, 2019)). The tools used in this work are part of the DOT-HUB toolbox and are already available open-source (www.github.com/DOT-HUB).

The image reconstruction pipeline demonstrated in this work incorporates models of light transport, enables anatomical and functional data to be related to one another, and enables the spatial characteristics of activation to be investigated and understood. As such, I envisage widespread use of image reconstruction in future publications of longitudinal infant fNIRS studies.

3.5 Conclusion

Using an image reconstruction approach to analyse longitudinally-acquired infant fNIRS data, it was found that inferences drawn from group-level channel-space fNIRS analyses are robust to variation in head size and array position. Variation in array position, not head size, is the dominant factor that drives differences between channel-space and image-space analyses at the group- and the individual-level. In addition, the influence of array position variation diminishes as group size increases. It is envisaged that the use of image reconstruction in longitudinal infant fNIRS studies will become widespread to permit the incorporation of anatomical information in data analysis and has the potential to enable the combination of functional data across modalities.

Chapter 3 is an adaptation of the journal article *Longitudinal infant fNIRS channel-space analyses are robust to variability parameters at the group-level: An image reconstruction investigation*, published in *NeuroImage* (Collins-Jones, Cooper, et al., 2021), licensed under CC BY 4.0.

Chapter 4

Construction and preliminary validation of a database of head models for functional imaging of the neonatal brain

4.1 Introduction

Functional magnetic resonance imaging (fMRI) has been used extensively to study functional development of the neonatal brain, for example, by mapping the sensorimotor cortex (Allievi et al., 2016; Arichi et al., 2010, 2012; Dall'Orso et al., 2018). Figure 4.1, published by Dall'Orso et al. (2018), maps the distinct areas to which functional responses are localised across the sensorimotor cortex in pre-term infants for passive stimulation of different parts of the body during natural sleep; the authors term this the *sensorimotor homunculus*.

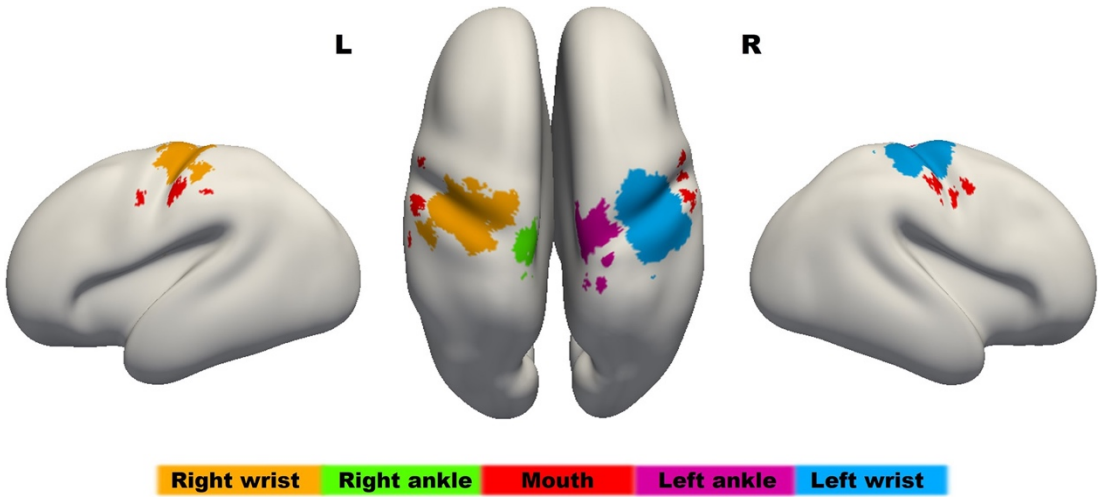

Figure 4.1: The sensorimotor homunculus of the pre-term infant, produced using data from a cohort of infants aged 34 weeks post-menstrual age, mapping the different areas exhibiting a functional response to passive movement of different body parts. Figure taken from Dall'Orso et al. (2018), licensed under CC BY 4.0.

Given the requirement that subjects remain still, in general fMRI data acquisition is limited to infants who are either asleep or sedated. Emerging advances in fMRI allow the imaging of awake infants (Deen et al., 2017); however the infant still needs to remain in a scanner, constraining the infant's movement and limiting the interaction with their environment. fMRI therefore cannot be used to study infants in naturalistic environments. Such constraints can be overcome by using other more motion tolerant and portable functional imaging techniques to collect functional data, such as DOT.

In the last two decades, a large body of research applying DOT to the study of the neonatal brain has been established to study functional activation. An early example of neonatal DOT was conducted by Austin et al. (2006), investigating cerebral oxygenation and blood flow in an infant with an intraventricular haemorrhage. Here, regional changes in blood volume and oxygen saturation were measured using a reference phantom with homogenous optical properties created from a computed tomography (i.e. CT) scan of a baby doll head (see Figure 4.2).

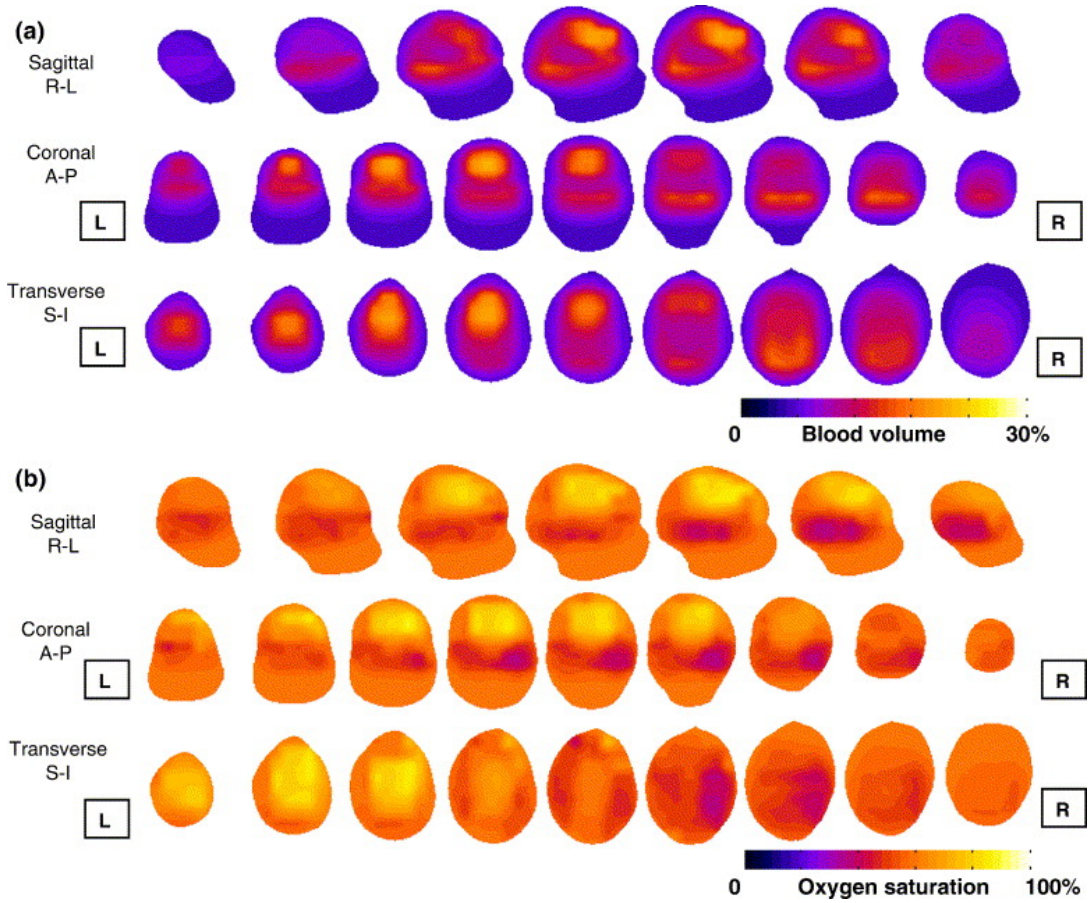

Figure 4.2: Example reconstructed images of regional (a) blood volume and (b) oxygen saturation from an infant aged 32 weeks PMA. Figure taken from Austin et al. (2006). Reprinted with permission from Elsevier[10].

[10] Reprinted from *NeuroImage*, *31*(4), Austin, T., Gibson, A. P., Branco, G., Yusof, R. M., Arridge, S. R., Meek, J. H., Wyatt, J. S., Delpy, D. T., & Hebden, J. C., Three dimensional optical imaging of blood volume and oxygenation in the neonatal brain, 1426–1433, Copyright (2006), with permission from Elsevier.

Another example is a study by Liao et al. (2012) who applied DOT to image visual cortex activation in neonatal infants in response to visual stimulation. Here, the authors use a two-layer hemispheric model to produce a finite element mesh for forward modelling.

In these two studies, no structural priors derived from realistic MRI data of the infant head were used. Historically, there has been a lack of publicly available structural MRI data from neonates (Makropoulos, Counsell, et al., 2018) which has limited the production of infant brain models. There have, however, been great advances in neonatal structural priors in the past decade or so. Heiskala et al. (2009), Oishi et al. (2011) and Shi et al. (2011) have all proposed spatial averaging of MRI data to produce a single population-level atlas for neonates.

These models do not encode any measure of post-menstrual age, which is important to consider given the rapid maturation of the neonatal brain (Makropoulos et al., 2016). As such, a more sophisticated approach is to produce population-level atlases for specific age points throughout the neonatal period. This was the method adopted by Kuklisova-Murgasova et al. (2011).

Here, the authors produced age-specific population-level MRI templates and tissue probability maps for infants aged 29-44 weeks post-menstrual age (PMA) at one-week intervals, shown in Figure 4.3. Serag et al. (2012) also produced an age-dependent atlas for a similar age range – 28-44 weeks PMA – using data from 204 neonatal infants non-rigidly registered to age-specific common spaces. Makropoulos et al. (2016) took a similar approach to produce a population-level atlas using data from 420 images acquired from infants aged 27-45 weeks PMA, and also includes a parcellation atlas delineating 82 brain structures.

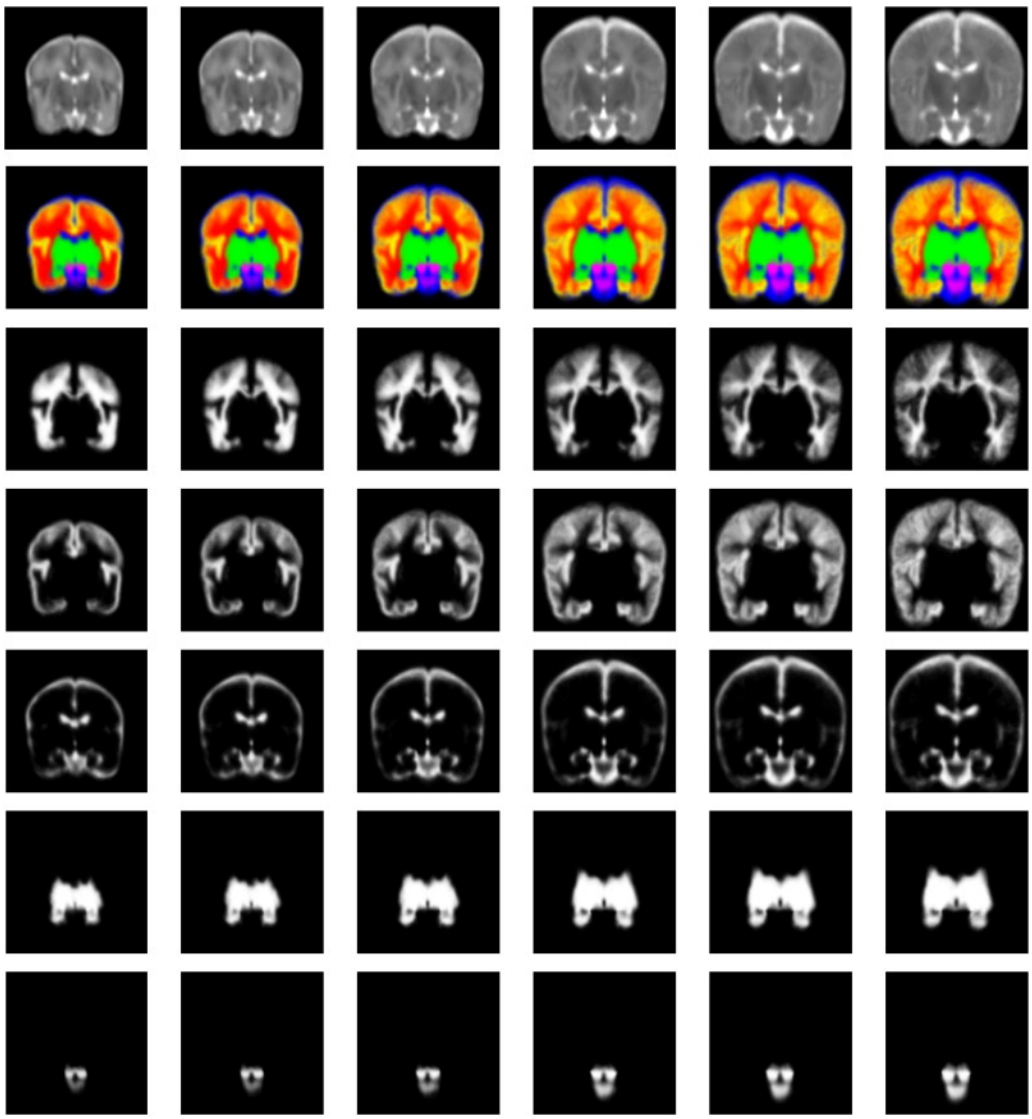

Figure 4.3: Brain intensity templates and tissue segmentation data from Kuklisova-Murgasova et al. (2011) at ages 29, 32, 35, 38, 41 and 44 weeks PMA. From top row to bottom: T_2-weighted intensity template, sum of tissue probability maps (TPMs), white matter TPM, grey matter TPM, cerebrospinal fluid TPM, subcortical grey matter, brainstem TPM. Figure taken from Kuklisova-Murgasova et al. (2011). Reprinted with permission from Elsevier[11].

A significant barrier to these infant atlases being used as spatial priors for DOT is that they do not routinely contain skull and scalp tissues. The primary application of these MRI atlases is to aid automated brain tissue segmentation

[11] Reprinted from *NeuroImage*, *54*(4), Kuklisova-Murgasova, M., Aljabar, P., Srinivasan, L., Counsell, S. J., Doria, V., Serag, A., Gousias, I. S., Boardman, J. P., Rutherford, M. A., Edwards, A. D., Hajnal, J. V., & Rueckert, D., A dynamic 4D probabilistic atlas of the developing brain, 2750–2763, Copyright (2011), with permission from Elsevier.

procedures (Makropoulos, Robinson, et al., 2018) and, as a result, the skull and scalp tissues need not be considered.

To overcome this issue, Brigadoi et al. (2014) produced a population-level atlas consisting of grey matter, white matter, cerebrospinal fluid (CSF) and extra-cerebral tissue for infants aged 28-44 weeks PMA at one-week intervals; this is shown in Figure 4.4. This atlas was constructed using age-specific tissue probability maps from the Kuklisova-Murgasova et al. atlas to produce a three-layer model for brain tissues. Skull and scalp tissues are difficult to separate on neonatal MRI due to their low thickness and lack of differential contrast (Brigadoi et al., 2014). However, because these tissues have relatively similar optical properties (Dehaes et al., 2013), Brigadoi et al. produced a combined segmentation for these two tissues (referred to as extra-cerebral tissue), using the Betsurf procedure (Jenkinson et al., 2005).

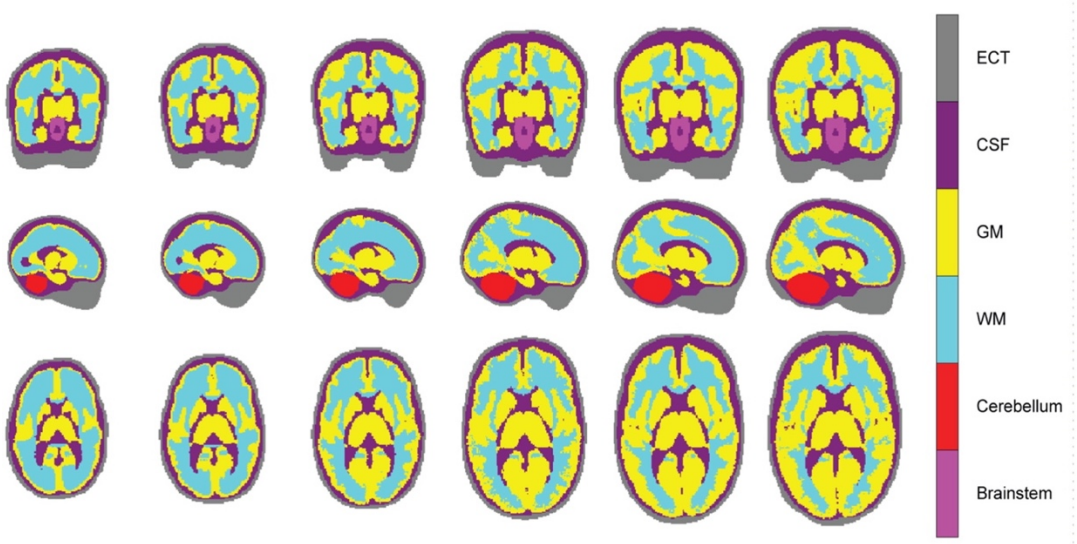

Figure 4.4: Slices in the coronal (top row), sagittal (middle row) and axial (top row) planes from the Brigadoi et al. atlas for example ages 29, 32, 35, 38, 41 and 44 weeks PMA. The atlas maps six tissue types: grey matter (GM), white matter (WM), cerebrospinal fluid (CSF), extra-cerebral tissue (ECT), brainstem and cerebellum. Figure taken from Brigadoi et al. (2014). Reprinted with permission from Elsevier[12].

[12] Reprinted from *NeuroImage*, *100*, Brigadoi, S., Aljabar, P., Kuklisova-Murgasova, M., Arridge, S. R., & Cooper, R. J., A 4D neonatal head model for diffuse optical imaging of pre-term to term infants, 385–394, Copyright (2014), with permission from Elsevier.

This atlas was the first of its kind and has been freely disseminated to researchers in a wide range of fields. It has been applied extensively in neonatal atlas-guided DOT, for example to investigate the link between the haemodynamic response and brain electrical activity in infants with neuropathology (Chalia et al., 2016; H. Singh et al., 2014); to study development in the sensorimotor cortex (de Oliveira et al., 2019); to study touch and pain processing (Verriotis et al., 2016); and to monitor the brain for extended periods (Brigadoi et al., 2019). The head model has also been applied for photoacoustic modelling (Ranjbaran et al., 2019), and optical phantom construction (Dempsey et al., 2017; Zhao et al., 2021).

However, a major limitation of the Brigadoi et al. head model is that the spatial error in activation localisation incurred using their model in place of a subject-specific prior could not be directly assessed. This was because the associated individual-level MRI data upon which their model was based was not publicly available. Nor was there an existing *gold-standard* model against which to compare. Furthermore, the accuracy of the extra-cerebral tissue segmentation was not evaluated, and to do so the authors would have faced the difficulties of manually segmenting a blurred averaged template. The authors noted that it is likely that their atlas underestimates the thickness of the extra-cerebral tissue.

A further issue that is true of the Brigadoi et al. model, and of many population-level atlases, is that detail is lost in the process of spatially-averaging the MRI data (Makropoulos, Counsell, et al., 2018). Given its highly variable folding pattern, the cortical surface tends to become smoothed following spatial averaging, and a similar smoothing effect is seen in the detail of the white matter. The resulting spatially-averaged models are therefore not representative of any single individual, and may therefore not offer an anatomically meaningful space in which the spatial distribution of a physical field can be modelled. In addition, surface registration techniques such as the well-established FreeSurfer software (Fischl et al., 1999) are increasingly used

to permit comparison between subjects and groups in functional neuroimaging and have been incorporated as part of the structural pipeline of the Human Connectome Project (Glasser et al., 2013). However, the use of atlases with smoothed cortical surfaces is often incompatible with surface-based registration techniques, which can limit the development of new data analysis pipelines.

The Developing Human Connectome Project (dHCP) – a collaboration between King's College London, Imperial College London and the University of Oxford – aims to build a dynamic map of human brain connectivity in early life (www.developingconnectome.org). The dHCP is acquiring structural, functional and diffusion MRI data from neonatal infants and foetuses. The dHCP has begun to make its data publicly available, with three data releases since 2017, including structural images and brain tissue segmentations. As part of my PhD, I led a collaboration with the Perinatal Functional Imaging Group at the Centre for the Developing Brain, King's College London, where the dHCP is based.

Structural priors are required to enable images of functional activation to be reconstructed in DOT, and my work aims to build structural priors for this purpose. The utility of structural priors, however, is not limited to DOT. Structural priors of the cranial anatomy can be beneficial to a wide range of neuroimaging and neuromodulation modalities that monitor brain function via neuronally-generated electromagnetic fields (electroencephalography, EEG; and magnetoencephalography, MEG), or via haemodynamics (such as fNIRS, DOT, diffuse correlation spectroscopy (DCS), and photoacoustic imaging) but do not simultaneously acquire structural data. Structural priors can be used to support image registration (Xiao et al., 2016), improve the targeting of neuromodulation (Mueller et al., 2017), or to model the spatial distribution of the electric, magnetic, ultrasonic or optical fields that underpin many imaging modalities (Arridge & Cooper, 2015; Azizollahi et al., 2016; Legon et al., 2018;

Pirondini et al., 2018; Ranjbaran et al., 2019; Roche-Labarbe et al., 2008; Routier et al., 2017; Selb et al., 2014).

This Chapter details how this newly available structural data from the dHCP was utilised to produce a database of multi-layered structural priors of the neonatal head for individuals aged 29-44 weeks PMA for use in DOT and other imaging modalities. Methods were investigated to accurately segment extra-cerebral tissue, and a package of multi-layer tissue masks and meshes were produced. Finally, using a leave-one-out approach, a preliminary analysis was conducted to quantify the spatial error incurred by one possible application of this database: using an age and size-matched individual in place of subject-specific structural model.

4.2 Methods

4.2.1 Structural MRI data

The MR images were acquired as part of the Developing Human Connectome Project, whose resources have been made open-source (www.developingconnectome.org). Images were obtained from infants using a 3 T Philips Achieva Scanner (Best, NL) at the Evelina Newborn Imaging Centre, St Thomas' Hospital, London, with a 32-channel dedicated neonatal head coil (Hughes et al., 2017). The T_2-weighted images were acquired in two stacks of slices acquired in sagittal and axial planes using parameters TR = 12 s, TE = 156 ms, SENSE factor 2.11 (axial) and 2.58 (sagittal) (Makropoulos, Robinson, et al., 2018). Overlapping slices (resolution $0.8 \times 0.8 \times 1.6\,mm^3$) were acquired, and the final up-sampled image resolution was $0.5 \times 0.5 \times 0.5\,mm^3$ after reconstruction and motion correction (Cordero-Grande et al., 2016, 2018; Kuklisova-Murgasova et al., 2012). All T_1-weighted images were acquired using an inversion recovery sequence at the same resolutions using parameters TI = 1740 ms, TR = 4.8 s, TE = 8.7 ms, SENSE factor 2.26 (axial) and 2.66 (sagittal). All images were reviewed by a paediatric neuroradiologist.

Through the collaboration, datasets were available from 634 individuals whose images had undergone the dHCP structural processing pipeline (Makropoulos et al., 2014; Makropoulos, Robinson, et al., 2018). The datasets included binary tissue segmentations for brain tissues (cortical grey matter, white matter, outer cerebrospinal fluid (CSF), ventricles, deep grey matter, hippocampus, brainstem and cerebellum) with voxel dimensions $0.5 \times 0.5 \times 0.5\,mm^3$, as well as T_1- and T_2-weighted MR images (voxel dimensions: $0.5 \times 0.5 \times 0.5\,mm^3$) for each individual. An evaluation of the quality of the brain tissue segmentations was conducted by Makropoulos, Robinson, et al. (2018).

In this work, each individual's T_1-weighted volume was visually inspected to determine whether the dataset would be appropriate for producing a multi-layer tissue model. Datasets were excluded if extra-cerebral tissue was cropped from the image field of view superiorly or laterally (this excluded 314 subjects); the pre-auricular points were not in the field of view of the T_1-weighted image (excluded 16 subjects); severe motion artifact was present in the T_1-weighted image that significantly distorted the outer scalp boundary (excluded 24); or a haematoma was present in the extra-cerebral tissue that impacted the outline of the outer scalp boundary (excluded 13). Through this process, a total of 267 datasets were identified as appropriate for inclusion. However, at the time of conducting the analysis and publishing this work, 53 of these datasets had not been made publicly available by the dHCP which meant that data from these datasets could not be included in the model construction and analysis in this work. In total, 214 datasets were therefore included, whose age distribution is shown in Figure 4.5.

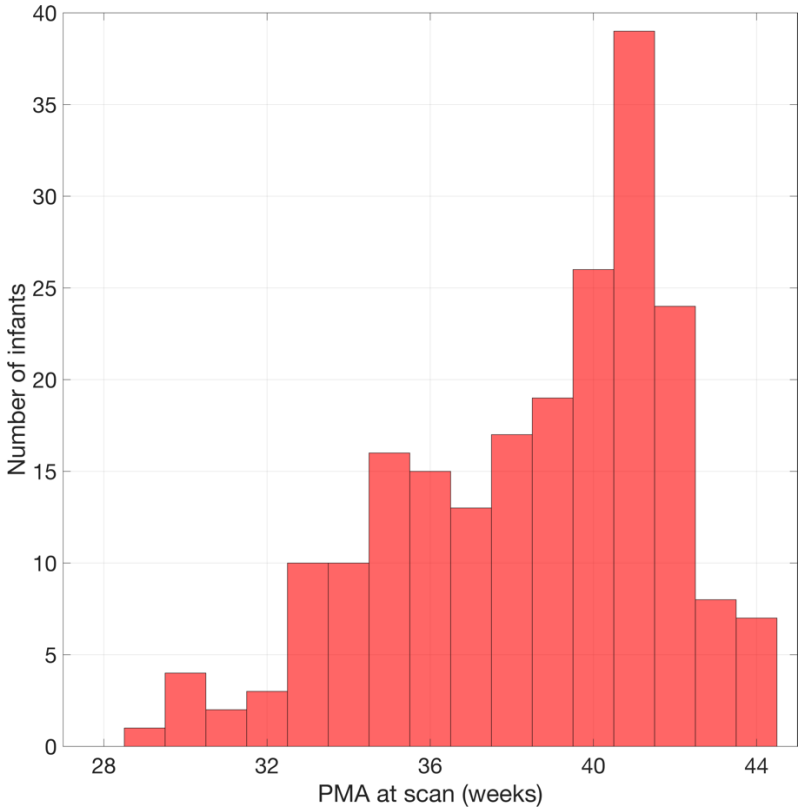

Figure 4.5: A histogram of the age distribution of infants whose structural data was used to produce the database of neonatal structural priors.

4.2.2 Segmentation of the extra-cerebral tissue

4.2.2.1 Automated segmentation methods

No *gold standard* method exists for the segmentation of skull and scalp layers from neonatal MRI data. Though studies have been published that propose methods to segment these tissues (Daliri et al., 2010; Ghadimi et al., 2008), these studies relied on manual segmentation of a small group of individuals. As a result, in this work a similar approach to Brigadoi et al. was developed to segment the scalp and skull as a combined label (i.e. the extra-cerebral tissue).

For each of the selected datasets, the pre-defined segmentations for brain tissues and CSF were combined and thresholded to produce a binary cerebral tissue mask, the outer extent of which was used to define the inner skull boundary. To define an extra-cerebral tissue mask, a method was needed to demarcate the outer scalp boundary. Once determined, the shape defined by this boundary could be filled in the axial, sagittal and coronal planes to produce a head mask. The cerebral tissue mask is then subtracted from the head tissue mask to produce the extra-cerebral tissue mask.

In this work, different approaches were investigated to segment extra-cerebral tissue, which in this case depended on determining the outer scalp boundary. One method investigated was Betsurf: a well-established tool that uses the intensity distribution of an MR image constrained to a robust range, to find the scalp surface (Jenkinson et al., 2005). Betsurf can be run with an individual's T_1-weighted image as its only input, or it can use both a T_1- and T_2-weighted image from the same individual. In this work, both of these implementations of Betsurf were evaluated. Another method investigated was Otsu thresholding (Otsu, 1979), a method that fits a bimodal model to the distribution of image intensities to determine a threshold between foreground and background voxels. Otsu thresholding has been previously employed by Tuan et al. (2018) to define the outer scalp boundary in an adult model. Using each of these

methods, an outer scalp boundary was delineated, and a one-voxel thick boundary was then extracted.

4.2.2.2 Suitability of manual segmentation

To quantify performance and determine the appropriateness of these different methods, a validation approach involving manual segmentation was the desired option. However, a validation needed to be completed to ensure that the scalp surface is visible in an MRI image and would be a reliable measure of the scalp boundary.

When an object with a high MRI contrast is placed in contact with the head, one would expect the high-contrast object to appear immediately adjacent to a visible scalp boundary if the scalp boundary is indeed visible to the naked eye in an MR image.

The oil in cod liver oil capsules has a short T_1 relaxation time; as a result, the capsules appear as high contrast features in an MRI scan. Two experiments were conducted with staff at the Centre for the Developing Brain. I underwent an MRI scan, using the dHCP inversion recovery sequence, with cod liver oil capsules taped to my head. Figure 4.6A shows an image of the cod liver oil capsule in the image. The capsule can be seen immediately adjacent to my scalp surface, which indicates that the outer scalp boundary is indeed visible in an MRI image.

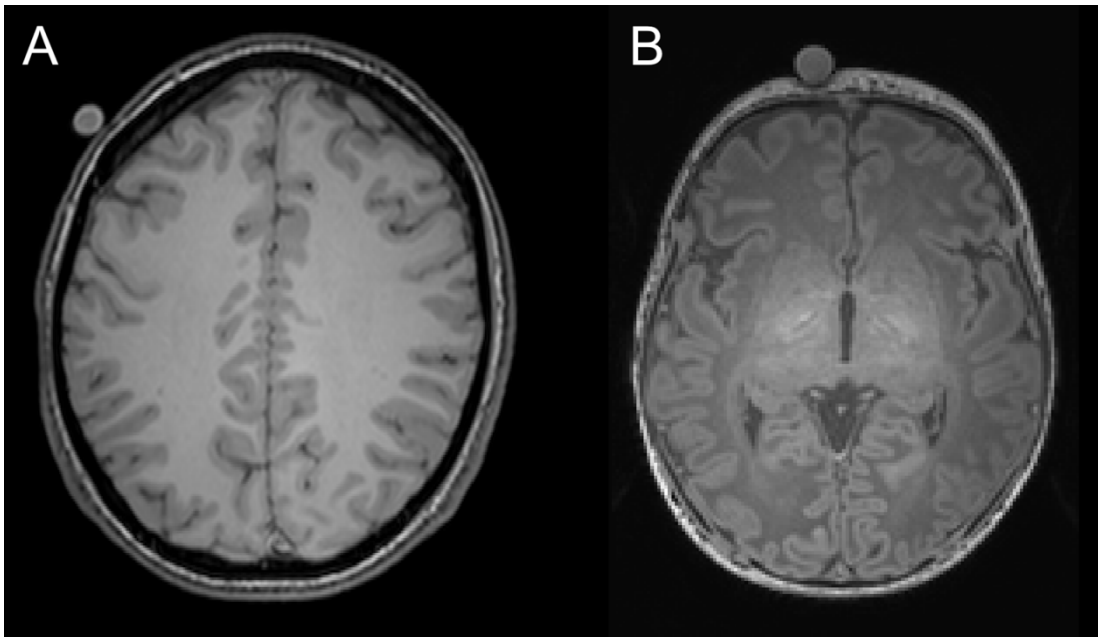

Figure 4.6: A) Inversion-recovery T_1-weighted image of the adult head with a cod liver oil capsule taped to the scalp (visible in the top right of the image). The capsule is clearly visible immediately adjacent to the scalp surface. B) Inversion-recovery T_1-weighted image of the neonatal head with a cod liver oil capsule placed in direct contact with the head (visible at the top of the image). The capsule is clearly visible immediately adjacent to the scalp surface.

Using a similar imaging sequence to the dHCP, a similar experiment was conducted with an infant at term-equivalent age who was undergoing an MRI scan for clinical reasons. Full informed consent was obtained from the infant's parents, and the experiment came under the ethical approval 12/LO/1247: "Investigating functional and structural brain development with MRI in the preterm period and early childhood" approved by the Research Ethics Committee at the Health Research Authority. As can be seen in Figure 4.6B, the cod liver oil capsule is once again immediately adjacent to a visible outer scalp boundary.

One can see that the cod liver oil capsule depresses the skin to a much greater extent on the neonatal infant head than is the case for the adult head. Nonetheless, the cod liver oil capsule clearly appears immediately adjacent to a visible outer scalp boundary, validating the assertion that an outer scalp boundary can be determined by visual inspection of the T_1-weighted image.

The significance of these experiments, therefore, was that manual segmentation could be used to evaluate the accuracy of automated scalp segmentation methods.

4.2.2.3 Scalp surface manual segmentation

The air-tissue boundary was manually segmented by a single rater for a subset of 12 individuals' T_1-weighted MR images using ITK-SNAP (Yushkevich & Gerig, 2017). The subset of 12 consisted of 3 arbitrarily-chosen infants at four age-points (32, 36, 40 and 44 weeks PMA). For the manual segmentation itself, T_1-weighted images were used, which offered better contrast for scalp tissue than T_2-weighted images. Manual segmentations were completed slice-by-slice in the axial plane then reviewed and modified in the sagittal and coronal planes. The segmentations were then filled slice-by-slice in the axial plane, before extracting a one-voxel thick outer boundary. To determine whether a single segmentation method was appropriate at all ages, infants were selected from a range of ages spanning 12 weeks to identify if there was any relationship between segmentation method performance and age.

For each individual, the one-voxel thick outer scalp boundaries from the manual segmentation were compared to each of the segmentations resulting from the automated methods. Three different metrics were used to compare each manual and automated segmentation. The mean surface distance (the mean of the distances from/to the centre of each manually segmented voxel to/from the centre of the nearest automated segmentation voxel) was used to provide an overall measure of similarity. The Hausdorff distance (the maximum of these distances) was used to quantify the maximum error, while the modified Hausdorff distance (the value of the 95^{th} percentile of these distances) was used to quantify the spread of error in the data without being biased towards outliers.

To obtain a measure of inter-rater variability, two students (one at King's College and another at University College London) were trained to manually

segment two of the twelve volumes that the primary rater had manually segmented. The similarity of these segmentations with the segmentations of the primary rater was compared using the same metrics outlined above. The mean surface distance between the primary rater's segmentation and those completed by the other two raters was 0.153 mm with a standard deviation of 0.236 mm. The Hausdorff distance was 1.5 mm and the modified Hausdorff distance was 0.5 mm.

4.2.3 Creating a multi-layer tissue mask

Having used the manual segmentations as gold standard to identify an appropriate automated method to identify the outer scalp boundary (see results in Section 4.3.1.1), the extra-cerebral tissue segmentation could be combined with the cerebral tissue mask. The full segmentation pipeline, used to produce multi-layer tissue masks for each of the 214 individuals, is outlined in Figure 4.7. When considering the optical properties of cerebral tissues, cortical and deep grey matter as well as the hippocampus can be grouped to become a single tissue label, grey matter; ventricles and outer CSF can be grouped to become a single label, CSF; and white matter, brainstem and cerebellum (which largely consists of white matter) can be grouped into one label, white matter.

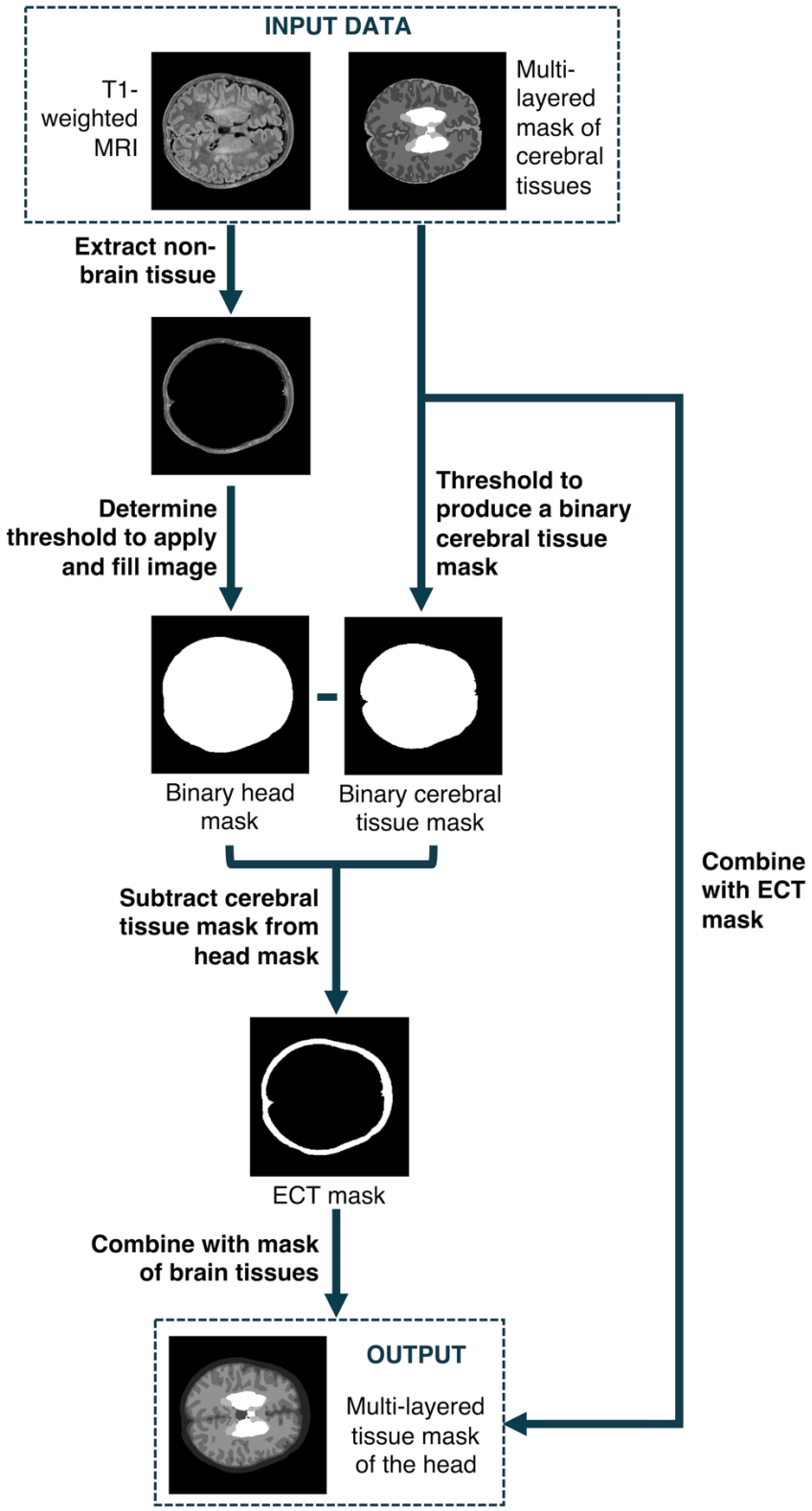

Figure 4.7: Flowchart describing the construction of structural priors for each neonatal individual using segmentations of cerebral tissues and an extra-cerebral tissue (ECT) segmentation extracted from a T_1-weighted MR image.

4.2.4 Constructing a volumetric tetrahedral mesh

A high-density tetrahedral volumetric mesh was produced for each of the 214 datasets using the iso2mesh toolbox (Fang & Boas, 2009). The multi-layered tissue masks were used as an input for a meshing procedure which assumes isotropic voxels: using the CGAL mesher option, the maximum element size was set to 1.5 unit cubed (where 1 unit is equal to 0.5 mm, the length of an isotropic voxel), while the maximum radius of the Delaunay sphere was set to 1 unit. The coordinates of the nodes of the resulting mesh were then rescaled into millimetre units. The quality of the volumetric meshes was assessed using the Joe-Liu quality index (Liu & Joe, 1994), expressed as

$$q_{vol} = \frac{12 \cdot (3 \cdot vol)^{\frac{2}{3}}}{\sum_{0 \le i \le j \le 3} l_{i,j}^2} \quad (4.1)$$

where q_{vol} is the Joe-Liu quality index, vol is the volume of a tetrahedron and $l_{i,j}$ are the lengths of the edges of the tetrahedron. Another metric, the mean Voronoi volume – the volume around a given mesh node which encompasses each point which is closer to the given node than any other mesh node – was used as an indication of mesh density; the lower the Voronoi volume, the higher the mesh density. In each tetrahedral volume mesh, the tissue labels (indexed from 1 to 9 specifying extra-cerebral tissue, outer CSF, cortical grey matter, white matter, ventricles, cerebellum, deep grey matter, brainstem and hippocampus, respectively) were assigned to each element and each node.

4.2.5 Cranial landmarks and 10/5 positions

The cranial landmarks positions (Nz, Iz, Ar, Al and an initial estimate of Cz) were visually determined using ITK-SNAP and these positions were used to calculate the 10/5 positions as detailed in Section 2.3.2.7. To preserve anonymisation of the dHCP data, the tissues around the eyes in the MR images have been intentionally distorted. The scalp surface therefore could not be recovered for the anteroinferior-most regions of the head. The 10/5

positions consist of 345 locations, however the lower-most curve of landmarks on the head (which lies below the axial reference curve) could not be reliably computed given the anterior distortion of the head. Due to this, all 10/5 positions below the axial reference curve (defined by Fpz anteriorly, T7 and T8 laterally, and Oz posteriorly) were excluded. The 10/5 positions in this work therefore included 249 locations on the scalp surface.

The mesh nodes were then transformed to a coordinate system where:

- the position of Iz defines the origin
- a line joining Iz to Nz defines the y-axis
- the z-coordinates of Ar and Al are approximately equal following rotation of mesh nodes around the y-axis.

4.2.5.1 Scalp-to-brain distance and extra-cerebral tissue thickness

Tissue thickness measures were derived for each model. The scalp-to-brain distance was computed for each 10/5 position as the distance to the nearest grey matter surface node, while extra-cerebral tissue thickness was computed as the distance to the nearest CSF node. The CSF thickness for each 10/5 position was computed as the scalp-to-brain distance minus the extra-cerebral tissue thickness.

4.2.6 Performance of the Model in an Example Application

Whilst subject-specific structural MRI data may not be available, knowledge of an infant's age and the external features of the head may be available and are far easier to obtain. This is often the case in both DOT and EEG studies of neonates. For a given subject, such characteristics can be used to choose a best-matching individual from the neonatal head model database. One such external feature could be head circumference, which is relatively easily and routinely acquired.

To demonstrate how this database can potentially be used, a simple example application and error quantification pipeline was developed. The functional imaging modalities outlined in this thesis rely on the placement of equipment on the scalp surface and so, in this example application, scalp positions from a subject-specific model and a matched model were projected to the cortical surface. These projection positions were compared to quantify the difference in cortical anatomy underlying equivalent scalp positions in the two models, which is used as a measure of the error incurred by using a matched model in place of a subject-specific model.

For each individual, the 10/5 positions were projected to the cortex. To do this, the nodes of the scalp surface of the volumetric mesh within a 5 mm radius of each 10/5 position were used to fit a plane. For a given 10/5 position, a ray vector was defined orthogonal to this plane. The ray was extended to find its intersection with a face on the cortical surface using the Möller-Trumbore algorithm (Mena-Chalco, 2009; Möller & Trumbore, 1997). The projection position for 10/5 positions whose ray vector did not intersect the cortical surface were assigned to be the nearest cortical surface node to the 10/5 position. The hemisphere of the resulting projection was also noted.

Initially, it was noticed that the distribution of projection distances for a given individual rarely exceeded 30 mm, however a small population of scalp locations lateral to the sagittal reference curve at the anteroinferior-most regions of the head appeared at 40 mm and beyond. In such cases, the projection from the scalp surface did not intersect with the cortical surface that was immediately underlying the scalp position. This was particularly a problem for the inferior-most 10/5 positions where a ray orthogonal to the scalp surface could extend a greater distance before meeting the cortical surface at a location nearer the midline. As such, if the ray intersected with the cortical surface at a distance greater than 35 mm for 10/5 positions not lying in the midline, this was deemed to be misleading, and such projection positions were

assigned the position of the nearest cortical surface node to the scalp location rather than the ray vector intersection position.

Each individual in the database was selected in turn to act as the target in a leave-one-out paradigm. This process is shown in flow diagram form in Figure 4.8. A pool of infants with an age equal to that of the target subject, plus or minus one week, was compiled. The infant from this pool with the nearest head circumference to that of the target individual was chosen to be the target's match. An affine transformation matrix was defined between the 10/5 positions of the match and the target. This transformation was then applied to the matched model's 10/5 positions and the nodes of the volumetric and cortical surface meshes to register them to the space of the target. In a process identical to that described previously, the 10/5 positions of this registered matched model were projected down to the cortical surface. This is illustrated in Figure 4.9.

Using Multimodal Surface Matching (MSM), a spherical registration method that allows flexible alignment of numerous different types of features on the cortical surface (Robinson et al., 2014, 2018), the registration between the cortical surfaces of the target and the match were computed. Mean curvature features were chosen to drive the registration, as these features reflect the finer-scale patterns of cortical folding (Bozek et al., 2018). In this work, surface registrations were computed between equivalent hemispheres (right and left) of the two different cortices.

For each projection of the matched individual, the cortical surface node nearest to the projection position was assigned a value of 1, while every other cortical surface node was assigned a value of 0, to obtain a single-valued image. MSM provides a transformation from the match cortical space to the target cortical space based on matching anatomical features of the cortex. This is so that *images* can be resampled from one space to another, rather than providing point-to-point mapping between surfaces. As such, a single-valued

image in the matched model's cortical surface will lead to a distribution of values when resampled into the space of the target cortical surface.

After applying the MSM transformation to the single-valued image in the match space, the subsequent resampled node values consisted of values between 0 and 1. To determine the transformed position of a given matched model projection on the cortical surface of the target, a weighted average was computed using the resampled values at each node as the weight for the position of each node.

This whole process results in two paired distributions of points in the coordinate space of the target cortical surface. These points represent the cortical locations underlying the 10/5 positions in the target individual (i.e. the ground truth positions) and the equivalent positions one would obtain if the match is used instead of the subject-specific structural prior. The Euclidean localisation error was defined as the Euclidean distance between each target projected position and their matched equivalent in the space of the target brain.

For each individual aged 41 weeks PMA (N = 39), the localisation error values associated with each projection position were interpolated to produce a map of localisation error as a function of position on the cortical surface. These individual localisation error cortical maps were transformed and resampled to the space of an age-appropriate cortical surface atlas (constructed by Bozek et al. (2018)) using MSM, and the mean and standard deviation of the node-wise localisation error values were computed.

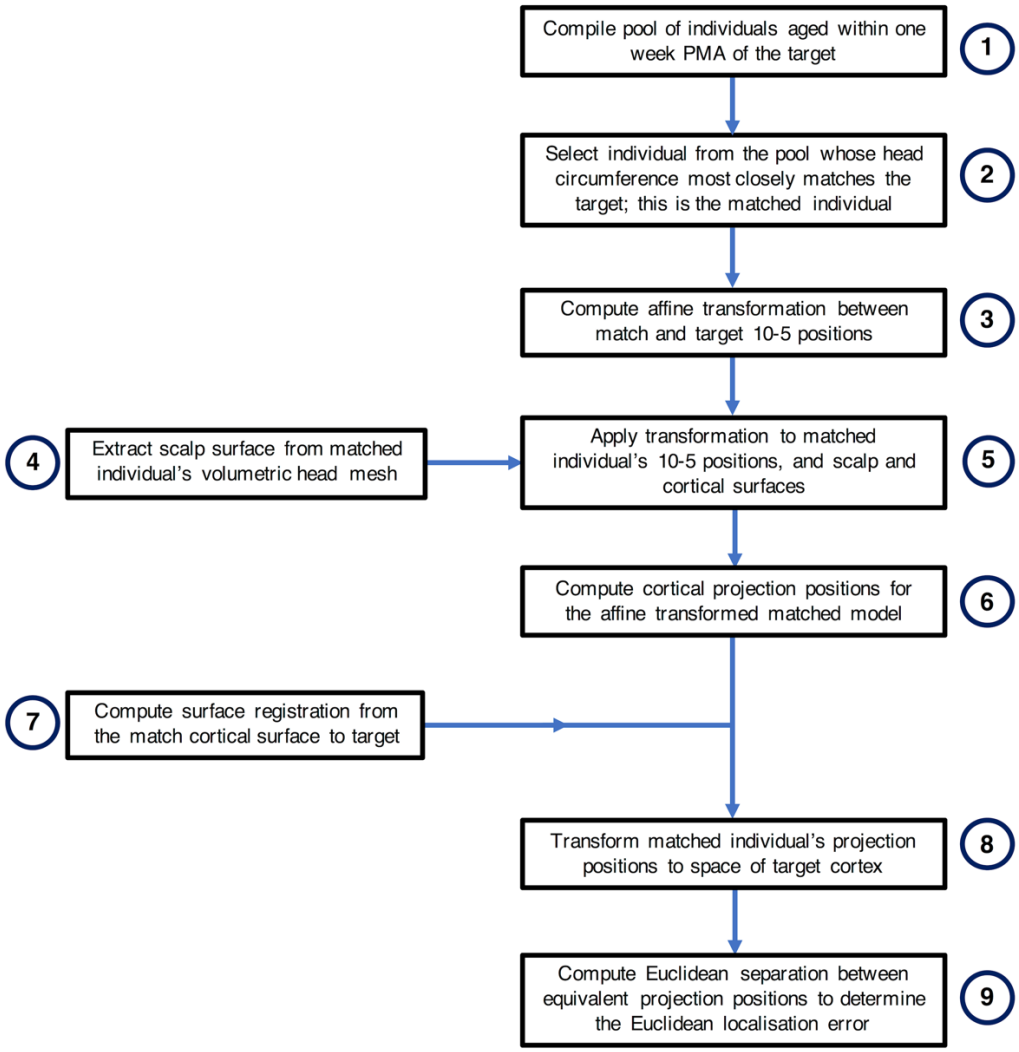

Figure 4.8: Flowchart of the process to compute the Euclidean localisation error for each individual acting as the target in a leave-one-out paradigm.

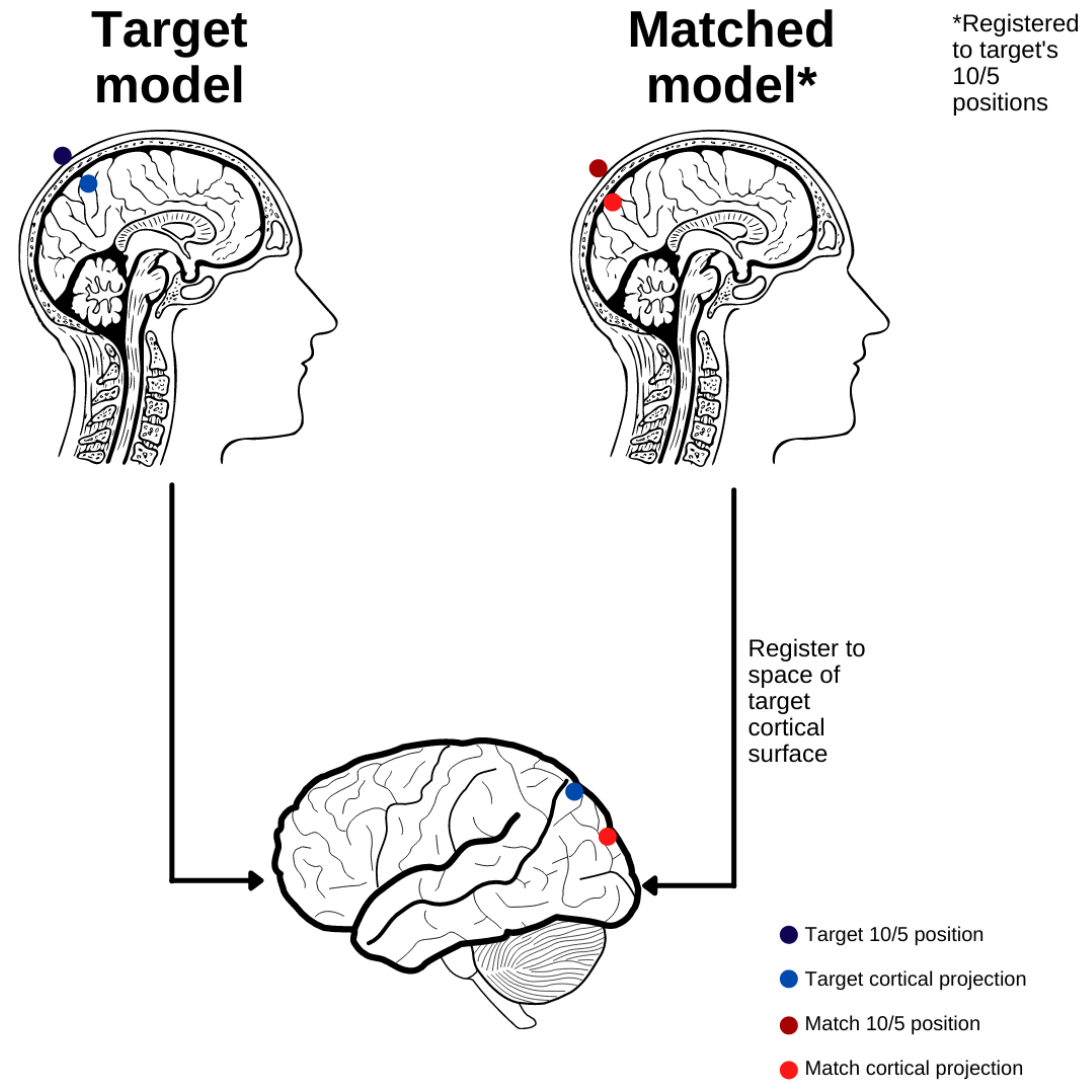

Figure 4.9: Illustration of cortical projection procedure for target and matched models for a given 10/5 position. For each given 10/5 position, the Euclidean localisation error is taken as the distance between the target and match cortical projections. Note: the matched model depicted will have first been registered (based on the transform to the target's 10/5 positions) *before* computing cortical projections.

4.3 Results

4.3.1 Model characteristics

4.3.1.1 Scalp segmentation

Three different automated methods to determine the outer scalp boundary were compared to manual segmentations for a subset of twelve individuals from the database, consisting of three different infants at 32, 36, 40 and 44 weeks PMA.

Compared to manual segmentation, the mean surface distance across all individuals of all ages was lowest among those segmented with Betsurf using the T_1-weighted image only, closely followed by Otsu thresholding (whose standard deviation was lower) followed by Betsurf using both T_1- and T_2-weighted images. The Hausdorff distance and the modified Hausdorff distance were lowest for Otsu thresholding, in addition to its lower surface distance standard deviation. Values for all metrics are shown in Table 4.1. Cumulative distribution functions displaying the data for all three automated segmentation methods compared to manual are shown in Figure 4.10.

The mean surface distance, modified Hausdorff distance and Hausdorff distance for each segmentation from each individual in the manually segmented subset is shown in Figure 4.11, and the resulting outer scalp boundaries from the different automated segmentation methods can be visualised in Figure 4.12. The modified Hausdorff distance indicates that Betsurf using both T_1- and T_2-weighted images is less reliable than the other two methods at all ages, while the Hausdorff distance indicates Otsu thresholding to be the most consistent at each age investigated. A statistically significant but very slight negative correlation was found between Otsu segmentation error and age ($r = -0.085$, $p < 0.001$). However, given its consistent performance and the fact that the mean surface distance was always less than 1 mm, it was concluded that it is appropriate to apply Otsu

segmentation to structural data across the range of ages covered in the database.

4.3.1.2 Database of individual structural priors

Example components from the completed database of individual multi-layered structural priors for neonates at different ages are shown in Figure 4.13. The cranial landmarks and 10/5 positions for an example individual are also shown in Figure 4.13.

Table 4.2 summarises the properties and quality indices of the volumetric meshes. The number of nodes increases with age as one would expect given the increase in head volume, observable in Figure 4.13. Across all volumetric meshes in the database, 81.0% of elements exhibit a q_{vol} value of 0.7 or greater, indicating that the majority of elements are close to being equilateral. The mean Voronoi volume of the volumetric mesh is 0.474 mm^3, indicating the high density of the mesh.

4.3.1.3 Anatomical features

Figure 4.14 shows the median thickness of the extra-cerebral tissue, the thickness of the CSF, and the median scalp-to-brain distance underlying the 10/5 positions for each individual as a function of age. Mesh-derived head circumference as a function of age is also shown in Figure 4.14

For 203 of the 214 infants in the database, data was available for the head circumference as measured at time of scan. Figure 4.15 displays the measured head circumference plotted against the head circumference derived from the mesh for these individuals. There is a high correlation between the two sets of measurements ($r = 0.91$, $p < 0.001$).

Table 4.1: Mean surface, Modified Hausdorff and Hausdorff distances for the three automated scalp surface segmentation methods relative to manual segmentation.

Method	Mean surface ± SD	Modified Hausdorff	Hausdorff
Otsu thresholding	0.295 mm ± 0.254 mm	0.5 mm	4.30 mm
Betsurf (T_1-weighted only)	0.266 mm ± 0.367 mm	0.707 mm	12.5 mm
Betsurf (T_1 and T_2)	0.466 mm ± 0.631 mm	1.87 mm	13 mm

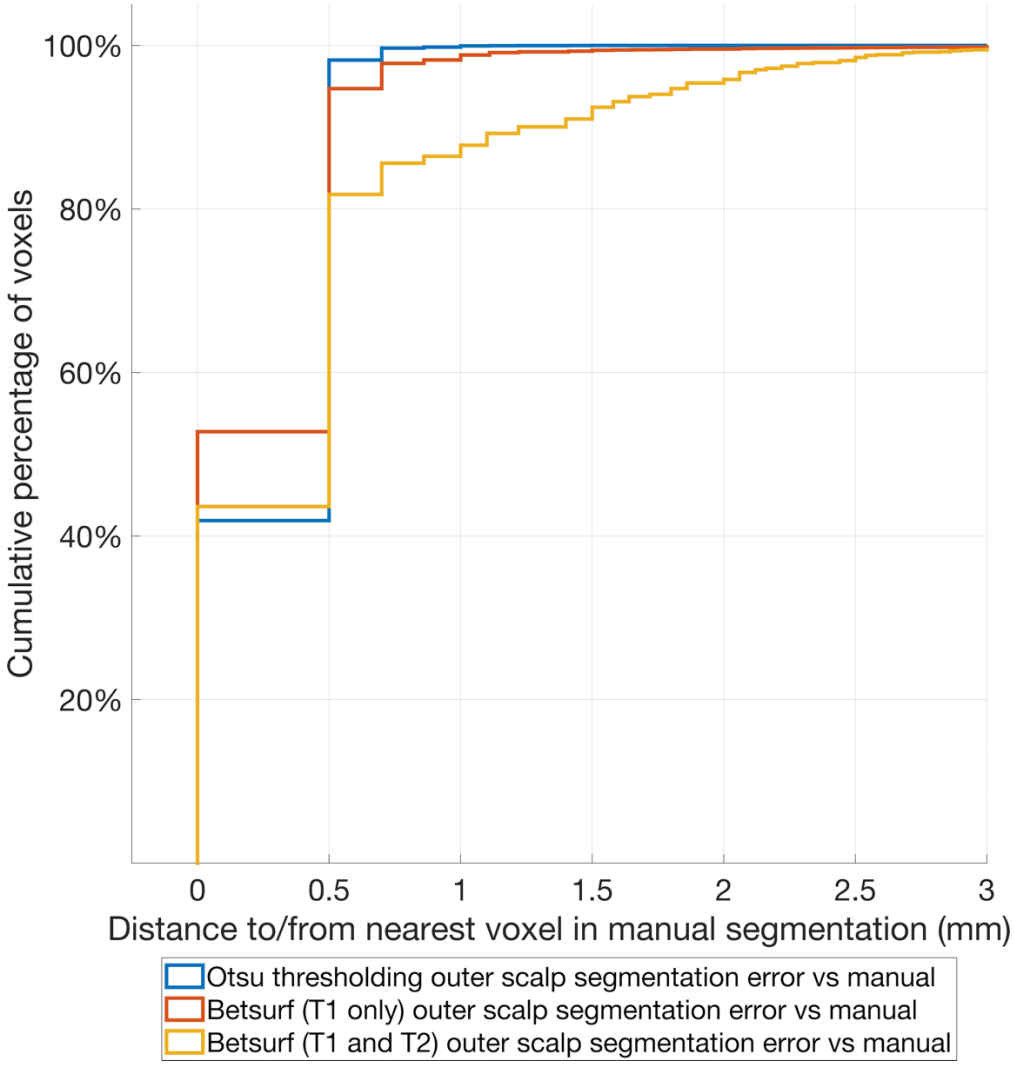

Figure 4.10: Cumulative distribution plot of the distances to/from the centre of each manually segmented boundary voxel from/to the centre of the nearest automated segmentation boundary voxel for each of the three automated methods. These distances are used as a measure of error in the outer scalp boundary relative to manual segmentation.

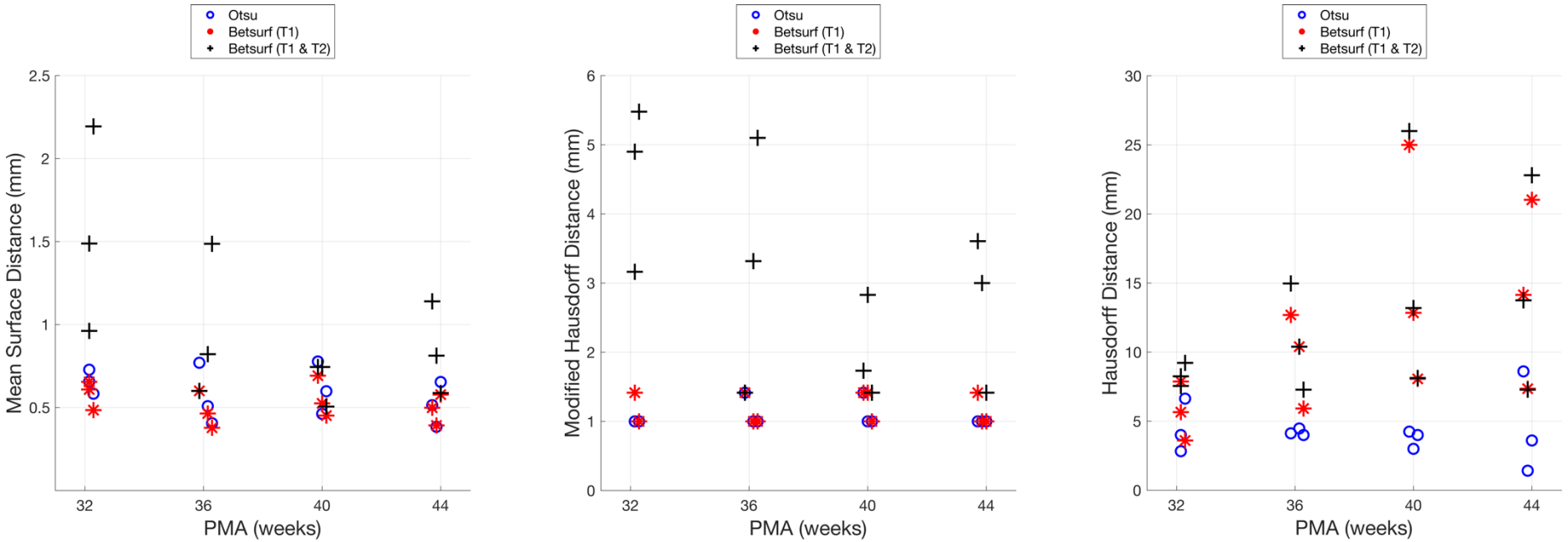

Figure 4.11: The metrics used to evaluate the automated segmentation methods are shown for each infant in the subset evaluated with manual segmentation.

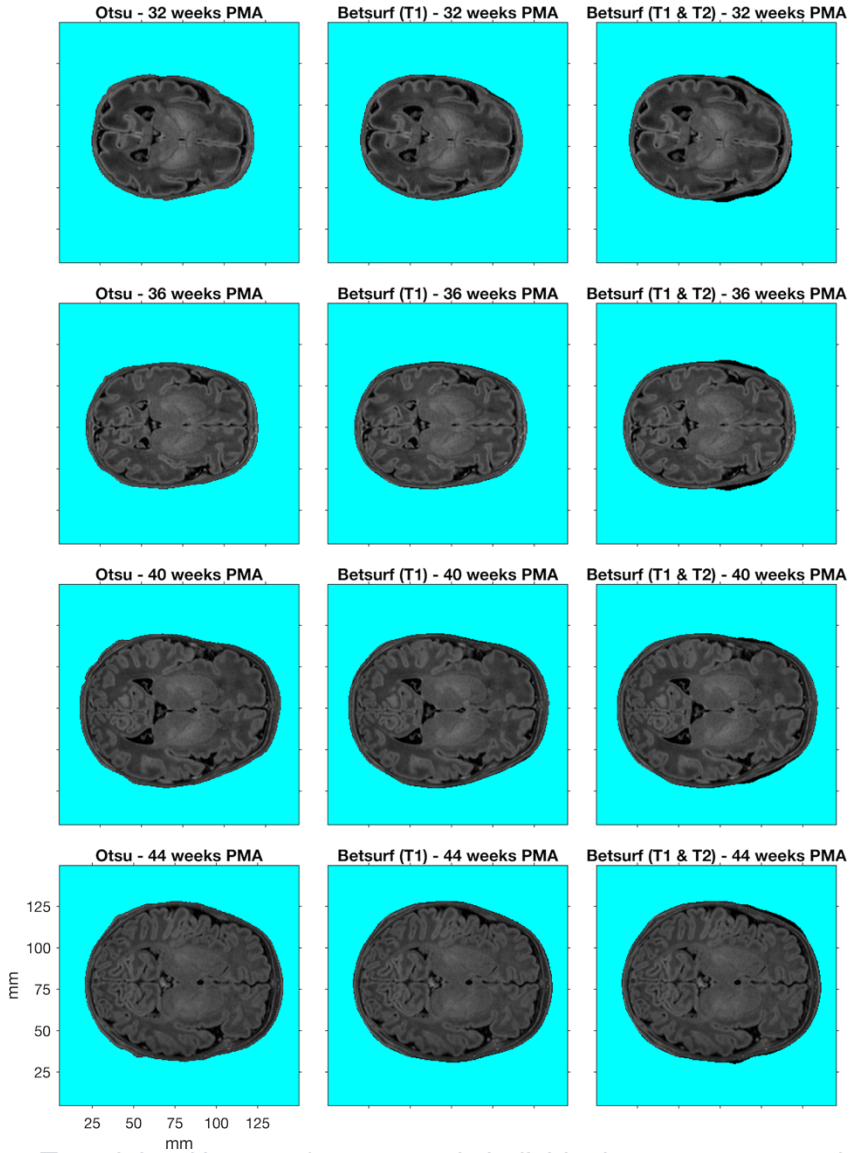

Figure 4.12: T_1-weighted images from example individuals at 32, 36, 40 and 44 weeks PMA. For each individual, the outer scalp boundaries determined using three different automated segmentation methods are shown (demarcated by the turquoise background).

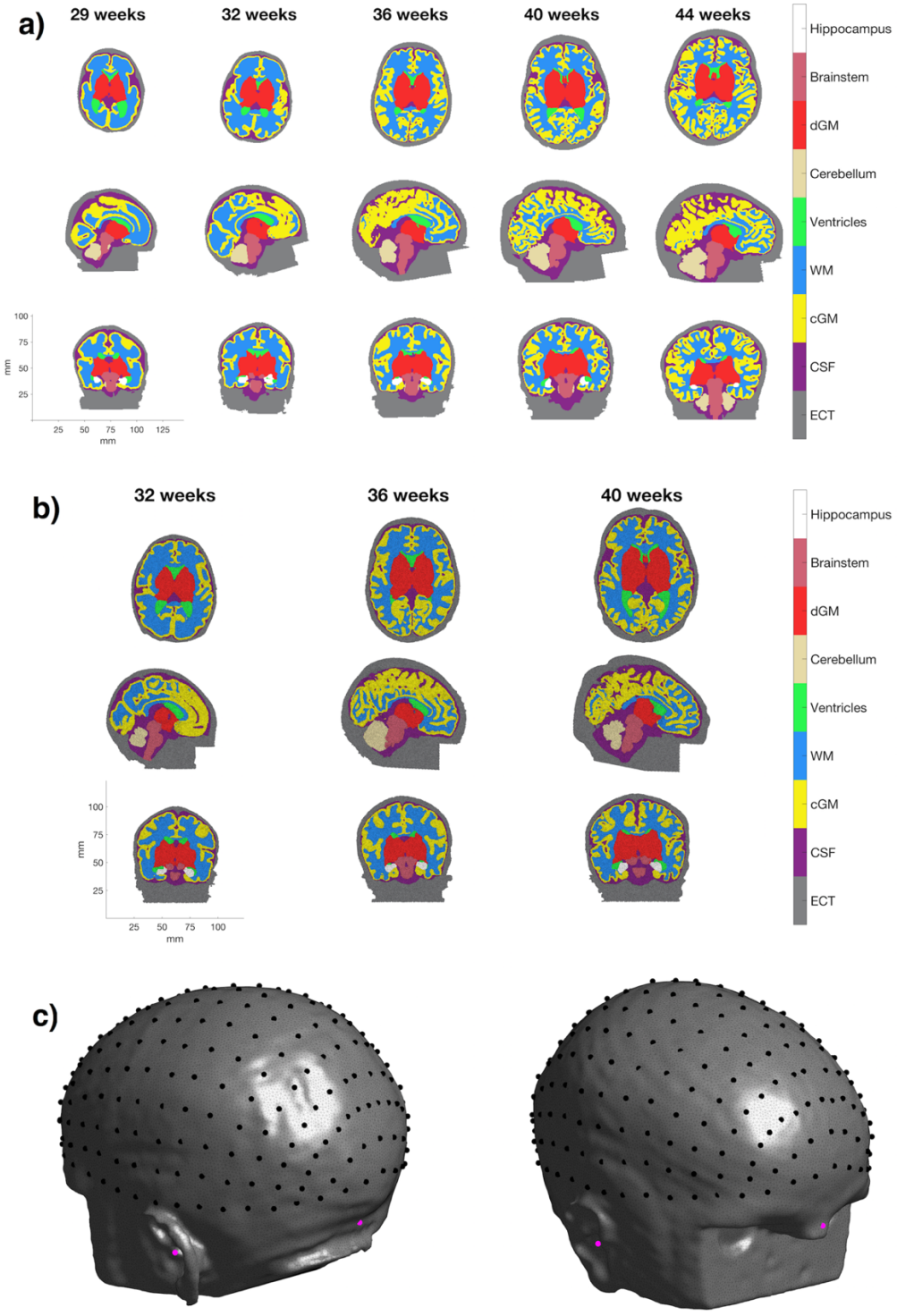

Figure 4.13: Example of multi-layered (a) tissue masks and (b) meshes from neonatal infants aged 29-44 weeks PMA (see colourbar). Tissues represented are extra-cerebral tissue (ECT), CSF, cortical grey matter (cGM), white matter (WM), ventricles, cerebellum, deep grey matter (dGM), brainstem and hippocampus. The 10/5 positions on the scalp surface from an example infant aged 41 weeks PMA are shown in (c) in black, while the cranial landmarks are shown in magenta.

Table 4.2: Features of the high-density volumetric meshes for each age in the database.

Age	Mean q_vol ± std	Mean Voronoi volume ± std (mm^3)	Mean N nodes ($x10^6$)	Mean N elements ($x10^6$)	Mean N faces ($x10^6$)	N subjects
29	0.803±0.115	0.473±0.210	0.62	3.59	1.06	1
30	0.802±0.116	0.468±0.210	0.63	3.67	1.08	4
31	0.802±0.116	0.466±0.210	0.70	4.12	1.22	2
32	0.800±0.117	0.472±0.210	0.77	4.50	1.35	3
33	0.802±0.116	0.474±0.210	0.82	4.81	1.40	10
34	0.802±0.116	0.476±0.208	0.95	5.55	1.60	10
35	0.802±0.116	0.477±0.209	1.05	6.16	1.78	16
36	0.801±0.116	0.475±0.207	1.07	6.32	1.85	15
37	0.801±0.117	0.475±0.207	1.17	6.90	2.01	13
38	0.799±0.117	0.482±0.206	1.20	7.10	2.12	17
39	0.800±0.117	0.477±0.207	1.34	7.94	2.31	19
40	0.800±0.117	0.479±0.206	1.36	8.06	2.37	26
41	0.799±0.117	0.479±0.206	1.39	8.21	2.44	39
42	0.799±0.117	0.468±0.205	1.46	8.69	2.58	24
43	0.799±0.117	0.472±0.206	1.54	9.15	2.7	8
44	0.798±0.117	0.471±0.204	1.56	9.27	2.78	7

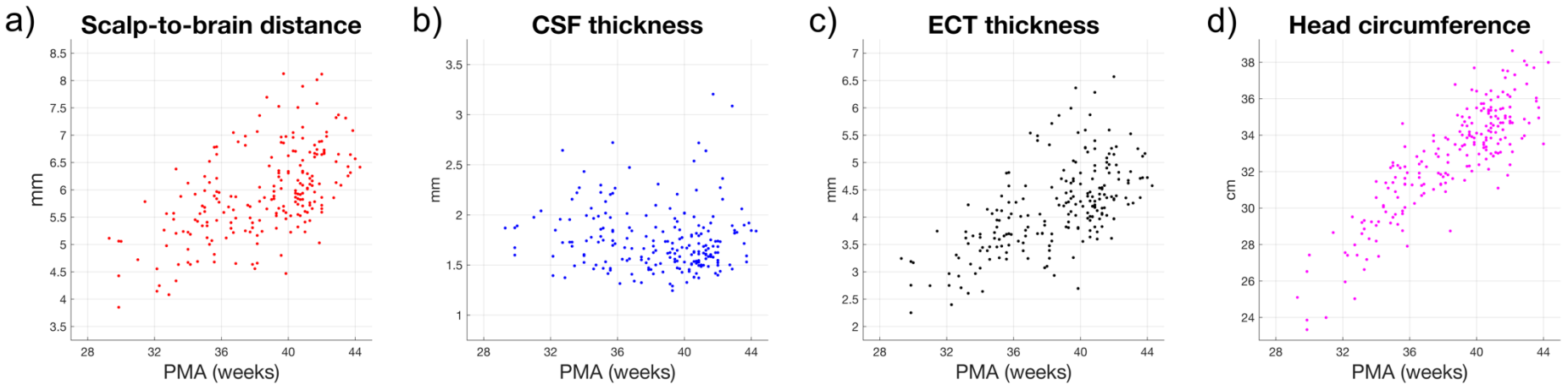

Figure 4.14: Median tissue thickness values for scalp-to-brain distance (a), CSF (b), extra-cerebral tissue i.e. ECT (c) underlying the 10/5 positions, and head circumference as a function of age for all individuals in the database (d).

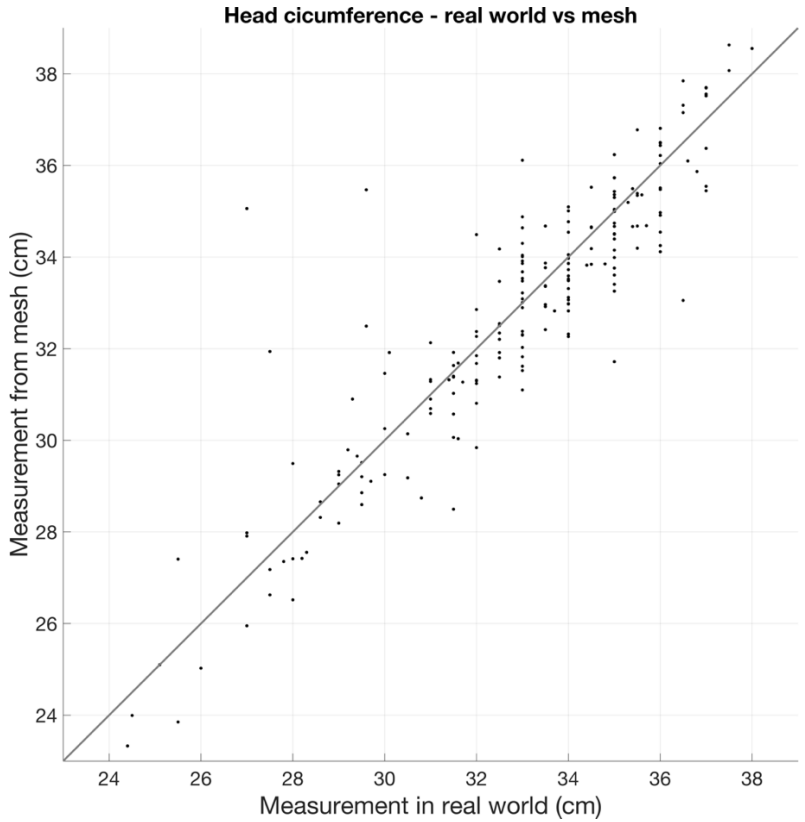

Figure 4.15: Head circumference measurements taken in vivo (x-axis) plotted against head circumference measurements taken from volumetric meshes (y-axis). The line of one-to-one proportion is shown. Outliers can be seen at real world head circumference measurements of approximately 27 cm and 29.5 cm. Though this figure implies that the real world measurement is ground truth, the real world measurements are still prone to error and uncertainty. These outliers likely relate to the extremes of this uncertainty in real world measurements, and are likely due to an experimental error in the real-world head measurement.

4.3.2 Performance of the model in an example application

The mean Euclidean localisation error across all projections from the 10/5 positions was determined to be 8.1 mm (median absolute deviation 3.7 mm), while 95% percent of projection points were within a Euclidean localisation error of 17.6 mm or less (see Figure 4.16 and Figure 4.17).

The localisation error cortical map at 41 weeks PMA is shown in Figure 4.18. The localisation error is lowest anteromedially (except for cortical areas proximate to the longitudinal fissure) and is highest posteromedially. A localisation error of 9.5 mm or below is apparent across almost the entirety of the sensorimotor cortex and over the vast majority of the superior and middle temporal gyri bilaterally. The node-wise standard deviation of the localisation error is 4 mm or below for the vast majority of the cortical surface.

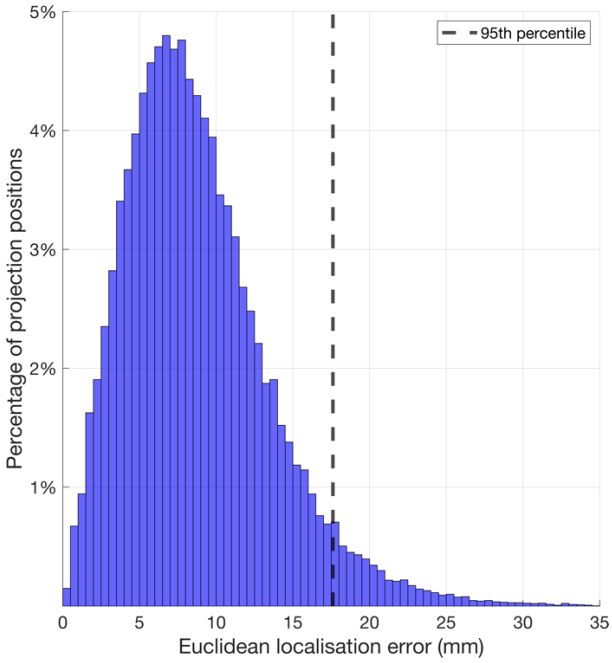

Figure 4.16: Histogram displaying the distribution of the Euclidean localisation error of each cortical projection position, combining data from each individual.

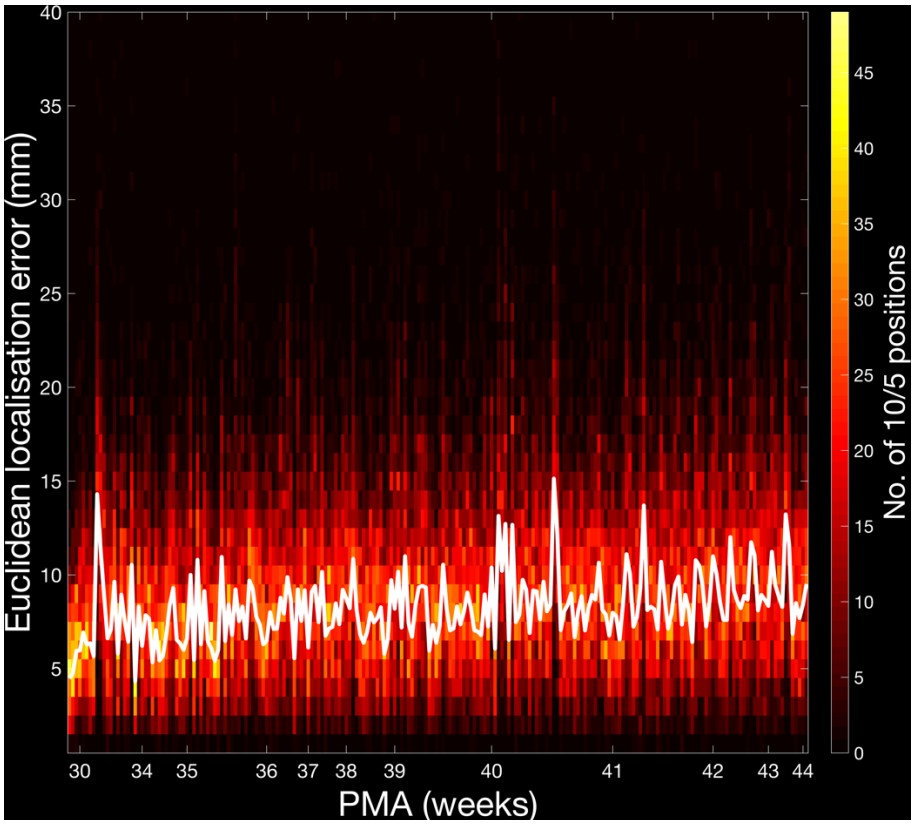

Figure 4.17: Histogram displaying the distribution of the Euclidean localisation error of the cortical projection positions per individual (see colourbar) and the median values for each individual (plotted as a white line).

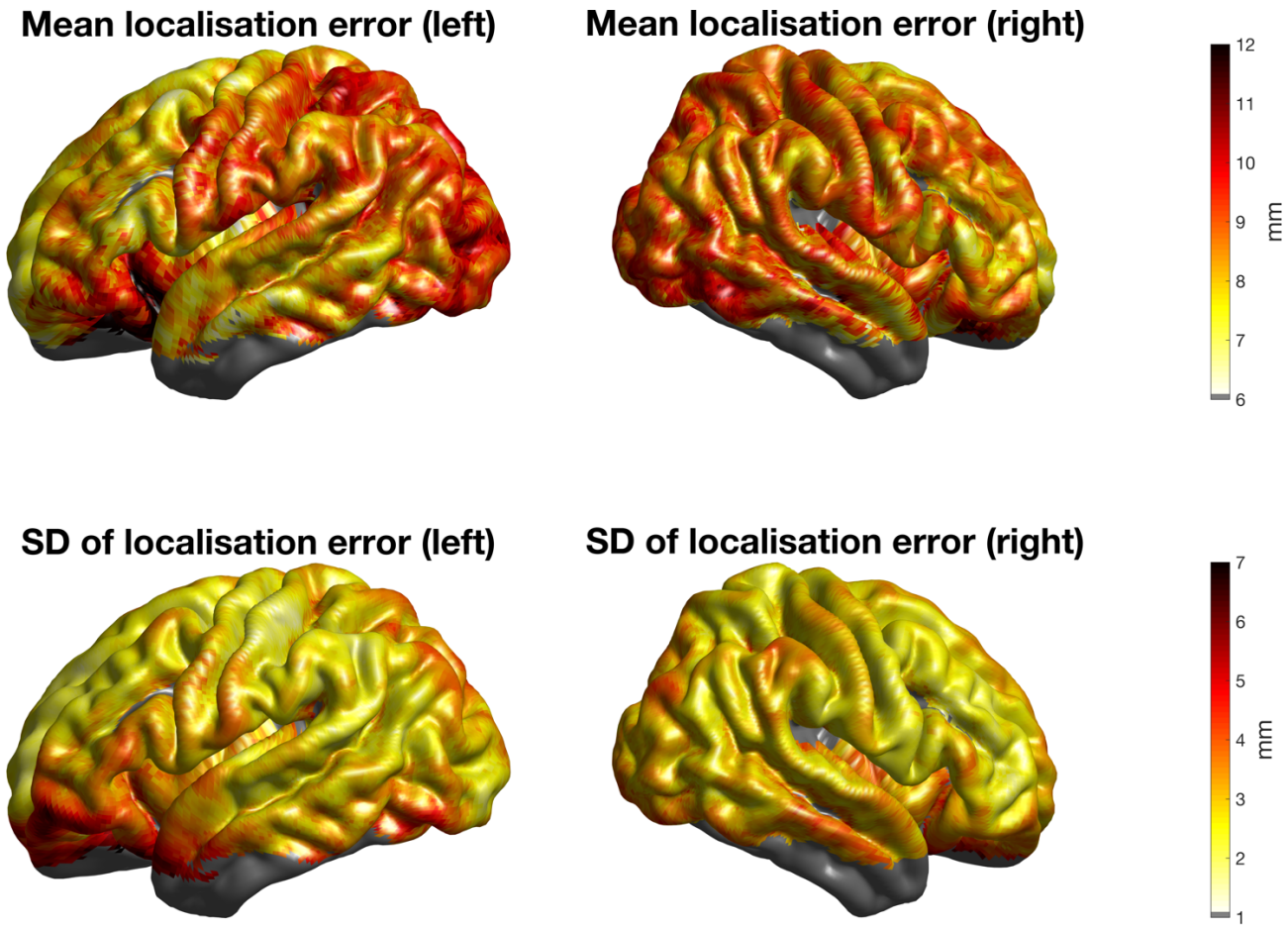

Figure 4.18: For each individual aged 41 weeks PMA, the Euclidean localisation error was interpolated across the cortical surface using the value at each projection position. The interpolated localisation error maps for each of these individuals were registered to the surface of a 41-week PMA cortical surface atlas and averaged. Here the node-wise values of the mean and standard deviation are displayed.

Figure 4.18 maps the error due to using a matched model in place of a subject-specific model. These errors represent the compound effect of anatomical differences, variation in the 10/5 positions between the target and matched models, and errors due to the process of registering from one cortex to another. Disentangling these errors is not entirely possible. However, two sources of variation can be investigated: variation in projection depth (i.e. depth-to-cortex, which relates to anatomical differences) and variation in 10/5 positions post-registration.

For each individual at 41 weeks PMA, the difference in projection depth to the cortex was computed between the target and match for each 10/5 projection. These values were projected to the cortical surface and interpolated, and the mean was taken across subjects. This is shown in Figure 4.19c and d. The error varies from around 2-6 mm and is highest in the inferior frontal gyrus.

For each individual at 41 weeks PMA, the Euclidean offsets between each 10/5 position in the target and registered match were computed. These values were projected to the cortical surface and interpolated, and the mean was taken across subjects. This is shown in Figure 4.19e and f. The error varies from around 1-3 mm and appears to be consistent across the cortical surface.

The node-wise values for 10/5 position offset and projection depth difference were summed in quadrature before being subtracted from the mean localisation error values (as are mapped in Figure 4.19a and b). These residual error values are mapped on the cortical surface in Figure 4.19g and h: these values can be taken as a measure of the contribution of the remaining sources of error (cortical registration processes, other aspects of anatomical difference, etc.). This residual error varies from 3-7 mm. This demonstrates that 10/5 positioning offset and depth-to-cortex variation do account for a significant proportion of the errors apparent in Figure 4.18, but that other sources of error are also apparent.

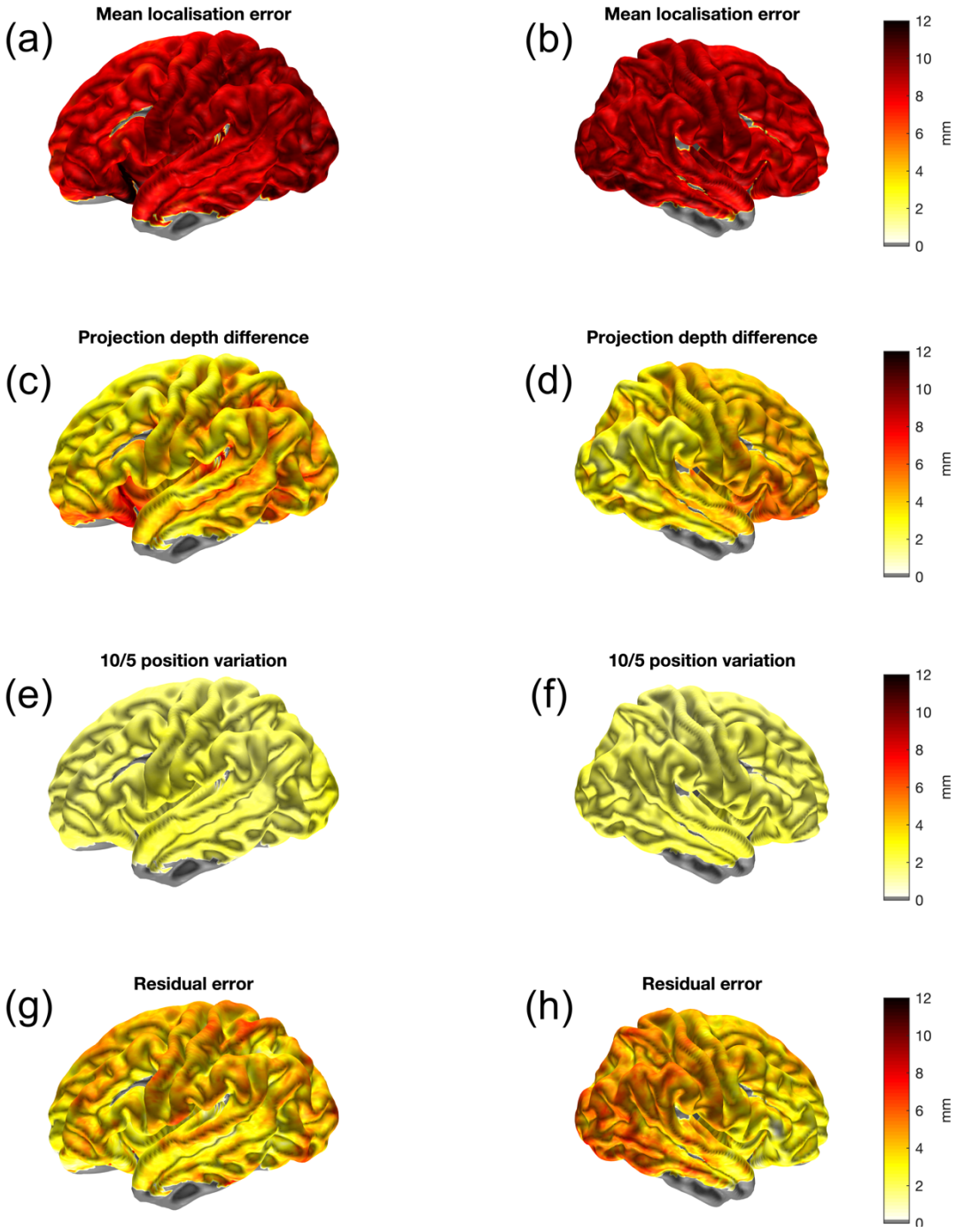

Figure 4.19: Mapping the contribution to the localisation error of difference in projection depth and variation in 10/5 positions.

4.4 Discussion

This Chapter describes the production of a database of 214 individual structural priors using data from infants aged 29-44 weeks PMA for use in a range of neuroimaging modalities. For each individual, the data package includes:-

- A voxelised mask of tissues of the head
- A tetrahedral mesh of tissues of the head
- A scalp surface mesh
- The coordinates of the 10/5 positions and cranial landmarks
- Cortical and white matter surface meshes, taken from the dHCP processing pipeline and re-aligned to the space of the tetrahedral meshes.

More datasets will be made publicly available by the dHCP in future, so more head models could be processed with the pipeline detailed in this work and added to the database in future.

Ideally, a structural prior would always be derived from an individual's own MRI scan, however this is often not available, and requiring each individual to undergo an MRI scan undermines the benefits of many functional imaging techniques that enable neonates to be studied at the cot-side. The use of an atlas removes the need for each subject to undergo an MRI scan, addressing the fundamental challenge posed by imaging modalities that do not simultaneously acquire structural and functional data. The database of neonatal structural priors established here will enable methods to be investigated of how to find a matching model that minimises the error incurred by using an individual-level atlas in place of subject-specific anatomy.

The structure of the neonatal brain is highly variable across ages and individuals, evident from Figure 4.13 which displays example structural models at different ages, with substantial structural changes occurring from 29 to 44 weeks PMA. A study of over 300 infants aged 28-44 weeks PMA (Makropoulos et al., 2016) found that the relative volume of white matter decreases during

this period while the relative volume of cortical grey matter increases, as does cortical surface area. The use of a single model for infants across this age range is therefore highly inappropriate.

Metrics of mesh quality are presented in Table 4.2. Measures of mean mesh quality are common in the literature, and the metrics presented here emulate the same metrics presented by Brigadoi et al. (2014). The metrics in this work indicate that the meshes in the head model database are, in general, of high quality and have a high density. However, a better approach may have been to also include the worst values of quality for the elements in each head model, which may give a better indication of how likely a numerical error is to arise in models of field propagation using these head models as a spatial prior.

The constraints imposed by a lack of structural information is not unique to DOT. Though the motivations for this work arise from the need for structural priors in DOT, the structural priors presented in this work can be used for many functional imaging modalities in neonates. These could be used as a space to which functional data can be registered, or to solve the forward problem in EEG, MEG, DCS, NIRS and DOT (Arridge & Cooper, 2015; Azizollahi et al., 2016; Legon et al., 2018; Mueller et al., 2017; Pirondini et al., 2018; Ranjbaran et al., 2019; Roche-Labarbe et al., 2008; Routier et al., 2017; Selb et al., 2014). The cranial landmarks and 10/5 positions are provided in this data package for each head model and can be acquired from an infant at the cotside using a magnetic positioning device or photogrammetry methods. Acquiring a subset of these positions can enable a structural prior to be registered to the dimensions of the subject. In addition, it is necessary to determine the position of sources and sensors placed on the scalp surface of a given subject, such as optodes or electrodes, and these can also be acquired from an infant in reference to particular 10/5 or cranial landmarks positions.

Appropriate properties need to be assigned to the nodes (or elements) of the structural prior, which may vary in correspondence with tissue type, as is the

case for optical properties, magnetic permeability and electrical conductivity. For the volumetric structural priors (tissue masks and tetrahedral meshes) presented in this work, tissue assignments are provided for the extra-cerebral tissue in addition to the 8 intra-cerebral tissue types as defined through the dHCP structural pipeline (Makropoulos, Robinson, et al., 2018).

Spatially averaging structural data results in the diminished detail of gyrification seen in population-level atlases. Such models of the head do not offer an anatomical volume representative of an individual head in which a field, such as the spatial distribution of photon migration, can be modelled. A population-level atlas, therefore, does not represent anatomy at the individual-level. The individual-level structural priors produced in this work exhibit gyri and sulci, signifying that the head models are truly representative of individual anatomy.

In the simple validation pipeline presented in this work, an approach was taken to find a matched individual from the database to be used in place of a subject-specific head model. The obvious limitation of implementing the database through a matched individual approach is that the use of an individual atlas may bias the resulting images, since the structural prior does not incorporate anatomical variation across infants at a particular age.

To address this bias, the database presented could also permit a probabilistic approach that makes use of head models from multiple individuals. For a given infant, a pool of closely matched individuals from the database could be compiled, and each of these head models could be spatially registered and used to reconstruct an image. The resulting reconstructed images could then be averaged in a common space using surface-based registration techniques such as MSM and FreeSurfer, so that the resulting image is influenced by a degree of anatomical variation in a well-targeted population without being biased towards a specific individual's anatomy. Alternatively, the pool of best-

matching individuals compiled from the database permits the production of a population-level atlas from a more demographically constrained cohort.

4.4.1 Extra-cerebral tissue segmentation

To build the database, a series of methods for automated segmentation of the extra-cerebral tissue were evaluated by comparison with manual segmentations from a subset of individuals. The purpose of this validation was to ensure that the head models realistically represent the anatomy of individual infants and to quantify the error associated with extra-cerebral tissue segmentation. The mean surface error associated with the use of Otsu thresholding is typically less than 0.5 mm at the outer scalp boundary, which is acceptable given the resolution of the associated MRI images and the typical resolution of DOT (Cooper et al., 2012; Ferradal et al., 2014, 2016).

Few publications exist that focus on the segmentation of neonatal extra-cerebral tissue. Ghadimi et al. (2008) produced probabilistic atlases for scalp and skull using T_1-weighted images from three subjects aged 39-42 weeks PMA that were manually segmented and transformed to the space of the GRAMFC neonatal brain template produced by Kazemi et al. (2007). To segment scalp and skull for a given subject, the T_1-weighted image was normalised to the GRAMFC atlas, and the probabilistic scalp and skull atlases were then used to identify scalp and skull points, followed by a threshold-value determination step to obtain closed surfaces. Daliri et al. (2010) applied a similar method by constructing a probabilistic atlas whereby six images (normalised to the space of the GRAMFC atlas) were manually segmented to produce atlases for scalp and skull tissues. A Bayesian classifier was then used to weight local features of the MR image against those of the probabilistic atlas, with the weighted features then being fed to a neural network classifier to obtain an estimation of the skull layer. An exciting avenue for future work would be to use the database to optimise automated methods to segment the extra-cerebral tissue. A tissue probability map for the extra-cerebral tissue

could be created for infants at a given age and could be employed as a spatial prior for segmentation.

The database of neonatal head models presented in this chapter was made using previously validated segmentations of neonatal MR images that retained brain tissues and CSF (Makropoulos, Robinson, et al., 2018). As such, the outer boundary of the cerebral tissues was taken as the inner skull boundary, and so only the outer scalp boundary was sought to produce a combined skull and scalp segmentation: the extra-cerebral tissue. The studies described above do present a method to separate skull and scalp tissue in infants, however the methods would be unfeasible for the purposes of our work. Firstly, the authors rely on manual segmentation of the outer and inner skull boundaries, a time-consuming method which can only provide data from a small number of individuals in a reasonable time frame. Secondly, the skull/scalp boundary is difficult to discern on a neonatal MRI scan, rendering such methods subjective and difficult to validate. Further, for optical applications, the optical properties of the skull and scalp are surprisingly relatively similar in the near-infrared range (at 800 nm: absorption coefficients are 0.018 mm^{-1} and 0.016 mm^{-1} for scalp and skull respectively, reduced scattering coefficients are 1.9 mm^{-1} and 1.6 mm^{-1} for scalp and skull respectively (Fukui et al., 2003)).

Despite this, the lack of distinct segmentations for skull and scalp in our models remains a limitation of this work, particularly for EEG applications where scalp and skull have different conductivity (Azizollahi et al., 2016; Roche-Labarbe et al., 2008; Routier et al., 2017). Another limitation is that the head models do not include any information on the structure of the fontanelles. It is known that the inclusion of the fontanelles in a head model improves the accuracy of the recovery of absorption changes in diffuse optical methods (Dehaes et al., 2013) and it is also known to improve source localisation in EEG (Roche-Labarbe et al., 2008). Computed tomography data is required to discern the fontanelles from bone (which cannot be achieved with MRI data

alone) and such data did not exist for the individuals whose data was used to produce the database presented in this work.

Some literature values are available for the thickness of extra-cerebral tissue and CSF, though they are somewhat difficult to compare to the current work. Beauchamp et al. (2011) conducted a study of the brain-to-scalp distances of subjects aged from birth to 12 years, derived from MRI data. This included data from 14 neonates, which yielded a highly variable pattern of brain-to-scalp distances, with mean values ranging from 5 to 10 mm between individuals. Brigadoi & Cooper (2015) computed the extra-cerebral tissue and CSF thicknesses underlying each surface node as well as overall scalp-to-brain distances for each age of the Brigadoi et al. head model (Brigadoi et al., 2014). The median values of CSF thickness from the Brigadoi et al. model are notably higher than the median values for individuals from the database in this work at corresponding ages; these values are plotted in Figure 4.20. The opposite is true for extra-cerebral tissue thickness, which is consistent with the authors assertion that their models likely underestimate the thickness of the extra-cerebral tissue. The close correspondence demonstrated here between segmentations completed manually and by Otsu thresholding, as well as the high correlation between measured and mesh-derived head circumference measures, underpins confidence that the models in this database accurately represent extra-cerebral tissues.

Over half of the prospective datasets, 367 of 634, acquired as part of the dHCP cohort and used in this work had to be excluded for reasons other than intellectual property. The reason for the vast majority of these exclusions (86% of 367) was that the extra-cerebral tissue extended out of the field of view in the T_1-weighted MR images. This is often found in clinical MRI scans where the duration of the scan is limited. To produce an accurate representation of non-brain tissues, it was ensured that all extra-cerebral tissues were visible across the image volume. An interpolation method could potentially have been used to correct for the missing extra-cerebral tissue in these excluded

datasets. However, this process would have required its own optimisation and validation and, given the large number of individuals that were acceptable, it was determined that it was better to rely solely on these datasets with complete structural images.

Another limitation of this work is the determination of the cranial landmarks positions. There is ambiguity in the definitions of the cranial landmarks, leading to issues with reproducibility in determining their positions. This is particularly the case for the inion (Jurcak et al., 2007). As such, there exists rater-originated variability in the determination of cranial landmarks positions and (by extension) the 10/5 positions calculated for each individual in the database.

4.4.2 Comparison to previous neonatal head modelling work

The database of structural priors presented in this work confers several advantages over the population-level atlas produced by Brigadoi et al., the most realistic model available for use in place of a subject-specific model. The database of structural priors was produced using MRI data of a superior resolution (0.5 mm x 0.5 mm x 0.5 mm in this work, 0.86 mm x 0.86 mm x 1 mm in Brigadoi et al.), and the segmentations used to build the model were obtained using a more up-to-date segmentation algorithm (Makropoulos et al., 2014; Makropoulos, Robinson, et al., 2018). A validation of the extra-cerebral tissue segmentation is included in this work, the likes of which was not included in the work published by Brigadoi et al.

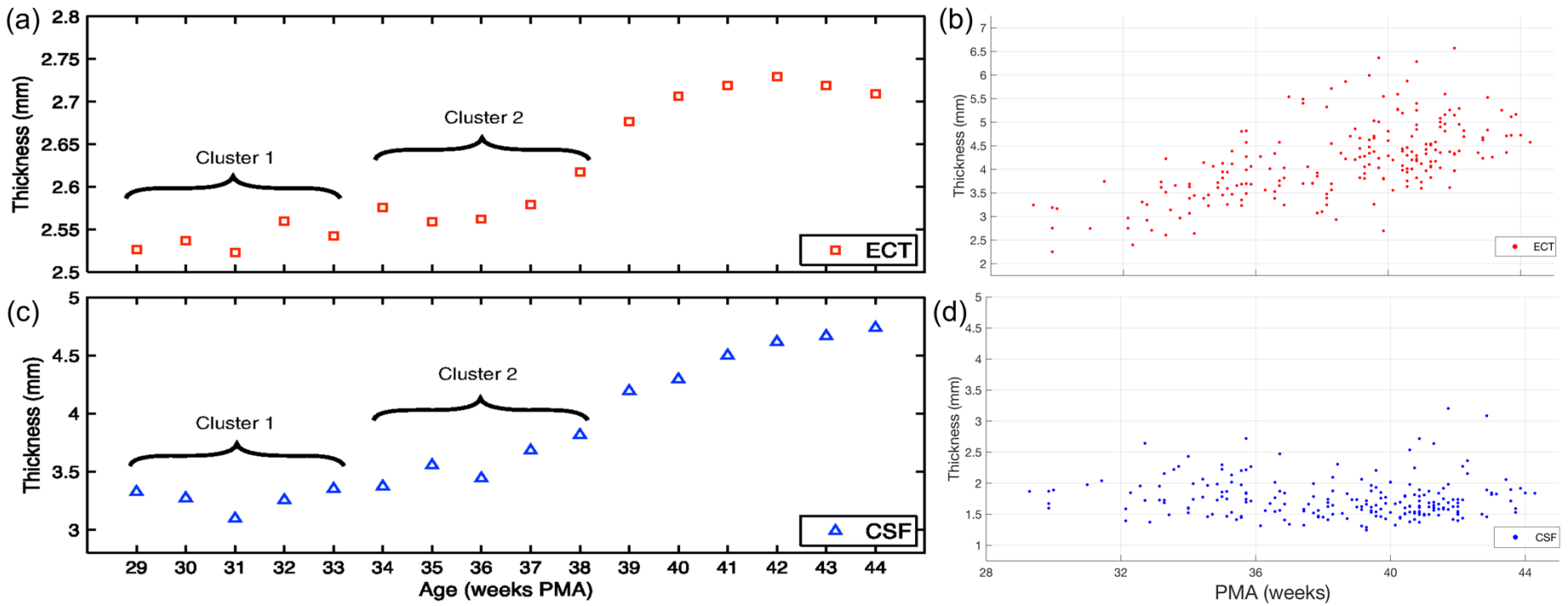

Figure 4.20: Median values for extra-cerebral tissue thickness taken from (a) the Brigadoi et al. head models and (b) individual head models in the neonatal structural prior database as a function of age. Median values for CSF thickness values taken from (c) the Brigadoi et al. head models and (d) individual head models in the neonatal structural prior database as a function of age. Figure adapted from Brigadoi & Cooper (2015). Reprinted with permission from SPIE and author[13].

[13] Reprinted from *Neurophotonics*, *2*(2), Brigadoi, S., & Cooper, R. J., How short is short? Optimum source–detector distance for short-separation channels in functional near-infrared spectroscopy, 025005, Copyright (2015), with permission from SPIE and one of the authors (R.J. Cooper).

Further, the models in the database are compatible with surface registration techniques. In this work a comparison of the error incurred by using a matched individual atlas with the error incurred by using a population-level neonatal atlas (such as that constructed by Brigadoi et al.) was not conducted. Given that the cortical surfaces in these population-level models are smooth, there is very little local variation in sulcal depth and curvature. Therefore, one cannot rely on these features to yield a meaningful mapping from an individual cortical surface exhibiting gyrification to that of a population-level atlas exhibiting gyrification to a much lesser degree. Such a registration would be prone to a high level of error which would be impossible to discern from the error incurred by using a population-level atlas itself. This lack of gyrification means that the use of surface registration techniques such as FreeSurfer and MSM may not be appropriate to quantify the error incurred by using a population-level atlas with respect to the use of a subject-specific model. The compatibility of the individual-level models in the database with these surface registration methods is a distinct advantage of the structural prior database as surface registrations can be used to meaningfully validate their application.

There exist cortical atlases, such as those constructed by Bozek et al. (used as a common space for analysis in this work), which make use of structural data at the population level and manage to preserve gyrification detail by averaging in the cortical surface space. However, to model the spatial distribution of a field within the head, a structural prior that represents a volume is required.

Macroanatomical labelling is of great benefit to functional neuroimaging methods as it allows an anatomical label to be associated with the location of cortical activation. The dHCP datasets used in this study include cortical parcellation maps that label 16 cortical regions per hemisphere plus the corpus callosum for each individual (Gousias et al., 2012; Makropoulos, Robinson, et al., 2018). These parcellation maps are also provided for each individual in the neonatal head model database in this work. Other neonatal

cortical surface parcellation atlases, such as those published by De Macedo Rodrigues et al. (2015) and Alexander et al. (2017), can be registered to each individual to expand the range of parcellations that can be used to label the anatomical location of functional activation. Such parcellation atlases will be instrumental in the application of these head models to the study of functional connectivity.

In this work, macroanatomical labelling of the positions of the cortical projections were not provided, which is a limitation of the work in this Chapter. Using a 12-month-old infant template, Tsuzuki et al. (2017) demonstrated that the 10/10 system (a lower density version of the 10/5 system) is sufficient to predict underlying macroanatomical cortical structures. Future work involving the database of structural priors described here could investigate whether such a consistent relationship is present in the neonatal population, using cortical projection and scalp projection protocols used by Tsuzuki et al., Kabdebon et al. (2014) and Matsui et al. (2014). This would aid the localisation of activation for modalities where data is analysed in channel-space, such as fNIRS and EEG.

4.4.3 Error incurred by using an individual-matched structural prior

This work describes the construction of a database of structural priors but it was also essential to quantify the error associated with an application of this database. For simplicity, an individual-matching approach using a leave-one-out analysis was chosen. At 41 weeks PMA, the localisation error associated with this application was approximately 10 mm or less across the majority of the motor cortex and the majority of the superior and middle temporal gyri bilaterally. The median localisation error across all 10/5 positions across all subjects was 8.1 mm. Assuming a circular spatial distribution of error, this suggests a geodesic point spread function of approximately 206 mm^2, with this extending to 437 mm^2 with an increase of one median absolute deviation

(3.7 mm) above the mean. For context, Bozek et al. (2018) report the average area of the posterior portion of the superior temporal gyrus to range from 1,175 mm^2 at 36 weeks PMA to 1,525 mm^2 at 44 weeks PMA. The frontal and temporal areas have been shown to be important in infant social development (Lloyd-Fox et al., 2010), and the analysis in this work provides evidence that using a matched brain from this database could potentially offer spatial precision at the gyral level in these areas.

There are three sources of error in atlas-guided DOT, as stated by Cooper et al. (2012), which were discussed in Section 1.3.3. The first is that there are **anatomical differences** between the matched model and the target subject. To reduce this error, future work will identify the external head features that are the best indicators of a match, which may include (but are not limited to) head circumference, head size, age, sex, and features derived from the cranial landmarks such as nasion-to-inion distance.

The second source of error is the **imperfect registration** of the matched model to the target's space. In this work, an affine registration was employed to spatially register the matched model to the target's space. In the adult, the error due to affine registration is estimated at 4-7 mm (Jurcak et al., 2007; A. K. Singh et al., 2005); an analogous assessment is needed in neonates. The simple analysis described in this chapter does not disentangle the affine registration error from the error introduced due to anatomical differences and, as such, future work will need to investigate factors that could affect these sources of error in combination. In practice, it will be difficult to acquire all 10/5 positions, so a further limitation of this work is the use of a more constrained (and likely more accurate) affine transformation than would be possible in a real-world application of this process.

The third source is the **error inherent to diffuse imaging**. The example application described and tested in this work was deliberately simple so as to

be generalisable across neuroimaging techniques, and so this work does not evaluate the error that image reconstruction itself will introduce.

4.4.4 Matched individual atlas or a population-level atlas?

What's the better option to represent infant anatomy in DOT studies when a subject-specific model isn't available: a population-level atlas or a matched individual atlas? A population-level atlas will never accurately represent a given *individual*, but such a model is designed such that it is an accurate representation of the average anatomy in a given population. An individual atlas will reflect anatomy – for instance, patterns of cortical folding – that is seen at the individual-level, but invariably it will never accurately represent a different *given* individual. Is it better to use an individual atlas, which we definitely know is inaccurate, or is it better to use a population-level atlas, which we know is (or, at least, should be) accurate for the population as a whole but is completely unrepresentative of anatomy at the individual-level?

Which of these categories of atlases are best to use in atlas-guided DOT is a question that is unanswered in the literature. A major reason why this has not already been addressed is that it is difficult (or potentially impossible) to reliably map from the smooth cortical surfaces of e.g. the Brigadoi et al. atlases to the highly-folded cortical surfaces at the individual-level. The inability to perform cortical registration prevents a like-for-like comparison of functional images, and renders it impossible to directly address the question of which atlas modelling approach is ultimately superior.

While this work also does not directly address this question, a key point is that the database of individual-level structural priors provided by this work can enable such questions to be answered. The database presented here can be used to produce population-level atlases at (e.g.) each week PMA (following the approach adopted by Brigadoi et al.), and having access to individual-level

data will enable a reliable registration approach between individual-level and population-level head models to be developed and validated. This has simply not been possible before.

Another consideration is whether the high level of detail found in individual-level head models will make a substantial difference to the modelling of light transport. This high-level of precision is necessary to best represent the effects of the CSF, whose median thickness varies on the scale of millimetres across the age-range in this database. But does such a high level of spatial precision really make a difference to forward modelling? Relatedly, does cortical folding make any tangible difference to light transport relative to a smooth cortical surface?

A further consideration is image interpretation. Images reconstructed in the space of a population-level atlas with a smooth cortical surface may be particularly difficult to interpret anatomically. This is a crucial point given the close relationship between brain anatomy and function. As such, reconstructing images using an individual atlas can aid the interpretation of images. The points outlined in this section therefore present a tension between the level of anatomical precision required to produce a forward model of diffuse light transport and the level of anatomical precision needed for image interpretation in reconstructed images.

4.4.5 Future work

The demonstration of a simple example application of how the individual-level head model database can be applied was not an attempt to demonstrate best practice. A best practice approach will involve external features of the head being used to find a match. These include the cranial landmarks positions and the 10/5 positions (and related scalp positions), which could feasibly be obtained at the infant cot-side using a three-dimensional magnetic digital position tracking system (Tsuzuki & Dan, 2014). In addition, modern photogrammetry methods enable a scalp surface mesh to be obtained with a

smartphone with reliable ease (Frijia et al., 2021). Such a photogrammetry-derived scalp surface could be used as (1) a simpler alternative to using a manual digitising system to collect positioning data to compute scalp positions, and (2) another way to quantify morphometry to find and to register a matching head model.

The database of structural priors presented in this work provides a novel opportunity for such ideas to be tested and validated. The next, and most critical, step was to determine which external features of the head allow the best possible matched model to be identified. In addition, an investigation was needed to determine the best way to register a matching head model using fewer scalp positions, such as the cranial landmarks and the 10/20 positions. In Chapter 5, multiple different methods will be tested to determine what is the best approach applying the individual-level head model database in the context of DOT.

4.5 Conclusion

Chapter 4 describes the construction of a database of multi-layered, individual-level models of the neonatal head for infants aged 29-44 weeks PMA, and demonstrates a simple application of this database. Given that no similar database exists for neonatal head anatomy at the individual-level, it is anticipated that this database will be of use across a range of neuroimaging, neuromonitoring and neurostimulation techniques, and particularly in DOT. In the Chapter 5, different applications of the database will be implemented to determine best practice to find a matching head model that minimises the localisation error.

Chapter 5

Optimising the selection of neonatal individual atlases for use in place of infant-specific structural priors

5.1 Introduction

The database of structural priors constructed in the previous chapter can be applied to a range of functional imaging modalities. The simple leave-one-out validation in the previous chapter provides an estimation of the localisation error that would be incurred using an individual atlas (i.e. a matched model) in place of a subject-specific head model, but it does not explicitly quantify the anatomical error between the target and matched model. Further, the simple analysis only investigates selecting a matched model based on head circumference, which is likely to be sub-optimal.

There are several characteristics of the infant and external features of the head that can be measured at the cotside with varying levels of difficulty. Some of these features are (shown in Figure 5.1):-

- **Head circumference**. This is routinely acquired from infants.
- **Gestational age**. This is a measure which is known for each neonatal infant and will be highly correlated to brain structure (Makropoulos et al., 2016) and to head size.
- **Cranial landmarks**, i.e. Nz, Iz, Ar, Al and Cz. These positions (in an arbitrary coordinate space) can be acquired using a three-dimensional digital positioning device or through photogrammetry methods.
- **10/20 positions**: These positions, 19 in total, can also be acquired using a digital positioning system. However, given the higher number of positions and the time required, this is more challenging than the obtaining just the cranial landmarks.
- **Scalp surface**. Modern photogrammetry methods can be used to extract a model of the scalp surface from photographs of a participant's head. In infants, this was recently demonstrated by Frijia et al. (Frijia et al., 2021). Such a surface model can also be used to obtain the cranial landmarks, 10/20 positions and another measurement of head circumference.

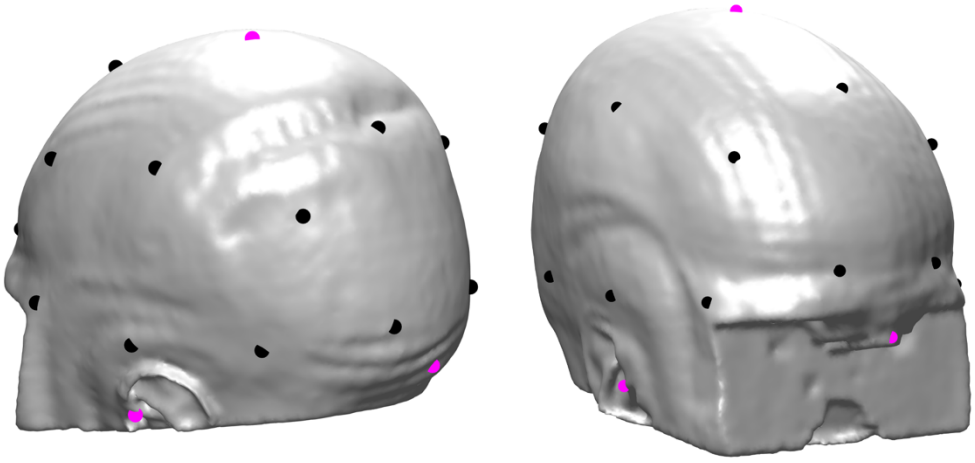

Figure 5.1: The 10/20 positions (black circles) and cranial landmarks positions (magenta circles) on the scalp surface of a neonatal infant. The 10/20 positions are a lower density derivative of the 10/5 positions.

Critically, each of these features can also be extracted from the head models in the database. In the case of the scalp surface, the scalp surface mesh from each model can be used to mimic a three-dimensional scalp surface extracted from photos of participants using photogrammetry methods.

Using these external features of this head, the work in this chapter aimed to determine:-

1. which **external feature** (or features) of the infant head, and
2. which **registration** method

minimise the anatomical-error incurred from using a matched-model in place of a subject-specific model. In addition, because the simple leave-one-out validation in Chapter 4 relies on cortical projection, it does not provide context on the error that would be incurred in DOT applications specifically. As such, a further aim of the work presented in this chapter was to conduct an optical analysis, employing simulated reconstructions, to investigate **how DOT image localisation error relates to methods of selecting a matched model**.

5.2 Methods

5.2.1 Anatomical validation

An extended leave-one-out analysis was undertaken to investigate the relationship between external features of the head and anatomical error when using a matched head model in place of a subject-specific model.

All 214 head models from the database were included in this analysis. Each individual in the database was used in turn as the target. The head models from all individuals aged within 2 weeks PMA and with a head circumference within 4 cm of the target were chosen as *potential matches*. The range of these parameters provided a wide range of potential matches for each target. Ideally, an analysis would have been implemented where every model in the database is used as a potential match, however this would have been time consuming and computationally burdensome.

5.2.1.1 Computing external feature offset

From each individual in the database, external features were extracted from the head models. Each of these features could be obtained in a clinical setting with various degrees of difficulty. The offset in each external feature between the target and each potential match was then calculated. *Head circumference offset* was calculated as the difference between the target and potential match head circumferences, while *age offset* was defined as the difference between the target and potential match post-menstrual ages (in days).

As stated in Section 4.2.5, mesh nodes were then transformed to a coordinate system where:

- the position of Iz defines the origin
- a line joining Iz to Nz defines the y-axis
- the z-coordinates of Ar and Al are approximately equal following rotation of mesh nodes around the y-axis.

The head models therefore all exist in an equivalent space based on their cranial landmarks positions. *Landmarks offset* was calculated as the mean of the Euclidean distances between equivalent cranial landmarks positions, while *10/20 offset* was calculated as the mean of the Euclidean distances between equivalent 10/20 positions. *Scalp offset* was defined as the mean surface distance between the target and match scalp surfaces above the plane where the pre-auricular points are situated. These three measures of offset, as well as head circumference offset, were measured *before* potential matches were spatially registered to the space of the target.

5.2.1.2 Registration to target model

For each target, each potential match was registered using several different methods. In this work, two registration methods were used, based on affine registration:-

1. **Landmarks-affine** registration, where the cranial landmarks positions alone were used to compute the transformation.
2. **10/20-affine** registration, where the 10/20 positions were used to compute the transformation.

Coherent point drift (CPD) affine registration was also used, which will be referred to simply as CPD. In simple terms, CPD is a registration method that computes a registration to align two sets of points. CPD computes the registration by solving a probability density estimation problem, fitting the centroids of a Gaussian Mixture Model (which represent the set of points to be registered) to a set of target data points (Myronenko & Song, 2010). In this work, three other registration methods were used, based on CPD registration:-

3. **Landmarks-CPD** registration, where the cranial landmarks positions alone were used to compute the transformation.
4. **10/20-CPD** registration, where the 10/20 positions were used to compute the transformation.

5. **Surface-CPD** registration, where the full scalp surfaces were used to compute the transformation. Here, both the target and potential match scalp surfaces are downsampled using a 3D box grid filter, reducing the number of surface nodes to ease the computational burden.

In total, there were therefore five registration methods. Following registration to the target space for each method, the anatomical error between each potential match and target was computed. Two metrics were chosen to quantify the anatomical error: *scalp error* and *cortical error*.

5.2.1.3 Quantifying anatomical offset: scalp error

The *scalp error* is a measure of how well the head shape of a registered potential match conforms to the head shape of the target. To quantify the scalp error, the mean offset between the 10/5 positions of the potential match and the target was computed *after registration*. Using the 10/5 positions enabled equivalent scalp positions to be compared between target and registered potential match. In DOT and fNIRS, optical arrays are placed in reference to equivalent positions on the scalp across individuals, and so establishing how well these points correspond between registered potential match and target will indicate how well scalp array placement can be replicated using a matched model.

5.2.1.4 Quantifying anatomical offset: cortical error

The *cortical error* is a measure of how well the cortical surface of a registered potential match conforms to the cortical surface of the target. To quantify the cortical error, the mean surface distance was computed between each equivalent cortical label as defined by the parcellation atlas in Gousias et al. (Gousias et al., 2012), shown in Figure 5.2. A mean of the mean surface distance values across cortical labels was used to define the cortical error.

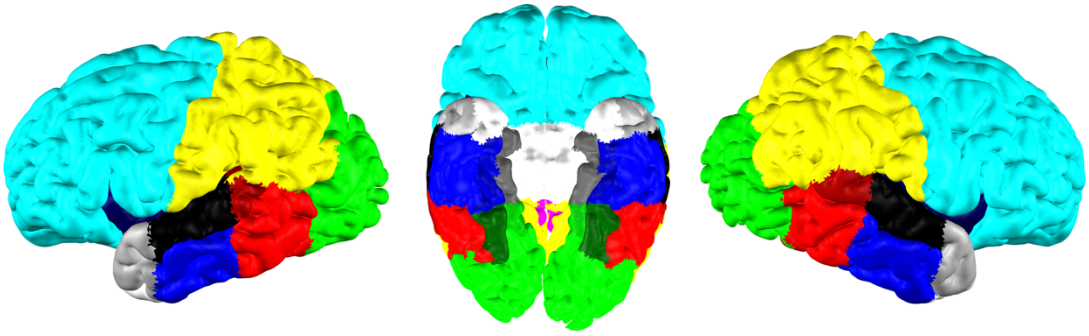

Figure 5.2: The parcellation atlas, published by Gousias et al., registered to the space of a neonatal infant.

5.2.1.5 Matching methods

For each of the five external features, the potential match which had the lowest offset relative to each target was chosen. This was completed for each target individual (i.e. all 214 individuals from the database). There were, therefore, five matching methods in total:-

1. Age-matching
2. Head circumference-matching
3. 10/20-matching
4. Landmarks-matching
5. Scalp-matching.

Further, for each target and registration method, an *optimal match* could also be found. This is the match that has either the lowest scalp error (the *scalp optimal match*) or the lowest cortical error (the *cortical optimal match*) as determined by a direct search. The optimal match for each target is the theoretical best possible match that can be found from the database in terms of the anatomical error metrics used in this work.

5.2.2 Optical validation

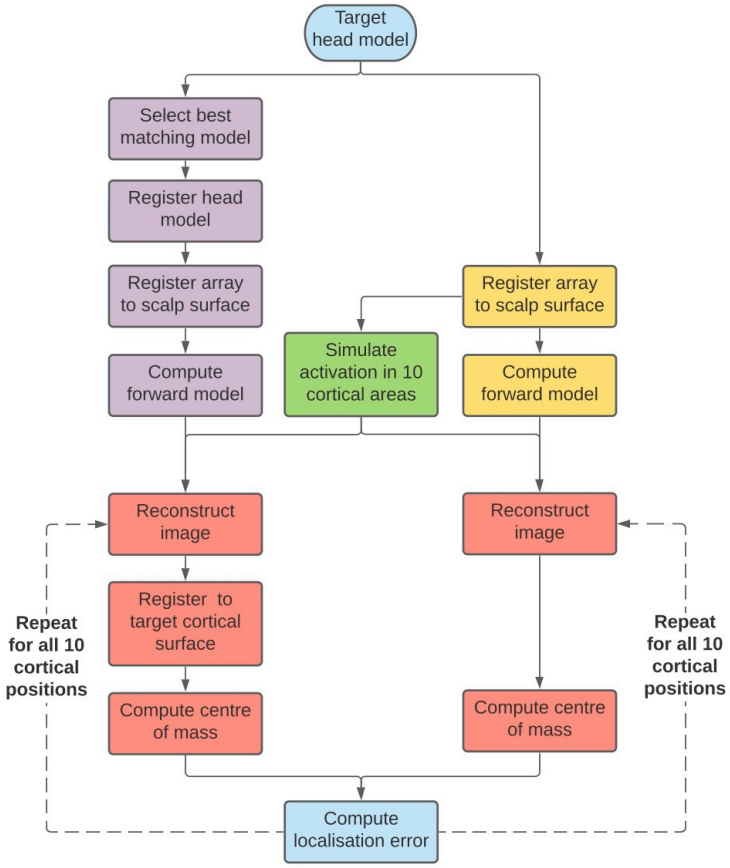

Figure 5.3: A flow diagram outlining the process for the optical analysis for each match selecting method.

The aim of the optical validation was to quantify the localisation error incurred by using a matched model in place of a subject-specific model. Forty-four head models were arbitrarily chosen from infants across the age-range of the database at ages 32 weeks PMA (N = 2), 34 weeks PMA (N = 8), 36 weeks PMA (N = 9), 38 weeks PMA (N = 7), 40 weeks PMA (N = 7), 42 weeks PMA (N = 7) and 44 weeks PMA (N = 4). An outline of the optical analysis is shown in Figure 5.3.

For each target, a matched model was found using four matching methods: 10/20-matching, head circumference-matching, scalp optimal matching and cortical optimal matching. 10/20-affine registration was used to register the

matched models. The analysis pipeline in Figure 5.3 was completed four times for each target, once for each of the four matching methods.

Ideally, a leave-one-out analysis would have been conducted involving all the models in the database, but this would have been hugely time-consuming given the time taken to calculate the synthetic changes in optical density measurements for each simulated activation.

5.2.2.1 Array registration

A simulated optical array comprised of 12 hexagonal modules, consisting of 36 sources and 42 detectors, was registered to the scalp surface of each head model.

This array layout is based on based on the Gowerlabs LUMO system (Vidal-Rosas et al., 2020, see https://www.gowerlabs.co.uk/lumo). The LUMO system, as well as the recent hardware advances based on this system and its applications to infants (Zhao et al., 2021), represents the cutting edge of the cortical sensitivity coverage that can be achieved in infants, which is why this array layout was chosen in this work.

Figure 5.4 displays scalp positions and curves along the scalp that were used to register the array to the scalp surface of each head model. First, a curve from T7 to T8 via Cz was defined. The first two module centre positions (M1 and M2) were placed 36 mm either side of Cz along the curve.

Two further curves were then defined, one from Fpz to Oz via M1 on the left and another from Fpz to Oz via M2 on the right. On each of these curves, one module centre position (M3 on the left and M4 on the right) was defined as 36 mm anterior from the middle of the curve, and another module centre position (M5 on the left and M6 on the right) was defined as 36 mm posterior from the middle of the curve. On each hemisphere, a point was defined 72 mm from Cz along the T7-Cz-T8 curve (J1 on the left and J2 on the right), and

used to define another curve from Fpz to Oz. Two module centre positions (M7 and M8) were defined 18 mm anterior to the middle of these curves, and another two module centres (M9 and M10) were defined as 18 mm posterior of the middle of these curves. In the midline, one module centre (M11) was defined as 18 mm anterior from Cz along the Fpz-Cz-Oz curve, while another module centre (M12) was defined as 18 mm posterior from Cz along the Fpz-Cz-Oz curve. The source and detector positions in each module were centred around the module centres (M1-M12) and were rotated such that the plane of the module was parallel to a plane tangential to the scalp surface at the module centre. The final source and detector positions were assigned the nearest surface mesh nodes to the original source and detector positions post-rotation.

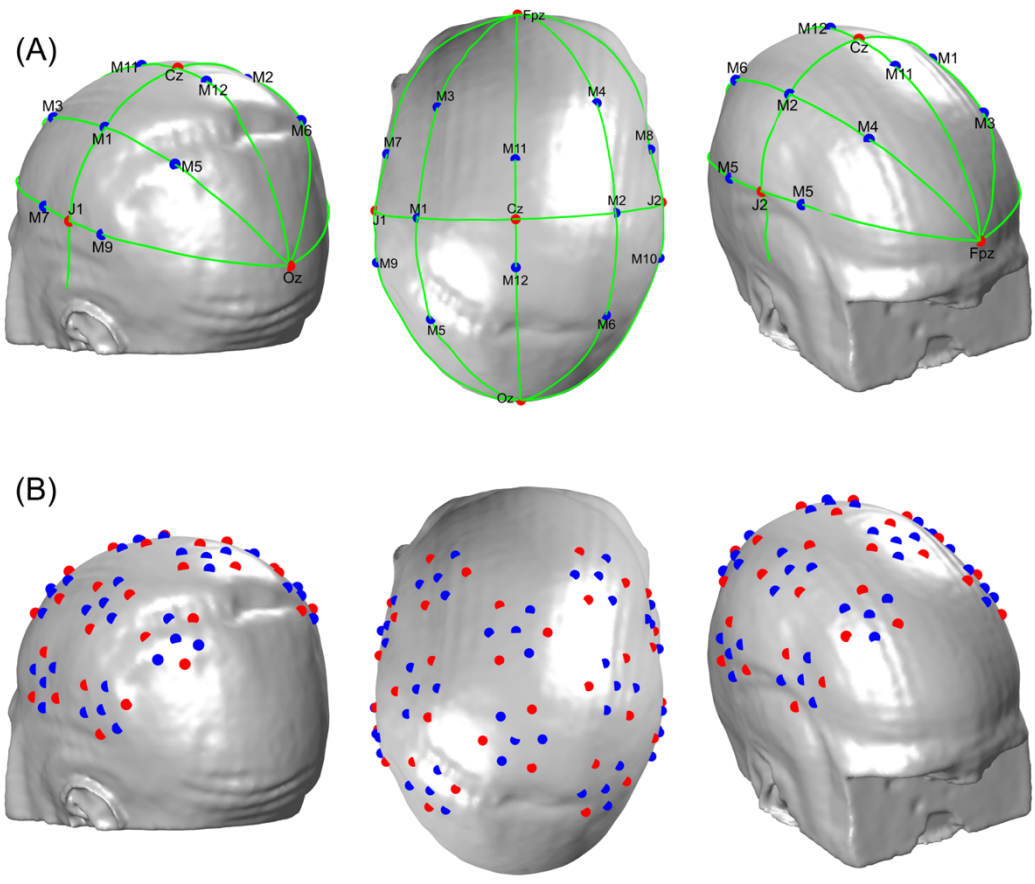

Figure 5.4: (A): Curves (in green) and scalp positions for array registration. Positions M1 to M12 (blue circles) mark the centre positions of the hexagonal modules. Red circles represent other scalp positions to define curves as described in Section 5.2.2.1. (B): 12 hexagonal modules registered to the scalp surface, consisting of 36 sources (red circles) and 42 detectors (blue circles).

5.2.2.2 Simulated absorption changes

For each of the four matched models, the centre of each non-midline hexagonal array was projected to the cortical surface, yielding a total of 10 cortical positions. At each of these 10 positions, perturbations in absorption coefficient at 850 nm with radius 10 mm were simulated on the cortical surface and the optical density changes that would result from the simulated change in absorption were calculated for each channel; this process was completed using Toast++ (Schweiger & Arridge, 2014).

Light propagation was modelled using Toast++ to produce a forward model for each of the four matched models and the target model. Using a regularization hyperparameter of 0.1, a zeroth-order Tikhonov regularized reconstruction was performed. As the absorption changes were simulated on the cortical surface, the image reconstruction was constrained to the grey matter nodes of the volume mesh, as was done in the image reconstruction procedure in Section 3.2.9.

To compute the localisation error for each reconstruction, each reconstructed image was registered to the space of the target cortical surface using Multi-modal Surface Matching based on mean curvature features of the cortical surface (Robinson et al., 2014, 2018). The centre of mass of the registered image was determined by computing a weighted-average of node positions in the grey matter surface mesh using the reconstructed absorption change values as weights for each node. For each simulated perturbation, the localisation error was defined as the Euclidean distance between the true absorption change centre of mass and the reconstructed absorption change image centre of mass.

5.3 Results

5.3.1 Anatomical error and external feature offset

Using data from each target's potential matches, Figure 5.5 presents the scalp and cortical errors as a function of offset in the 5 external features: age offset, head circumference offset, 10/20 offset, landmarks offset and scalp offset.

5.3.1.1 Anatomical error as a function of mismatch in external features

For all registration methods, the scalp and cortical errors do not vary significantly as a function of age offset (Figure 5.5A(i) and B(i)). Scalp and cortical error also do not vary significantly as a function of head circumference offset (Figure 5.5A(ii) and B(ii)).

There is a much clearer relationship between anatomical error and 10/20 offset (Figure 5.5A(iii) and B(iii)), landmarks offset (Figure 5.5A(iv) and B(iv)), and scalp offset (Figure 5.5A(v) and B(v)). Across registration methods, anatomical error decreases as the offset in these external features decreases. Offset in age and head circumference have a very weak (or non-existent) relationship with anatomical error and will be excluded from subsequent analyses on finding a best matching individual. As such, only 10/20-matching, landmarks-matching, and scalp-matching will be investigated in subsequent matching analyses.

5.3.1.2 Comparing registration methods

Across different external features, 10/20-affine and 10/20-CPD incur a similar level of anatomical error (see Figure 5.5). These registration methods also minimise the scalp error, while surface-CPD registration minimises the cortical error. Landmarks-CPD and landmarks-affine appear to perform similarly in terms of anatomical error, and consistently yield the highest levels of both scalp and cortical error (see Figure 5.5). To reduce the computational burden arising from CPD registration and to reduce redundancy, the subsequent

analyses will not focus on registering with CPD except for surface-CPD registration. As such, only 10/20-affine registration, surface-CPD registration and landmarks-affine registration will be investigated in the subsequent matching analyses.

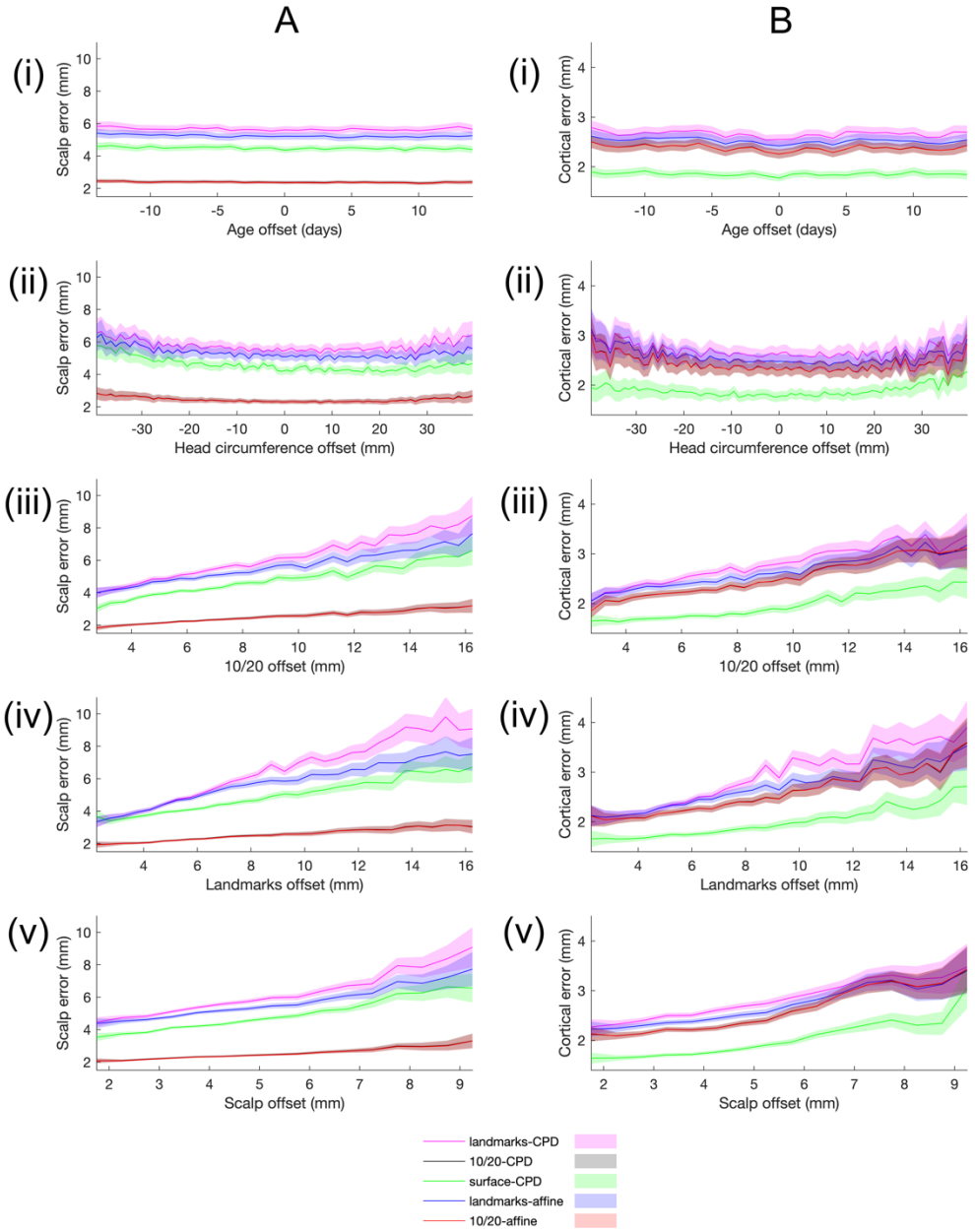

Figure 5.5: Scalp error (column A) and cortical error (column B) across potential matches for each target individual as a function of offset in age (i), head circumference (ii), landmarks (ii), 10/20 positions (iv) and scalp (v). The solid line plots the mean error, while the shaded error plots the standard error of the mean. Bin width 1 day for age offset, 2 mm for head circumference offset and 0.5 mm for 10/20, landmarks and scalp offsets. Data displayed for bins containing at least 50 potential matches.

5.3.2 Matched models and anatomical error

For each target, a match was found using each of the three matching methods. Figure 5.6 plots the scalp and cortical error for the models found using each of the three matching methods based on external features.

5.3.2.1 External feature matching methods

The 10/20-matching method results in a lower scalp error for 10/20-affine and surface-CPD registrations. This is demonstrated in Figure 5.6a where the cumulative distribution curves for these matching methods (represented by the red and green solid lines) are shifted to the left of the curves for the other matching methods. Figure 5.6c shows that this decrease in scalp error by using 10/20-matching is statistically significant compared to landmarks- and scalp-matching.

Landmarks-matching performed best to find a match when landmarks-affine registration was used. This is demonstrated by the blue dashed line being to the left of the other blue cumulative distribution curves in Figure 5.5a. This difference was statistically significant compared to 10/20- and scalp-matching, as shown in Figure 5.6c.

In terms of cortical error, 10/20-matching lead to the lowest mean cortical error for each registration method (see Figure 5.6d). This decrease was statistically significant relative to the two other matching methods when using 10/20-affine registration. For surface-CPD, the decrease was only statistically significant compared to landmarks matching. No matching method led to a statistically significant decrease in cortical error when using landmarks-affine registration.

However, all three matching methods lead to similar levels of cortical error when a given registration method is used, as can be seen in Figure 5.6b. The results for the best matching method for each registration technique are summarised in Table 5.1.

5.3.2.2 Registration methods

Figure 5.7 plots data from Figure 5.6 for the matching method that minimises the scalp error for each registration method. For scalp error, 10/20-affine performs best ($p < 0.0001$ vs surface-CPD); for cortical error, surface-CPD registration performs best ($p < 0.0001$ vs 10/20-affine).

5.3.2.3 Comparing external feature matching with optimal matching

Two optimal matched models, as described in Section 5.2.1.5, can be found for each target individual based directly on its scalp and cortical errors. For each registration method, Figure 5.8 plots the anatomical errors for the scalp optimal match and the cortical optimal match.

In Figure 5.8a-f, the cumulative distribution curves plotting the anatomical error of these optimal matches are substantially shifted to the left relative to the corresponding curves for external matching methods (with the exception of Figure 5.8c). This indicates that, in most cases, there exists a model in the database that is better at reducing the anatomical error than those identified by the external feature match-selecting methods that have been investigated.

The 10/20-affine registration method coupled with optimal matching is best to minimise the scalp error (see Figure 5.8g), though 10/20-affine with 10/20-matching performs similarly to optimal matching (see Figure 5.8c). The surface-CPD registration method coupled with optimal matching is best to minimise the cortical error (see Figure 5.8h).

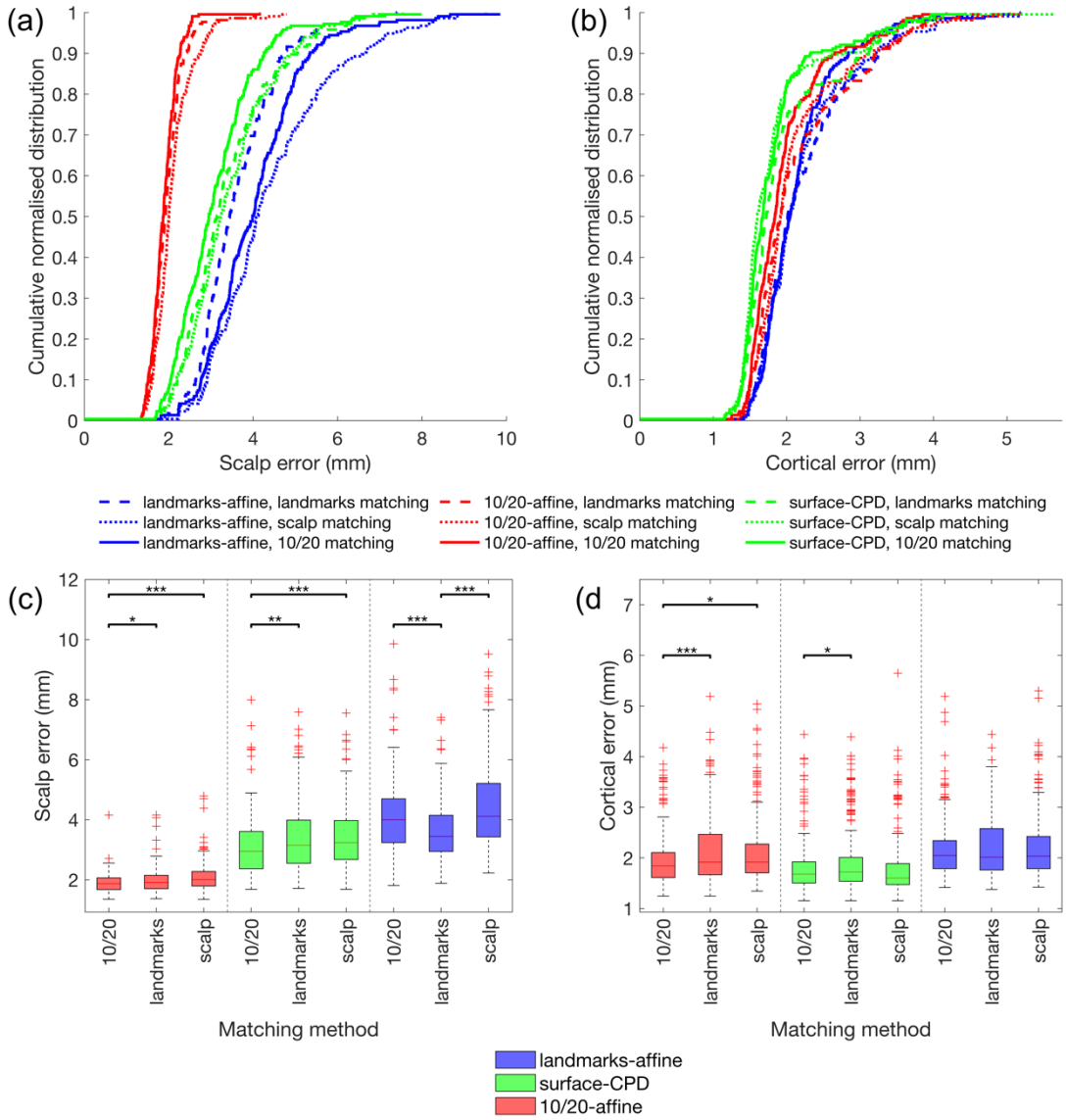

Figure 5.6: Cumulative distribution functions for scalp error (a) and cortical error (b) for each registration and match selecting method (see legend). Box-and-whisker plots for the distribution of scalp error (c) and cortical error (d) for each registration and match selecting method (see legend). * represents $p < 0.05$ (corrected), ** represents $p < 0.01$ (corrected), *** represents $p < 0.001$ (corrected).

Table 5.1: Summary of the matching methods which result in the lowest scalp error and cortical error for each registration method.

Registration methods	**Matching method to minimise scalp error**	**Matching method to minimise cortical error**
Landmarks-affine	Landmarks-matching	10/20-matching
10/20-affine	10/20-matching	10/20-matching
Surface-CPD	10/20-matching	10/20-matching

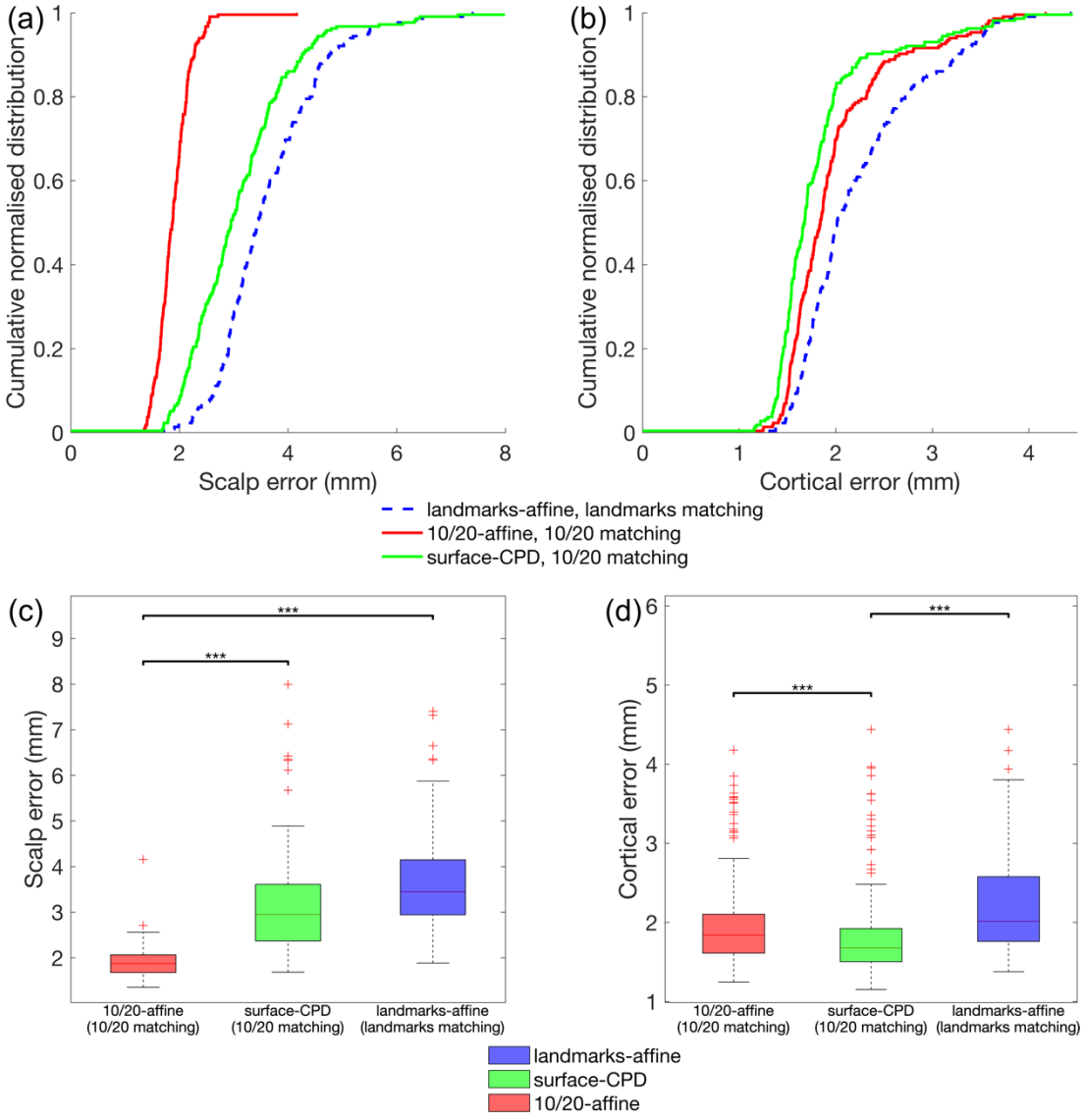

Figure 5.7: Cumulative distribution functions for scalp error (a) and cortical error (b) for each registration method for the match selecting method that results in the lowest level of scalp error (see legend). Box-and-whisker plots for the distribution of scalp error (c) and cortical error (d) for each registration method for the match selecting method that results in the lowest level of scalp error (see legend). * represents $p < 0.05$ (corrected), ** represents $p < 0.01$ (corrected), *** represents $p < 0.001$ (corrected).

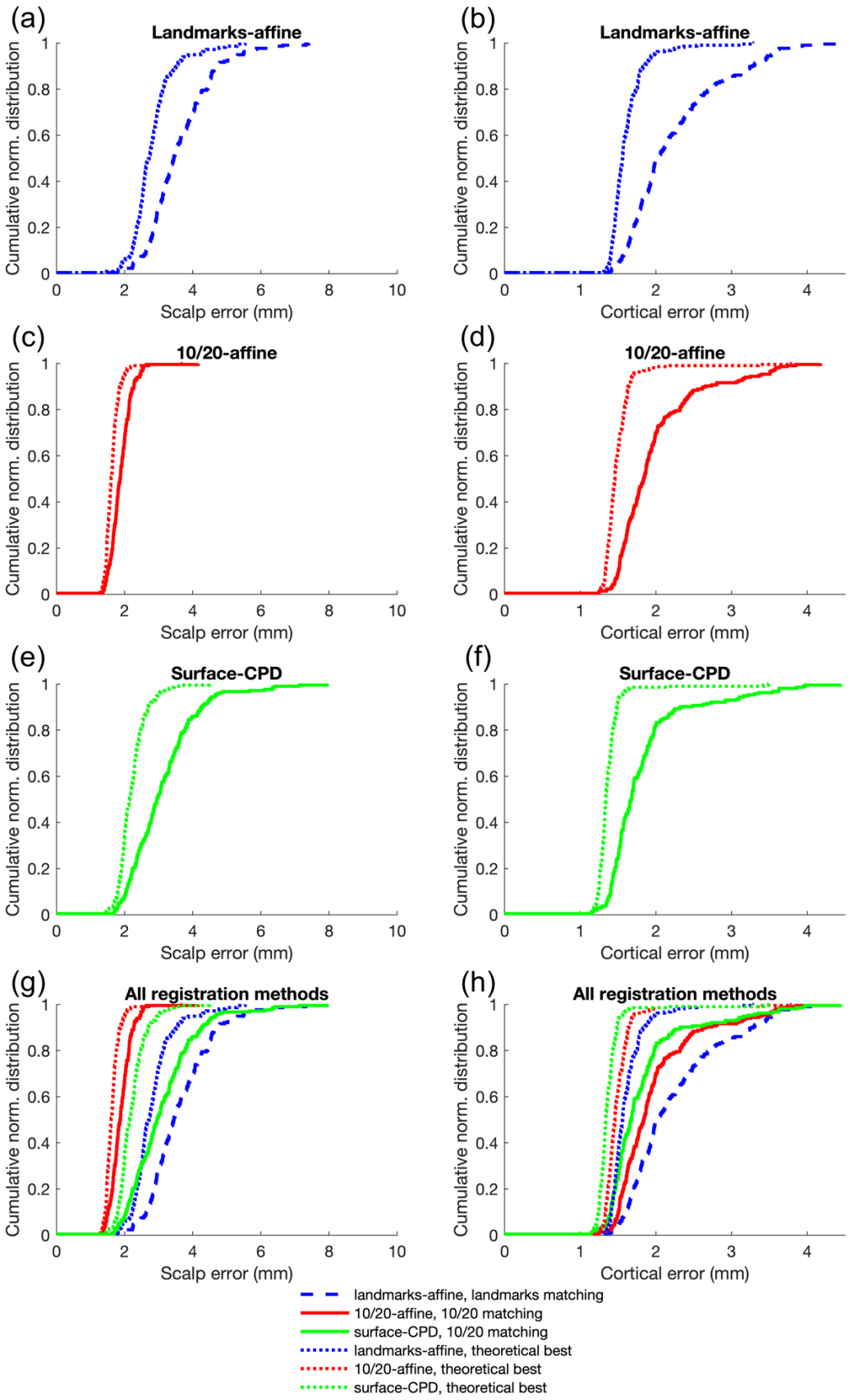

Figure 5.8: Cumulative distribution functions for scalp error (left) and cortical error (right) for each registration method compared to the optimal match selection methods.

5.3.3 Optical validation

Figure 5.9 shows the results from the optical validation. The localisation error was of course at its lowest value when using the target model (i.e. a subject-specific model). Using the head model found with 10/20-matching reduces the localisation error relative to head circumference-matching ($p = 0.0341$, $T = -2.1259$, mean difference = -0.4541 mm). The cortical optimal matching method leads to a decreased localisation error relative to 10/20-matching ($p = 0.0030$, $T = -2.9838$, mean difference = -0.6058 mm). The scalp optimal matching method also leads to a decreased localisation error relative to 10/20-matching, however this difference is not statistically significant ($p = 0.1274$, $T = -1.5274$, mean difference = -0.3160 mm).

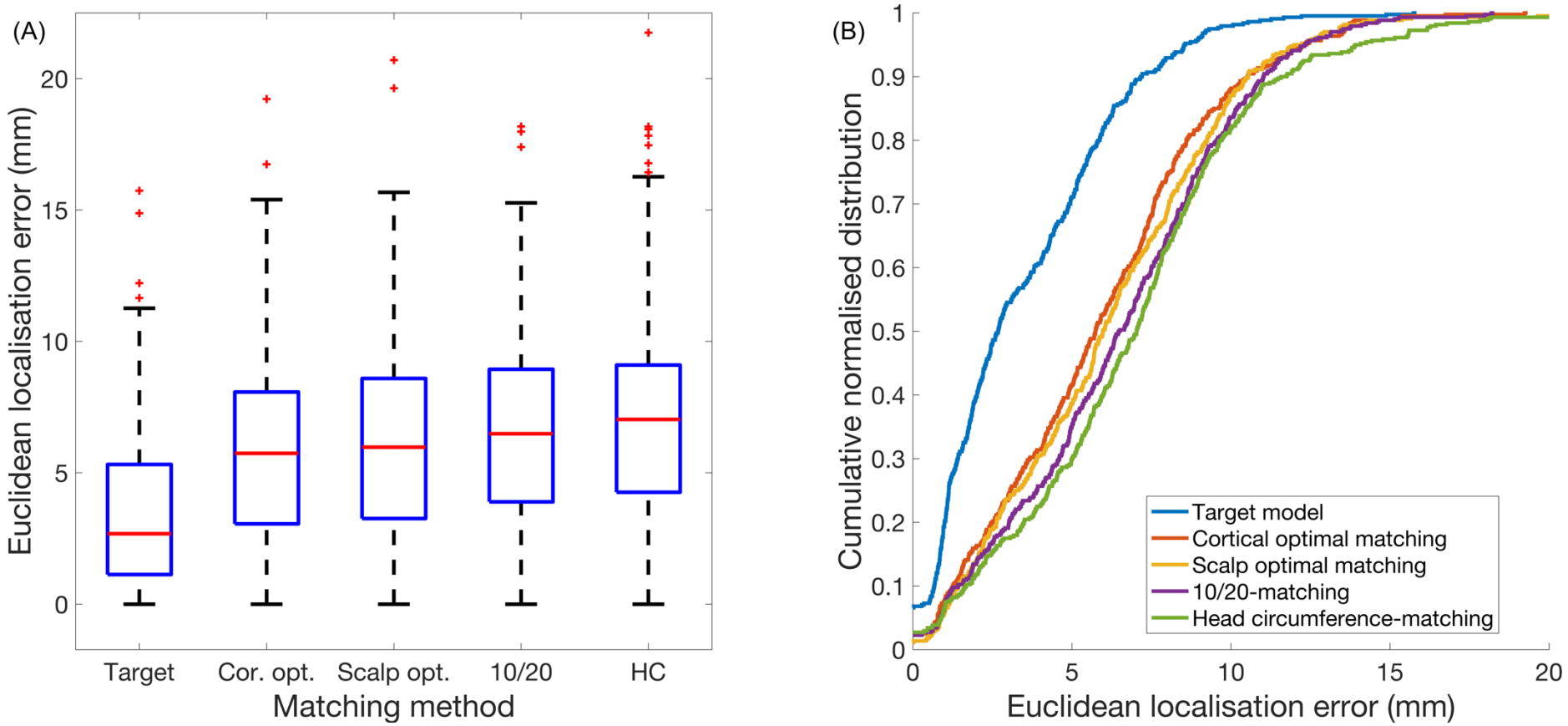

Figure 5.9: Distribution of the localisation error resulting from head models selected using different matching methods. The distributions are displayed as box-and-whisker plots in (A) and as cumulative distribution functions in (B).

5.4 Discussion

In Chapter 4, the construction of a database of structural priors was detailed. This current chapter has investigated how to implement the database in a way that minimises the anatomical error and, ultimately, improves the localisation accuracy in DOT. Given the difficulty and impracticality of collecting subject-specific MRI, this work is important to optimise atlas-selecting methods to improve confidence in the spatial localisation of activation.

5.4.1 Anatomical validation

5.4.1.1 External features and matching methods

The work in this chapter has investigated which matched model selection method and which registration method minimise the anatomical error incurred by using an individual atlas in lieu of a subject-specific model. The external features explored in this work were selected as they can be feasibly acquired at the cotside, and so this study aimed to mimic a real-world scenario where these data are available.

Figure 5.5 shows that anatomical error (both cortical and scalp) does not vary significantly as a function of mismatch in either head circumference or PMA, suggesting that an overall measure of head size such as head circumference or age is a poor indication of the appropriateness of a model. There is a high correlation between age and head circumference of head models in the database ($R = 0.86$, $p < 0.0001$), so it is not surprising that they have similar trends. However, it was anticipated that there would be a clearer finding given that there are many neonatal brain atlases which are grouped by gestational age. The analysis in Figure 5.5 showed that potential matches with reduced offsets in cranial landmarks, 10/20 positions and scalp resulted in the lowest levels of anatomical error. The fact that offset in these external features had a stronger relationship with anatomical error suggests that data on the shape of the head is more predictive of finding a matching model to reduce anatomical error than broad measures such as circumference and age.

Across all registration methods, scalp matching is the worst performing matching method. The scalp error metric was calculated based on the post-registration 10/5 positions offset. The 10/20 positions are a lower density version of the 10/5 positions; while this may help to explain the decreased scalp error, one must consider that the 10/20 positions include fewer than 8% of the 10/5 positions used in this work. The results in this chapter suggest that such a high density of scalp positions to find a match may risk over-fitting the data to find a matched model that is not as faithful to the overall shape of the head.

No matching method was conclusively found that minimised the cortical error for surface-CPD or landmarks-affine registration (see Figure 5.6d). This likely relates to the complex shape of the cortex and that the shape of the cortical surface is less likely than the scalp surface shape to be related to external positions on the head.

5.4.1.2 Registration methods

In Figure 5.6, 10/20-affine registration resulted in a lower scalp error. The greater number of points used in the 10/20-affine registration constrains the registration problem and helps to explain the improvement in scalp error with regards to landmarks-affine registration. Similar to scalp-matching, using the alignment of the scalp surfaces potentially risks not preserving the overall shape of the scalp which leads to an increased scalp error.

Surface-CPD registration minimised the cortical error. This reveals that computing the registration by aligning the high-density scalp information as closely as possible best aligns the cortical surfaces, suggesting a broad relationship between scalp shape and cortical surface shape.

Landmarks-affine is the worst performing registration method for both scalp and cortical error. The results in this work therefore suggest that, in practice,

it is best not to use the cranial landmarks for matched model registration if data with a higher number of scalp positions are available.

This work does not include an investigation of non-linear registration methods to register a matched head model to the dimensions of the target. Non-linear registration methods are known to improve fitting in regions of the scalp where higher levels of curvature are present, for example in occipital regions (Ferradal et al., 2014). The database of neonatal head models can be applied in future to investigate whether non-linear registration methods improve the cortical error as well as the optical localisation error. Non-linear registration will likely decrease the scalp error, which leads to a decrease (though not statistically significant in this study) in the optical localisation error as seen in Figure 5.9. However, this improvement may not be global, for instance areas of the cortex underlying scalp regions with lower levels of curvature may not benefit to the same extent as occipital regions. It would be interesting to see which regions of the cortex may benefit from non-linear registration, which could be used to inform whether a linear or non-linear registration method is best when reconstructing data sampled from a particular cortical region.

5.4.1.3 Photogrammetry methods

A significant limitation to using the 10/20 positions is that, typically, these data need to be obtained using a digital positioning device, which is not practicable in the context of infant data collection. Cranial landmarks are a more feasible alternative that many studies use to spatially register head models, but the results in this chapter show that this will result in a worse scalp and cortical error.

However, given the recent rise of photogrammetry methods, a simple smartphone scan can obtain a scalp surface from which the cranial landmarks positions can be determined, and then used to calculate the 10/20 positions. Photogrammetry can therefore overcome a huge methodological roadblock to enable a greater level of detail from the scalp surface to be obtained. Such

photogrammetry methods will need to be validated in terms of depth-perception accuracy to enable a scalp surface to be recovered that is faithful to the participant. The characteristics of the extracted surface itself also need to be investigated as it needs to be realistic to enable reliable 10/20 positions to be determined.

5.4.1.4 Optimal matching methods

The optimal matching methods revealed that there often exists a model in the database that is better at minimising anatomical error than any matching method based on external features. For 10/20-affine registration, 10/20-matching appeared to incur a very similar level of scalp error to the scalp optimal match. However, for the other registration methods, there is a large discrepancy in the scalp error between the optimal match and the best performing matching methods based on external characteristics.

To minimise the cortical error, surface-CPD using 10/20-matching was the best performing registration-match combination based on external features (see Figure 5.8), however this was outperformed by the cortical optimal match for landmarks-affine i.e. the worst performing registration method with optimal matching. This discrepancy in cortical error between match selection methods based on external features and optimal match selection suggests that, to reduce the anatomical error, future work should focus on improving match selecting methods rather than registration methods. A matched model can only be selected based on characteristics of the head available at the cotside, and further external head characteristics could be investigated in addition to those used in this work.

5.4.2 Optical validation

To be relevant to a range of functional imaging modalities that require structural priors, the anatomical error incurred by using a matched model in place of a subject-specific model was investigated in this work. For DOT-specific applications, the accuracy of the scalp and cortical surfaces are

important for optode placement and image interpretation respectively. From the optical analysis, the mean difference between using 10/20-matching and head circumference matching is far less substantial than the anatomical error would suggest. However, the difference in the localisation error distribution resulting from using head circumference-matching and 10/20-matching shows that there is a small but clear improvement in using the 10/20-matching method.

5.4.2.1 Limitations

Only 10 positions on the cortical surface were used to simulate activation, and a better approach would have been to simulate at many more locations across the cortical surface. In this work, computation time was the main limitation (completing the simulations, forward modelling, reconstructions and registrations took approximately 4 hours in total for each target model included in the analysis) and so a less comprehensive validation was devised & implemented. It would be interesting to see how the localisation error changes as a function of position on the cortical surface.

Further, activation was simulated directly under the centre of the module, which was directly beneath a detector. This approach likely overestimates the localisation error as, in each case, the activation is occurring at the point of minimum sensitivity for several channels.

An issue with any evaluation of localisation error is that it will be dependent on the array used. There is no standardised or universally accepted array position for DOT and so that will limit the applicability of any localisation error study in DOT. Nonetheless this work is still useful as it incorporates models of photon migration using realistic representations of neonatal anatomy.

5.4.2.2 Future work

The localisation error can be used as an indication of whether interpretations may differ in images reconstructed using models chosen through different

match selecting methods. However, this difference in interpretation of activation location is not explicitly investigated in terms of cortical regions.

The simulated activation study in this work could be repeated where the cortical label of activation in the ground truth and reconstructed images can be compared. This would be a better indication of the anatomical correspondence of where activation is being localised using target and matched models. This approach is possible, though the cortical parcellation used in this work had very large areas for certain cortical parcels, such as a single label for the entire frontal lobe. Other parcellation atlases exist that are much more granular, such as the M-CRIB (Melbourne Children's Regional Infant Brain) atlas published by Alexander et al 2017 (Alexander et al., 2017) based on the Desikan-Killiany atlas (Desikan et al., 2006), shown in Figure 5.10.

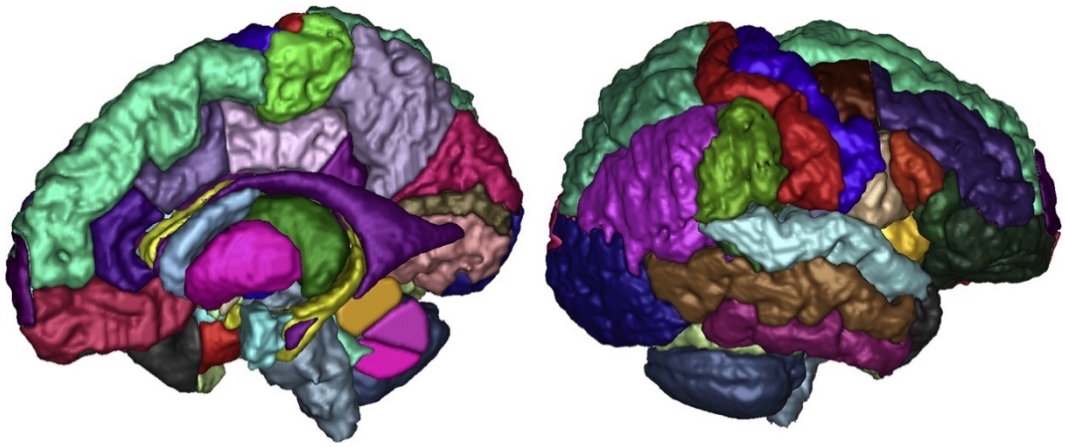

Figure 5.10: The M-CRIB atlas, consisting of 33 cortical regions per hemisphere, is based on the Desikan-Killiany atlas. Figure adapted from Alexander et al. (2017). Figure reprinted with permission from Elsevier[14].

These more granular atlases were not used in this work as the registration process is computationally burdensome and time consuming; nonetheless, such an analysis can potentially be achieved. This may show that the main

[14] Reprinted from *NeuroImage, 147,* Alexander, B., Murray, A. L., Loh, W. Y., Matthews, L. G., Adamson, C., Beare, R., Chen, J., Kelly, C. E., Rees, S., Warfield, S. K., Anderson, P. J., Doyle, L. W., Spittle, A. J., Cheong, J. L. Y., Seal, M. L., & Thompson, D. K., A new neonatal cortical and subcortical brain atlas: the Melbourne Children's Regional Infant Brain (M-CRIB) atlas, 841–851, Copyright (2017), with permission from Elsevier.

benefit of structural priors is in the anatomical interpretation of images rather than improving the accuracy of photon propagation models. This is particularly important when considering that the complexity of the cortical surface matures rapidly with PMA (Makropoulos et al., 2016).

5.5 Conclusion

This study investigated methods to optimise the implementation of the neonatal structural prior database produced in the previous chapter. Selecting a matched model based on the offset of the 10/20 positions often resulted in the lowest levels of anatomical error for any matching method based on external features of the head. Surface-CPD registration led to the lowest level of cortical error, while 10/20-affine registration resulted in a reduced scalp error. Selecting a matched model based on external head features resulted in a notable increase in anatomical error relative to the optimal matched models to minimise scalp and cortical error. In the optical validation, there was a small but clear reduction in localisation error using 10/20-matching relative to head circumference-matching. Future work should employ parcellation atlases of the cortex to investigate the effect of head model selection on the cortical label of activation.

Chapter 6

Future work and further scientific gains

This thesis has demonstrated methods to improve diffuse optical imaging in infants aged from pre-term to 24-months of age. The work in previous chapters has mainly focussed on the production and application of structural priors, which have been used to evaluate the effects of variation in array position and head size on fNIRS analyses, and to evaluate the error incurred by using an atlas in place of a subject-specific model.

This final chapter will consider other research directions based on the outcomes of the work presented in this thesis. The first section of Chapter 6 concerns future directions to improve the capabilities of DOT to enable the widespread application of high-quality brain imaging in infants. The final section of this chapter will review further scientific gains resulting from the work described in this thesis.

6.1 Future work

6.1.1 Recent advances in DOT hardware

Let us first consider recent advances in wearable DOT hardware. Frijia et al. (2021) demonstrated the use of a wearable DOT device in infants in the first year of life (see Figure 6.1), using the LUMO device from Gowerlabs (https://www.gowerlabs.co.uk/lumo). Based on LUMO, Zhao et al. (2021) developed flexible modules embedded with sources and detectors that can conform to the curved shape of the infant head, known as the ANIMATE array (see Figure 6.2). Another advance in wearable hardware is the “Flow” device from Kernel (https://www.kernel.com/flow). By using a high-density arrangement of sources and detectors placed on the scalp, these hardware advances have the capability of sampling the near-entirety of the cortex.

Figure 6.1: The wearable Gowerlabs LUMO device, used by Frijia et al. to study responses in the infant brain. Figure adapted from Frijia et al. (2021), licensed under CC BY 4.0.

Figure 6.2: The ANIMATE system, developed by Zhao et al., whose hexagonal modules can conform to the shape of the infant head. Figure adapted from Zhao et al. (2021), licensed under CC BY 4.0.

6.1.2 Whole-cortex network analyses

Developing DOT imaging methodologies that incorporate activation measures from across the brain could provide a robust tool to study the emergence of atypical brain development in certain neurological conditions. In addition, given the motion tolerant and silent nature of DOT, such methodologies would enable more widespread application of high-quality brain imaging as a tool to predict which infants are at risk of developing neurological conditions, enabling earlier therapeutic intervention.

There is potential, therefore, to develop methodologies to enable extensive functional networks to be studied in naturalistic environments, harnessing recent advances in DOT hardware and whole-cortex imaging. Functional connectivity has been demonstrated in the past in infants using high-density DOT (Ferradal et al., 2016), as shown in Figure 6.3. As part of this study by Ferradal et al., functional connectivity using DOT was compared to fMRI. The functional connectivity measures obtained using both techniques were notably

similar. However, there was limited coverage across the cortex as the array covered only the occipital, temporal and inferior parietal cortices.

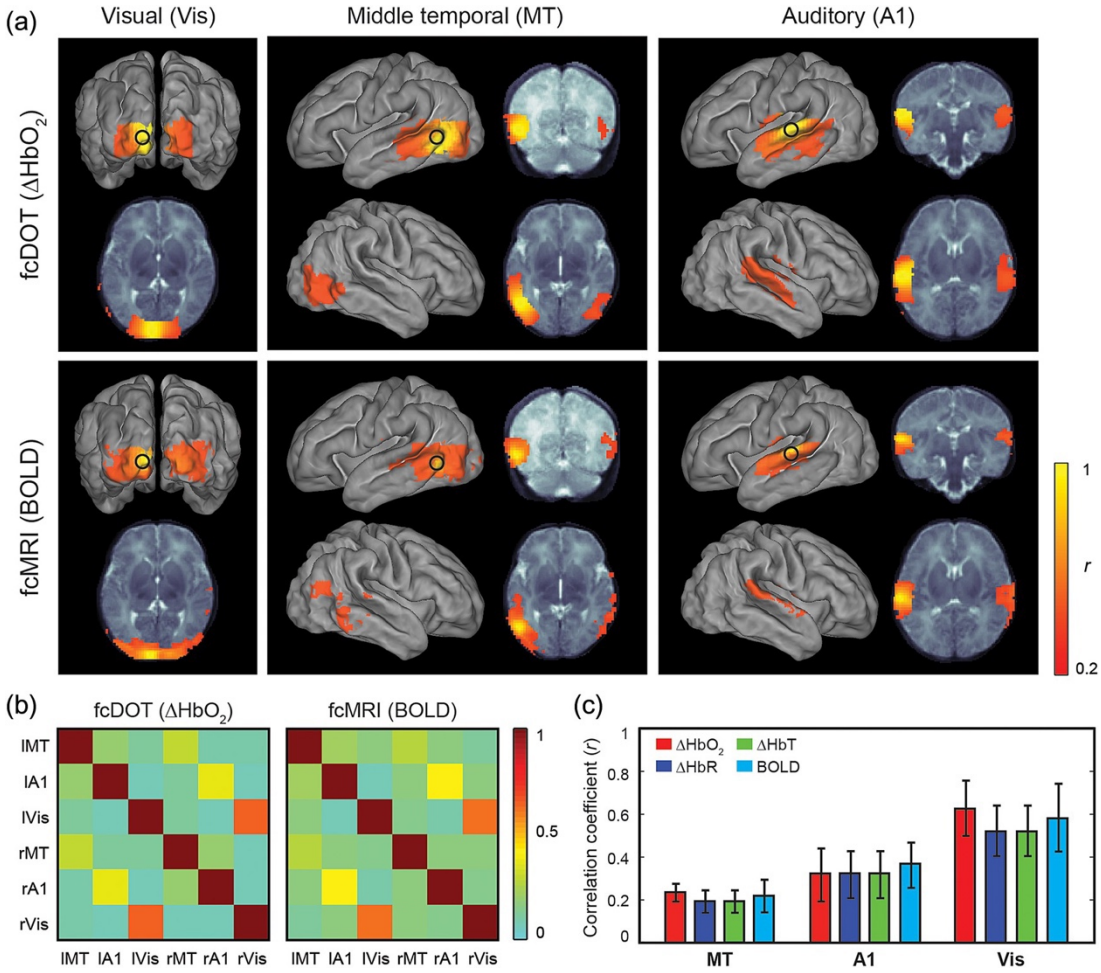

Figure 6.3: Group-level images (a) mapping the average correlation of three seeds across the cortex from a cohort of neonatal infants at term, comparing results between DOT and fMRI approaches. Three seeds were used, one in the visual cortex, one in the middle temporal cortex and another in the auditory cortex. Measures of correlation are shown in (b) and (c). Figure taken from Ferradal et al. (2016) and reprinted with permission from Oxford University Press[15].

Enabling functional connectivity to be studied using whole-cortex DOT, using atlases in place of subject-specific structural priors, can enable the widespread use of DOT to *study* the emergence of neurological conditions in early life.

[15] Ferradal, S. L., Liao, S. M., Eggebrecht, A. T., Shimony, J. S., Inder, T. E., Culver, J. P., & Smyser, C. D., Functional Imaging of the Developing Brain at the Bedside Using Diffuse Optical Tomography, *Cerebral Cortex*, 2016, *26*(4), 1558–1568, by permission of Oxford University Press.

Further, developing DOT to use measures across the brain surface could be a robust tool to *predict* the emergence of neurological conditions in infants. One such research area where network analyses using whole-cortex imaging could be applied is to study the emergence and development of autism spectrum disorder (ASD).

6.1.3 Application to autism spectrum disorder

In the UK, roughly 1 in 100 people have a diagnosis of ASD, a neurodevelopmental disability (British Medical Association, 2020). Early intervention is critical to supporting infants with ASD (Jones et al., 2014) and the importance of early diagnosis is recognised in a recent UK Government strategy (UK Government, 2021). However, high stability and reliability of autism diagnosis has been found only to occur from the age of 2-3 years when behavioural signs begin to present (Cox et al., 1999; Lord, 1995; Lord et al., 2006; Moore & Goodson, 2003; Stone et al., 1999).

Functional connectivity studies using MRI have shown that adults with ASD exhibit atypical patterns of functional connectivity spanning multiple networks of brain regions (Cherkassky et al., 2006; Just et al., 2007). Differences in development are also apparent in at-risk infants in the first year of life (Ciarrusta et al., 2019; McKinnon et al., 2019), but the motion-constraining requirement of MRI severely limits its ability to be used as a widespread tool to predict autism emergence.

6.1.4 Methodological roadblocks

A previous longitudinal study using fNIRS showed that the response to social stimuli of infants aged 4-6 months is predictive of autism diagnosis at 2 years of age (Lloyd-Fox et al., 2018). Whole-cortex DOT has the capability to be a robust tool, based on sampling regions spanning multiple cortical networks, to improve our understanding of the neural emergence of ASD and to enable the widespread prediction of autism emergence. There are, however, some key

methodological roadblocks that need to be overcome to enable recent hardware advances to study functional connectivity across the brain. These include: high-quality infant head models, improving image precision, headgear design, and motion artifact correction.

6.1.4.1 High-quality infant head models

In Chapter 2, an approach was taken to use averaged MRI data for infants aged 1- to 24-months. This was due to a lack of high-quality individual-level data. There exists individual-level data as part of the National Institutes of Health MRI Study of Normal Brain Development data repository (Almli et al., 2007; Evans, 2006), but the data quality is low and some of the models have facial blurring which limits scalp segmentation and determining the position of Nz which is critical to calculating positions on the scalp surface.

Using individual-level models (1) enables validation and reliable mapping between cortical surfaces, (2) aids the anatomical interpretation of reconstructed images, and (3) incorporates realistic data at the individual-level to improve the accuracy of forward models of light transport. One study to highlight is the Brain Imaging in Babies Study (BIBS) at King's College London, which aims to improve understanding of brain development from birth to toddlerhood (https://www.kcl.ac.uk/research/bibs-brain-imaging-in-babies). The study involves the acquisition of MRI data, which could be an excellent dataset to address the lack of available high-quality individual-level data from infants aged 1- to 24-months. This opens the possibility of producing a database of individual-level structural priors as was done in Chapter 4 for neonatal infants.

6.1.4.2 Further improving image precision

Structural priors produced from high-quality individual-level data will improve the accuracy of forward modelling and provide a space that can be used to anatomically interpret images of activation. There are also possibilities to

develop methodologies involving individual-level data to further improve image precision.

The *multi-atlas* methodology (Makropoulos et al., 2014) has been applied widely to MRI tissue segmentation. In outline, tissue segmentations from individuals that have already been segmented are registered to a target MRI intensity image; a segmentation of the target image is obtained by assigning each voxel the tissue label it is most often assigned in the registered tissue segmentations. By using individual-level data, the structural prior is a much more realistic representation of individual anatomy than a population-level atlas.

A proposed *multi-atlas reconstruction* approach would take several matching individual atlases and reconstruct an image using each as a structural prior before averaging the resulting images in a common space. In this way, structural priors are used which are truly representative of individual-level anatomy, and the use of several models aims to not bias the images by the anatomy of a single individual. Surface registrations can then be used to accurately map between cortical surfaces.

6.1.4.3 Headgear design

Whilst hardware for whole-cortex imaging already exists, specialised headgear needs to be manufactured for infants. Whole-cortex imaging aims to sample the entire cortical surface, however there will inevitably be variation in sensitivity between different cortical areas, which may illicit artifactual differences in measures of brain function.

As such, to study networks for a particular condition, it is important to first identify the key networks and ensure that sensitivity is maximised to those key areas. Using individual atlases, light transport can be modelled to determine the optimal placement of sources and detectors on the scalp headgear that

are most likely to maximise sampling sensitivity to relevant brain networks for a given condition.

McKinnon et al. (2019) investigated the relationship between behaviour and functional connectivity in infants at low and high familial risk for ASD. Links between behavioural manifestations of ASD and functional connectivity were found in the temporal default mode network, the dorsal attention network, and the posterior frontoparietal control network (see Figure 6.4). The sensitivity to these cortical networks will therefore need to be maximised, and light transport modelling will illicit the best source and detector positions to achieve this, thus informing headgear production.

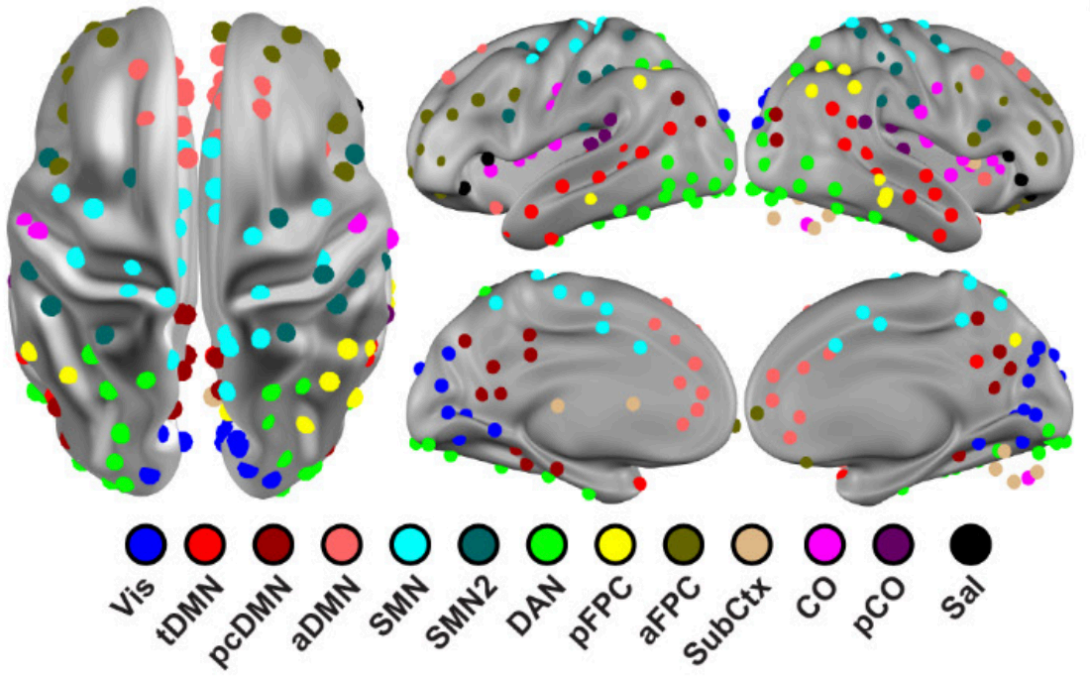

Figure 6.4: The networks investigated by McKinnon et al. (2019). The authors found a relationship between behavioural manifestations of ASD and functional connectivity in the temporal default mode network (tDMN), the dorsal attention network (DAN), and the posterior frontoparietal control network (pFPC). Figure adapted from McKinnon et al. (2019). Reprinted with permission from Elsevier[16].

[16] Reprinted from *Biological Psychiatry: Cognitive Neuroscience and Neuroimaging*, *4*(1), McKinnon, C. J., Eggebrecht, A. T., Todorov, A., Wolff, J. J., Elison, J. T., Adams, C. M., Snyder, A. Z., Estes, A. M., Zwaigenbaum, L., Botteron, K. N., McKinstry, R. C., Marrus, N.,

6.1.4.4 Motion artifacts

The benefit of using DOT is that it enables the brain to be investigated in an environment where movement does not need to be severely restricted, as is the case in MRI. However, movement can still lead to motion artifacts in DOT and this is particularly an issue for infants, who are unlikely to stay still. A major limitation of previous motion correction methodologies is the lack of ground truth data against which the methodologies can be validated. Future motion correction methodologies could be developed involving robotics to induce motion and provide a ground truth against which to compare. Further, this opens the door to the use of artificial intelligence which could be used to learn the link between motion and aberrations in optical signals, leading to a method to correct motion artifacts.

6.2 Further scientific gains

Several publications have resulted from collaborations with other researchers outside the immediate focus of the PhD project detailed in this thesis. Four of these works will be briefly discussed.

6.2.1 Frijia et al. (2021)

A paper published in *NeuroImage* by Frijia et al. (2021) details the first demonstration of a wearable high-density DOT imaging system in the infant population. The work demonstrated the clear and marked improvement of using high-density optical sampling for DOT image reconstruction rather than lower density data acquired using conventional fNIRS arrays. The 6-month model created using the Sanchez et al. data (see Section 2.3.2) was used as a structural prior in the image reconstruction pipeline, where the positions of the cranial landmarks on the 6-month atlas were used to register the model to the dimensions of each infant participant. Example reconstructed images are shown in Figure 6.5.

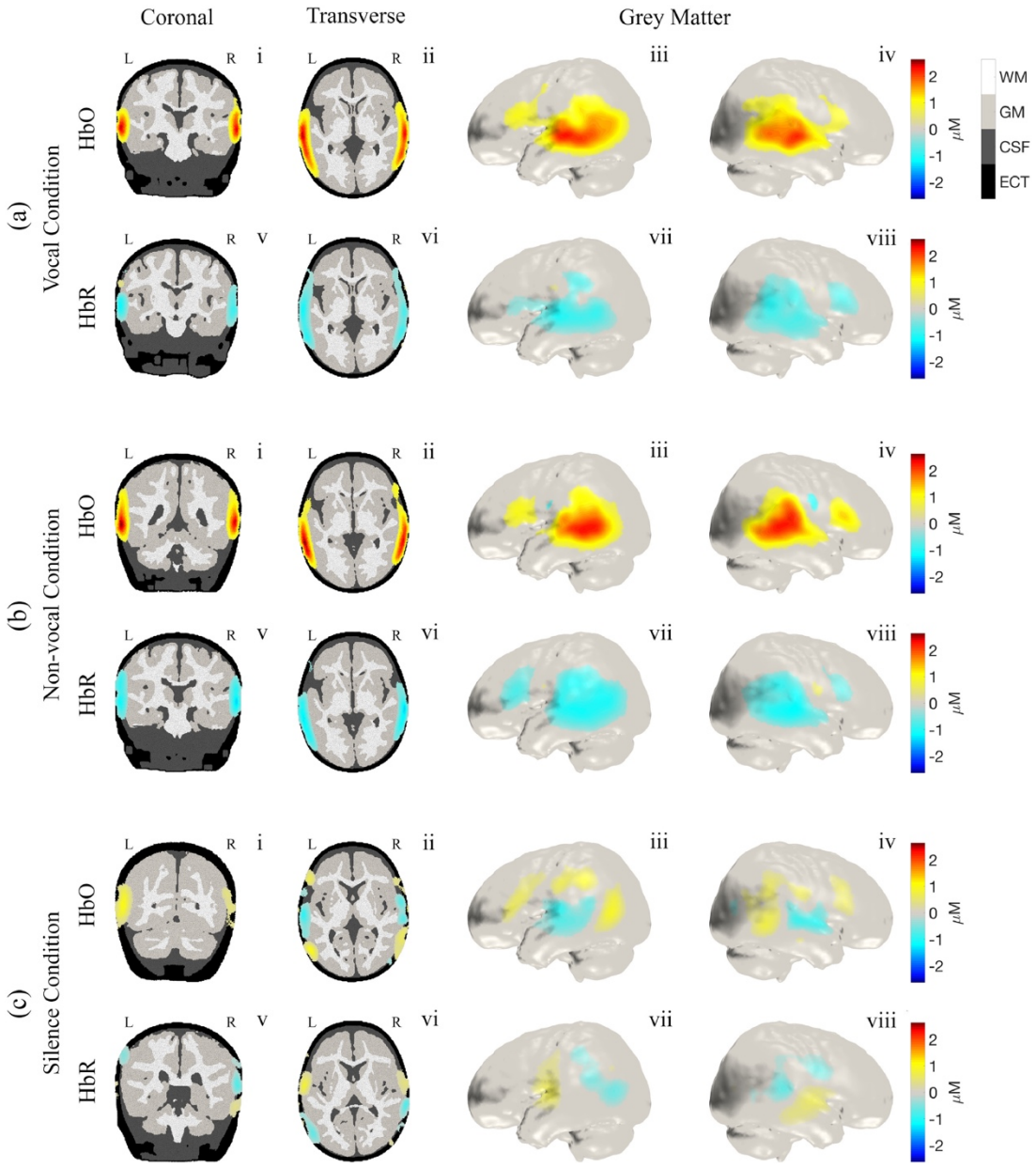

Figure 6.5: Group-level T-statistic images of changes in oxy-haemoglobin (i, ii, iii, iv) and deoxy-haemoglobin (v, vi, vii, viii) concentration in response to the auditory vocal condition (a), non-vocal condition (b) and silence condition (c) relative to baseline. The displayed T-statistic values are thresholded at a value equivalent to $p < 0.05$, Bonferroni corrected on the basis of number of nodes in the grey matter surface mesh. Note: the volume images indicate a well-localised response to the cortex. Figure taken from Frijia et al. (2021), licensed under CC BY 4.0.

6.2.2 Fiske et al. (2021)

An investigation conducted by Fiske et al. (2021) aimed to investigate the neural emergence of inhibitory control, a core executive function, in infants aged 10-months using fNIRS. To improve confidence in the spatial localisation of activation, the Shi et al. atlas (see Section 2.3.3) was employed. An optode registration pipeline based on the Homer2 spring relaxation mechanism (Aasted et al., 2015) was developed which enabled a sensitivity profile to be created for the array. As such, a cortical label was assigned to each channel based on the channel sensitivity centre of mass position, as shown in Figure 6.6. An image reconstruction pipeline was also developed to reconstruct images from a cohort of 59 infants, and the responses in the resulting images were investigated in various time windows post stimulus onset (see Figure 6.7).

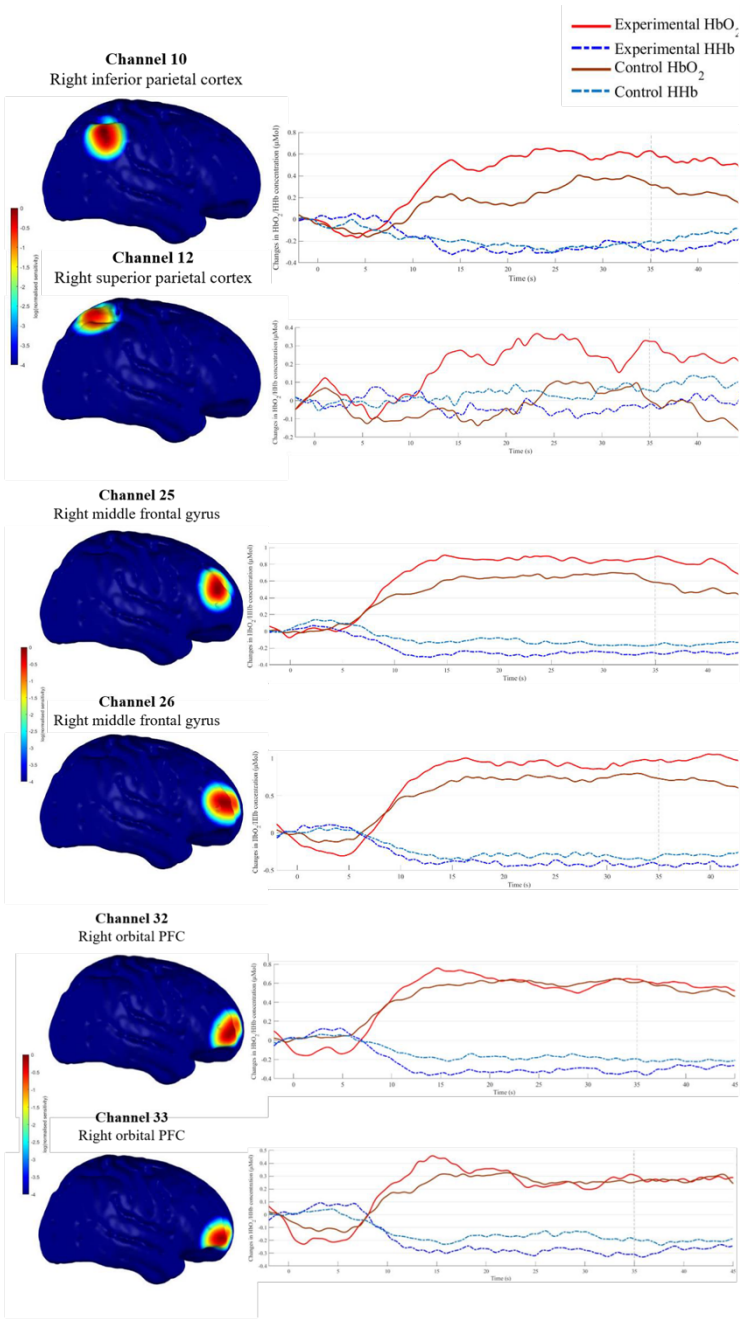

Figure 6.6: Channel sensitivity (left column) and haemodynamic response time-course (right column) of six channels where a significant effect was found in the channel-space analysis. Figure adapted from Fiske et al. (2021), licensed under CC BY 4.0.

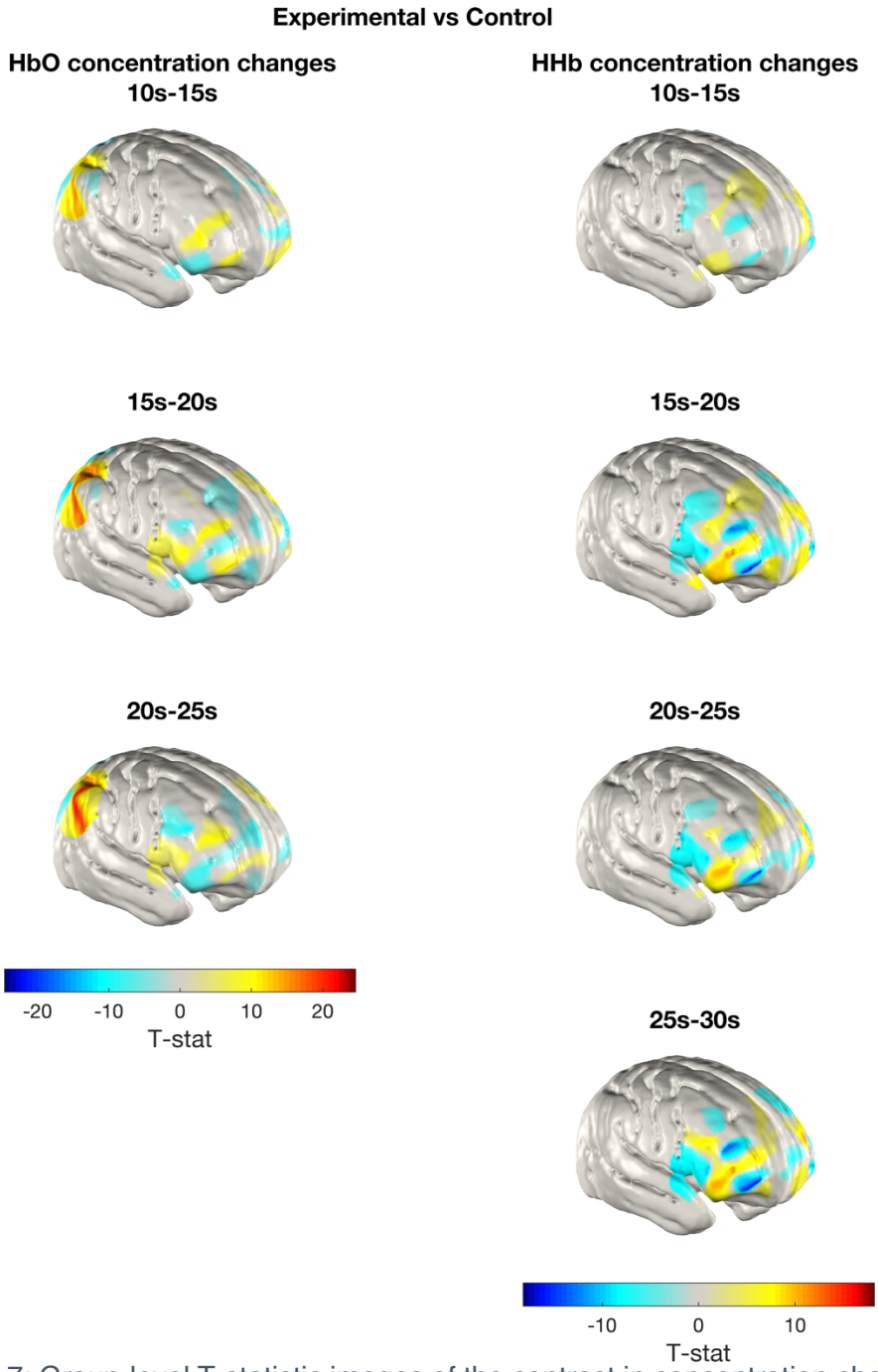

Figure 6.7: Group-level T-statistic images of the contrast in concentration changes of oxy- (left) and deoxy-haemoglobin (right) between experimental and control blocks. The displayed T-statistic values are thresholded at a value of $p < 0.01$. Figure adapted from Fiske et al. (2021), licensed under CC BY 4.0.

6.2.3 Blanco et al. (2021)

Blanco et al. (2021) published a paper in *Neurophotonics* using fNIRS to investigate resting-state functional connectivity in monolingual and bilingual infants. The 6-month population-level atlas, created from the Sanchez at al. data, was used to model the sensitivity distribution of the optical array to determine a cortical position for each channel. Using intensity templates, the 6-month parcellation atlas published by Akiyama et al. (2013) was registered using ANTS registration to the 6-month model created using the Sanchez et al. data. As such, a cortical label could be assigned to each channel position, as is shown in Figure 6.8, to enable a functional connectivity analysis to occur.

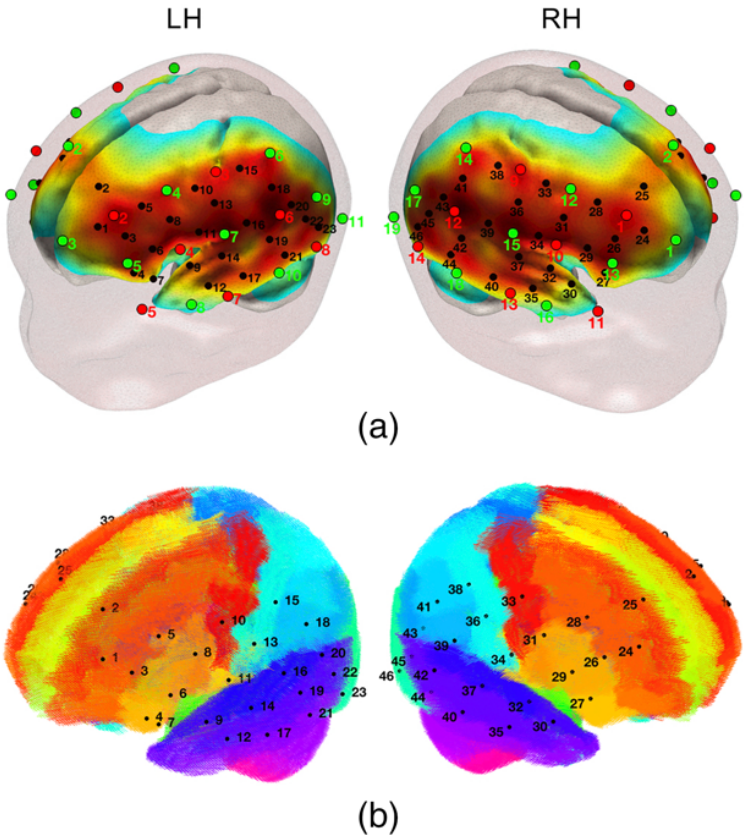

Figure 6.8: (a): Positions of sources (in red) and detectors (in green) on the scalp surface of the 6-month head model, shown overlying the sensitivity profile on the cortical surface. (b): Cortical positions to which channels were localised, shown in reference to the Akiyama et al. parcellation atlas registered to the 6-month head model. Figure taken from Blanco et al. (2021), licensed under CC BY 4.0.

6.2.4 Uchitel et al. (2021)

Work conducted by Uchitel et al., submitted for presentation at the fNIRS 2021 Virtual Conference, aimed to investigate functional connectivity in neonatal infants in different sleep states using high-density DOT. Using a multi-atlas segmentation approach (Blesa et al., 2021), the M-CRIB neonatal parcellation atlas (Alexander et al., 2017) was used to parcellate a neonatal structural prior which enabled a region-based functional connectivity analysis to occur (see Figure 6.9).

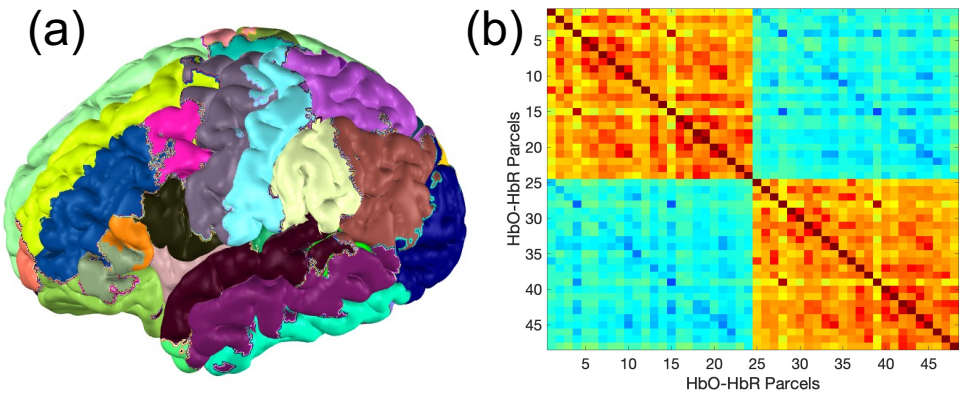

Figure 6.9: The M-CRIB parcellation atlas registered to a neonatal brain (a) and a group functional connectivity matrix using the parcels in the parcellation atlas (b). Figure adapted from work submitted by Uchitel et al. (2021) for the fNIRS 2021 Virtual Conference.

References

Aasted, C. M., Yücel, M. A., Cooper, R. J., Dubb, J., Tsuzuki, D., Becerra, L., Petkov, M. P., Borsook, D., Dan, I., & Boas, D. A. (2015). Anatomical guidance for functional near-infrared spectroscopy: AtlasViewer tutorial. *Neurophotonics*, *2*(2), 020801. https://doi.org/10.1117/1.nph.2.2.020801

Akiyama, L. F., Richards, T. R., Imada, T., Dager, S. R., Wroblewski, L., & Kuhl, P. K. (2013). Age-Specific Average Head Template for Typically Developing 6-Month-Old Infants. *PLOS ONE*, *8*(9), e73821. https://doi.org/10.1371/journal.pone.0073821

Alexander, B., Murray, A. L., Loh, W. Y., Matthews, L. G., Adamson, C., Beare, R., Chen, J., Kelly, C. E., Rees, S., Warfield, S. K., Anderson, P. J., Doyle, L. W., Spittle, A. J., Cheong, J. L. Y., Seal, M. L., & Thompson, D. K. (2017). A new neonatal cortical and subcortical brain atlas: the Melbourne Children's Regional Infant Brain (M-CRIB) atlas. *NeuroImage*, *147*, 841–851. https://doi.org/10.1016/j.neuroimage.2016.09.068

Allievi, A. G., Arichi, T., Tusor, N., Kimpton, J., Arulkumaran, S., Counsell, S. J., Edwards, A. D., & Burdet, E. (2016). Maturation of Sensori-Motor Functional Responses in the Preterm Brain. *Cerebral Cortex*, *26*(1), 402–413. https://doi.org/10.1093/cercor/bhv203

Almli, C. R., Rivkin, M. J., & McKinstry, R. C. (2007). The NIH MRI study of normal brain development (Objective-2): Newborns, infants, toddlers, and preschoolers. *NeuroImage*, *35*(1), 308–325. https://doi.org/https://doi.org/10.1016/j.neuroimage.2006.08.058

Altaye, M., Holland, S. K., Wilke, M., & Gaser, C. (2008). Infant brain probability templates for MRI segmentation and normalization. *NeuroImage*, *43*(4), 721–730. https://doi.org/https://doi.org/10.1016/j.neuroimage.2008.07.060

Arichi, T., Fagiolo, G., Varela, M., Melendez-Calderon, A., Allievi, A., Merchant, N., Tusor, N., Counsell, S. J., Burdet, E., Beckmann, C. F., & Edwards, A. D. (2012). Development of BOLD signal hemodynamic responses in the human brain. *NeuroImage*, *63*(2), 663–673. https://doi.org/10.1016/j.neuroimage.2012.06.054

Arichi, T., Moraux, A., Melendez, A., Doria, V., Groppo, M., Merchant, N., Combs, S., Burdet, E., Larkman, D. J., Counsell, S. J., Beckmann, C. F., & Edwards, A. D. (2010). Somatosensory cortical activation identified by functional MRI in preterm and term infants. *NeuroImage*, *49*(3), 2063–2071. https://doi.org/10.1016/j.neuroimage.2009.10.038

Arridge, S. (1995). Photon-measurement density functions. Part I: Analytical forms. *Applied Optics*, *34*(31), 7395–7409. https://doi.org/10.1364/AO.34.007395

Arridge, S. (1999). Optical tomography in medical imaging. *Inverse Problems*, *15*(2), R41–R93. https://doi.org/10.1088/0266-5611/15/2/022

Arridge, S., & Cooper, R. J. (2015). Optical Image Reconstruction. In A. W. Toga (Ed.), *Brain Mapping: An Encyclopedic Reference* (Vol. 1, pp. 217–222). Elsevier Science. https://doi.org/10.1016/B978-0-12-397025-1.00288-8

Arridge, S., Dehghani, H., Schweiger, M., & Okada, E. (2000). The finite element model for the propagation of light in scattering media: A direct method for domains with nonscattering regions. *Medical Physics*, *27*(1), 252–264. https://doi.org/https://doi.org/10.1118/1.598868

Arridge, S., Schweiger, M., Hiraoka, M., & Delpy, D. T. (1993). A finite element approach for modeling photon transport in tissue. *Medical Physics*, *20*(2), 299–309. https://doi.org/https://doi.org/10.1118/1.597069

Austin, T., Gibson, A. P., Branco, G., Yusof, R. M., Arridge, S. R., Meek, J. H., Wyatt, J. S., Delpy, D. T., & Hebden, J. C. (2006). Three dimensional

optical imaging of blood volume and oxygenation in the neonatal brain. *NeuroImage*, *31*(4), 1426–1433. https://doi.org/10.1016/j.neuroimage.2006.02.038

Azhari, A., Truzzi, A., Neoh, M. J.-Y., Balagtas, J. P. M., Tan, H. H., Goh, P. P., Ang, X. A., Setoh, P., Rigo, P., Bornstein, M. H., & Esposito, G. (2020). A decade of infant neuroimaging research: What have we learned and where are we going? *Infant Behavior and Development*, *58*, 101389. https://doi.org/https://doi.org/10.1016/j.infbeh.2019.101389

Azizollahi, H., Aarabi, A., & Wallois, F. (2016). Effects of uncertainty in head tissue conductivity and complexity on EEG forward modeling in neonates. *Human Brain Mapping*, *37*(10), 3604–3622. https://doi.org/10.1002/hbm.23263

Beauchamp, M. S., Beurlot, M. R., Fava, E., Nath, A. R., Parikh, N. A., Saad, Z. S., Bortfeld, H., & Oghalai, J. S. (2011). The developmental trajectory of brain-scalp distance from birth through childhood: Implications for functional neuroimaging. *PLoS ONE*, *6*(9), e24981. https://doi.org/10.1371/journal.pone.0024981

Begus, K., Lloyd-Fox, S., Halliday, D., Papademetriou, M., Darboe, M. K., Prentice, A. M., Moore, S. E., & Elwell, C. E. (2016). *Using fNIRS to Study Working Memory of Infants in Rural Africa BT - Oxygen Transport to Tissue XXXVII* (C. E. Elwell, T. S. Leung, & D. K. Harrison (eds.); pp. 273–279). Springer New York.

Berke, I. M., Miola, J. P., David, M. A., Smith, M. K., & Price, C. (2016). Seeing through Musculoskeletal Tissues: Improving In Situ Imaging of Bone and the Lacunar Canalicular System through Optical Clearing. *PLOS ONE*, *11*(3), e0150268. https://doi.org/10.1371/journal.pone.0150268

Bevilacqua, F., Piguet, D., Marquet, P., Gross, J. D., Tromberg, B. J., &

Depeursinge, C. (1999). In vivo local determination of tissue optical properties: applications to human brain. *Applied Optics*, *38*(22), 4939–4950. https://doi.org/10.1364/AO.38.004939

Bigio, I. J. (2016). *Quantitative biomedical optics : theory, methods, and applications / Irving Bigio, Sergio Fantini.* (S. Fantini (ed.)). Cambridge, United Kingdom : Cambridge University Press.

Binding, J., Ben Arous, J., Léger, J.-F., Gigan, S., Boccara, C., & Bourdieu, L. (2011). Brain refractive index measured in vivo with high-NA defocus-corrected full-field OCT and consequences for two-photon microscopy. *Optics Express*, *19*(6), 4833. https://doi.org/10.1364/oe.19.004833

Blanco, B., Molnar, M., Carreiras, M., Collins-Jones, L. H., Rosas, E. E. V., Cooper, R. J., & Caballero-Gaudes, C. (2021). Group-level cortical functional connectivity patterns using fNIRS: assessing the effect of bilingualism in young infants. *Neurophotonics*, *8*(2), 1–19. https://doi.org/21005R

Blasi, A., Lloyd-Fox, S., Johnson, M. H., & Elwell, C. (2014). Test–retest reliability of functional near infrared spectroscopy in infants. *Neurophotonics*, *1*(2), 025005. https://doi.org/10.1117/1.NPh.1.2.025005

Blasi, A., Lloyd-Fox, S., Katus, L., & Elwell, C. E. (2019). fNIRS for tracking brain development in the context of global health projects. *Photonics*, *6*(3), 89. https://doi.org/10.3390/photonics6030089

Blesa, M., Galdi, P., Cox, S. R., Sullivan, G., Stoye, D. Q., Lamb, G. J., Quigley, A. J., Thrippleton, M. J., Escudero, J., Bastin, M. E., Smith, K. M., & Boardman, J. P. (2021). Hierarchical Complexity of the Macro-Scale Neonatal Brain. *Cerebral Cortex*, *31*(4), 2071–2084. https://doi.org/10.1093/cercor/bhaa345

Boas, D. A., Culver, J. P., Stott, J. J., & Dunn, A. K. (2002). Three dimensional Monte Carlo code for photon migration through complex

heterogeneous media including the adult human head. *Optics Express*, *10*(3), 159–170. https://doi.org/10.1364/OE.10.000159

Boas, D. A., & Dale, A. M. (2005). Simulation study of magnetic resonance imaging–guided cortically constrained diffuse optical tomography of human brain function. *Applied Optics*, *44*(10), 1957–1968. https://doi.org/10.1364/AO.44.001957

Boas, D. A., Dale, A. M., & Franceschini, M. A. (2004). Diffuse optical imaging of brain activation: Approaches to optimizing image sensitivity, resolution, and accuracy. *NeuroImage*, *23*(SUPPL. 1), S275–S288. https://doi.org/10.1016/j.neuroimage.2004.07.011

Boas, D. A., Gaudette, T., & Arridge, S. R. (2001). Simultaneous imaging and optode calibration with diffuse optical tomography. *Optics Express*, *8*(5), 263–270. https://doi.org/10.1364/OE.8.000263

Boas, D. A., O'Leary, M. A., Chance, B., & Yodh, A. G. (1994). Scattering of diffuse photon density waves by spherical inhomogeneities within turbid media: Analytic solution and applications. *Proceedings of the National Academy of Sciences of the United States of America*, *91*(11), 4887–4891. https://doi.org/10.1073/pnas.91.11.4887

Bornstein, M. H. (2014). Human infancy...and the rest of the lifespan. *Annual Review of Psychology*, *65*(1), 121–158. https://doi.org/10.1146/annurev-psych-120710-100359

Bozek, J., Makropoulos, A., Schuh, A., Fitzgibbon, S., Wright, R., Glasser, M. F., Coalson, T. S., O'Muircheartaigh, J., Hutter, J., Price, A. N., Cordero-Grande, L., Teixeira, R. P. A. G., Hughes, E., Tusor, N., Baruteau, K. P., Rutherford, M. A., Edwards, A. D., Hajnal, J. V., Smith, S. M., … Robinson, E. C. (2018). Construction of a neonatal cortical surface atlas using Multimodal Surface Matching in the Developing Human Connectome Project. *NeuroImage*, *179*, 11–29.

https://doi.org/10.1016/j.neuroimage.2018.06.018

Brett, M., Johnsrude, I. S., & Owen, A. M. (2002). The problem of functional localization in the human brain. *Nature Reviews Neuroscience*, *3*(3), 243–249. https://doi.org/10.1038/nrn756

Brigadoi, S., Aljabar, P., Kuklisova-Murgasova, M., Arridge, S. R., & Cooper, R. J. (2014). A 4D neonatal head model for diffuse optical imaging of pre-term to term infants. *NeuroImage*, *100*, 385–394. https://doi.org/10.1016/j.neuroimage.2014.06.028

Brigadoi, S., & Cooper, R. J. (2015). How short is short? Optimum source–detector distance for short-separation channels in functional near-infrared spectroscopy. *Neurophotonics*, *2*(2), 025005. https://doi.org/10.1117/1.nph.2.2.025005

Brigadoi, S., Galderisi, A., Pieropan, E., Cooper, R. J., Cutini, S., Baraldi, E., Cobelli, C., Dell'Acqua, R., Sparacino, G., & Trevisanuto, D. (2019). *Mapping hemodynamic changes during hypoglycemia in the very preterm neonatal brain: preliminary results*. https://doi.org/10.1117/12.2526974

British Medical Association. (2020). *Autism spectrum disorder*. https://www.bma.org.uk/what-we-do/population-health/improving-the-health-of-specific-groups/autism-spectrum-disorder

Bulgarelli, C., Blasi, A., Pollonini, L., Lloyd-Fox, S., Pirazzoli, L., Perdue, K. L., Nelson, C. A., & Elwell, C. E. (2020). Standardising an infant fNIRS analysis pipeline to investigate neurodevelopment in global health. *Optics InfoBase Conference Papers*, *Part F176-*, paper BM2C.2. https://doi.org/10.1364/BRAIN.2020.BM2C.2

Chalia, M., Lee, C. W., Dempsey, L. A., Edwards, A. D., Singh, H., Michell, A. W., Everdell, N. L., Hill, R. W., Hebden, J. C., Austin, T., & Cooper, R. J. (2016). Hemodynamic response to burst-suppressed and

discontinuous electroencephalography activity in infants with hypoxic ischemic encephalopathy. *Neurophotonics*, *3*(3), 031408. https://doi.org/10.1117/1.nph.3.3.031408

Cheong, W. F., Prahl, S. A., & Welch, A. J. (1990). A review of the optical properties of biological tissues. *IEEE Journal of Quantum Electronics*, *26*(12), 2166–2185. https://doi.org/10.1109/3.64354

Cherkassky, V. L., Kana, R. K., Keller, T. A., & Just, M. A. (2006). Functional connectivity in a baseline resting-state network in autism. *NeuroReport*, *17*(16). https://journals.lww.com/neuroreport/Fulltext/2006/11060/Functional_connectivity_in_a_baseline.6.aspx

Choi, J. H., Wolf, M., Toronov, V. Y., Wolf, U., Polzonetti, C., Hueber, D. M., Safonova, L. P., Gupta, R., Michalos, A., Mantulin, W. W., & Gratton, E. (2004). Noninvasive determination of the optical properties of adult brain: near-infrared spectroscopy approach. *Journal of Biomedical Optics*, *9*(1), 221–229. https://doi.org/10.1117/1.1628242

Ciarrusta, J., O'Muircheartaigh, J., Dimitrova, R., Batalle, D., Cordero-Grande, L., Price, A., Hughes, E., Steinweg, J. K., Kangas, J., Perry, E., Javed, A., Stoencheva, V., Akolekar, R., Victor, S., Hajnal, J., Murphy, D., Edwards, D., Arichi, T., & McAlonan, G. (2019). Social Brain Functional Maturation in Newborn Infants With and Without a Family History of Autism Spectrum Disorder. *JAMA Network Open*, *2*(4), e191868–e191868. https://doi.org/10.1001/jamanetworkopen.2019.1868

Collins-Jones, L. H., Arichi, T., Poppe, T., Billing, A., Xiao, J., Fabrizi, L., Brigadoi, S., Hebden, J. C., Elwell, C. E., & Cooper, R. J. (2021). Construction and validation of a database of head models for functional imaging of the neonatal brain. *Human Brain Mapping*, *42*(3), 567–586. https://doi.org/https://doi.org/10.1002/hbm.25242

Collins-Jones, L. H., Cooper, R. J., Bulgarelli, C., Blasi, A., Katus, L., McCann, S., Mason, L., Mbye, E., Touray, E., Ceesay, M., Moore, S. E., Lloyd-Fox, S., & Elwell, C. E. (2021). Longitudinal infant fNIRS channel-space analyses are robust to variability parameters at the group-level: an image reconstruction investigation. *NeuroImage*, 118068. https://doi.org/https://doi.org/10.1016/j.neuroimage.2021.118068

Cooper, R. J., Caffini, M., Dubb, J., Fang, Q., Custo, A., Tsuzuki, D., Fischl, B., Wells, W., Dan, I., & Boas, D. A. (2012). Validating atlas-guided DOT: A comparison of diffuse optical tomography informed by atlas and subject-specific anatomies. *NeuroImage*, *62*(3), 1999–2006. https://doi.org/10.1016/j.neuroimage.2012.05.031

Cordero-Grande, L., Hughes, E. J., Hutter, J., Price, A. N., & Hajnal, J. V. (2018). Three-dimensional motion corrected sensitivity encoding reconstruction for multi-shot multi-slice MRI: Application to neonatal brain imaging. *Magnetic Resonance in Medicine*, *79*(3), 1365–1376. https://doi.org/10.1002/mrm.26796

Cordero-Grande, L., Teixeira, R. P. A. G., Hughes, E. J., Hutter, J., Price, A. N., & Hajnal, J. V. (2016). Sensitivity Encoding for Aligned Multishot Magnetic Resonance Reconstruction. *IEEE Transactions on Computational Imaging*, *2*(3), 266–280. https://doi.org/10.1109/tci.2016.2557069

Correia, T. M., Gibson, A. P., & Hebden, J. C. (2010). Identification of the optimal wavelengths for optical topography: a photon measurement density function analysis. *Journal of Biomedical Optics*, *15*(5), 1–14. https://doi.org/10.1117/1.3484747

Correia, T. M., Gibson, A. P., Schweiger, M., & Hebden, J. C. (2009). Selection of regularization parameter for optical topography. *Journal of Biomedical Optics*, *14*(3), 1–11. https://doi.org/10.1117/1.3156839

Correia, T. M., Lloyd-Fox, S., Everdell, N., Blasi, A., Elwell, C., Hebden, J. C., & Gibson, A. (2012). Three-dimensional optical topography of brain activity in infants watching videos of human movement. *Physics in Medicine and Biology*, *57*(5), 1135–1146. https://doi.org/10.1088/0031-9155/57/5/1135

Cox, A., Klein, K., Charman, T., Baird, G., Baron-Cohen, S., Swettenham, J., Drew, A., & Wheelwright, S. (1999). Autism Spectrum Disorders at 20 and 42 Months of Age: Stability of Clinical and ADI-R Diagnosis. *The Journal of Child Psychology and Psychiatry and Allied Disciplines*, *40*(5), 719–732. https://doi.org/DOI: 10.1111/1469-7610.00488

Currie, J., & Almond, D. (2011). *Chapter 15 - Human capital development before age five**We thank Maya Rossin and David Munroe for excellent research assistance, participants in the Berkeley Handbook of Labor Economics Conference in November 2009 for helpful comments, and Christine Pal a* (D. Card & O. B. T.-H. of L. E. Ashenfelter (eds.); Vol. 4, pp. 1315–1486). Elsevier. https://doi.org/https://doi.org/10.1016/S0169-7218(11)02413-0

Cusick, S. E., & Georgieff, M. K. (2012). Nutrient Supplementation and Neurodevelopment: Timing Is the Key. *Archives of Pediatrics & Adolescent Medicine*, *166*(5), 481–482. https://doi.org/10.1001/archpediatrics.2012.199

Custo, A., Boas, D. A., Tsuzuki, D., Dan, I., Mesquita, R., Fischl, B., Grimson, W. E. L., & Wells, W. (2010). Anatomical atlas-guided diffuse optical tomography of brain activation. *NeuroImage*, *49*, 561–567. https://doi.org/10.1016/j.neuroimage.2009.07.033

Custo, A., Wells III, W. M., Barnett, A. H., Hillman, E. M. C., & Boas, D. A. (2006). Effective scattering coefficient of the cerebral spinal fluid in adult head models for diffuse optical imaging. *Applied Optics*, *45*(19), 4747–4755. https://doi.org/10.1364/AO.45.004747

Daliri, M., Abrishami Moghaddam, H., Ghadimi, S., Momeni, M., Harirchi, F., & Giti, M. (2010). Skull segmentation in 3D neonatal MRI using hybrid Hopfield Neural Network. *2010 Annual International Conference of the IEEE Engineering in Medicine and Biology Society, EMBC'10*, 4060–4063. https://doi.org/10.1109/IEMBS.2010.5627619

Dall'Orso, S., Steinweg, J., Allievi, A. G., Edwards, A. D., Burdet, E., & Arichi, T. (2018). Somatotopic mapping of the developing sensorimotor cortex in the preterm human brain. *Cerebral Cortex*, *28*(7), 2507–2515. https://doi.org/10.1093/cercor/bhy050

De Macedo Rodrigues, K., Ben-Avi, E., Sliva, D. D., Choe, M. S., Drottar, M., Wang, R., Fischl, B., Grant, P. E., & Zöllei, L. (2015). Afreesurfer-compliantconsistentmanualsegmentationofinfantbrainsspanningthe0–2yearagerange. *Frontiers in Human Neuroscience*, *9*(FEB), 21. https://doi.org/10.3389/fnhum.2015.00021

de Oliveira, S. R., Machado, A. C. C. P., de Paula, J. J., Novi, S. L., Mesquita, R. C., de Miranda, D. M., & Bouzada, M. C. F. (2019). Changes of functional response in sensorimotor cortex of preterm and full-term infants during the first year: An fNIRS study. *Early Human Development*, *133*, 23–28. https://doi.org/10.1016/j.earlhumdev.2019.04.007

Deen, B., Richardson, H., Dilks, D. D., Takahashi, A., Keil, B., Wald, L. L., Kanwisher, N., & Saxe, R. (2017). Organization of high-level visual cortex in human infants. *Nature Communications*, *8*(1), 13995. https://doi.org/10.1038/ncomms13995

Dehaes, M., Kazemi, K., Pélégrini-Issac, M., Grebe, R., Benali, H., & Wallois, F. (2013). Quantitative effect of the neonatal fontanel on synthetic near infrared spectroscopy measurements. *Human Brain Mapping*, *34*(4), 878–889. https://doi.org/10.1002/hbm.21483

Dehghani, H., Arridge, S. R., Schweiger, M., & Delpy, D. T. (2000). Optical tomography in the presence of void regions. *Journal of the Optical Society of America A*, *17*(9), 1659–1670. https://doi.org/10.1364/JOSAA.17.001659

Dehghani, H., Brooksby, B. A., Pogue, B. W., & Paulsen, K. D. (2005). Effects of refractive index on near-infrared tomography of the breast. *Applied Optics*, *44*(10), 1870–1878. https://doi.org/10.1364/AO.44.001870

Dehghani, H., Srinivasan, S., Pogue, B. W., & Gibson, A. (2009). Numerical modelling and image reconstruction in diffuse optical tomography. *Philosophical Transactions of the Royal Society A: Mathematical, Physical and Engineering Sciences*, *367*(1900), 3073–3093. https://doi.org/10.1098/rsta.2009.0090

Delpy, D. T., & Cope, M. (1997). Quantification in tissue near-infrared spectroscopy. *Philosophical Transactions of the Royal Society B: Biological Sciences*, *352*(1354), 649–659. https://doi.org/10.1098/rstb.1997.0046

Delpy, D. T., Cope, M., Zee, P. van der, Arridge, S., Wray, S., & Wyatt, J. (1988). Estimation of optical pathlength through tissue from direct time of flight measurement. *Physics in Medicine and Biology*, *33*(12), 1433–1442. https://doi.org/10.1088/0031-9155/33/12/008

Dempsey, L. A., Persad, M., Powell, S., Chitnis, D., & Hebden, J. C. (2017). Geometrically complex 3D-printed phantoms for diffuse optical imaging. *Biomedical Optics Express*. https://doi.org/10.1364/boe.8.001754

Desikan, R. S., Ségonne, F., Fischl, B., Quinn, B. T., Dickerson, B. C., Blacker, D., Buckner, R. L., Dale, A. M., Maguire, R. P., Hyman, B. T., Albert, M. S., & Killiany, R. J. (2006). An automated labeling system for subdividing the human cerebral cortex on MRI scans into gyral based

regions of interest. *NeuroImage*, *31*(3), 968–980. https://doi.org/https://doi.org/10.1016/j.neuroimage.2006.01.021

Di Lorenzo, R., Pirazzoli, L., Blasi, A., Bulgarelli, C., Hakuno, Y., Minagawa, Y., & Brigadoi, S. (2019). Recommendations for motion correction of infant fNIRS data applicable to multiple data sets and acquisition systems. *NeuroImage*, *200*(April), 511–527. https://doi.org/10.1016/j.neuroimage.2019.06.056

Duncan, A., Meek, J. H., Clemence, M., Elwell, C. E., Tyszczuk, L., Cope, M., & Delpy, D. (1995). Optical pathlength measurements on adult head, calf and forearm and the head of the newborn infant using phase resolved optical spectroscopy. *Physics in Medicine and Biology*, *40*(2), 295–304. https://doi.org/10.1088/0031-9155/40/2/007

Eggebrecht, A. T., & Culver, J. P. (2019). NeuroDOT: An extensible Matlab toolbox for streamlined optical functional mapping. *Clinical and Preclinical Optical Diagnostics II*, *EB101*, 11074_26. https://doi.org/10.1117/12.2527164

Eggebrecht, A. T., Ferradal, S. L., Robichaux-Viehoever, A., Hassanpour, M. S., Dehghani, H., Snyder, A. Z., Hershey, T., & Culver, J. P. (2014). Mapping distributed brain function and networks with diffuse optical tomography. *Nature Photonics*, *8*, 448–454. https://doi.org/10.1038/nphoton.2014.107

Eggebrecht, A. T., White, B. R., Ferradal, S. L., Chen, C., Zhan, Y., Snyder, A. Z., Dehghani, H., & Culver, J. P. (2012). A quantitative spatial comparison of high-density diffuse optical tomography and fMRI cortical mapping. *NeuroImage*, *61*(4), 1120–1128. https://doi.org/https://doi.org/10.1016/j.neuroimage.2012.01.124

Eggermont, P. P. B., Herman, G. T., & Lent, A. (1981). Iterative algorithms for large partitioned linear systems, with applications to image

reconstruction. *Linear Algebra and Its Applications*, *40*, 37–67. https://doi.org/https://doi.org/10.1016/0024-3795(81)90139-7

Evans, A. C. (2006). The NIH MRI study of normal brain development. *NeuroImage*, *30*(1), 184–202. https://doi.org/https://doi.org/10.1016/j.neuroimage.2005.09.068

Everdell, N. L., Gibson, A. P., Tullis, I. D. C., Vaithianathan, T., Hebden, J. C., & Delpy, D. T. (2005). A frequency multiplexed near-infrared topography system for imaging functional activation in the brain. *Review of Scientific Instruments*, *76*(9), 93705. https://doi.org/10.1063/1.2038567

Fang, Q. (2010). Mesh-based Monte Carlo method using fast ray-tracing in Plücker coordinates. *Biomedical Optics Express*, *1*(1), 165–175. https://doi.org/10.1364/BOE.1.000165

Fang, Q., & Boas, D. A. (2009). Tetrahedral mesh generation from volumetric binary and grayscale images. *Proceedings - 2009 IEEE International Symposium on Biomedical Imaging: From Nano to Macro, ISBI 2009*. https://doi.org/10.1109/ISBI.2009.5193259

Ferradal, S. L., Eggebrecht, A. T., Hassanpour, M., Snyder, A. Z., & Culver, J. P. (2014). Atlas-based head modeling and spatial normalization for high-density diffuse optical tomography: In vivo validation against fMRI. *NeuroImage*, *85 (Pt 1)*, 117–126. https://doi.org/10.1016/j.neuroimage.2013.03.069

Ferradal, S. L., Liao, S. M., Eggebrecht, A. T., Shimony, J. S., Inder, T. E., Culver, J. P., & Smyser, C. D. (2016). Functional Imaging of the Developing Brain at the Bedside Using Diffuse Optical Tomography. *Cerebral Cortex*, *26*(4), 1558–1568. https://doi.org/10.1093/cercor/bhu320

Ferrari, M., & Quaresima, V. (2012). A brief review on the history of human

functional near-infrared spectroscopy (fNIRS) development and fields of application. *NeuroImage*, *63*(2), 921–935. https://doi.org/https://doi.org/10.1016/j.neuroimage.2012.03.049

Firbank, M., Arridge, S. R., Schweiger, M., & Delpy, D. T. (1996). An investigation of light transport through scattering bodies with non-scattering regions. *Physics in Medicine and Biology*, *41*(4), 767–783. https://doi.org/10.1088/0031-9155/41/4/012

Fischl, B., Sereno, M. I., & Dale, A. M. (1999). Cortical surface-based analysis: II. Inflation, flattening, and a surface-based coordinate system. *NeuroImage*, *9*(2), 195–207. https://doi.org/10.1006/nimg.1998.0396

Fishell, A. K., Arbeláez, A. M., Valdés, C. P., Burns-Yocum, T. M., Sherafati, A., Richter, E. J., Torres, M., Eggebrecht, A. T., Smyser, C. D., & Culver, J. P. (2020). Portable, field-based neuroimaging using high-density diffuse optical tomography. *NeuroImage*, *215*, 116541. https://doi.org/https://doi.org/10.1016/j.neuroimage.2020.116541

Fiske, A., de Klerk, C., Lui, K. Y. K., Collins-Jones, L. H., Hendry, A., Greenhalgh, I., Hall, A., Scerif, G., Dvergsdal, H., & Holmboe, K. (2021). The Neural Correlates of Inhibitory Control in 10-month-old Infants: A Functional Near-infrared Spectroscopy Study. *PsyArXiv*. https://doi.org/https://doi.org/10.31234/osf.io/r8m9b

Fonov, V. S., Evans, A. C., Botteron, K., Almli, C. R., McKinstry, R. C., & Collins, D. L. (2011). Unbiased average age-appropriate atlases for pediatric studies. *NeuroImage*, *54*(1), 313–327. https://doi.org/10.1016/j.neuroimage.2010.07.033

Fonov, V. S., Evans, A. C., McKinstry, R. C., Almli, C. R., & Collins, D. L. (2009). Unbiased nonlinear average age-appropriate brain templates from birth to adulthood. *NeuroImage*, *47*, S102. https://doi.org/https://doi.org/10.1016/S1053-8119(09)70884-5

Frijia, E. M., Billing, A., Lloyd-Fox, S., Vidal Rosas, E., Collins-Jones, L., Crespo-Llado, M. M., Amadó, M. P., Austin, T., Edwards, A., Dunne, L., Smith, G., Nixon-Hill, R., Powell, S., Everdell, N. L., & Cooper, R. J. (2021). Functional imaging of the developing brain with wearable high-density diffuse optical tomography: A new benchmark for infant neuroimaging outside the scanner environment. *NeuroImage*, *225*, 117490. https://doi.org/10.1016/j.neuroimage.2020.117490

Fukui, Y., Ajichi, Y., & Okada, E. (2003). Monte Carlo prediction of near-infrared light propagation in realistic adult and neonatal head models. *Applied Optics*, *42*(16), 2881–2887. https://doi.org/10.1364/AO.42.002881

Ghadimi, S., Abrishami-Moghaddam, H., Kazemi, K., Grebe, R., Goundry-Jouet, C., & Wallois, F. (2008). Segmentation of scalp and skull in neonatal MR images using probabilistic atlas and level set method. *Proceedings of the 30th Annual International Conference of the IEEE Engineering in Medicine and Biology Society, EMBS'08 - "Personalized Healthcare through Technology,"* 3060–3063. https://doi.org/10.1109/iembs.2008.4649849

Gibson, A. P., Austin, T., Everdell, N. L., Schweiger, M., Arridge, S. R., Meek, J. H., Wyatt, J. S., Delpy, D. T., & Hebden, J. C. (2006). Three-dimensional whole-head optical tomography of passive motor evoked responses in the neonate. *NeuroImage*, *30*(2), 521–528. https://doi.org/https://doi.org/10.1016/j.neuroimage.2005.08.059

Glasser, M. F., Sotiropoulos, S. N., Wilson, J. A., Coalson, T. S., Fischl, B., Andersson, J. L., Xu, J., Jbabdi, S., Webster, M., Polimeni, J. R., Van Essen, D. C., & Jenkinson, M. (2013). The minimal preprocessing pipelines for the Human Connectome Project. *NeuroImage*, *80*, 105–124. https://doi.org/10.1016/j.neuroimage.2013.04.127

Gousias, I. S., Edwards, A. D., Rutherford, M. A., Counsell, S. J., Hajnal, J.

V., Rueckert, D., & Hammers, A. (2012). Magnetic resonance imaging of the newborn brain: Manual segmentation of labelled atlases in term-born and preterm infants. *NeuroImage*, *62*(3), 1499–1509. https://doi.org/10.1016/j.neuroimage.2012.05.083

Hansen, P. C., & O'Leary, D. P. (1993). The Use of the L-Curve in the Regularization of Discrete Ill-Posed Problems. *SIAM Journal on Scientific Computing*, *14*(6), 1487–1503. https://doi.org/10.1137/0914086

Hayashi, T., Kashio, Y., & Okada, E. (2003). Hybrid Monte Carlo-diffusion method for light propagation in tissue with a low-scattering region. *Applied Optics*, *42*(16), 2888–2896. https://doi.org/10.1364/AO.42.002888

Heiskala, J., Pollari, M., Metsäranta, M., Grant, P. E., & Nissilä, I. (2009). Probabilistic atlas can improve reconstruction from optical imaging of the neonatal brain. *Optics Express*, *17*(17), 14977–14992. https://doi.org/10.1364/oe.17.014977

Hennig, B. J., Unger, S. A., Dondeh, B. L., Hassan, J., Hawkesworth, S., Jarjou, L., Jones, K. S., Moore, S. E., Nabwera, H. M., Ngum, M., Prentice, A., Sonko, B., Prentice, A. M., & Fulford, A. J. (2017). Cohort Profile: The Kiang West Longitudinal Population Study (KWLPS)—a platform for integrated research and health care provision in rural Gambia. *International Journal of Epidemiology*, *46*(2), e13–e13. https://doi.org/10.1093/ije/dyv206

Hernandez, S. M., & Pollonini, L. (2020). NIRSplot: A Tool for Quality Assessment of fNIRS Scans. *Biophotonics Congress: Biomedical Optics 2020 (Translational, Microscopy, OCT, OTS, BRAIN)*, paper BM2C.5. https://doi.org/10.1364/BRAIN.2020.BM2C.5

Hielscher, A. H., Alcouffe, R. E., & Barbour, R. L. (1998). Comparison of

finite-difference transport and diffusion calculations for photon migration in homogeneous and heterogeneous tissues. *Physics in Medicine and Biology*, *43*(5), 1285–1302. https://doi.org/10.1088/0031-9155/43/5/017

Hiraoka, M., Firbank, M., Essenpreis, M., Cope, M., Arridge, S. R., Zee, P. van der, & Delpy, D. T. (1993). A Monte Carlo investigation of optical pathlength in inhomogeneous tissue and its application to near-infrared spectroscopy. *Physics in Medicine and Biology*, *38*(12), 1859–1876. https://doi.org/10.1088/0031-9155/38/12/011

Hughes, E. J., Winchman, T., Padormo, F., Teixeira, R., Wurie, J., Sharma, M., Fox, M., Hutter, J., Cordero-Grande, L., Price, A. N., Allsop, J., Bueno-Conde, J., Tusor, N., Arichi, T., Edwards, A. D., Rutherford, M. A., Counsell, S. J., & Hajnal, J. V. (2017). A dedicated neonatal brain imaging system. *Magnetic Resonance in Medicine*, *78*(2), 794–804. https://doi.org/10.1002/mrm.26462

Huppert, T. J., Diamond, S. G., Franceschini, M. A., & Boas, D. A. (2009). HomER: a review of time-series analysis methods for near-infrared spectroscopy of the brain. *Applied Optics*, *48*(10), D280–D298. https://doi.org/10.1016/j.drugalcdep.2008.02.002.A

Jenkinson, M., Pechaud, M., & Smith, S. (2005). BET2: MR-based estimation of brain, skull and scalp surfaces. *Eleventh Annual Meeting of the Organization for Human Brain Mapping*. https://doi.org/citeulike-article-id:1179617

Jones, E. J. H., Gliga, T., Bedford, R., Charman, T., & Johnson, M. H. (2014). Developmental pathways to autism: A review of prospective studies of infants at risk. *Neuroscience & Biobehavioral Reviews*, *39*, 1–33. https://doi.org/https://doi.org/10.1016/j.neubiorev.2013.12.001

Jurcak, V., Tsuzuki, D., & Dan, I. (2007). 10/20, 10/10, and 10/5 systems revisited: Their validity as relative head-surface-based positioning

systems. *NeuroImage*, *34*(4), 1600–1611. https://doi.org/10.1016/j.neuroimage.2006.09.024

Just, M. A., Cherkassky, V. L., Keller, T. A., Kana, R. K., & Minshew, N. J. (2007). Functional and Anatomical Cortical Underconnectivity in Autism: Evidence from an fMRI Study of an Executive Function Task and Corpus Callosum Morphometry. *Cerebral Cortex*, *17*(4), 951–961. https://doi.org/10.1093/cercor/bhl006

Kabdebon, C., Leroy, F., Simmonet, H., Perrot, M., Dubois, J., & Dehaene-Lambertz, G. (2014). Anatomical correlations of the international 10-20 sensor placement system in infants. *NeuroImage*, *99*, 342–356. https://doi.org/10.1016/j.neuroimage.2014.05.046

Kazemi, K., Moghaddam, H. A., Grebe, R., Gondry-Jouet, C., & Wallois, F. (2007). A neonatal atlas template for spatial normalization of whole-brain magnetic resonance images of newborns: Preliminary results. *NeuroImage*, *37*(2), 463–473. https://doi.org/10.1016/j.neuroimage.2007.05.004

Khan, R., Gul, B., Khan, S., Nisar, H., & Ahmad, I. (2021). Refractive index of biological tissues: Review, measurement techniques, and applications. *Photodiagnosis and Photodynamic Therapy*, *33*, 102192. https://doi.org/https://doi.org/10.1016/j.pdpdt.2021.102192

Kocsis, L., Herman, P., & Eke, A. (2006). The modified Beer–Lambert law revisited. *Physics in Medicine and Biology*, *51*(5), N91–N98. https://doi.org/10.1088/0031-9155/51/5/n02

Koyama, T., Iwasaki, A., Ogoshi, Y., & Okada, E. (2005). Practical and adequate approach to modeling light propagation in an adult head with low-scattering regions by use of diffusion theory. *Applied Optics*, *44*(11), 2094–2103. https://doi.org/10.1364/AO.44.002094

Kuklisova-Murgasova, M., Aljabar, P., Srinivasan, L., Counsell, S. J., Doria,

V., Serag, A., Gousias, I. S., Boardman, J. P., Rutherford, M. A., Edwards, A. D., Hajnal, J. V., & Rueckert, D. (2011). A dynamic 4D probabilistic atlas of the developing brain. *NeuroImage*, *54*(4), 2750–2763. https://doi.org/10.1016/j.neuroimage.2010.10.019

Kuklisova-Murgasova, M., Quaghebeur, G., Rutherford, M. A., Hajnal, J. V., & Schnabel, J. A. (2012). Reconstruction of fetal brain MRI with intensity matching and complete outlier removal. *Medical Image Analysis*, *16*(8), 1550–1564. https://doi.org/10.1016/j.media.2012.07.004

Lee, C. W., Cooper, R. J., & Austin, T. (2017). Diffuse optical tomography to investigate the newborn brain. *Pediatric Research*, *82*, 376–386. https://doi.org/10.1038/pr.2017.107

Legon, W., Bansal, P., Tyshynsky, R., Ai, L., & Mueller, J. K. (2018). Transcranial focused ultrasound neuromodulation of the human primary motor cortex. *Scientific Reports*, *8*(1), 10007. https://doi.org/10.1038/s41598-018-28320-1

León-Carrión, J., & León-Domínguez, U. (2012). *Functional Near-Infrared Spectroscopy (fNIRS): Principles and Neuroscientific Applications*. https://doi.org/10.5772/23146

Li, W., Lin, L., & Li, G. (2014). Wavelength selection method based on test analysis of variance: Application to oximetry. *Analytical Methods*, *6*(4), 1082–1089. https://doi.org/10.1039/c3ay41601a

Liao, S. M., Ferradal, S. L., White, B. R., Gregg, N. M., Inder, T. E., & Culver, J. P. (2012). High-density diffuse optical tomography of term infant visual cortex in the nursery. *Journal of Biomedical Optics*, *17*(8), 1–8. https://doi.org/10.1117/1.JBO.17.8.081414

Liu, A., & Joe, B. (1994). Relationship between tetrahedron shape measures. *BIT*, *34*(2), 268–287. https://doi.org/10.1007/BF01955874

Lloyd-Fox, S., Begus, K., Halliday, D., Pirazzoli, L., Blasi, A., Papademetriou, M., Darboe, M. K., Prentice, A. M., Johnson, M. H., Moore, S. E., & Elwell, C. E. (2017). Cortical specialisation to social stimuli from the first days to the second year of life: A rural Gambian cohort. *Developmental Cognitive Neuroscience*, *25*, 92–104. https://doi.org/10.1016/j.dcn.2016.11.005

Lloyd-Fox, S., Blasi, A., & Elwell, C. E. (2010). Illuminating the developing brain: The past, present and future of functional near infrared spectroscopy. *Neuroscience and Biobehavioral Reviews*, *34*(3), 269–284. https://doi.org/10.1016/j.neubiorev.2009.07.008

Lloyd-Fox, S., Blasi, A., Elwell, C. E., Charman, T., Murphy, D., & Johnson, M. H. (2013). Reduced neural sensitivity to social stimuli in infants at risk for autism. *Proceedings of the Royal Society B: Biological Sciences*, *280*(1758), 20123026. https://doi.org/10.1098/rspb.2012.3026

Lloyd-Fox, S., Blasi, A., Everdell, N., Elwell, C. E., & Johnson, M. H. (2011). Selective Cortical Mapping of Biological Motion Processing in Young Infants. *Journal of Cognitive Neuroscience*, *23*(9), 2521–2532. https://doi.org/10.1162/jocn.2010.21598

Lloyd-Fox, S., Blasi, A., McCann, S., Rozhko, M., Katus, L., Mason, L., Austin, T., Moore, S. E., & Elwell, C. E. (2019). Habituation and novelty detection fNIRS brain responses in 5- and 8-month-old infants: The Gambia and UK. *Developmental Science*, *22*(5), e12817. https://doi.org/10.1111/desc.12817

Lloyd-Fox, S., Blasi, A., Mercure, E., Elwell, C. E., & Johnson, M. H. (2012). The emergence of cerebral specialization for the human voice over the first months of life. *Social Neuroscience*, *7*(3), 317–330. https://doi.org/10.1080/17470919.2011.614696

Lloyd-Fox, S., Blasi, A., Pasco, G., Gliga, T., Jones, E. J. H., Murphy, D. G.

M., Elwell, C. E., Charman, T., Johnson, M. H., Baron-Cohen, S., Bedford, R., Bolton, P., Cheung, H. M. C., Davies, K., Elsabbagh, M., Fernandes, J., Gammer, I., Guiraud, J., Liew, M., … Yemane, F. (2018). Cortical responses before 6 months of life associate with later autism. *European Journal of Neuroscience*, *47*(6), 736–749. https://doi.org/10.1111/ejn.13757

Lloyd-Fox, S., Blasi, A., Volein, A., Everdell, N., Elwell, C. E., & Johnson, M. H. (2009). Social perception in infancy: A near infrared spectroscopy study. *Child Development*, *80*(4), 986–999. https://doi.org/10.1111/j.1467-8624.2009.01312.x

Lloyd-Fox, S., Papademetriou, M., Darboe, M. K., Everdell, N. L., Wegmuller, R., Prentice, A. M., Moore, S. E., & Elwell, C. E. (2014). Functional near infrared spectroscopy (fNIRS) to assess cognitive function in infants in rural Africa. *Scientific Reports*, *4*(1), 4740. https://doi.org/10.1038/srep04740

Lloyd-Fox, S., Richards, J. E., Blasi, A., Murphy, D. G. M., Elwell, C. E., & Johnson, M. H. (2014). Coregistering functional near-infrared spectroscopy with underlying cortical areas in infants. *Neurophotonics*, *1*(2), 025006. https://doi.org/10.1117/1.nph.1.2.025006

Lord, C. (1995). Follow-Up of Two-Year-Olds Referred for Possible Autism. *Journal of Child Psychology and Psychiatry*, *36*(8), 1365–1382. https://doi.org/https://doi.org/10.1111/j.1469-7610.1995.tb01669.x

Lord, C., Risi, S., DiLavore, P. S., Shulman, C., Thurm, A., & Pickles, A. (2006). Autism From 2 to 9 Years of Age. *Archives of General Psychiatry*, *63*(6), 694–701. https://doi.org/10.1001/archpsyc.63.6.694

Lunn, P G, Northrop-Clewes, C. A., & Downes, R. M. (1991). Intestinal permeability, mucosal injury, and growth faltering in Gambian infants. *The Lancet*, *338*(8772), 907–910.

https://doi.org/https://doi.org/10.1016/0140-6736(91)91772-M

Lunn, Peter G. (2000). The impact of infection and nutrition on gut function and growth in childhood. *Proceedings of the Nutrition Society*, *59*(1), 147–154. https://doi.org/DOI: 10.1017/S0029665100000173

Makropoulos, A., Aljabar, P., Wright, R., Hüning, B., Merchant, N., Arichi, T., Tusor, N., Hajnal, J. V., Edwards, A. D., Counsell, S. J., & Rueckert, D. (2016). Regional growth and atlasing of the developing human brain. *NeuroImage*, *125*, 456–478. https://doi.org/10.1016/j.neuroimage.2015.10.047

Makropoulos, A., Counsell, S. J., & Rueckert, D. (2018). A review on automatic fetal and neonatal brain MRI segmentation. *NeuroImage*, *170*, 231–248. https://doi.org/10.1016/j.neuroimage.2017.06.074

Makropoulos, A., Gousias, I. S., Ledig, C., Aljabar, P., Serag, A., Hajnal, J. V., Edwards, A. D., Counsell, S. J., & Rueckert, D. (2014). Automatic whole brain MRI segmentation of the developing neonatal brain. *IEEE Transactions on Medical Imaging*, *33*(9), 1818–1831. https://doi.org/10.1109/TMI.2014.2322280

Makropoulos, A., Robinson, E. C., Schuh, A., Wright, R., Fitzgibbon, S., Bozek, J., Counsell, S. J., Steinweg, J., Vecchiato, K., Passerat-Palmbach, J., Lenz, G., Mortari, F., Tenev, T., Duff, E. P., Bastiani, M., Cordero-Grande, L., Hughes, E., Tusor, N., Tournier, J. D., … Rueckert, D. (2018). The developing human connectome project: A minimal processing pipeline for neonatal cortical surface reconstruction. *NeuroImage*, *173*, 88–112. https://doi.org/10.1016/j.neuroimage.2018.01.054

Matsui, M., Homae, F., Tsuzuki, D., Watanabe, H., Katagiri, M., Uda, S., Nakashima, M., Dan, I., & Taga, G. (2014). Referential framework for transcranial anatomical correspondence for fNIRS based on manually

traced sulci and gyri of an infant brain. *Neuroscience Research*, *80*, 55–68. https://doi.org/10.1016/j.neures.2014.01.003

McCoy, D. C., Peet, E. D., Ezzati, M., Danaei, G., Black, M. M., Sudfeld, C. R., Fawzi, W., & Fink, G. (2016). Early Childhood Developmental Status in Low- and Middle-Income Countries: National, Regional, and Global Prevalence Estimates Using Predictive Modeling. *PLoS Medicine*, *13*(6), e1002034. https://doi.org/10.1371/journal.pmed.1002034

McKinnon, C. J., Eggebrecht, A. T., Todorov, A., Wolff, J. J., Elison, J. T., Adams, C. M., Snyder, A. Z., Estes, A. M., Zwaigenbaum, L., Botteron, K. N., McKinstry, R. C., Marrus, N., Evans, A., Hazlett, H. C., Dager, S. R., Paterson, S. J., Pandey, J., Schultz, R. T., Styner, M. A., … Pruett, J. R. (2019). Restricted and Repetitive Behavior and Brain Functional Connectivity in Infants at Risk for Developing Autism Spectrum Disorder. *Biological Psychiatry: Cognitive Neuroscience and Neuroimaging*, *4*(1), 50–61. https://doi.org/https://doi.org/10.1016/j.bpsc.2018.09.008

Mena-Chalco, J. P. (2009). *Ray/Triangle Intersection*. https://uk.mathworks.com/matlabcentral/fileexchange/25058-ray-triangle-intersection

Mendez, M. A., & Adair, L. S. (1999). Severity and Timing of Stunting in the First Two Years of Life Affect Performance on Cognitive Tests in Late Childhood. *The Journal of Nutrition*, *129*(8), 1555–1562. https://doi.org/10.1093/jn/129.8.1555

Möller, T., & Trumbore, B. (1997). Fast, Minimum Storage Ray-Triangle Intersection. *Journal of Graphics Tools*, *2*(1), 21–28. https://doi.org/10.1080/10867651.1997.10487468

Moore, V., & Goodson, S. (2003). How well does early diagnosis of autism stand the test of time? Follow-up study of children assessed for autism at age 2 and development of an early diagnostic service. *Autism*, *7*(1),

47–63. https://doi.org/10.1177/1362361303007001005

Mueller, J. K., Ai, L., Bansal, P., & Legon, W. (2017). Numerical evaluation of the skull for human neuromodulation with transcranial focused ultrasound. *Journal of Neural Engineering*, *14*(6), 066012. https://doi.org/10.1088/1741-2552/aa843e

Myronenko, A., & Song, X. (2010). Point Set Registration: Coherent Point Drift. *IEEE Transactions on Pattern Analysis and Machine Intelligence*, *32*(12), 2262–2275. https://doi.org/10.1109/TPAMI.2010.46

Obrig, H., & Villringer, A. (2003). Beyond the Visible—Imaging the Human Brain with Light. *Journal of Cerebral Blood Flow & Metabolism*, *23*(1), 1–18. https://doi.org/10.1097/01.WCB.0000043472.45775.29

Ogbole, G. I., Adeyomoye, A. O., Badu-Peprah, A., Mensah, Y., & Nzeh, D. A. (2018). Survey of magnetic resonance imaging availability in West Africa. *Pan African Medical Journal*, *30*. https://doi.org/10.11604/pamj.2018.30.240.14000

Oishi, K., Mori, S., Donohue, P. K., Ernst, T., Anderson, L., Buchthal, S., Faria, A., Jiang, H., Li, X., Miller, M. I., van Zijl, P. C. M., & Chang, L. (2011). Multi-contrast human neonatal brain atlas: Application to normal neonate development analysis. *NeuroImage*, *56*(1), 8–20. https://doi.org/10.1016/j.neuroimage.2011.01.051

Okada, E., & Delpy, D. T. (2003). Near-infrared light propagation in an adult head model. I. Modeling of low-level scattering in the cerebrospinal fluid layer. *Applied Optics*, *42*(16), 2906–2914. https://doi.org/10.1364/AO.42.002906

Oostenveld, R., & Praamstra, P. (2001). The five percent electrode system for high-resolution EEG and ERP measurements. *Clinical Neurophysiology*, *112*(4), 713–719. https://doi.org/10.1016/S1388-2457(00)00527-7

Otsu, N. (1979). THRESHOLD SELECTION METHOD FROM GRAY-LEVEL HISTOGRAMS. *IEEE Trans Syst Man Cybern*, *9*(1), 62–66. https://doi.org/10.1109/tsmc.1979.4310076

Papademetriou, M. D., Richards, J., Correia, T., Blasi, A., Murphy, D. G., Lloyd-Fox, S., Johnson, M. H., & Elwell, C. E. (2013). Cortical mapping of 3D optical topography in infants. *Advances in Experimental Medicine and Biology*, *789*, 455–461. https://doi.org/10.1007/978-1-4614-7411-1_61

Perdue, K. L., Jensen, S. K. G., Kumar, S., Richards, J. E., Kakon, S. H., Haque, R., Petri Jr, W. A., Lloyd-Fox, S., Elwell, C., & Nelson, C. A. (2019). Using functional near-infrared spectroscopy to assess social information processing in poor urban Bangladeshi infants and toddlers. *Developmental Science*, *22*(5), e12839. https://doi.org/10.1111/desc.12839

Perrin, F. H. (1948). Whose Absorption Law? *Journal of the Optical Society of America*, *38*(1), 72–74. https://doi.org/10.1364/JOSA.38.000072

Pirondini, E., Babadi, B., Obregon-Henao, G., Lamus, C., Malik, W. Q., Hämäläinen, M. S., & Purdon, P. L. (2018). Computationally efficient algorithms for sparse, dynamic solutions to the EEG source localization problem. *IEEE Transactions on Biomedical Engineering*, *65*(6), 1359–1372. https://doi.org/10.1109/TBME.2017.2739824

Pollonini, L., Bortfeld, H., & Oghalai, J. S. (2016). PHOEBE: a method for real time mapping of optodes-scalp coupling in functional near-infrared spectroscopy. *Biomedical Optics Express*, *7*(12), 5104–5119. https://doi.org/10.1364/boe.7.005104

Powell, C. A., Walker, S. P., Himes, J. H., Fletcher, P. D., & Grantham-McGregor, S. M. (1995). Relationships between physical growth, mental development and nutritional supplementation in stunted children: the

Jamaican study. *Acta Paediatrica*, *84*(1), 22–29. https://doi.org/https://doi.org/10.1111/j.1651-2227.1995.tb13479.x

Ranjbaran, S. M., Kratkiewicz, K., Manwar, R., Fallah, H., Hajimahmoodzadeh, M., & Nasiri Avanaki, M. R. (2019). Numerical study on tumor volume detection in the human brain using photoacoustic tomography. *Proceedings Volume 10878, Photons Plus Ultrasound: Imaging and Sensing 2019*, 108785P. https://doi.org/10.1117/12.2510572

Richards, J. E., Sanchez, C., Phillips-Meek, M., & Xie, W. (2016). A database of age-appropriate average MRI templates. *NeuroImage*, *124*, 1254–1259. https://doi.org/10.1016/j.neuroimage.2015.04.055

Richards, J. E., & Xie, W. (2015). Brains for All the Ages: Structural Neurodevelopment in Infants and Children from a Life-Span Perspective. In *Advances in Child Development and Behavior* (Vol. 48, pp. 1–52). Elsevier. https://doi.org/10.1016/bs.acdb.2014.11.001

Roberts, S. B., Franceschini, M. A., Krauss, A., Lin, P. Y., de Sa, A. B., Có, R., Taylor, S., Brown, C., Chen, O., Johnson, E. J., Pruzensky, W., Schlossman, N., Balé, C., Tony Wu, K. C., Hagan, K., Saltzman, E., & Muentener, P. (2017). A pilot randomized controlled trial of a new supplementary food designed to enhance cognitive performance during prevention and treatment of malnutrition in childhood. *Current Developments in Nutrition*, *1*(11), e000885. https://doi.org/10.3945/cdn.117.000885

Roberts, S. B., Franceschini, M. A., Silver, R. E., Taylor, S. F., de Sa, A. B., Có, R., Sonco, A., Krauss, A., Taetzsch, A., Webb, P., Das, S. K., Chen, C.-Y., Rogers, B. L., Saltzman, E., Lin, P.-Y., Schlossman, N., Pruzensky, W., Balé, C., Chui, K. K. H., & Muentener, P. (2020). Effects of food supplementation on cognitive function, cerebral blood flow, and nutritional status in young children at risk of undernutrition: randomized

controlled trial. *BMJ*, *370*, m2397. https://doi.org/10.1136/bmj.m2397

Robinson, E. C., Garcia, K., Glasser, M. F., Chen, Z., Coalson, T. S., Makropoulos, A., Bozek, J., Wright, R., Schuh, A., Webster, M., Hutter, J., Price, A., Cordero Grande, L., Hughes, E., Tusor, N., Bayly, P. V., Van Essen, D. C., Smith, S. M., Edwards, A. D., … Rueckert, D. (2018). Multimodal surface matching with higher-order smoothness constraints. *NeuroImage*, *167*, 453–465. https://doi.org/10.1016/j.neuroimage.2017.10.037

Robinson, E. C., Jbabdi, S., Glasser, M. F., Andersson, J., Burgess, G. C., Harms, M. P., Smith, S. M., Van Essen, D. C., & Jenkinson, M. (2014). MSM: A new flexible framework for multimodal surface matching. *NeuroImage*, *100*, 414–426. https://doi.org/10.1016/j.neuroimage.2014.05.069

Roche-Labarbe, N., Aarabi, A., Kongolo, G., Gondry-Jouet, C., Dümpelmann, M., Grebe, R., & Wallois, F. (2008). High-resolution electroencephalography and source localization in neonates. *Human Brain Mapping*, *29*(2), 167–176. https://doi.org/10.1002/hbm.20376

Routier, L., Mahmoudzadeh, M., Panzani, M., Azizollahi, H., Goudjil, S., Kongolo, G., & Wallois, F. (2017). Plasticity of neonatal neuronal networks in very premature infants: Source localization of temporal theta activity, the first endogenous neural biomarker, in temporoparietal areas. *Human Brain Mapping*, *38*(5), 2345–2358. https://doi.org/10.1002/hbm.23521

Sanchez, C. E., Richards, J. E., & Almli, C. R. (2012). Neurodevelopmental MRI brain templates for children from 2 weeks to 4 years of age. *Developmental Psychobiology*, *54*(1), 77–91. https://doi.org/10.1002/dev.20579

Sassaroli, A., & Fantini, S. (2004). Comment on the modified Beer–Lambert

law for scattering media. *Physics in Medicine and Biology*, *49*(14), N255–N257. https://doi.org/10.1088/0031-9155/49/14/n07

Scholkmann, F., & Wolf, M. (2013). General equation for the differential pathlength factor of the frontal human head depending on wavelength and age. *Journal of Biomedical Optics*, *18*(10), 105004. https://doi.org/10.1117/1.JBO.18.10.105004

Schweiger, M., & Arridge, S. (2014). The Toast++ software suite for forward and inverse modeling in optical tomography. *Journal of Biomedical Optics*, *19*(4), 040801. https://doi.org/10.1117/1.jbo.19.4.040801

Selb, J. J., Boas, D. A., Chan, S.-T., Evans, K. C., Buckley, E. M., & Carp, S. A. (2014). Sensitivity of near-infrared spectroscopy and diffuse correlation spectroscopy to brain hemodynamics: simulations and experimental findings during hypercapnia. *Neurophotonics*, *1*(1), 1–15. https://doi.org/10.1117/1.NPh.1.1.015005

Serag, A., Aljabar, P., Ball, G., Counsell, S. J., Boardman, J. P., Rutherford, M. A., Edwards, A. D., Hajnal, J. V., & Rueckert, D. (2012). Construction of a consistent high-definition spatio-temporal atlas of the developing brain using adaptive kernel regression. *NeuroImage*, *59*(3), 2255–2265. https://doi.org/10.1016/j.neuroimage.2011.09.062

Shi, F., Yap, P. T., Wu, G., Jia, H., Gilmore, J. H., Lin, W., & Shen, D. (2011). Infant brain atlases from neonates to 1- and 2-year-olds. *PLoS ONE*, *6*(4), e18746. https://doi.org/10.1371/journal.pone.0018746

Singh, A. K., Okamoto, M., Dan, H., Jurcak, V., & Dan, I. (2005). Spatial registration of multichannel multi-subject fNIRS data to MNI space without MRI. *NeuroImage*, *27*(4), 842–851. https://doi.org/10.1016/j.neuroimage.2005.05.019

Singh, H., Cooper, R. J., Wai Lee, C., Dempsey, L., Edwards, A., Brigadoi, S., Airantzis, D., Everdell, N., Michell, A., Holder, D., Hebden, J. C., &

Austin, T. (2014). Mapping cortical haemodynamics during neonatal seizures using diffuse optical tomography: A case study. *NeuroImage: Clinical*, *6*(5), 256–265. https://doi.org/10.1016/j.nicl.2014.06.012

Stone, W. L., Lee, E. B., Ashford, L., Brissie, J., Hepburn, S. L., Coonrod, E. E., & Weiss, B. H. (1999). Can Autism Be Diagnosed Accurately in Children Under 3 Years? *The Journal of Child Psychology and Psychiatry and Allied Disciplines*, *40*(2), 219–226. https://doi.org/DOI: 10.1111/1469-7610.00435

Strangman, G., Franceschini, M. A., & Boas, D. A. (2003). Factors affecting the accuracy of near-infrared spectroscopy concentration calculations for focal changes in oxygenation parameters. *NeuroImage*, *18*(4), 865–879. https://doi.org/https://doi.org/10.1016/S1053-8119(03)00021-1

Swinehart, D. F. (1962). The Beer-Lambert Law. *Journal of Chemical Education*, *39*(7), 333. https://doi.org/10.1021/ed039p333

Tak, S., & Ye, J. C. (2014). Statistical analysis of fNIRS data: A comprehensive review. *NeuroImage*, *85*, 72–91. https://doi.org/https://doi.org/10.1016/j.neuroimage.2013.06.016

Tsuzuki, D., & Dan, I. (2014). Spatial registration for functional near-infrared spectroscopy: From channel position on the scalp to cortical location in individual and group analyses. *NeuroImage*, *85 Pt 1*, 92–103. https://doi.org/10.1016/j.neuroimage.2013.07.025

Tsuzuki, D., Homae, F., Taga, G., Watanabe, H., Matsui, M., & Dan, I. (2017). Macroanatomical landmarks featuring junctions of major sulci and fissures and scalp landmarks based on the international 10-10 system for analyzing lateral cortical development of infants. *Frontiers in Neuroscience*, *11*, 394. https://doi.org/10.3389/fnins.2017.00394

Tuan, T. A., Kim, J. Y., & Bao, P. T. (2018). 3D brain magnetic resonance imaging segmentation by using bitplane and adaptive fast marching.

International Journal of Imaging Systems and Technology, *28*, 223–230. https://doi.org/10.1002/ima.22273

UK Government. (2021). *The national strategy for autistic children, young people and adults: 2021 to 2026*. https://assets.publishing.service.gov.uk/government/uploads/system/uploads/attachment_data/file/1004528/the-national-strategy-for-autistic-children-young-people-and-adults-2021-to-2026.pdf

UNICEF. (2013). Improving Child Nutrition - The achievable imperative for global progress. United Nations Children's fund. In *Division of Communication, UNICEF*. https://doi.org/978-92-806-4686-3

van der Merwe, L. F., Moore, S. E., Fulford, A. J., Halliday, K. E., Drammeh, S., Young, S., & Prentice, A. M. (2013). Long-chain PUFA supplementation in rural African infants: a randomized controlled trial of effects on gut integrity, growth, and cognitive development. *The American Journal of Clinical Nutrition*, *97*(1), 45–57. https://doi.org/10.3945/ajcn.112.042267

Verriotis, M., Fabrizi, L., Lee, A., Cooper, R. J., Fitzgerald, M., & Meek, J. (2016). Mapping cortical responses to somatosensory stimuli in human infants with simultaneous near-infrared spectroscopy and event-related potential recording. *ENeuro*, *3*(2), e0026-16.2016. https://doi.org/10.1523/ENEURO.0026-16.2016

Vidal-Rosas, E. E., Hill, R., Smith, G., Dunne, L., Zhao, H., Powell, S., Everdell, N. L., & Cooper, R. J. (2020). Wearable High-Density Diffuse Optical Tomography (HD-DOT) for Unrestricted 3D Functional Neuroimaging. *Biophotonics Congress: Biomedical Optics 2020 (Translational, Microscopy, OCT, OTS, BRAIN)*, STu1D.3. https://doi.org/10.1364/OTS.2020.STu1D.3

Villringer, A., & Chance, B. (1997). Non-invasive optical spectroscopy and

imaging of human brain function. *Trends in Neurosciences*, *20*(10), 435–442. https://doi.org/https://doi.org/10.1016/S0166-2236(97)01132-6

Wang, L., Jacques, S. L., & Zheng, L. (1995). MCML—Monte Carlo modeling of light transport in multi-layered tissues. *Computer Methods and Programs in Biomedicine*, *47*(2), 131–146. https://doi.org/https://doi.org/10.1016/0169-2607(95)01640-F

Weissleder, R. (2001). A clearer vision for in vivo imaging. *Nature Biotechnology*, *19*(4), 316–317. https://doi.org/10.1038/86684

White, B. R. (2010). Quantitative evaluation of high-density diffuse optical tomography:in vivo resolution and mapping performance. *Journal of Biomedical Optics*, *15*(2), 026006. https://doi.org/10.1117/1.3368999

Wijeakumar, S., Kumar, A., Delgado Reyes, L. M., Tiwari, M., & Spencer, J. P. (2019). Early adversity in rural India impacts the brain networks underlying visual working memory. *Developmental Science*, *22*(5), e12822. https://doi.org/10.1111/desc.12822

World Health Organization. (2007). WHO Child Growth Standards: Head Circumference-for-Age, Arm Circumference-for-Age, Triceps Skinfold-for-Age and Subscapular Skinfold-for-Age: Methods and Development. In *American Journal of Clinical Nutrition*.

Wray, S., Cope, M., Delpy, D. T., Wyatt, J. S., & Reynolds, E. O. R. (1988). Characterization of the near infrared absorption spectra of cytochrome aa3 and haemoglobin for the non-invasive monitoring of cerebral oxygenation. *Biochimica et Biophysica Acta (BBA) - Bioenergetics*, *933*(1), 184–192. https://doi.org/https://doi.org/10.1016/0005-2728(88)90069-2

Xiao, Y., Gerard, I. J., Fonov, V., De Nigris, D., Therrien, C., Aubert-Broche, B., Drouin, S., Kochanowska, A., Tampieri, D., & Collins, D. L. (2016). Atlas-guided transcranial doppler ultrasound examination with a neuro-

surgical navigation system: Case study. *Lecture Notes in Computer Science (Including Subseries Lecture Notes in Artificial Intelligence and Lecture Notes in Bioinformatics)*. https://doi.org/10.1007/978-3-319-31808-0_3

Yücel, M. A., Selb, J. J., Huppert, T. J., Franceschini, M. A., & Boas, D. A. (2017). Functional Near Infrared Spectroscopy: Enabling routine functional brain imaging. *Current Opinion in Biomedical Engineering*, *4*, 78–86. https://doi.org/https://doi.org/10.1016/j.cobme.2017.09.011

Yushkevich, P. A., & Gerig, G. (2017). ITK-SNAP: An Intractive Medical Image Segmentation Tool to Meet the Need for Expert-Guided Segmentation of Complex Medical Images. *IEEE Pulse*, *8*(4), 54–57. https://doi.org/10.1109/MPUL.2017.2701493

Zhan, Y., Eggebrecht, A. T., Culver, J. P., & Dehghani, H. (2012). Image Quality Analysis of High-Density Diffuse Optical Tomography Incorporating a Subject-Specific Head Model . In *Frontiers in Neuroenergetics* (Vol. 4). https://www.frontiersin.org/article/10.3389/fnene.2012.00006

Zhao, H., Frijia, E. M., Rosas, E. V., Collins-Jones, L., Smith, G., Nixon-Hill, R., Powell, S., Everdell, N. L., & Cooper, R. J. (2021). Design and validation of a mechanically flexible and ultra-lightweight high-density diffuse optical tomography system for functional neuroimaging of newborns. *Neurophotonics*, *8*(1), 1–18. https://doi.org/10.1117/1.NPh.8.1.015011